Iodine Chemistry in the Remote Troposphere

Samantha Marie MacDonald

Submitted in accordance with the requirements for the degree of Doctor of Philosophy

The University of Leeds

School of Chemistry

September 2013

The candidate confirms that the work submitted is her own, except where work which has formed part of jointly authored publications has been included. The contribution of the candidate and the other authors to this work has been explicitly indicated below. The candidate confirms that appropriate credit has been given within the thesis where reference has been made to the work of others.

Summary of Contributions to Jointly Authored Work

1. Lucy J. Carpenter, Samantha M. MacDonald, Marvin D. Shaw, Ravi Kumar, Russell W. Saunders, Rajendran Parthipan, Julie Wilson & John M. C. Plane (2013). *Atmospheric iodine levels influenced by sea surface emissions of inorganic iodine.* Nature Geoscience, **6**, 108-111, doi:10.1038/ngeo1687.

    S. M. MacDonald performed the experiments using the iodine oxide particle method, analysed the data and contributed to the production of the paper. L. J. Carpenter wrote the paper and developed the kinetic model. M. D. Shaw and R. Parthipan performed the spectrophotometric experiments. J. Wilson performed the multiple linear regression analysis and J. M. C. Plane provided the modelling work using THAMO. R. Kumar and R. W. Saunders helped with initial set up of the experiments. The experimental work is included in Chapter 3 and the modelling work in Chapter 4.

2. Juan Carlos Gómez Martín , Anoop Mahajan , Timothy Hay , Cristina Prados-Román , Carlos Ordóñez , Samantha MacDonald , John Plane , Mar Sorribas , Manuel Gil , Jimmy Francisco Paredes Mora , Mario Virgilio Agama Reyes , David Oram, Emma Leedham & Alfonso Saiz-Lopez (2013). *Iodine chemistry in the Eastern Pacific marine boundary layer*. Journal of Geophysical Research: Atmospheres, **118**,1-18, doi:10.1002/jgrd.50132.

    S. M. MacDonald participated in 2 field campaigns in September – October 2010 and February – March 2011. S. M. MacDonald helped with the initial set up of the DOAS and ancillary measurement instruments, running of the equipment and data processing and initial analysis of the DOAS data. The final analysis of the LP-DOAS and MAX-DOAS data was performed by A. S. Mahajan, T. Hay, C. Prados-Roman. Correlation studies were performed by J. C. Gomez Martin who also wrote the paper. CH_3I measurements were made by D. Oram and E. Leedham and particle measurements by M. Sorribas and M. Gil. A. Saiz-Lopez was PI of the project and J. M. C. Plane provided the DOAS instruments. This work is discussed in Chapter 5.

Acknowledgements

First and foremost I would like to thank my supervisor Professor John Plane for giving me the opportunity to pursue this project, and providing the funding for me to spend a field campaign in such an incredible place as the Galapagos Islands. You have provided guidance throughout my PhD (along with a raised eyebrow or two) and always asked the right questions to keep me moving forward in this project.

I would also like to thank the many people I have had the pleasure to work with over the last four years. To my fellow group members (past and present) - JC, Vicki, Anna, David, Sandy, Juan Diego, Tamas, Erin, Wuhu, Sarah, Charlotte, Russell, Ravi, Hilke and Anoop - I am grateful for your daily support, conversation and general good company. You made the whole experience much more bearable, and it was always encouraging to know that, however badly things were going, I was never alone. Special thanks must go to Anoop and Hilke who introduced me to the wonders of DOAS analysis and guided me through my MChem project and the initial few months of my PhD, even making a dark and dingy basement office an enjoyable place to work. Ravi also deserves a special mention for all the help he provided in setting up and carrying out the laboratory experiments, as does JC for all his help with the laser experiments.

During my PhD I have been fortunate enough to take part in two field campaigns and work with some truly wonderful people, in some often trying circumstances. In Galapagos I had the pleasure of working with Alfonso, Anoop and JC during the first campaign, where it seemed like it would be a miracle if our equipment ever arrived, let alone if we made any measurements. The same team were assembled in Galicia, Spain (along with the lovely Mar) for a two week campaign, fraught with malfunctioning equipment, vengeful fishermen and plenty of algae. Despite the trials and tribulations, you still managed to make it an enjoyable experience, banishing the bad spirits – and not forgetting the surprise birthday cake!

The second campaign in Galapagos also gave me the chance to meet some more great people from around the globe: Deb, Tim, Maria, Marcos, Emmy and Fei you all helped

to make the experience truly memorable, even when coping with cockroaches, giant spiders, sunburn, military coups and a tsunami warning.

I also owe great thanks to all my friends in Leeds who I've had the pleasure of knowing for the past 8 years, and those who have now moved further afield. I won't name them all for fear of leaving someone out but you know who you are. From the fun adventures to just sitting on the sofa with a cup of tea, you've made living in Leeds the best time of my life (so far) and are the reason I consider it home.

The biggest thanks have to go to my family, Mum, Dad and Rory who have supported me (both morally and financially) throughout my life and education, and always allowed me to pursue my interests, whatever they may be. I've never doubted that I had your complete support and I hope that you'll think it was worth the effort to see me wearing the gown and floppy hat.

I've been lucky enough during my PhD to have the support of not just one loving family, but two. To the Wrights – Malcolm, Ali, Jo and Grace – you've always welcomed me with open arms (quite literally) and I'm so grateful for all the love and encouragement you've given me over the last 7 years.

Finally, to the other Sam, I think you'll be the most pleased to be reading this, knowing that you finally have your fiancé back after all those months of shutting myself away in front of a laptop, occasionally appearing searching for more tea. Thanks for tidying the house, making my dinner and keeping me (mostly) sane. I really couldn't have done it without you.

Abstract

Measurements of the flux of I_2 and HOI from the heterogeneous reaction of gaseous ozone with aqueous iodide were performed by conversion to iodine oxide particles and detection using a nano-differential mobility analyser. Fluxes were measured as a function of $[O_3]$, $[I^-]$, salinity, temperature, and in the presence of organic species. A linear response was observed for O_3 and salinity; iodide showed some deviation at higher concentrations. The temperature dependence of the $I^- + O_3$ reaction was found not to be significant and none of the organic species investigated had a significant effect on the resulting I_2 and HOI fluxes. A kinetic model of the interfacial layer was then employed to verify the experimental results and good agreement was found, apart from observations at high iodide where the I_2 flux was over-predicted. Parameterised expressions for the flux of I_2 and HOI were then produced from the model outputs using multiple linear regression analysis.

The differential optical absorption spectroscopy (DOAS) technique was used to measure IO on the Galapagos Islands in the Eastern Pacific. The long path (LP) DOAS instrument was unable to measure IO above the detection limit (0.9 pptv) and measurements from the multi-axis (MAX) DOAS instrument ranged from below the detection limit to 0.9 ± 0.2 pptv. IO_x (IO + I) was inferred from the measured O_3 concentrations and correlation analyses were conducted with available ancillary measurements (O_3, wind speed, temperature) and satellite data (Chl-*a*, CDOM, SST, and salinity). A significant positive correlation was observed with both SST and salinityand this was linked to variations in sea surface I^-.

The parameterised expressions for I_2 and HOI were then input into the 1-D chemistry-transport model THAMO (Tropospheric HAlogen chemistry MOdel) to compare the predicted IO and IO_x mixing ratios with measurements performed on the Cape Verde islands in the Atlantic ocean and during the HaloCarbon Air Sea Transect-Pacific (HaloCAST-P) cruise in the Eastern Pacific. The predicted fluxes were in agreement at higher wind speeds, however, at lower wind speeds, IO was over-predicted byaround a factor of three; O_3 concentrations were reduced to 2 ppb (20 times lower than calculated) to match the observations.

Contents

List of Figures

List of Tables

List of Abbreviations

AMF	Air Mass Factor
ASA	Aerosol Surface Area
BB-CRDS	Broadband Cavity Ring Down Spectrometry
BL	Boundary layer
HaloCAST-P	HaloCarbon Air Sea Transect-Pacific
CCD	Charge Coupled Device
CCN	Cloud Condensation Nuclei
CDOM	Chromophoric Dissolved Organic Matter
CEAS	Cavity Enhanced Absorption Spectroscopy
CE-DOAS	Cavity Enhanced Differential Optical Absorption Spectroscopy
CHARLEX	Climate and HAlogen Reactivity tropical EXperiment
DL	Detection Limit
DMA	Differential Mobility Analyser
DMS	Dimethyl Sulphide
DOAS	Differential Optical Absorption Spectroscopy
DOM	Dissolved Organic Matter
dSCD	differential slant column density
ENSO	El-Niño-Southern Oscillation
FCE	Faraday Cup Electrometer
FCU	Flow Control Unit
FFT	Fast Fourier Transform
FWHM	Full-Width Half-Maximum

GC-MS	Gas Chromatography Mass Spectrometry
HDPE	High Density Polyethylene
HOX	Hypohalous Acids
HSI-DOAS	Hemispheric Scanning Imaging Differential Optical Absorption Spectroscopy
HX	Hydrogen Halides
IBBCEAS	Incoherent Broadband Cavity Enhanced Absorption Spectroscopy
ICP-MS	Inductively Coupled Plasma Mass Spectrometry
IDOAS	Imaging Differential Optical Absorption Spectroscopy
IOP	Iodine Oxide Particle
IR	Infrared
ITCZ	Intertropical Convergence Zone
LED	Light Emitting Diode
LIF	Lased Induced Fluorescence
LP	Long Path
LT	Local Time
MAX	Multi Axis
MBL	Marine Boundary Layer
MIE	Multistep Implicit Explicit
MODIS	Moderate Resolution Imaging Spectroradiometer
MSA	Methane Sulfonic Acid
NECC	North Equatorial Countercurrent
Nd:YAG	Neodymium-doped Yttrium Aluminium Garnet
NMHC	Non-Methane Hydrocarbons

OD	Optical Density
PDA	Photodiode Array
PI-TOF-MS	Photo Ionisation Time-of-Flight Mass Spectrometry
ppb	Parts per Billion
pph	Parts per Hundred
ppt	Parts per Trillion
RGM	Reactive Gaseous Mercury
RH	Relative Humidity
RHaMBLe	Reactive Halogens in the Marine Boundary Layer
RMS	Root mean squared
ROFLEX	Resonance and Off-Resonance Fluorescence by Lamp Excitation
RTM	Radiative Transfer Model
SAA	Solar Azimuth Angle
SCD	Slant Column Density
SCIAMACHY	Scanning Imaging Absorption Spectrometer for Atmospheric Chartography
SDS	Sodium Dodecyl Sulphate
SEC	South Equatorial Current
SHADOZ	Southern Hemisphere Additional Ozonesondes
SMPS	Scanning Mobility Particle Sizer
SOA	Secondary Organic Aerosol
SOI	Soluble Organic Iodine
SST	Sea Surface Temperature
SUVA	Specific Ultraviolet Absorbance

SZA   Solar Zenith Angle

THAMO   Tropospheric HAlogen chemistry MOdel

UCPC   Ultrafine Concentration Particle Counter

UTLS   Upper-Troposphere Lower-Statosphere

UV   Ultraviolet

VCD   Vertical Column Density

VMR   Volume Mixing Ratio

Chapter 1

Introduction to the Earth's Atmosphere

The Earth's atmosphere consists of a layer of gases which surround the planet extending from the surface up to several hundred km and retained by the Earth's gravity. The atmosphere contains a variety of chemical species, with N_2 and O_2 being the most abundant (at around 78 and 21 % respectively). The chemistry of the Earth's atmosphere is influenced by a multitude of factors and the composition evolved over time due to inputs from the lithosphere, from the seas and oceans, extra-terrestrial sources and the biosphere. Understanding the chemical processes in the atmosphere requires knowledge of all of these systems and the interactions between them. The chemistry of the atmosphere is of huge importance due to its influence on living organisms and its ability to sustain life on Earth. Changes in the chemical composition of the atmosphere through natural and anthropogenic forces will influence the balance between the biological, chemical and physical processes occurring on Earth. The study of atmospheric chemistry aims to increase our knowledge of these processes and explain past and present changes in the atmosphere, and those that will occur in the future of the planet.

1.1 Structure of the Earth's Atmosphere

The structure of the atmosphere can be split into several distinct layers, deriving from the temperature dependence in these regions with increasing altitude (Figure 1.1).

The lowermost layer of the atmosphere is the troposphere, reaching from the surface up to around 10-15 km (the tropopause) which is characterized by a decrease in temperature with increasing altitude and fast vertical mixing. The reason for this decrease in temperature is that the air nearest the surface of the Earth is heated by the infrared (IR) radiation from the surface and the heating decreases with height. The

troposphere can be further split into the planetary boundary layer which is the lowest 1 km of the troposphere and the free troposphere from 1 km upwards. The boundary layer is directly affected by changes at the surface of the Earth with rapid fluctuations in temperature and moisture, leading to a turbulent atmosphere. The boundary layer is also directly affected by exchange of gases between the oceans, terrestrial surfaces and with the biosphere and shows rapid vertical mixing. The boundary layer shows variation across the globe from around 200 m at the poles to around 1 km at the equator, and also varies diurnally, increasing in height during the day due to convective heating from the surface (Seinfeld, 2006). The marine boundary layer (MBL) refers to the layer directly above the oceans which will be particularly influenced by sea-air transfer of gases at the surface and changes in temperature due to variations in ocean currents.
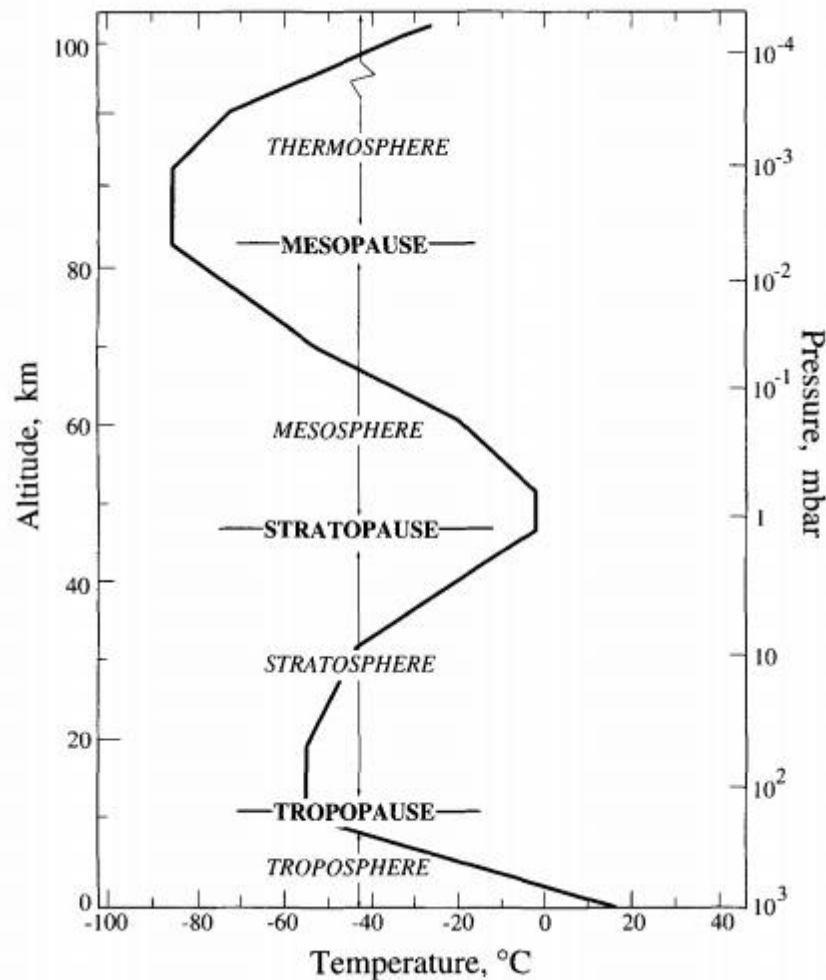
Figure 1.1 The structure of the atmosphere showing the four different layers based on the variation of temperature with altitude. Figure taken from Seinfeld and Pandis (2006).

The next layer is the stratosphere where, in contrast to the troposphere, temperature begins to increase with height owing to the presence of O_3 which absorbs high energy ultraviolet (UV) radiation from the sun. This photolyses O_3 to form O_2 and O atoms or excited $O(^1D)$ which is then quenched to the ground state via collisions with a bath gas (either O_2 or N_2). This cycle of reactions (Figure 1.2) was first proposed by Chapman in the 1930s (Chapman, 1930) and describes well the overall structure of O_3 in the stratosphere, however, results in an over-prediction in the absolute values by a factor of around two. Both the destruction of O_3 and subsequent recombination of O_2 and O are exothermic processes, releasing heat into the stratosphere. At higher altitudes O atoms are more abundant due to more high energy UV radiation ($\lambda < 242$ nm).
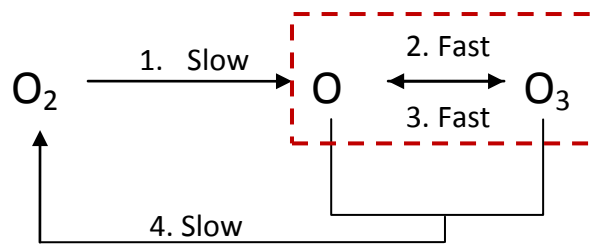
Figure 1.2 The Chapman cycle

In the upper stratosphere a steady state can be assumed to exist where the positive temperature gradient with height leads to slow vertical mixing as a result of a lack of convection and turbulence, however, due to the stratification, rapid horizontal mixing occurs in the stratosphere. The stratosphere extends from the tropopause up to the stratopause at 45–55 km. The temperature increases from around 217 K at the tropopause to around 271 K at the stratopause, not much lower than at the Earth's surface (288 K) (Seinfeld, 2006).

Above this lies the mesosphere which extends to the mesopause at 80–90 km. This is the coldest part of the atmosphere due to the decrease in temperature with height observed in the mesosphere. This decrease in temperature is caused by decreasing solar heating and increased cooling by CO_2 radiative emission. The mesosphere is characterized by strong zonal winds, gravity and planetary waves which travel upwards from the lower atmosphere and dissipate in the mesosphere leading to large scale circulations. The mesosphere is also the part of the ionosphere where the D layer occurs, extending from around 60–90 km; minor constituents such as NO or metal atoms are ionized by H Lyman-α radiation at 121.6 nm (Wayne, 2000). It also contains metal layers extending from and consisting of elements such as sodium, iron and potassium, which arise from the ablation of meteoric material in the upper atmosphere. In addition, formation of polar mesospheric clouds occurs in the mesosphere.

The thermosphere then extends from the mesopause up to around 500 km where high temperatures exist due to absorption by N_2 and O_2 of short wavelength radiation. At

this altitude the atmosphere is extremely thin and collisions between atoms or molecules become infrequent, hence inefficient equilibration of energy between energy modes occurs, with an excess of translational energy leading to the rise in temperature with altitude. The E and F ionospheric regions lie within the thermosphere; the presence of ionizing solar radiation (extreme UV and X-ray) leads to the formation of positive ions. The E region extends from around 100–150 km and the major ions in this region are NO^+ and O_2^+ formed from extreme UV radiation between 80–103 nm and X-rays from 1–10 nm in wavelength. The F region begins around 150 km with the dominant ions consisting of N^+ and O^+, although at the highest altitudes H^+ and He^+ ions begin to dominate due to gravitational separation. Above the thermosphere lies the exosphere where gas molecules possessing sufficient energy can escape the gravitational field of the Earth into space (Seinfeld, 2006; Wayne, 2000).

Pressure in the atmosphere also varies with height due to the effect of gravity and there is no distinct boundary between the atmosphere and space as the mass gradually fades outwards. The majority of the mass of the atmosphere is therefore contained within the troposphere (around the first 10 km) accounting for around 75 % of the total mass of the atmosphere. The pressure drops exponentially with height according to Equation 1.1:

$$p_z = p_0 e^{\frac{z}{H_z}} \qquad (1.1)$$

where p_z is the pressure at a height, z, p_0 is the pressure at the surface and H is the scale height of the atmosphere which is defined as the height at which the pressure drops to $1/e$ of that at the surface. H_z can be described by Equation 1.2.

$$H_z = \frac{k_B T}{mg} \qquad (1.2)$$

where k_B is Boltzmann's constant (1.38 x 10^{-23} J K^{-1}), T is the temperature, m is the molecular mass and g is the acceleration due to gravity. It should be noted that the temperature is assumed to be constant in Equation 1.1; and therefore a scale height must be calculated at a set temperature. Using the average temperature of the

troposphere, 253 K, gives a scale height of 7.4 km. This means that the pressure falls by about an order of magnitude every 16 km (Seinfeld, 2006).

Variations in pressure in the atmosphere also lead to winds which are responsible for transport and mixing of chemical species. Wind can be thought of as the air flow response to pressure differentials between locations on the planet and remove these differences by transporting heat (in both latent and sensible forms). At the Earth's surface, winds are highly variable and turbulent, whereas higher up, away from surface features and friction, the wind motions become much more regular. The atmospheric general circulation describes the pattern of global winds, averaged over several days or weeks. This can be reasonably approximated using a three cell model, where the winds are driven by the energy imbalance caused by the larger input of solar energy at the equator than at the poles, and also the *Coriolis* force which results from the rotation of the Earth about its axis. These winds are summarised in Figure 1.3.
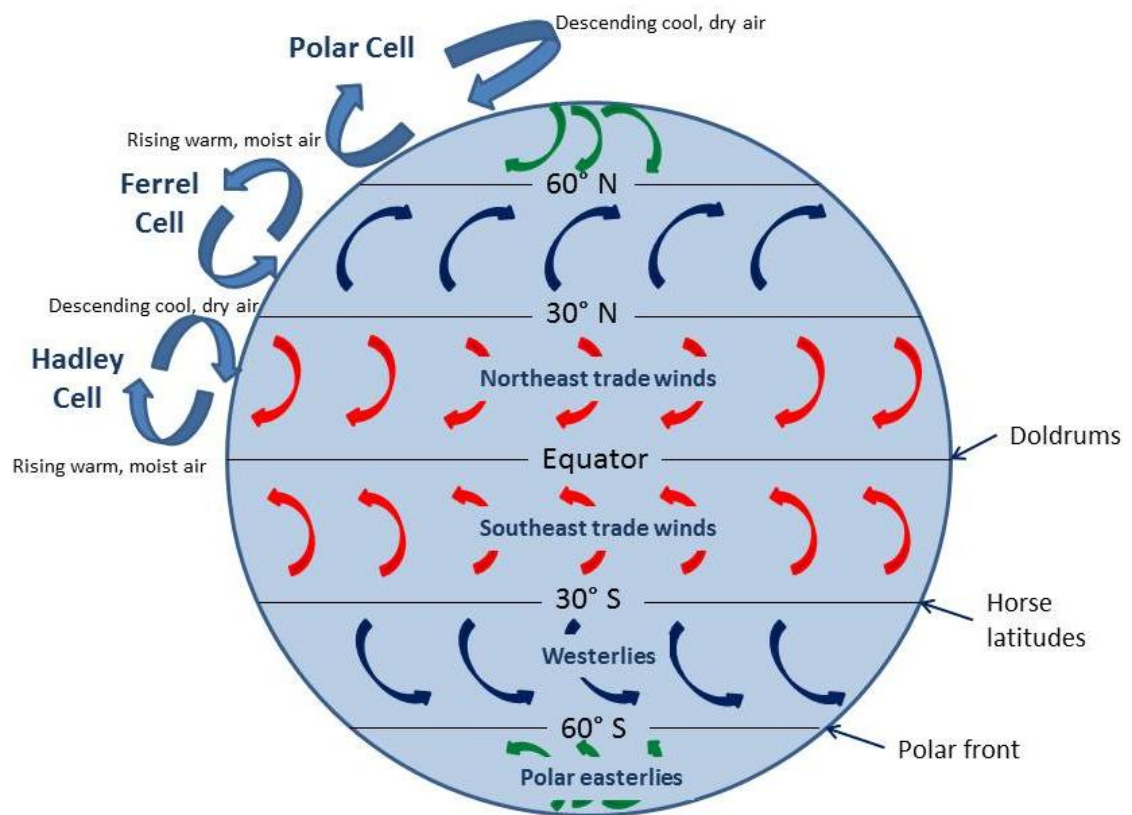
Figure 1.3 General circulation of the atmosphere showing the three cell model.

At the equator, hot air rises and is forced towards the cooler poles by higher pressures in the higher temperature regions. Each hemisphere has its own circulation cell known as a Hadley cell and these converge near the equator at the intertropical convergence zone (ITCZ). The transition occurs a few degrees north of the equator and this region is characterised by very strong upward motion and heavy rainfall. This is caused by the returning surface air becoming saturated with water as it passes over the ocean; as it rises, the water condenses, resulting in heavy precipitation. This also releases latent heat causing convective instability, resulting in a reduced lapse rate and increase in the pressure differential.

At 30° latitude, the surface high pressure causes air near the ground to diverge and forces the air from above downwards to fill in for the surface air moving away. The air flowing northward from the equator higher up in the atmosphere is warm and moist compared to the air nearer the poles and causes a strong temperature gradient between the two different air masses. This is what causes the jet stream which moves from west to east in both the Northern and Southern Hemispheres. Some of the air that sinks at 30° latitude returns to the equator to complete the Hadley cell, producing the northeast trade winds in the Northern Hemisphere and the southeast trade winds in the Southern Hemisphere.

The air descending to the surface at 30° latitude that does not move southward towards the equator, moves north and is deflected to the right by the *Coriolis* force. The winds north and south of the trade wind belt tend to blow from west to east (westerlies). Baroclinic instabilities arise in this region when the temperature gradients and upper level winds are sufficiently large, causing the westerly flow to break into large-scale eddies. These baroclinic instabilities are the source of the weather experienced in the mid latitudes. At 60°, warm, moist air rises and some of this air, when it reaches the tropopause, moves southwards towards the region of convergence above 30°N, completing the Ferrel cell.

At the polar front (~60° latitude), the air that does not move towards the equator instead moves towards the poles, where it converges and sinks. The sinking cold air

then flows towards the equator at the surface and the *Coriolis* force drives the winds towards the west, producing the polar easterlies above 60°. This polar cell is the weakest of the three circulation cells (Wayne, 2000).

1.2 Chemical Composition of the Atmosphere

The main constituents of the Earth's atmosphere remain almost constant over time and predominantly consist of N_2 and O_2 (99 %) with small variations in trace gas concentrations. This is true up to around 100 km, above which gravitational settling becomes important. This allows the atmosphere to be separated into two sections, the "homosphere" below 100 km and the "heterosphere" above. As well as N_2 and O_2 there are a number of other inert gases which dominate the chemical composition of the atmosphere along with a vast number of trace gases. The dominant chemical species in the atmosphere and their percentage concentrations for a dry atmosphere (i.e. containing no water vapour) are summarised in Table 1.1.

In addition to the chemical species in Table 1.1, water vapour (H_2O) is also present in significant quantities in the atmosphere but at variable concentrations, averaging around 0.4 % over the whole atmosphere and around 1–4 % at the surface. Ozone (O_3) is another species which shows significant variability with height, but is of great importance in the chemistry of the atmosphere and can range from parts per billion (ppb) to parts per million (ppm). O_3 plays a vital role in protecting life on Earth by absorbing potentially harmful UV radiation in the stratosphere. In the troposphere, however, O_3 is harmful to health, causing respiratory problems in humans and animals and is damaging to crops (Fumagalli et al., 2001; Kampa and Castanas, 2008).

Table 1.1 The main chemical constituents of the atmosphere and their percentage concentrations. Data from NASA NSSDC (**http://nssdc.gsfc.nasa.gov/planetary/factsheet/earthfact.html**).

Chemical Species	Percentage concentration / %
Nitrogen, N_2	78.084
Oxygen, O_2	20.946
Argon, **Ar**	0.934
Carbon Dioxide, CO_2	0.0394
Neon, **Ne**	0.00182
Helium, **He**	0.000524
Methane, CH_4	0.000179
Krypton, **Kr**	0.000114
Hydrogen, H_2	0.000055

There are also a vast number of trace gas species which exist in ppm, ppb or ppt (parts per trillion) concentrations that include volatile organic compounds (VOCs), nitrogen oxides (NO and NO_2), alkyl halides (e.g. CH_3I, CH_2I_2), sulphur-containing compounds such as dimethyl sulphide (DMS) and halogen oxides (IO, BrO).

1.3 Solar Radiation and Photochemistry in the Troposphere

The radiation reaching the Earth's surface from the sun is altered from the radiation reaching the top of the atmosphere due to absorption by chemical species and aerosols in the atmosphere and due to scattering by aerosols and clouds (Figure 1.4). Different wavelength regions are affected depending on the molecules which absorb in these regions. For instance, in the region below 290 nm, almost all of the radiation from the sun has been absorbed by O_2 and O_3 before it reaches the Earth's surface.

However, atmospheric absorption between 300 and 800 nm is less strong leading to so called "window regions" in the spectrum. The degree to which species absorb electromagnetic radiation is dependent on the properties of the molecule. Molecules such as H_2O have a permanent dipole moment whereby positive charge is localised on the H atoms whereas negative charge accumulates at the O atom. This results in strong interactions between the electromagnetic wave and the dipole.
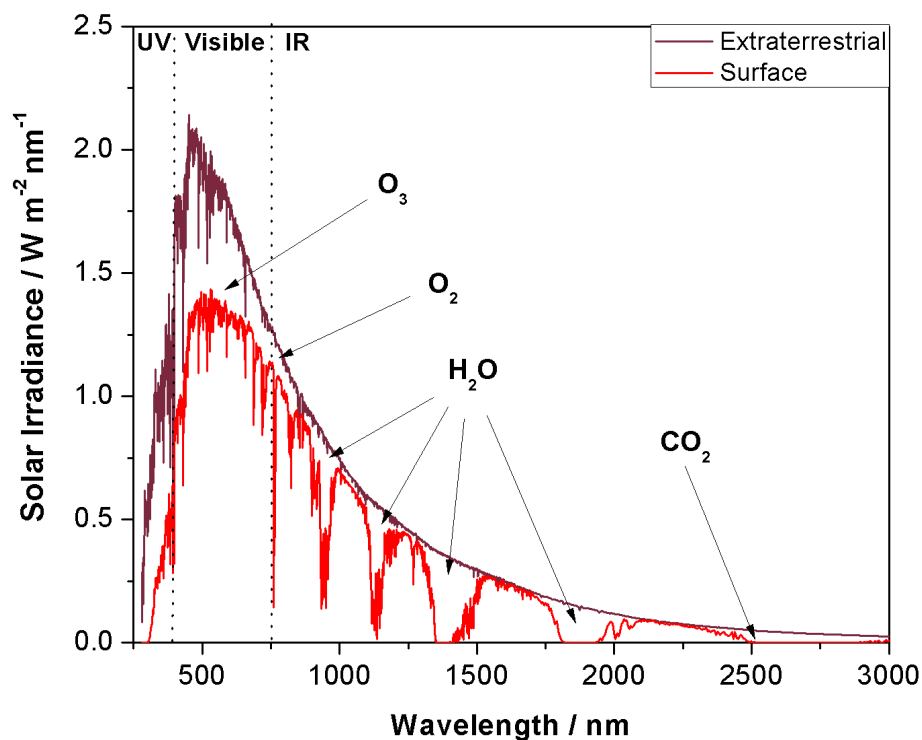
Figure 1.4 Solar irradiance at the top of the atmosphere (purple line) and at the Earth's surface (red line). The difference is due to scattering and absorption by the molecules indicated. Data from: American Society for Testing and Materials, Terrestrial Reference Spectra for Photovoltaic Performance Evaluation.

The Earth's surface will emit radiation in the IR region of the spectrum, the region from around 7–13 μm is a window region, with the majority of the radiation escaping to space. A number of greenhouse gases absorb efficiently in this region such as N_2O, O_3, CH_4 and chlorofluorocarbons (CFCs), and therefore small fluctuations in their concentrations will have a significant effect on radiative forcing. However, band saturation can occur when an increase in concentration of a greenhouse gas causes complete absorption in a particular wavelength band, and so further increases in the

gas will have less and less effect on climate. In the case of CO_2, an increase in concentration in the troposphere does not show a one-to-one relationship with climate warming, as much of the radiation in the 15 μm region has already been absorbed by the CO_2 already present in the atmosphere. This means a doubling of CO_2 from current concentrations will show around a 10–20 % increase in its warming effect (Seinfeld and Pandis, 2006).

Due to the absorption of radiation higher in the atmosphere, the photochemistry occurring in the troposphere will be dependent on the available wavelengths at the surface. The solar radiation at the surface is measured in terms of actinic flux which is defined as the amount of radiation received at some point in the atmosphere per unit time. Photolysis involves the breaking down of molecules due to the action of photons, and the rate of photolysis of a species depends on the actinic flux, absorption cross section of the species and the quantum yield from photolysis. Species with short photolysis lifetimes will be of most importance in the troposphere (and those with longer lifetimes such as CFCs are of greater importance in the stratosphere) and include NO_2, alkyl halides and O_3. Photolysis reactions lead to the production of reactive species and initialise many oxidation processes in the troposphere as discussed in the next section.

1.4 Oxidation Processes in the Troposphere

The hydroxyl radical (OH) is the most important oxidising species in the troposphere due to its high reactivity and relatively high concentration. It reacts with most trace gases in the atmosphere in catalytic cycles, maintaining the concentration of OH at around 1×10^6 molecule cm^{-3} during daylight hours (Krol and Lelieveld, 2003; Prinn et al., 2001). It is produced in the troposphere through the photolysis of O_3. Although the majority of the short-wavelength UV light is absorbed by O_3 and O_2 in the stratosphere, sufficient light at wavelengths < 319 nm reaches the troposphere to photolyse O_3. This process produces both ground state (O) and excited state (O^{1}D) oxygen atoms (R1.1a and R1.1b). O(^{1}D) may also be produced from photolysis of O_3 at wavelengths up to

330 nm due to dissociation of internally excited O_3 and via the spin forbidden pathway (R1.1c).

$$O_3 + h\nu \rightarrow O_2 + O \qquad \text{(R1.1a)}$$

$$O_3 + h\nu \rightarrow O_2 + O\left(^1D\right) \qquad \text{(R1.1b)}$$

$$O_3 + h\nu \rightarrow O_2\left(^3\Sigma_g\right) + O\left(^1D\right) \qquad \text{(R1.1c)}$$
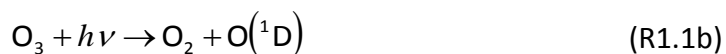
The ground state O atom will react rapidly with O_2 to re-form O_3 (R1.2) so that reaction R1.1a followed by reaction R1.2 produces a null cycle.

$$O_2 + O + M \rightarrow O_3 + M \qquad \text{(R1.2)}$$

In the case of the excited state $O(^1D)$, the spontaneous $O(^1D)$ → O transition is forbidden and therefore the $O(^1D)$ must react with another species which in most instances will be either N_2 or O_2, so that the $O(^1D)$ will be quenched to the ground state (R1.3).

$$O(^1D) + M \rightarrow O + M \qquad \text{(R1.3)}$$

The resulting ground state O can then react with O_2 via reaction 1.2 to reproduce O_3 resulting in another null cycle. However, if the excited state $O(^1D)$ reacts with a water molecule (H_2O) then two OH radicals will be produced (R1.4).

$$O(^1D) + H_2O \rightarrow 2OH \qquad \text{(R1.4)}$$

The highest concentrations of OH are predicted around the tropics due to the high humidities and strong actinic fluxes leading to increased O_3 photolysis and production of OH from $O(^1D)$. Higher OH levels are also expected in the Southern Hemisphere because of the increased concentrations of CO from anthropogenic activities in the Northern Hemisphere which will react with OH and reduce its concentration. OH will

also react with many other atmospheric trace species including methane (CH_4) which is an important greenhouse gas and whose sources are predominantly biogenic including emissions from wetlands, decaying organic matter and emissions from agriculture and cattle (Jacob, 1999). These oxidation processes ultimately lead to the formation of CO_2 and H_2O and so provide a route for the removal of anthropogenic and biogenic emissions from the gas phase. The oxidation of CH_4 will initially lead to the formation of CO which can then be oxidised further to CO_2, another key greenhouse gas (Seinfeld, 2006; Wayne, 2000). The oxidation cycle for CH_4 is shown below.

$$OH + CH_4 \rightarrow CH_3 + H_2O \tag{R1.5}$$

$$CH_3 + O_2 + M \rightarrow CH_3O_2 + M \tag{R1.6}$$

$$CH_3O_2 + NO \rightarrow CH_3O + NO_2 \tag{R1.7}$$

$$CH_3O + O_2 \rightarrow HCHO + HO_2 \tag{R1.8}$$

$$HCHO + h\nu(\lambda < 338\,nm) \rightarrow HCO + H \tag{R1.9}$$

$$H + O_2 + M \rightarrow HO_2 + M \tag{R1.10}$$

$$HCO + O_2 \rightarrow CO + HO_2 \tag{R1.11}$$
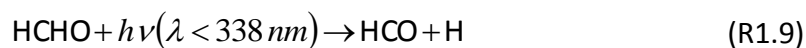
The oxidation of CO proceeds as follows:

$$OH + CO \rightarrow H + CO_2 \tag{R1.12}$$

$$H + O_2 + M \rightarrow HO_2 + M \tag{R1.13}$$

The oxidation of CH_4 and of CO leads to the production of HO_2 radicals which can reform the OH radical through reaction with NO, leading to a chain reaction.

$$HO_2 + NO \rightarrow OH + NO_2 \qquad \text{(R1.14)}$$

This self-catalytic process relies on the presence of NO; in remote locations the concentrations of NO tend to be low (< 1 ppb) and therefore reaction R1.14 (or R1.7) does not dominate. In this case the HO_2 will undergo self-reaction to form peroxides and can then undergo photolysis to reproduce OH or may be lost from the gas phase by heterogeneous uptake onto aerosol.

$$HO_2 + HO_2(+M) \rightarrow H_2O_2 + O_2(+M) \qquad \text{(R1.15)}$$

$$CH_3O_2 + HO_2 \rightarrow CH_3OOH + O_2 \qquad \text{(R1.16)}$$

$$H_2O_2 + h\nu \rightarrow 2OH \qquad \text{(R1.17)}$$
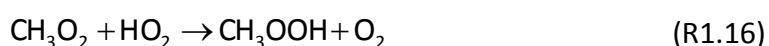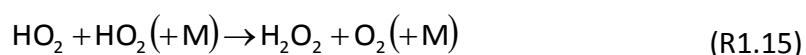
NO_x (NO and NO_2) is important in the troposphere as it affects the oxidising capacity through production of O_3. The sources of NO_x in the atmosphere include lightning and soil emissions as well as anthropogenic sources such as the combustion of fossil fuels. NO_2 is photolysed at wavelengths < 424 nm to produce NO and O atoms. These O atoms will then react with O_2 as in reaction 2 to produce O_3. The O_3 produced can then react with NO to reform NO_2 and form a photostationary state.

$$NO_2 + h\nu \rightarrow NO + O \qquad \text{(R1.18)}$$

$$O_2 + O + M \rightarrow O_3 + M \qquad \text{(R1.2)}$$

$$NO + O_3 \rightarrow NO_2 + O_2 \qquad \text{(R1.19)}$$

Reaction of NO_2 with OH is a terminating step which produces nitric acid (HNO_3) which can be removed by dry deposition or uptake onto aerosol. This removes both HO_x (OH plus HO_2) and NO_x from the system.

$$NO_2 + OH + M \rightarrow HNO_3 + M \qquad \text{(R1.20)}$$

At night another nitrogen species, NO_3 becomes an important oxidising species in polluted environments. It is produced through the reaction of NO_2 with O_3. NO_3 will not play a major role in daytime oxidation processes as it is rapidly photolysed to NO_2. It may also form N_2O_5 through reaction with NO_2, which can be removed by uptake onto aerosol and dry deposition, leading to the removal of NO_x from the gas phase. NO_3 may also react with NO to reform NO_2 (Seinfeld, 2006; Wayne et al., 1991; Wayne, 2000).

$$NO_2 + O_3 \rightarrow NO_3 + O_2 \qquad \text{(R1.21)}$$

$$NO_3 + NO_2 + M \rightarrow N_2O_5 + M \qquad \text{(R1.22)}$$

$$NO_3 + NO \rightarrow 2NO_2 \qquad \text{(R1.23)}$$
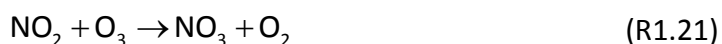
In addition to the above reactions there are many other species which will be broken down in the troposphere through oxidation processes. These include oceanic emissions such as alkyl halides and dimethyl sulphide (DMS). The chemistry of these alkyl halides and the halogen cycles they are involved in is discussed in the next chapter. DMS may be oxidised by OH or NO_3 in the troposphere to produce methane sulfonic acid (MSA) and further to produce SO_2. DMS is an important biogenic emission which plays a role in aerosol formation in the marine boundary layer. Details of the properties of aerosols and their formation processes are discussed in the next section.

1.5 Aerosols in the Troposphere

Aerosols can be defined as an "ensemble of solid, liquid, or mixed phase particles suspended in air" (Jacobson, 2005), with the aerosol particle describing a singular such particle. Aerosols in the atmosphere arise from a number of different sources including natural sources such as windborne dust, sea spray and volcanoes and anthropogenic

sources such as fuel combustion. The composition and size of aerosols shows large variability from region to region as the lifetime of aerosols in the atmosphere tends to be on the order of a few hours to a few days.

Aerosols can be formed directly from particle emission (primary) or form in the atmosphere from gas-to-particle conversion processes (secondary). The size of aerosols also varies depending upon their sources and formation processes and can range from nm up to tens of μm. Aerosols can be broadly divided into two classes based on size; those with a diameter smaller than 2.5 μm are termed "fine" aerosol and those greater than 2.5 μm in diameter are termed "coarse". The sources, formation processes, composition, optical properties and removal mechanisms of fine and coarse aerosol all differ and therefore the distinction between the two classes is vital when discussing the chemistry, measurement and health effects of aerosol.

The fine aerosol can be sub-divided into three further categories or modes. Those smaller than 10 nm are nucleation mode aerosol and are formed from condensation of vapours in combustion processes or the nucleation of atmospheric species (Figure 1.5). Aitken mode aerosols are in the size range 10–100 nm, and aerosol in the size range 100 nm–2.5 μm are accumulation mode aerosols. The accumulation mode aerosols are formed by coagulation of nucleation mode particles and from condensation onto existing particles. Coarse mode aerosol are formed through mechanical processes and predominantly arise from combustion or from natural dust emissions (Seinfeld, 2006).
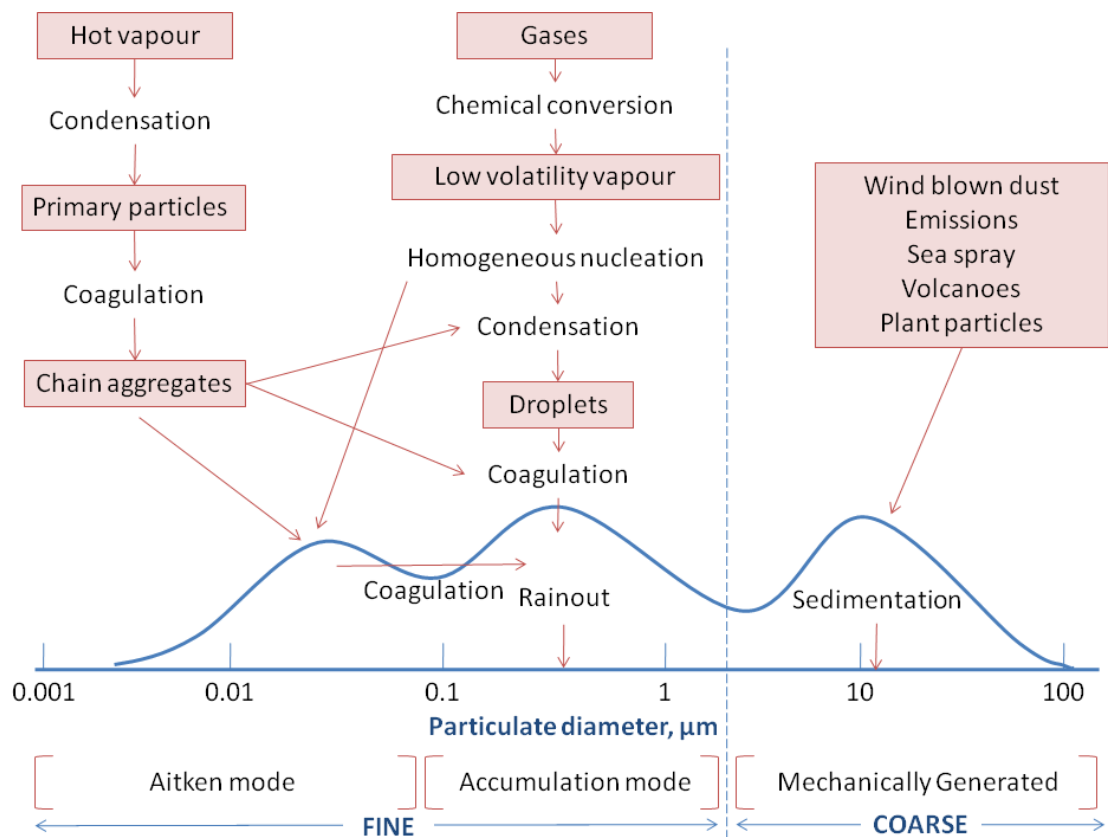
Figure 1.5 Aerosol size classifications and formation pathways. The shaded boxes indicate the various sources and phases of particles during the formation process. Adapted from Seinfeld and Pandis (2006).

Changes in aerosol size and composition can occur through condensation and evaporation, coagulation with other aerosol, chemical reaction and activation in supersaturated water vapour to form cloud droplets and fog. The composition of aerosols varies greatly throughout the atmosphere; it can include contributions from sulphate, ammonium, nitrate, sodium, chloride, trace metals, carbonaceous materials, crustal elements and water.

Carbonaceous material may include elemental carbon (or "black carbon") which comes entirely from fuel combustion and will absorb radiation to have a heating effect on the atmosphere. Organic species can form aerosol either directly or from condensation of atmospheric vapours. Organic aerosols have been implicated in a number of health effects on humans and may contain species which are carcinogenic or mutagenic (Poschl, 2005). Mineral dust also provides a source of aerosol from windborne particles, predominantly from the deserts of North Africa, and this also provides a source of iron

to the world's oceans, an important driver of biological productivity (Jickells et al., 2005).

The effects of atmospheric aerosols on climate are both direct and indirect (Figure 1.6). They can back-scatter incoming solar radiation to give a cooling effect or, as in the case of elemental carbon, absorb the radiation to produce a warming effect and therefore directly influence climate. They can also influence climate indirectly through acting as cloud condensation nuclei (CCN) and therefore affecting the formation of clouds. This will have an effect on the way in which the clouds absorb or reflect solar radiation and therefore impact on climate. Calculation of the direct and indirect forcing effects of aerosol remains one of the largest uncertainties in predicting future climate change (Forster and Ramaswamy, 2007).
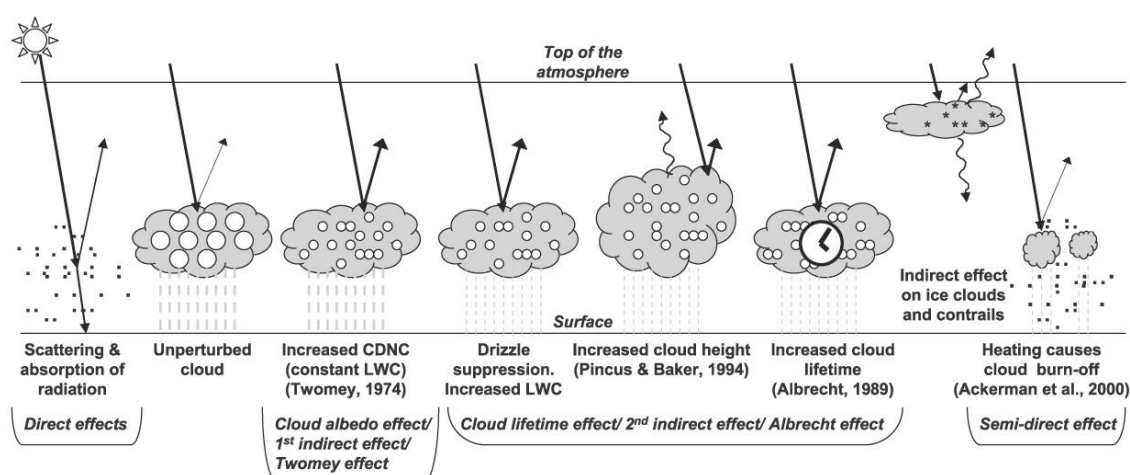
Figure 1.6 Summary of aerosol direct and indirect effects on the radiative balance (Forster and Ramaswamy, 2007).

Aerosols can also influence tropospheric chemistry by providing sites for heterogeneous reactions to occur, in particular, the emission of large amounts of halogen species from heterogeneous reactions on sea-salt aerosols (discussed further in Chapter 2).

The formation of particles through gas to particle conversion remains an area of uncertainty, however, the dominant gaseous sources are considered to be DMS emitted from the oceans and non-methane hydrocarbons from both natural emissions

from vegetation and anthropogenic emissions which undergo oxidation in the troposphere (Andreae and Crutzen, 1997). Iodine oxides have also been found to be a source of particles in the troposphere in areas with increased iodine emissions and may lead to the formation of CCN (McFiggans et al., 2004; O'Dowd et al., 2002). The mechanism for iodine oxide particle formation is discussed further in Chapter 2.

Chapter 2

Halogen Chemistry in the Marine Boundary Layer

2.1 Sources of Halogens in the Atmosphere

The primary sources of reactive halogens in the atmosphere are biogenic, with oceanic sources dominating, including sea-salt aerosol and emissions from marine macro and microalgae.

2.1.1 Sea-salt Aerosol

The release of halogen compounds from sea-salt aerosols represents a significant biogenic source of reactive halogen species in the troposphere. Chloride, bromide and iodide salts are present in sea water and are released to the atmosphere through droplets of spray (although this is a minor source in the case of iodine) (von Glasow, 2008). The mechanism by which halogen species are released from sea-salt aerosols involves heterogeneous reactions with nitrogen oxides, hypohalous acids (HOX, where X=Cl, Br, I) and strong acids (e.g. H_2SO_4 and HNO_3) (Saiz-Lopez and Plane, 2004a).

Uptake of HOX onto sea-salt aerosol allows conversion of halide ions (Cl^-, Br^- and I^-) into di-halogens (e.g. Br_2, IBr, and BrCl). This process requires the presence of protons (H^+) (Fickert et al., 1999) which are supplied by strong acids such as H_2SO_4 and HNO_3, present in the atmosphere from anthropogenic or biogenic sources.

$$HOX_{aq} + Y^- + H^+ \rightarrow XY_{aq} + H_2O \qquad \text{(R2.1)}$$

Extremely efficient heterogeneous halogen activation occurs in the Polar Regions during spring, involving bromine in sea ice; the so-called "bromine explosion" (Barrie et al., 1988; Wennberg, 1999). This occurs via reaction R2.1, where X and Y are Br, and

the sea-ice is covered by brine. The Br_2 produced is emitted into the gas phase and is readily photolysed to produce two Br atoms. These will then react with O_3 to form two BrO molecules, which then go on to react with HO_2 to form two HOBr molecules. These can then be recycled through the brine-covered ice to form two Br_2 molecules, therefore leading to an exponential growth in BrO concentration (von Glasow and Crutzen, 2003).

Uptake of $XONO_2$ can also lead to the release of dihalogen molecules in a similar way as for HOX. The $XONO_2$ is converted to HOX in the aqueous phase and this can then go on to react in the same catalytic cycle as mentioned previously. This process will occur in the presence of polluted air masses containing high levels of halogen nitrates, which can lead to an increase in gas phase halogen species (von Glasow and Crutzen, 2003).

$$XONO_{2g} + H_2O \rightarrow HOX_{aq} + HNO_{3aq} \qquad \text{(R2.2)}$$

$$HOX_{aq} + Y^- + H^+ \rightarrow XY_{aq} + H_2O \qquad \text{(R2.1)}$$
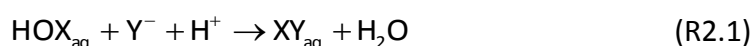
The mechanism involving uptake of strong acids, such as H_2SO_4 and HNO_3, onto aerosol releases halogens in the form hydrogen halides (HX) (Wayne, 1995). These HX species are highly soluble and will most likely be taken up by the sea-salt aerosol (McFiggans et al., 2002; Vogt et al., 1999). The X^- ions produced can then be released back into the gas phase as dihalogen molecules as in the previous case.

In polluted environments, the release of halogenated nitrogen oxides occurs through reactions of NO_2 and N_2O_5 with NaX in sea-salt aerosol (Behnke et al., 1991; Zetzsch and Behnke, 1992). These halogenated nitrates will then photolyse or react further with the sea-salt to release dihalogens. Recent work by Roberts et al. (2009) looked into the uptake of N_2O_5 onto chloride containing aerosols and found that $ClNO_2$ production increased with increasing aerosol chloride concentration, in agreement with field observations.

In addition, the uptake of halogen species onto sea-salt aerosol can lead to activation of other halogen species within the aerosol, leading to depletion of halides (in the case of Br and Cl) in the aerosol compared to sea water (Ayers et al., 1999).

2.1.2 Marine Algae

Iodine species in the atmosphere predominantly originate from macro algae (seaweed) and micro algae (phytoplankton), which produce organic iodine species e.g. methyl iodide (CH_3I), dimethyl iodide (CH_2I_2) and molecular iodine (I_2). They also provide a significant source of brominated and chlorinated organic compounds such as $CHBr_3$, CH_3Br, $CHCl_3$, and CH_2BrCl. Of these compounds the most important for tropospheric chemistry will be those with short lifetimes with respect to photolysis such as CH_2I_2, CH_2IBr and I_2 (with lifetimes of around 5 minutes, 1 hour and 5–10 seconds respectively (Carpenter et al., 1999; Saiz-Lopez and Plane, 2004b)). The longer lived halocarbons (e.g. CH_3Cl, CH_2Cl_2, CH_3Br, CH_2Br_2) will be transported to the stratosphere where they can influence stratospheric O_3 (Saiz-Lopez and Plane, 2004b). Alternatively, the halocarbon may live just long enough to reach the upper-troposphere lower-stratosphere (UTLS) region where it will destroy O_3, such as in the case of CH_3I, which has a lifetime of 3–5 days (Tegtmeier et al., 2013). Once in the atmosphere these species are photolysed by sunlight to give halogen atoms which go on to react with O_3 in the air, producing halogen oxides.

The release of iodocarbons, such as CH_3I and CH_2I_2, has been found to occur during low tide when macro algae are exposed to sunlight (Carpenter et al., 1999) and coastal halocarbon mixing ratios are generally higher than open ocean mixing ratios (Saiz-Lopez et al., 2011). The reason for these halocarbons being emitted is believed to be a response to oxidative stress (Pedersen et al., 1996). The mechanism for production of halocarbons involves either a methyl transferase enzyme (mono-halogenated organic compounds) or a haloperoxidase enzyme (di and tri-halogenated organic compounds). Hydrogen peroxide is released during cell metabolism and when the organism is exposed to oxidative stress. It is a highly oxidative species and therefore its removal is vital to protect the cell from harm. The hydrogen peroxide can oxidise halides in the

cell, catalysed by the haloperoxidase enzyme. This produces electrophilic halogenating species which can go on to react with organic matter within the cell via the iodoform reaction whereby the hypohalite ion can react with a methyl ketone to form an organohalogen compound. The resulting volatile halocarbons are then released into the surrounding water or air (Carpenter, 2003).
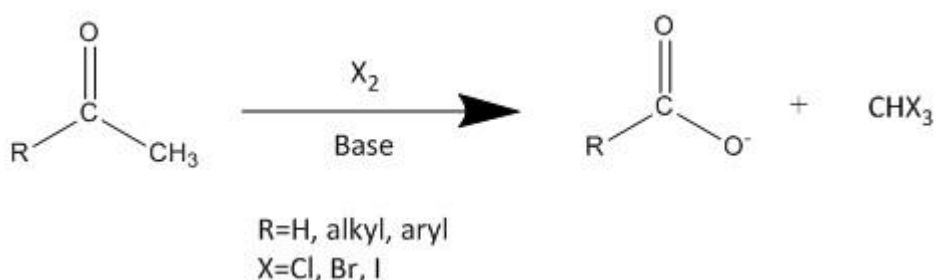
Figure 2.1 Haloform reaction producing volatile CHX_3 which can then be released to the atmosphere.

In addition to emissions from macroalgae, in the open ocean phytoplankton species are the main emitters of halocarbon species. Several studies have found emissions of halocarbons (including $CHCl_3$, CCl_4, CH_2Br, $CHBr_3$ and CH_3I) from phytoplankton species (e.g. Abrahamsson et al., 2004; Moore et al., 1996; Roy, 2010; Smythe-Wright et al., 2006) which are highly variable and often show a seasonal trend, coinciding with phytoplankton blooms. The rate of production of halocarbons is also highly species dependent (Tokarczyk and Moore, 1994) and is also influenced by nutrient concentration (Smythe-Wright et al., 2010). As well as the emissions from phytoplankton, cyanobacteria have also been shown to be a significant source of halocarbons during summer blooms in the Baltic sea (Karlsson et al., 2008).

I_2 has also been found to be a significant source of reactive iodine in the atmosphere (McFiggans et al., 2004; Saiz-Lopez and Plane, 2004a), and is also emitted by certain macroalgae. Originally, emissions were thought to be primarily from the species *Laminaria digitata* (Ball et al., 2010; Küpper et al., 2008; Palmer et al., 2005), however, recent studies have shown that additional macroalgae species (*Fucus vesiculosus* and *Ascophyllum nodosum*) can also be major contributors (Huang et al., 2013). The mechanism of its release is suggested to involve an equilibrium between HOI, I^- and I_2 in solution:

$$HOI + I^- + H^+ \rightarrow I_2 + H_2O \qquad \text{(R2.3)}$$

At low tide, the laminaria become exposed to the oxidising atmosphere, leading to the formation of HOI and displacing the equilibrium towards molecular iodine. Molecular iodine is relatively volatile and will therefore partition between the aqueous and gaseous phases. For I_2 to be emitted into the troposphere it must volatilise to the gas phase before it can react with dissolved organic matter in sea water, and this can only occur at low tide (McFiggans et al., 2004). Alternatively, Küpper et al. (2008) suggested that under conditions of oxidative stress, I^- is released in large quantities to the thallus surface (outside the cell membrane) where it reacts with oxidants such as H_2O_2 and O_3, leading to production of I_2. Recent studies have shown that I_2 can also be released by seaweed species even under low-stress conditions (Nitschke et al., 2011) and the emissions will depend upon the degree of emersion as the tide level rises and falls (Ashu-Ayem et al., 2012).

In addition to the emissions from macroalgae, measurements by Hill and Manley (2009) have shown that polar marine diatom species also emit large quantities of both HOI and HOBr, much higher than previously measured emissions of organic halogens and could be released to the polar MBL through brine channels in the sea ice (Saiz-Lopez et al., 2011).

2.1.3 Ozone Deposition to Seawater

Recent laboratory studies have shown that O_3 deposition to the ocean surface in the presence of dissolved organic matter could also lead to emissions of iodocarbons (Martino et al., 2009). This process involves the reaction of dissolved organic matter with molecular iodine, formed by the reaction of ozone with iodide at the sea surface (Martino et al., 2009). In addition, the photolysis of CH_2I_2 in the sea surface micro-layer leads to the production of CH_2ClI which can subsequently escape into the atmosphere (Martino et al., 2005).

The reaction of O_3 with dissolved iodide in seawater can also lead to the release of I_2 to the atmosphere (Garland and Curtis, 1981). Recent studies have found that I_2 and IO are emitted from the reaction of O_3 with iodide solutions (Sakamoto et al., 2009) and that the emission of both species is affected by the presence of organic species such as phenol (Hayase et al., 2010), and by organic surfactants such as octanol (Rouviere and Ammann, 2010). These processes could lead to significant release of reactive iodine species from the open ocean, and therefore have a considerable impact upon the global ozone budget.

2.1.4 Terrestrial Sources

The presence of iodine in soil is due to input from the atmosphere and through decomposition of plant matter containing iodine (Carpenter, 2003). The terrestrial sources of CH_3I are believed to comprise around 30 % of the total global budget and include emissions from rice paddies, wetlands and biomass burning (Carpenter, 2003).

Alkylation of halide ions during the oxidation of organic matter has been found to produce volatile halogenated organic compounds in the presence of an electron acceptor (Fe^{III}); in this case sunlight is not required (Keppler et al., 2000). The magnitude of this source will depend on a number of factors including temperature, moisture and soil acidity.

2.1.5 Volcanic Eruptions

Reactive halogen species (e.g. BrO and ClO) have been shown to be present as minor constituents in the gas plumes from volcanic eruptions at a number of locations (Bobrowski et al., 2003; Bobrowski and Platt, 2007; Bobrowski et al., 2007; Lee et al., 2005a).

Chlorine is in general the most abundant halogen species found in volcanic gas plumes with concentrations increasing with increasing water content and decreasing SO_2 content (Aiuppa et al., 2009). Fluorine is around five times less abundant than Cl in volcanic gas plumes and does not appear to show a correlation with water content.

Both Cl and F are thought to be transported in gas plumes predominantly as HCl and HF.

Measurements of BrO have been recorded at a site in Montserrat (Bobrowski et al., 2003) and suggest that emissions of halogen species from volcanoes could have a significant impact on both tropospheric and stratospheric chemistry. Long-path DOAS observations of BrO at Masaya Volcano, Nicaragua (Kern et al., 2009) were consistently below the detection limit of the instrument at night suggesting that BrO is not emitted directly from the volcano but is the result of photochemistry within the volcanic plume.

Aiuppa et al. (2005) measured total Br and I emissions (mainly in the form of HBr and HI) from the volcanic plume of Mount Etna and estimate the global budget of Br and I from volcanic degassing to be 13 and 0.11 Kt yr^{-1}, respectively. This suggests that volcanoes are a significant source of reactive bromine to the atmosphere whereas they represent only a minor contribution to the global reactive iodine budget (Aiuppa et al., 2005).

The presence of these compounds in volcanic plumes could cause substantial ozone depletion in the vicinity of the volcano. Reactive halogen emissions from volcanic degassing will predominantly play a role in the chemistry of the free troposphere and the stratosphere as the lifetime of atomic Br is sufficiently long to be transported to these altitudes (Bobrowski et al., 2003).

2.1.6 Anthropogenic Emissions

Although biogenic emissions are the dominant source of reactive halogen species in the troposphere, anthropogenic sources also play a part. Biomass burning and fossil fuel combustion have been shown to be sources of Br$^-$ in aerosols in polluted environments (Keene et al., 1999).

2.2 Impacts of Halogens in the Atmosphere

There are large numbers of different halogen containing species released into the troposphere and these can have a significant effect on the chemistry occurring in the lower atmosphere. A simple scheme of the chemistry involving halogen species occurring in the troposphere is shown in Figure 2.2.
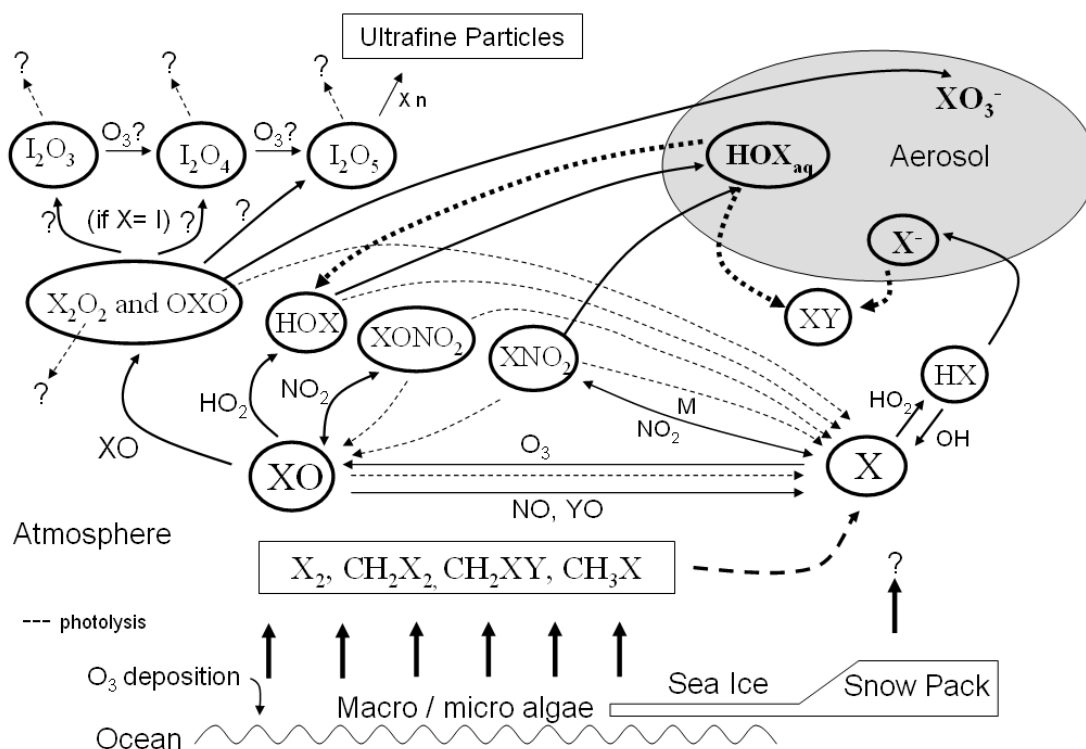
Figure 2.2 A schematic diagram of the chemistry involving halogen species in the marine boundary layer, dashed lines show photolysis reactions (Mahajan, 2009).

2.2.1 Ozone Depletion

The destruction of ozone in the stratosphere by halogen radicals is a well known phenomenon; however, this process also occurs in the troposphere through reactions involving halogen oxide radicals (McFiggans et al., 2000; Saiz-Lopez and Plane, 2004b):

$$X + O_3 \rightarrow XO + O_2 \tag{R2.4}$$

$$Y + O_3 \rightarrow YO + O_2 \qquad \text{(R2.5)}$$

$$\underline{XO + YO \rightarrow X + Y + O_2} \qquad \text{(R2.6)}$$

$$Net: 2O_3 \rightarrow 3O_2$$
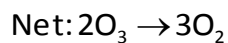
In the polar regions during springtime complete removal of ozone in the troposphere can occur within days due to catalytic bromine cycles involving the BrO self-reaction and the so called "bromine explosion" as mentioned previously in section 2.1.1 (von Glasow and Crutzen, 2003).

$$2(Br + O_3 \rightarrow BrO + O_2) \qquad \text{(R2.7)}$$

$$BrO + BrO \rightarrow 2Br + O_2 \qquad \text{(R2.8)}$$

$$BrO + BrO \rightarrow Br_2 + O_2 \qquad \text{(R2.9)}$$

$$\underline{Br_2 + h\nu \rightarrow 2Br} \qquad \text{(R2.10)}$$

$$Net: 2O_3 \rightarrow 3O_2$$
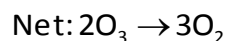
Studies by Read et al. (2008) showed that combined bromine and iodine cycles could account for almost 50 % of ozone loss at the Cape Verde islands in the tropical north Atlantic, suggested to be representative of the open ocean. This is due to the following reaction, which increases the rate at which BrO is converted back to Br:

$$IO + BrO \rightarrow Br + OIO \qquad \text{(R2.11)}$$

Reaction with HO_2 radicals becomes important at lower halogen oxide concentrations and under low NO_x conditions, leading to significant ozone depletion at remote marine environments at sunrise due to the photolysis of halogen species that have built up overnight through release from sea salt aerosol (Saiz-Lopez and Plane, 2004b).

$$X + O_3 \rightarrow XO + O_2 \quad \text{(R2.4)}$$

$$XO + HO_2 \rightarrow HOX + O_2 \quad \text{(R2.12)}$$

$$HOX + h\nu \rightarrow X + OH \quad \text{(R2.13)}$$

$$OH + CO \xrightarrow{O_2} CO_2 + HO_2 \quad \text{(R2.14)}$$

$$Net: CO + O_3 \rightarrow CO_2 + O_2$$
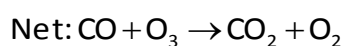
Under high NO_x conditions formation of halogen nitrates occurs, leading to ozone depletion:

$$XO + NO_2 \rightarrow XONO_2 \quad \text{(R2.15)}$$

$$XONO_2 + h\nu \rightarrow X + NO_3 \quad \text{(R2.16)}$$

$$NO_3 + h\nu \rightarrow NO + O_2 \quad \text{(R2.17)}$$

$$X + O_3 \rightarrow XO + O_2 \quad \text{(R2.4)}$$

$$NO + O_3 \rightarrow NO_2 + O_2 \quad \text{(R2.18)}$$

$$Net: 2O_3 \rightarrow 3O_2$$
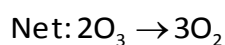
The efficiency of this cycle will be reduced, however, by the photolysis of XNO_3 to $XO + NO_2$ and also the fact that the major photolysis pathway of NO_3 produces $NO_2 + O$, therefore leading to no overall ozone depletion (Saiz-Lopez and Plane, 2004b).

The self-reaction of IO results in the formation of OIO, a starting block for particle formation. A recent study by Gómez Martín et al. (2009) shows that OIO photolysis occurs in the visible region with a quantum efficiency of unity and produces I atoms; much smaller sources of iodine precursors will therefore be required for substantial ozone depletion. Particle production from polymerisation of OIO will be inhibited

during the day due to its rapid photolysis, with a peak occurring at sunset when OIO photolysis ceases.

2.2.2 Oxidation of Organic Compounds

Atomic Cl and Br can react with non-methane hydrocarbons (NMHCs) in the same manner as OH to abstract a hydrogen atom and in some cases Cl is even more reactive towards these compounds than OH (von Glasow and Crutzen, 2003).

Reactions of halogen atoms with HO_2 radicals produce hydrogen halides which are removed from the gas phase through wet/dry deposition. HOI uptake onto halide rich surfaces can enhance bromine release in the form of IBr (Saiz-Lopez et al., 2007b).

Halogen oxides (BrO and ClO) and atomic chlorine (Cl) can oxidise DMS in the marine boundary layer at a rate around an order of magnitude faster than by OH in coastal Antarctica (Saiz-Lopez et al., 2007b). The products of these reactions (dimethyl sulfoxide, dimethyl sulfone, methyl sulfinic acid) do not produce new particles, they can only condense onto existing particles unlike the H_2SO_4 and SO_2 produced from OH + DMS reaction. The differing products will affect the number and size of cloud condensation nuclei (CCN), thereby influencing cloud formation and chemistry-climate feedbacks (von Glasow and Crutzen, 2004).

2.2.3 Changes to the NO_x and HO_x Balance

During the daytime OH is the principal oxidising agent in the troposphere and it determines the lifetime of innumerable chemical species. Reaction of OH with CO leads to the formation of HO_2 and a steady state between the two species is established. Halogens affect the $[HO_2]/[OH]$ ratio through the XO + HO_2 reaction. This can be followed by photolysis or uptake of HOX onto aerosol (Bloss et al., 2005).

$$XO + HO_2 \rightarrow HOX + O_2 \qquad \text{(R2.12)}$$

$$HOX + h\nu \rightarrow OH + X \qquad \text{(R2.13)}$$

$$HOX + aerosol \rightarrow loss \qquad \text{(R2.19)}$$

HOX acts as a sink for HO_2 and provides a route to OH formation causing the $[HO_2]/[OH]$ balance to decrease. Measurements at Mace Head, Ireland showed that the $XO + HO_2$ reaction could account for 40 ± 12 % of HO_2 loss and subsequent photolysis of HOX provided up to 15 % of OH production (Bloss et al., 2005). Studies at Cape Verde also found a significant effect on the HO_x ratio when halogen chemistry was included in model simulations, accounting for an overall 9 % increase in OH concentrations (Whalley et al., 2010). This reaction is particularly important in the presence of iodine as HOI photolysis is more rapid than that of HOBr (typically HOI has a lifetime against photolysis of around 2 minutes at ground levels at noon compared to HOBr which is typically around 1 hour) (Saiz-Lopez and Plane, 2004b).

A similar relationship exists between NO and NO_2 in the troposphere, controlled by the following reactions:

$$NO + O_3 \rightarrow NO_2 + O_2 \qquad \text{(R2.18)}$$

$$NO_2 + h\nu \rightarrow O(^3P) + NO \qquad \text{(R2.20)}$$

The presence of significant halogen concentrations shifts the $[NO_2]/[NO]$ balance towards NO_2 through the following reaction (Davis et al., 1996):

$$XO + NO \rightarrow X + NO_2 \qquad \text{(R2.21)}$$

2.2.4 Oxidation of Elemental Mercury

The lifetime of atomic mercury (Hg^0) in the troposphere is around one year and it is released into the atmosphere from a number of sources including coal combustion (Schroeder and Munthe, 1998). Atomic Br and Cl are highly reactive towards Hg^0 at low

temperatures, and lead to conversion of Hg^0 into reactive gaseous mercury (RGM) in the form $HgBr_2/HgCl_2$ (Saiz-Lopez and Plane, 2004b). This RGM can then quickly enter the food-chain in the Arctic ecosystem. Hg^0 depletion events correlate well with those of O_3 suggesting that they must involve similar elevated bromine levels. The proposed oxidation pathways may involve atomic Br or BrO (Saiz-Lopez and Plane, 2004b; Simpson et al., 2007):

$$Br + O_3 \rightarrow BrO + O_2 \tag{R2.7}$$

$$BrO + Hg^0 \rightarrow HgO + Br \tag{R2.22}$$

$$BrO + Hg^0 \rightarrow HgBrO \tag{R2.23}$$

$$BrO + Hg^0 \rightarrow HgBr + O \tag{R2.24}$$

$$Hg^0 + Br(+M) \leftrightarrow HgBr \tag{R2.25}$$

$$HgBr + Br(+M) \rightarrow HgBr_2 \tag{R2.26}$$
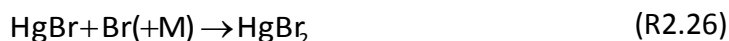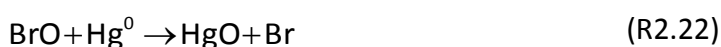
Atomic Br is thought to be the more important oxidant in atomic mercury depletion events (AMDEs) in the Arctic (Simpson et al., 2007), and it is believed that the reactions of Cl, Cl_2 and Br_2 with Hg^0 are too slow to compete with the atomic Br reaction during these events (Goodsite et al., 2004).

2.2.5 New Particle Formation

The ability of iodine oxides to form new particles in the troposphere has been extensively studied over recent years; however, the mechanism by which new particles are formed is still poorly understood. Ultrafine particles (diameter < 100 nm) formed in the troposphere will affect the radiative balance of the atmosphere, through their direct scattering effects and absorption of incoming radiation and also their ability to form cloud condensation nuclei (CCN) as mentioned in Chapter 1. This could have a

significant impact on climate, therefore understanding formation mechanisms for these particles will provide valuable information for climate modelling.

Studies at Mace Head, Ireland suggested a clear link between iodine/bromine oxide species and new particle formation (O'Dowd et al., 2002) with levels of 10^6 particles cm^{-3} observed. A strong correlation between IO and ultra fine particles was also observed at Roscoff in Northern France during the 2006 RHaMBLe (Reactive Halogens in the Marine Boundary Layer) campaign, further evidence that iodine oxide species are involved in new particle formation (Furneaux et al., 2010).

OIO is produced from the self reaction of IO and the reaction of IO with BrO (Cox et al., 1999). It can then undergo further self-reactions to produce higher iodine oxides such as I_2O_2, I_2O_3, I_2O_4 and I_2O_5.

Laboratory and modelling studies of particles generated from I_2 by Saunders and Plane (2005) suggested that the main component of iodine aerosol is I_2O_5 (inferred from the average O/I ratio of 2.45±0.08). The mechanism they propose for particle formation involves a series of exothermic oxidation reactions of ozone with I_2O_2, I_2O_3 and I_2O_4 to produce I_2O_5. The I_2O_5 molecules can then form larger clusters through polymerisation and coagulation.

Alternatively, studies by Jimenez et al. (2003) of particle formation from photolysis of CH_2I_2 suggested that the main component of the iodine oxide particles was I_2O_4, and that production of particles was through polymerisation of iodine oxides such as OIO. Recent laboratory studies have shown that iodine oxide particles (IOPs) can be produced from IO in the absence of O_3, suggesting IOPs form from the polymerisation of I_2O_3 and I_2O_4, produced from the OIO self reaction or recombination of IO and OIO (Mahajan et al., 2010a). The mechanism of IOP formation is discussed further in Chapter 3.

Growth of ultra-fine particles into CCN has been suggested to occur through the condensation of iodine compounds onto ammonium-sulphate clusters (McFiggans et al., 2004). Concentrations of ammonia and sulphuric acid in the atmosphere are

unable to account for the observed particle growth to observable sizes, therefore it has been postulated that iodine vapours will condense onto thermodynamically stable NH_3-H_2O-H_2SO_4 clusters. Modelling work has shown that iodine oxide particles can act as condensation nuclei themselves with sulphuric acid condensing onto the surface of these particles in the presence of ammonia once a threshold size of a few nm has been reached (Mahajan, 2009). The growth of IOPs to CCN size is a highly non-linear process, and modelling studies have shown that it is highly dependent on both IO concentration and background aerosol surface area (Figure 2.3).
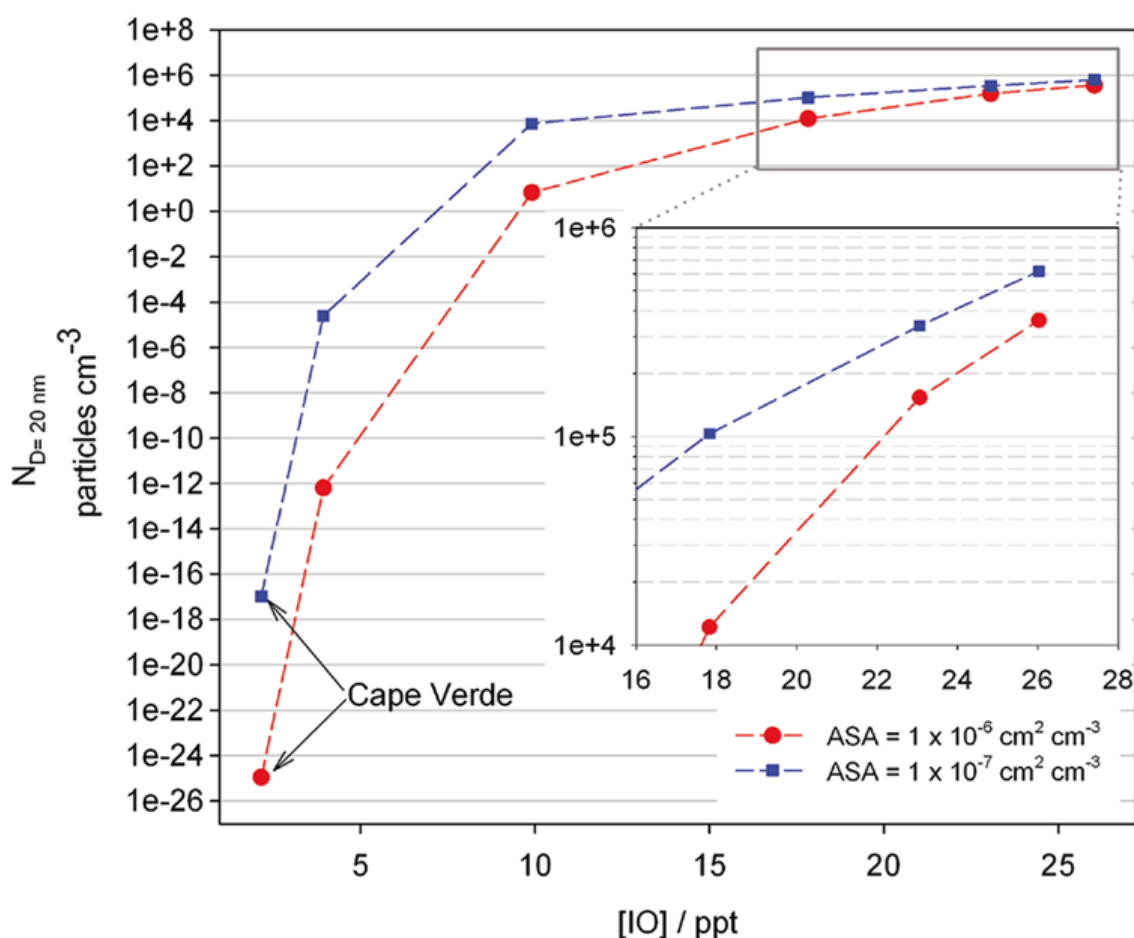
Figure 2.3 Number of potential CCN (D=20 nm) formed at 10 m as a function of mean daytime IO. Two cases are shown with different aerosol surface areas: a typical MBL value of 1 x 10^{-6} cm^2 cm^{-3} (red line); and an ultra-clean value of 1 x 10^{-7} cm^2 cm^{-3} (blue line). Figure from Mahajan et al. (2010).

2.3 Previous Measurements of Halogen Species

2.3.1 Measurement Techniques

Differential Optical Absorption Spectroscopy (DOAS) has been used for a number of years to measure halogen species in a wide variety of locations (e.g. Bobrowski et al., 2003; Honninger et al., 2004b; Mahajan et al., 2009b; Mahajan et al., 2010a; Saiz-Lopez et al., 2006; Saiz-Lopez et al., 2007b). The long-path DOAS technique employs the Beer-Lambert law to determine the concentration of specific species in the atmosphere based on its absorption cross section and light absorption in the atmosphere. The technique is particularly useful as it allows simultaneous measurement of more than one species in a particular wavelength region (Plane and Saiz-Lopez, 2006). The DOAS technique is discussed in detail in Chapter 5.

In addition to the various DOAS techniques, there are a number of other techniques which have been employed to measure halogen species in the boundary layer. For instance, broadband cavity ring down spectrometry (BB-CRDS) (Bitter et al., 2005), inductively coupled plasma mass spectrometry (ICP-MS) (Saiz-Lopez et al., 2006) and molecular fluorescence (Gómez Martín et al., 2011) techniques have all been used to successfully measure I_2. Measurements of IO have also been conducted by CRDS (Wada et al., 2007) and laser induced fluorescence (LIF) (Whalley et al., 2007). One advantage of the in situ measurements is the ability to measure localized emissions, particularly in coastal locations, which can be up to an order of magnitude higher than the DOAS measurements which are averaged over a much larger distance (Saiz-Lopez et al., 2011). The majority of halocarbon measurements have been performed using gas chromatography-mass spectrometry (GC-MS) (e.g. Jones et al., 2009).

2.3.2 Bromine Oxide - BrO

BrO has been observed in a number of different environments including over the snow pack in the Polar regions (Saiz-Lopez et al., 2007b), over salt lakes (Stutz et al., 2002) and in volcanic plumes (Bobrowski et al., 2003). The first measurements of BrO were

conducted in the Arctic boundary layer by Hausmann and Platt (1994) using the DOAS technique. This triggered further measurements in Polar regions which showed that significant mixing ratios (up to 30 ppt) of BrO could be observed during spring time (Frieβ et al., 1999; Honninger and Platt, 2002).

In later years BrO was also observed over salt lakes such as the Dead Sea and in Salt Lake City with mixing ratios up to 176 ppt (Honninger et al., 2004a; Matveev et al., 2001; Stutz et al., 2002; Wagner et al., 2007).

More recently, BrO has been detected in the tropical marine boundary layer, at a site in Cape Verde (Read et al., 2008) with an average mixing ratio of 2.5 ppt (detection limit 0.5–1.0 pptv). BrO has also been detected in the mid-latitude marine boundary layer at a coastal site in Brittany (Mahajan et al., 2009a) where it was observed with mixing ratios up to 7.5 ppt and at Mace Head in Ireland where a maximum mixing ratio of 6 ppt and a daytime average of 2.3 ppt were observed (Saiz-Lopez et al., 2006). These measurements were all performed using the long-path DOAS technique.

BrO has also been measured in a number of volcanic plumes using either the long-path or multi-axis DOAS techniques. Mixing ratios of ~1000 ppt have been observed (Aiuppa et al., 2005; Bobrowski et al., 2003; Lee et al., 2005a).

In addition to the ground based measurements mentioned above, satellite measurements have also been carried out which show elevated BrO mixing ratios of up to 30 ppt over polar regions (Wagner and Platt, 1998; Wagner et al., 2001). Balloon-borne measurements of BrO using solar occultation DOAS and in situ resonance fluorescence over the tropics showed mixing ratios up to 21.5 ppt in the stratosphere (33 km) but negligible amounts (< 1 ppt) in the lower and middle troposphere (Dorf et al., 2008).

2.3.3 Iodine Species – IO, OIO, I$_2$ and I

The majority of iodine measurements have been conducted at coastal sites where there are increased biogenic sources, however, increasingly measurements have been

performed over the open ocean, where alternative sources of reactive iodine will dominate. A summary of the current measurements of IO, OIO, I_2 and I made in a variety of locations, both coastal and open ocean, is provided in Table 2.1.

Measurements in coastal Antarctica made by Frieβ et al. (2001) showed slant column densities up to 10^{14} molecules cm^{-2}, equivalent to around 10 pptv if confined to the marine boundary layer (< 1300 m), with higher IO during the summer. Later measurements by Saiz-Lopez et al. (2007b) showed maximum mixing ratios of IO over 20 pptv during springtime, the highest concentrations recorded anywhere at the time. Satellite measurements have shown that the IO over Antarctica is not just confined to the coasts, but extends over a large area of the continent (Saiz-Lopez et al., 2007a; Schönhardt et al., 2008). This suggests that there must be significant recycling of iodine species through the snowpack; IO concentrations up to 50 ppbv have been measured within the snowpack (Frieß et al., 2010), however, these measurements remain to be confirmed.

In contrast to the very large IO mixing ratios observed over Antarctica, IO measurements in the Arctic show much lower mixing ratios, and the gas phase iodine chemistry is much more localised. Measurements from Spitsbergen of total gaseous iodine using activated charcoal and detection of the isotope I^{128} were typically 1–2 pptv with a maximum of 8 pptv during a high bromine loading event, but IO was not observed above the detection limit using the DOAS technique (2–4 pptv) (Martinez et al., 1999). Mahajan et al. (2010b) measured a maximum of 3.4 pptv IO at Hudson Bay, Canada, which coincided with higher iodocarbon emissions from open water "polynyas" formed in the sea ice. The sporadic nature of the IO measurements are also in contrast to the regional scale "clouds" of BrO observed in the Arctic, due to the "bromine explosion" described in section 2.1.3 (Saiz-Lopez, 2011).

Table 2.1 Summary of gas phase iodine species measurements in a variety of locations across the world. Adapted from Saiz-Lopez et al. (2011).

Species	Location	Mixing Ratio / pptv		Reference
		Max.	**LOD**	
IO	Antarctica	~10		(Frieβ et al., 2001)
		20±1	0.5	(Saiz-Lopez et al., 2007b)
		12		(Saiz-Lopez et al., 2007a)
		~10		(Schonhardt et al., 2008)
	Arctic	0.8±0.2	0.3	(Wittrock et al., 2000)
		3.4±1.2	1.3	(Mahajan et al., 2010b)
		0.4±0.1	0.2	(Oetjen, 2009)
	North Sea (Germany)	2.0±0.7	0.28	(Peters et al., 2005)
		1.4±0.3	0.14	(Oetjen, 2009)
	Mace Head (Ireland)	6.6±0.5	0.9	(Alicke et al., 1999)
		3.0±0.3	0.2	(Allan et al., 2000)
		7.0±0.5	0.5	(Saiz-Lopez and Plane, 2004a)
		29±9	14	(Seitz et al., 2010)
		30±1	1.4	(Commane et al., 2011)
	Brittany	7.7±0.5	0.23	(Peters et al., 2005)
		10.1±0.7	0.5	(Mahajan et al., 2009b)
		54±18	12	(Wada et al., 2007)
		30±7	1.1	(Furneaux et al., 2010)
	Gulf of Maine (USA)	4.0±0.5		(Stutz et al., 2007)
	Cape Grim (Australia)	2.2±0.3	0.2	(Allan et al., 2000)
	Heraklion (Greece)	1.9	0.8	(Oetjen, 2009)
	Dead Sea (Israel)	10±1	3	(Zingler and Platt, 2005)
	Tenerife	4.0±0.3	0.2	(Allan et al., 2000)
		0.4±0.2	0.2	(Puentedura et al., 2012)
	Cape Verde	3.1±0.4	0.4	(Read et al., 2008)
	Maldives	2.8±0.7	0.9	(Oetjen, 2009)
	Eastern Pacific	0.9±0.1		(Mahajan et al., 2012)
	Western Pacific	2.2±0.5		(Großmann et al., 2013)
	Alcantara (Brazil)	0.8±0.3	0.3	(Butz et al., 2009)
OIO	Mace Head (Ireland)	3.0±0.4	0.5	(Saiz-Lopez and Plane, 2004a)
		9.2±1.3	3.2	(Peters et al., 2005)
		13±4	4	(Bitter et al., 2005)
	Brittany (France)	8.7±2.3	3	(Mahajan et al., 2009b)
	Gulf of Maine (USA)	27±7		(Stutz et al., 2007)
	Cape Grim (Australia)	3.0±0.4	0.5	(Allan et al., 2001)
I₂	Mace Head (Ireland)	93±5	3	(Saiz-Lopez and Plane, 2004a)
		61±12	10	(Peters et al., 2005)
		94±20	20	(Bitter et al., 2005)
		~200		(Bale et al., 2008)

	Mweenish Bay (Ireland)	115 302±4	0.2	(Saiz-Lopez et al., 2006) (Huang et al., 2010)
	Brittany (France)	52±4 50±10	5 10	(Mahajan et al., 2009b) (Leigh et al., 2010)
	Ria de Arousa (Spain)	300±100	30	(Mahajan et al., 2011)
	California (USA)	4.0±0.6	0.1	(Finley and Saltzman, 2008)
I	Mace Head (Ireland)	22±5	2.5	(Bale et al., 2008)
	Ria de Arousa (Spain)	10±5	2	(Mahajan et al., 2011)

High concentrations of IO were recorded by Whalley et al. (2007) in Roscoff, Brittany, where levels reached a maximum of 27.6±2.3 pptv. The laser-induced fluorescence (LIF) technique was employed and as such represents a point measurement. During the same campaign LP-DOAS measurements recorded a maximum IO concentration of 10.1±0.7 pptv (Mahajan et al., 2009b). This indicates hot-spots for reactive iodine species which may be lost when using the DOAS technique as concentrations are averaged over a much larger distance of around 3.4 km.

OIO has been successfully observed at a number of coastal sites including Mace Head, Ireland, Cape Grim, Australia and Roscoff, France (Allan et al., 2001; Mahajan et al., 2009b; Saiz-Lopez and Plane, 2004a). Mixing ratios of up to 8.7 pptv have been observed at night in the semi polluted coastal environment at Roscoff, France (Mahajan et al., 2009b).

Butz et al. (2009) performed measurements of IO and OIO using balloon-borne solar occultation in the upper troposphere and lower stratosphere (UTLS). They found an upper limit of 0.1 pptv for both species based on the detection limit of the instrument, indicating that iodine does not have a significant ozone depleting effect at these altitudes and at this location. However, they state iodine could be transported to the UTLS in particulate form which could not be detected. Ground-based zenith sky spectroscopy measurements showed up to 0.8 pptv IO in the stratosphere at Spitsbergen during polar spring (Wittrock et al., 2000).

The first measurements of I_2 were recorded using the long-path DOAS technique by Saiz-Lopez and Plane (2004a) at Mace Head, in August 2002 with mixing ratios of up to 93 pptv. Since then I_2 has been observed at a coastal site in Brittany in 2003 with mixing ratios up to 61±12 pptv. Its presence was only observed at very low tide when

the *laminaria* were directly exposed to ambient air (Peters et al., 2005). I_2 was also observed at Roscoff, again using the long-path DOAS technique, with mixing ratios up to 52.3 ppt at night (Mahajan et al., 2009b). Diffusion denuder measurements of I_2 taken directly above an algal bed showed concentrations varied from 110 up to 302 pptv (Huang et al., 2010).

Recently, satellite measurements of IO have been recorded using the Scanning Imaging Absorption Spectrometer for Atmospheric Chartography (SCIAMACHY) satellite instrument (Schonhardt et al., 2008) and showed high slant columns (up to 8×10^{12} molecules cm^{-2}) along the coast of South America. To relate these concentrations to mixing ratios in the marine boundary layer, it must first be assumed that the IO is confined to the lowest layer of the atmosphere. Assuming a layer of 1 km thickness, this gives a mixing ratio for IO of 3.2 pptv, however if the IO were confined to an even smaller height within the marine boundary layer, around 300 m (as has been modelled), this would give maximum IO mixing ratios of 10.7 pptv. This is much higher than the average IO measured at Cape Verde in the Atlantic Ocean (~1.5 pptv) and measurements in the Eastern (maximum ~1 pptv (Mahajan et al., 2012)) and Western Pacific Ocean (maximum 2.2 pptv (Groβmann et al., 2013)). The low reflectivity of the ocean surface means that satellite observations have comparatively low signal-to-noise and therefore these measurements should be treated with caution (Saiz-Lopez et al., 2011).

2.3.4 Halocarbons

Measurements of halocarbons in the atmosphere are generally performed using GC-MS, a technique which is able to detect a number of different halocarbon species simultaneously. Among the halocarbons which have been measured in the atmosphere are CH_2Br_2, $CHBr_3$, CH_3Br, CH_2I_2, CH_3I, CH_2ICl, CH_2IBr and C_2H_5I. These species have been observed at a number of European locations (Carpenter et al., 1999; Peters et al., 2005).

The mixing ratios of the iodine containing halocarbons for Mace Head (Carpenter et al., 1999) and Roscoff (Jones et al., 2009) were generally below 1 ppt, however the same species were observed in much higher concentrations in Lilia, Brittany (Peters et al., 2005). The extremely high levels of CH_3I and CH_3Br observed (up to 1830 and 875 ppt respectively) were linked to exceptional levels of bioactivity. A comparison of measurements from Cape Grim, Australia and Mace Head (Carpenter et al., 2003) found mixing ratios of $CHBr_3$, $CHBr_2Cl$, CH_2Br_2, CH_3I and CH_2ICl were around 25–50 % lower at Cape Grim; the emissions at Mace Head were directly influenced by the adjacent seaweed beds, whereas this was not the case in the cliff top location of Cape Grim.

Concentrations of iodocarbons are generally in the order $CH_3I > C_2H_5I \approx C_3H_7I > CH_2ICl > CH_2I_2 > CH_2IBr$ and as a consequence, open ocean CH_3I measurements are much more abundant than the other iodocarbons. Yokouchi et al. (2008) observed methyl iodide at a number of locations: at high, mid and low latitudes in both hemispheres. They found considerable median concentrations of CH_3I at San Cristobal Island, in the Galapagos of 1.05 pptv with a maximum of 2.55 pptv. CH_3I has a distinct latitudinal distribution with higher concentrations observed at low latitudes (with slightly lower values at the equator)(Butler et al., 2007; Yokouchi et al., 2008) and also a clear seasonality with maximum concentrations observed in summer (Archer et al., 2007; Sive et al., 2007; Yokouchi et al., 2001). C_2H_5I, CH_2ICl, CH_2I_2 and CH_2IBr followed a similar seasonal pattern to CH_3I in the shelf region of the English Channel, although less pronounced (Archer et al., 2007).

2.3.5 Iodine Speciation – IO_3^-, I^- and SOI

The cycling of iodine through water, snow, ice and aerosols is dependent upon the speciation of iodine within these media. As I^- participates in halogen activation to yield IX, it was originally assumed that IO_3^- would be the only stable iodine species in aerosol (McFiggans et al., 2000; Vogt et al., 1999). However, measurements from marine rainwater and aerosol have shown that the I^-/IO_3^- ratio is in fact highly variable, and the mechanisms controlling this ratio are still unclear (Saiz-Lopez, 2011).

Several measurements have also indicated a significant fraction of soluble organic iodine (SOI) in rainwater and aerosol; the proportion is highly variable but can often constitute the major fraction of total iodine (Baker et al., 2000; Baker, 2005; Gilfedder et al., 2007a, b; Gilfedder et al., 2008; Lai et al., 2008). The majority of these SOI species have not been determined; only one species, iodoacetic acid, has been tentatively identified (Gilfedder et al., 2007a, b; Gilfedder et al., 2008). The source of this SOI has been proposed to be the release of iodinated organic matter from bubble bursting at the sea surface (Seto and Duce, 1972) or from reactions of organic matter with HOI within the aerosol. There can also be a significant insoluble iodine fraction (Tsukada et al., 1987), which is most likely to be organic (Baker et al., 2000) or consist of iodine species adsorbed to mineral or black carbon surfaces (Gilfedder et al., 2010).

Observations of IO in Mace Head and Tenerife (Allan et al., 2000) cannot be reproduced in models without recycling of iodine through the particulate phase (McFiggans et al., 2000), with suggestions of a reduction of iodate occurring through inorganic cycles (Pechtl et al., 2007). The pH dependent Dushman reaction reduces iodate to molecular iodine through the presence of iodide under acidic conditions (Schmitz, 1999). Recent work by Saunders et al. (2012) has shown that iodate can be reduced to iodide by irradiation with light ($\lambda < 310$ nm) in the presence of humic material (commonly found in marine aerosol); a significant organically bound iodine fraction was also produced.

Large variations also exist in the ratio of iodate to iodide in seawater, and the controls on this ratio are biological, chemical and physical. Iodide is generally much higher in surface waters than in deeper waters, where iodate dominates the total iodine, however, total iodine is often depleted at the surface, showing that iodine is being removed from the surface waters (Elderfield and Truesdale, 1980). Elderfield and Truesdale (1980) suggested that the interconversion of iodate and iodide in surface waters of the Atlantic and Pacific oceans is most likely due to biological processes, which are more active in equatorial and temperate waters than at higher latitudes. Huang et al. (2005) also found higher iodide concentrations in warmer waters,

presumed to be due to biological processes, and also measured a small organically bound fraction in surface waters that was not present at depth.

Spokes and Liss (1996) suggested a photochemical mechanism mediated by organic matter could be responsible for the reduction of iodate to iodide in seawater. Measurements in the Sargasso sea and Bermuda (Jickells et al., 1988) showed that iodide formation only occurred when waters had been isolated for a considerable amount of time, and could be due to a photoreduction mechanism or bacterial activity. Iodide may also be expected to vary due to the mixing of different ocean waters, and stratification in the water column and changes in replenishment of iodate from deeper waters was found to be important for measurements in the Atlantic ocean (Truesdale et al., 2000).

2.4 Project Aims

Despite the great progress achieved in understanding halogen chemistry in the MBL over the past several decades, there remain several unanswered questions in relation to the sources and impacts of iodine over the remote oceans. Several studies have shown that the levels of reactive iodine (in the form of IO) measured over the open ocean cannot be accounted for by measurements of organoiodines alone, and alternative sources are required to match these observations. A number of mechanisms have been proposed for the release of reactive iodine in inorganic forms from non-biological processes as discussed previously.

The aims of this work were to try to better understand the mechanism by which iodine could be released into the atmosphere from the open ocean through the reaction of O_3 and iodide in the sea surface. In the atmosphere, this process will be affected by a number of different physical and chemical parameters, and this work aimed to investigate these effects with the aim of quantifying the inorganic source of iodine from the ocean.

The experiments could then be used to produce parameterisations for the inorganic iodine flux based on measurable parameters such as sea surface iodide concentration

and atmospheric ozone concentration. Comparison of the predicted fluxes with field measurements of iodine oxides taken over the remote ocean in the Galapagos Islands provided a useful method for assessing the applicability of these expressions to the real atmosphere. The motivation for producing these expressions is to provide a useful tool for use in atmospheric global models, so that the impacts of iodine chemistry can be assessed on a global scale.

Chapter 3

Measurements of the Iodine Flux from the I⁻ + O₃ Reaction

An important element of this PhD project involved laboratory experiments to investigate the so-called "inorganic iodine flux" produced from the reaction of O_3 deposited to the surface of an iodide solution. Several recent field measurements have shown that the observed levels of gaseous IO cannot be explained by the measured halocarbon fluxes and that an additional inorganic iodine source is required to match the observations (Groβmann et al., 2012; Mahajan et al., 2010a; Mahajan et al., 2012). The reaction of gaseous O_3 with I⁻ in surface seawater has been demonstrated to produce significant amounts of I_2, which may provide the explanation for the missing source of I_2 in these field measurements (Garland and Curtis, 1981). The aim of these experiments was to try to quantify the I_2 flux produced via this mechanism and study the effects of a number of ocean physical variables such as temperature, salinity and organic compounds on the resulting flux.

The method employed involved conversion of the reactive iodine from solution into iodine oxide particles (IOPs) and subsequent detection using a nano-differential mobility analyser. Measurements were performed using the Tapcon (EMS VIE-10) instrument, which measures both the number and size of the iodine particles produced. A description of the various components of the Tapcon system, the process of IOP formation and the experimental set-up is provided in section 3.1. Section 3.2 goes on to discuss the experiments performed using iodide solutions, where the effects of various atmospherically relevant parameters on the resulting inorganic iodine flux are presented.

3.1 Experimental Technique

3.1.1 The Tapcon Instrument

The Tapcon instrument is an electrical mobility spectrometer made up of a number of different components which allow the separation of particles based upon their size. The instrument is capable of measuring down to thousands of particles, and this indirect method gives detection limits for I$_2$ of 1–2 ppt, a greater sensitivity than is currently achievable with traditional direct absorption techniques. This level of sensitivity is necessary due to the very low fluxes of I$_2$ and HOI expected under atmospherically relevant conditions. The main body of the instrument which provides the separation is the differential mobility analyser (DMA) which separates the particles based on electrical mobility. This electrical mobility determines the drift velocity of the particle under the influence of an electric field and is dependent upon the size of the particle. The basis of this technique is discussed in detail by Reischl (1991), and a brief description is provided below along with a schematic diagram of the various components of the Tapcon system (Figure 3.1).
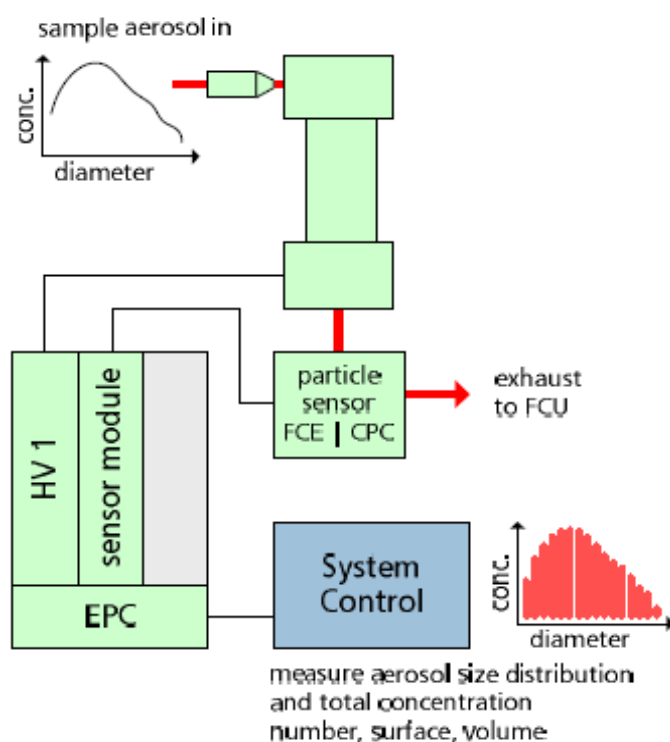
Figure 3.1 Tapcon instrument set-up (figure taken from Berner et al., (2006)) showing all components including: neutraliser, differential mobility analyser, Faraday cup electrometer and EMS control system.

For the determination of the electrical mobility distribution, the particles must first be brought into charge equilibrium; this is achieved by flowing the aerosol through a neutralizer. The neutralizer consists of a radioactive source (Am-241), contained within a lead shielded stainless steel cylinder, that produces both positive and negative ions through bipolar diffusion charging (Figure 3.2). The alpha particles emitted by the radioactive source ionise the surrounding air molecules (N_2 and O_2) producing N_2^+ and O_2^+ ions (Reischl et al., 1996; Winklmayr et al., 1991). The aerosol sample is then introduced into the chamber where it is exposed to the high ion concentration. Diffusion charging occurs due to the random thermal motion of the ions and particles, leading to ion-particle collisions which give rise to charged particles through ion capture (Winklmayr et al., 1991). An equal number concentration of both positive and negative ions are produced within the cylinder; however, an imbalance arises downstream of the ionisation chamber due to increased wall losses of negative ions due to their greater mobility. This leads to a greater concentration of positive to negative ions in the connection space between the neutraliser and the DMA (Lee et al., 2005b).
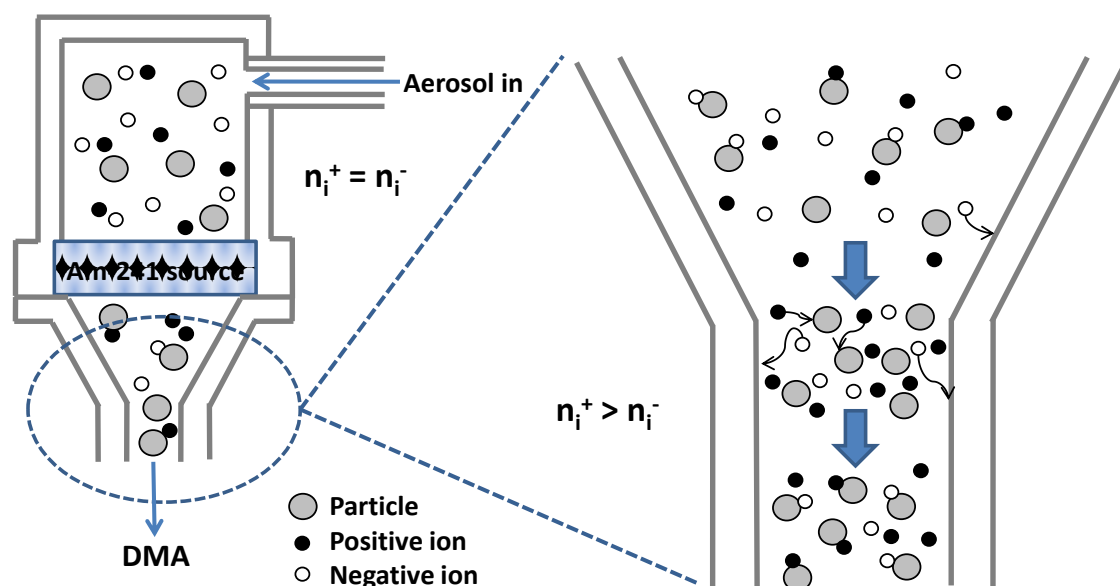
Figure 3.2 Schematic diagram of the Am-241 ionisation source and the mechanism of ionisation occurring downstream with a greater number of positive than negative ions produced (adapted from Figure 10 in Lee et al. (2005b)).

After this the particles are flowed into the DMA which is used to classify particles in the size range 0.6–40 nm. The DMA has a cylindrical arrangement with a grounded outer electrode and an inner electrode held at a set voltage, producing an electrical field in the space between the two (Figure 3.3). The aerosol flow is introduced close to the outside wall of the DMA and an additional particle-free "sheath" air flow is injected which fills the remaining space between the electrodes. A tangential inlet into the entrance channel gives a uniform flow along the length of the DMA and low diffusional losses of fine particles, which is essential to achieve optimum performance of the instrument (Flagan, 2008; Winklmayr et al., 1991). Particles flow towards the central electrode with a velocity determined by their electrical mobility (which will be dependent on both their size and electric charge); the smaller the particle (or higher the electric charge), the higher its electrical mobility. The particle size distribution is measured over a range of particle mobilities by varying the voltage on the central electrode in discrete steps. A small slit at the far end of the electrode allows through particles with mobilities in a narrow range (Knutson and Whitby, 1975; Reischl, 1991).
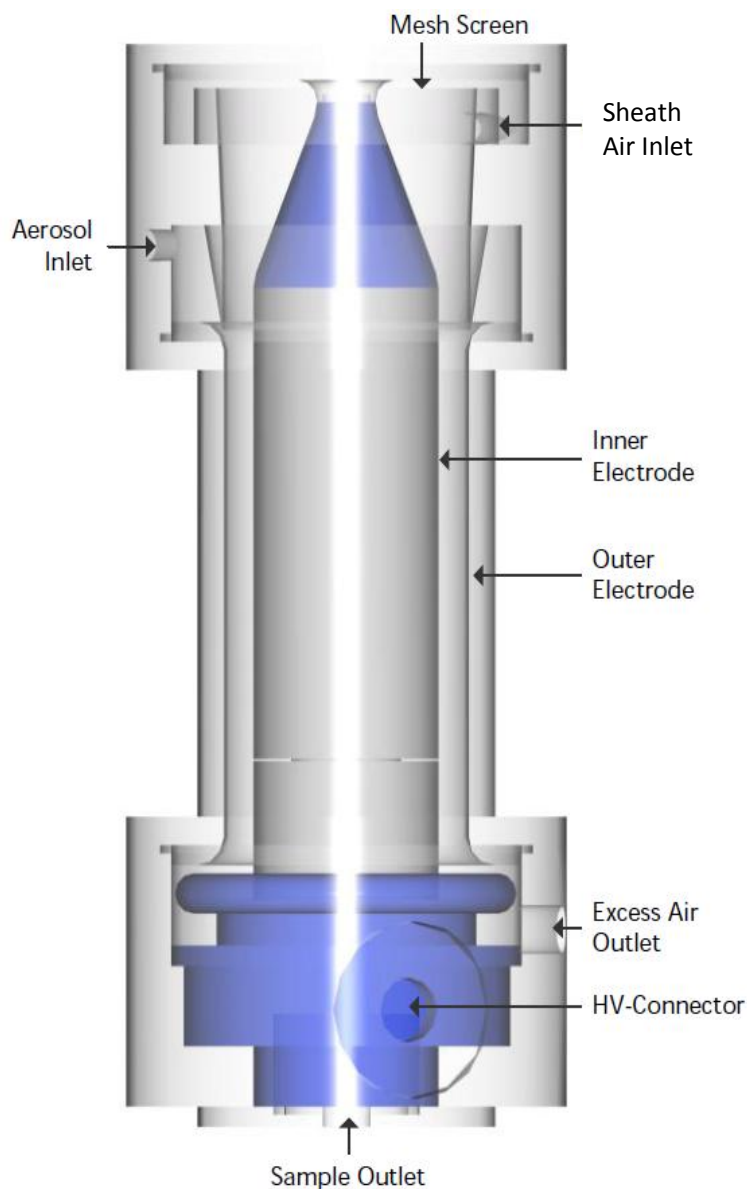
Figure 3.3 Diagram showing the essential components of the DMA including the aerosol and sheath air inlets, inner and outer electrodes, sample and excess air outlets and the high voltage supply (taken from Berner et al. (2006)).

The particles then flow into the Faraday Cup electrometer (FCE) which is based on the principles of a Faraday cage. In the FCE, the electrical charges of the particles entering the cage are compensated by a current on the outside of the cup which is measured by an amplifier. The current signal is then converted to a voltage signal and fed to the Electromobility Spectrometer Process Controller (EMS EPC-10) where, after further processing, it can be related to the number of particles entering the Faraday Cup per unit time using the system software (Berner, 2006).

The stability of the air flow through the instrument is paramount for optimal functioning of the DMA. Stability is achieved through the use of a flow control unit (FCU) which uses a recycling process for the sheath air passing through the DMA. The FCU consists of a number of components: a coalescence filter to remove particles; a critical orifice to determine flow rate; a vacuum pump; a dryer consisting of silica gel; activated charcoal to eliminate hydrocarbons and reactive components from the air; and a flow meter to check the sheath air flow rate. These components provide the necessary gas conditioning and vacuum generation for the DMA (Berner, 2006; Winklmayr et al., 1991).

3.1.2 Mechanism of IOP Formation

The current experimental set-up involves the production of iodine oxide particles from the reaction of gaseous O_3 with a solution containing iodide and subsequent photolysis of the gaseous products. The reaction between O_3 deposited on the surface of the solution and I^- in the interfacial layer produces iodine molecules (I_2) and hypoiodous acid (HOI) that are then released into the gas phase. These I_2 and HOI molecules must then be photolysed to produce I atoms. The I atoms can then go on to react with ozone (O_3) to produce iodine oxide particles (IOPs).

There remain a number of uncertainties regarding the exact mechanism of IOP formation, although there has been significant progress in this area over the last few years. Measurements by Saunders et al. (2010) showed that IOPs were produced from IO even in the absence of O_3, which conflicted with the initially proposed mechanism involving a series of O_3 oxidation steps to produce I_2O_5 which then undergoes polymerisation and coagulation (Saunders and Plane, 2005) (summarised in Figure 3.4 below).
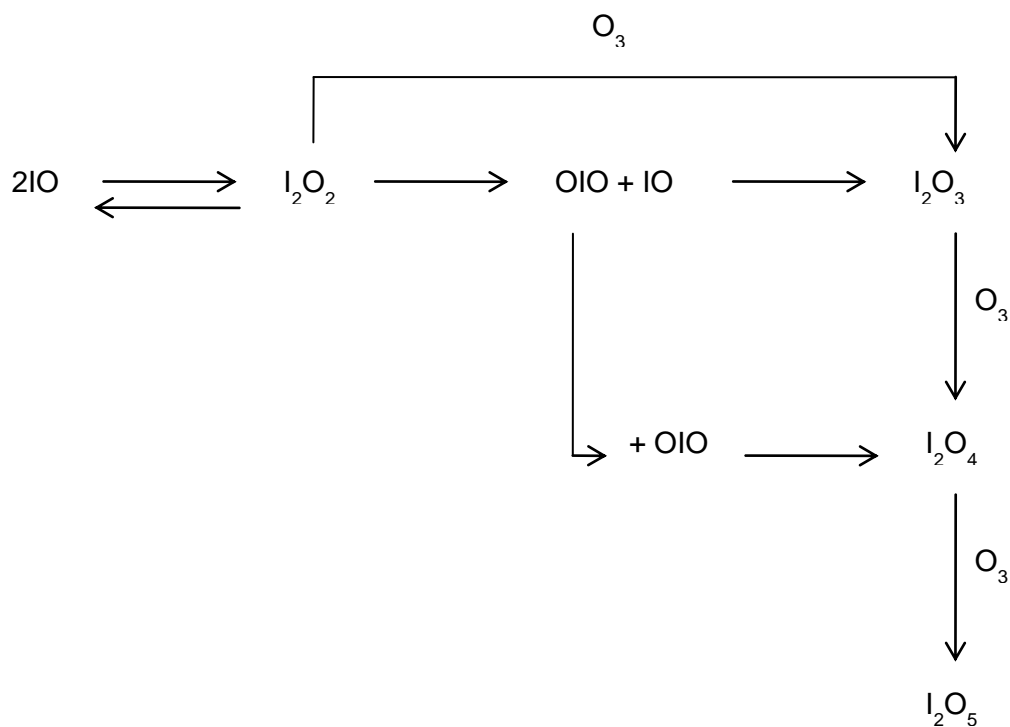
Figure 3.4 IOP production mechanism as described in Saunders and Plane (2005).

More recent studies by Gómez Martín et al. (2013) using photo-ionisation time-of-flight mass spectrometry (PI-TOF-MS) and complementary quantum calculations have shown that the most likely precursor to IOP formation is in fact I_4O_8 formed from the dimerisation of I_2O_4. The I_2O_4 dimer was found to be remarkably stable compared to the other iodine oxide aggregates due to the presence of two I—O bonds with highly covalent character. Therefore the currently proposed mechanism proceeds via the following steps:
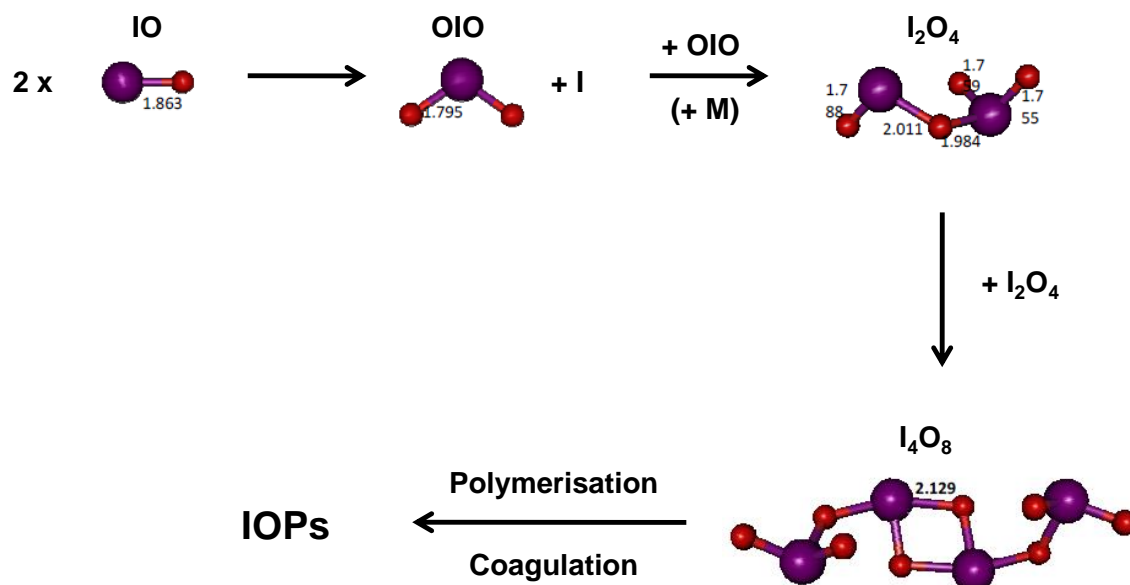
Figure 3.5 Updated IOP mechanism based on work by Gomez Martin et al. (2013) showing stable I_4O_8 dimer.

I_4O_8 may then polymerise and the subsequent iodine oxide aggregates coagulate. There is also the possibility that I_2O_2, I_2O_3 and I_2O_5 may attach to the I_4O_8, but direct formation of IOPs from any of these three species is not viable, especially considering the very slow O_3 oxidation rates.

The results of Saunders and Plane (2005) predict that the IOPs produced will consist predominantly of I_2O_5. This is assumed to be the case when working out the mass of iodine contained within the particles (this procedure is described in the next section). This likely occurs through restructuring in the solid phase and liberation of I_2 (Gómez Martín et al. (2013)):

$$5I_2O_4 \rightarrow 4I_2O_5 + I_2 \tag{R3.1}$$

3.1.3 Experimental Set-up

As mentioned above the current experimental set-up requires air containing IOPs to be flowed into the DMA of the instrument through the neutraliser for the particles to be separated and detected. The iodide solution is contained within a jacketed glass cell to

allow control over the solution temperature and is covered with black cloth to prevent stray light entering. A mixture of N_2 and O_3/O_2 is flowed through the cell at varying rates to produce I_2 molecules which are then transported to the IOP cell. At this point additional flows of N_2 and O_3/O_2 are added.

The O_3 flow is produced from photolysis of O_2 using UV light (λ = 185 nm) from a mercury pen lamp. The total flow at the entrance to the IOP cell is kept constant at 600 sccm (standard cubic centimetres per minute). At the other end of the cell a tungsten lamp is positioned to photolyse the I_2 or HOI molecules to produce I atoms. An additional flow of N_2 (2500 sccm) is added at this point and the total flow is then passed through the radioactive source and into the DMA. A flow diagram for the experiment is given in Figure 3.6.
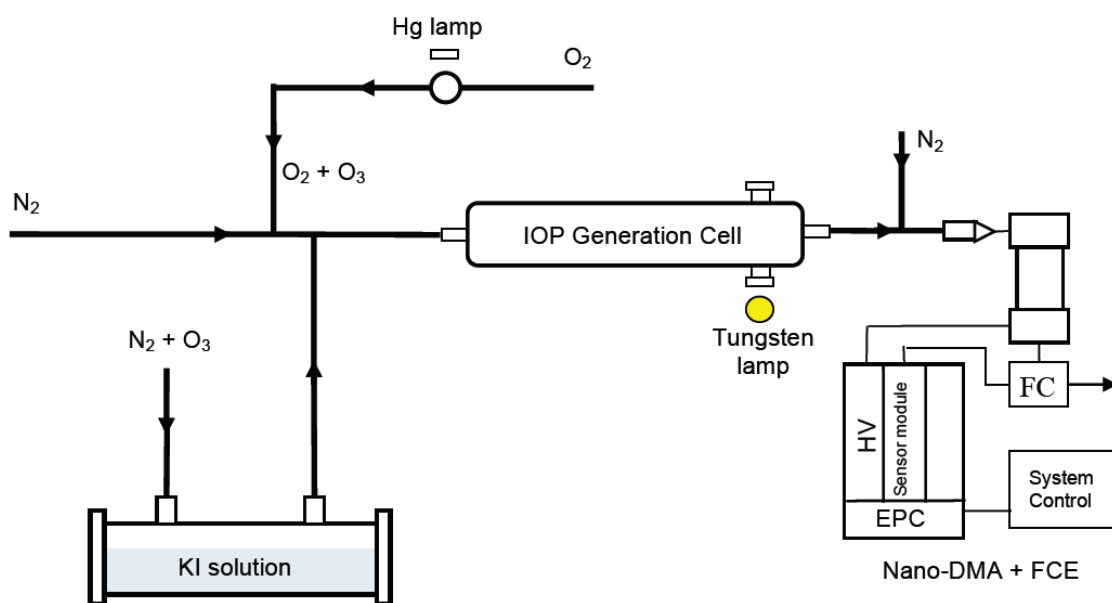
Figure 3.6 Flow diagram for I⁻ + O₃ experiments. Arrows indicate the direction of air flow.

Each experimental run takes approximately three minutes and a size distribution plot is obtained from which the total number of particles can be deduced and also the total volumetric mass of iodine in the particles. The instrument is able to detect particles in the range 0.6–40 nm in diameter. The volumetric mass of iodine in the particles is calculated by assuming that the IOPs produced have a composition I_2O_5 (as previously determined by Saunders et al. (2005)), with spherical particles for diameters of

0.6-6.6 nm and fractal particles for diameters > 6.6 nm. The density of the former is taken as 5.0 g cm^{-3} (ρ bulk = density of I_2O_5) and for the fractal particles are assumed to have dimensions D_f = 2.5 (Saunders and Plane, 2006) and size-dependent densities where $\rho < \rho$ bulk and ranges from 4.95 g cm^{-3} at a diameter of 6.7 nm down to 2.03 g cm^{-3} for a particle diameter of 40 nm.

3.1.4 Calibration of the Tapcon Instrument

To ensure that the mass of iodine in the IOPs determined from the size distribution of the Tapcon can be related to the amount of I_2 released from solution, the instrument was calibrated using I_2 crystals. This allowed a measure of the amount of I_2 released as vapour from the iodine crystals which ended up in the IOPs, which takes into account the various points at which the efficiency of the detection system may not be one hundred percent, such as the photolysis of the I_2 molecules and reaction with O_3 to form particles.

A cell containing a few iodine crystals was added to the experimental set-up in place of the solution cell. N_2 was flowed over the cell at varying flow rates from 5 sccm to 25 sccm. The experiment was conducted at 0.4 °C to reduce the vapour pressure of I_2, because at room temperature the IOPs produced were beyond the detectable range of the Tapcon instrument (> 40 nm). The measurements show a linear trend which can be seen in Figure 3.7 below.
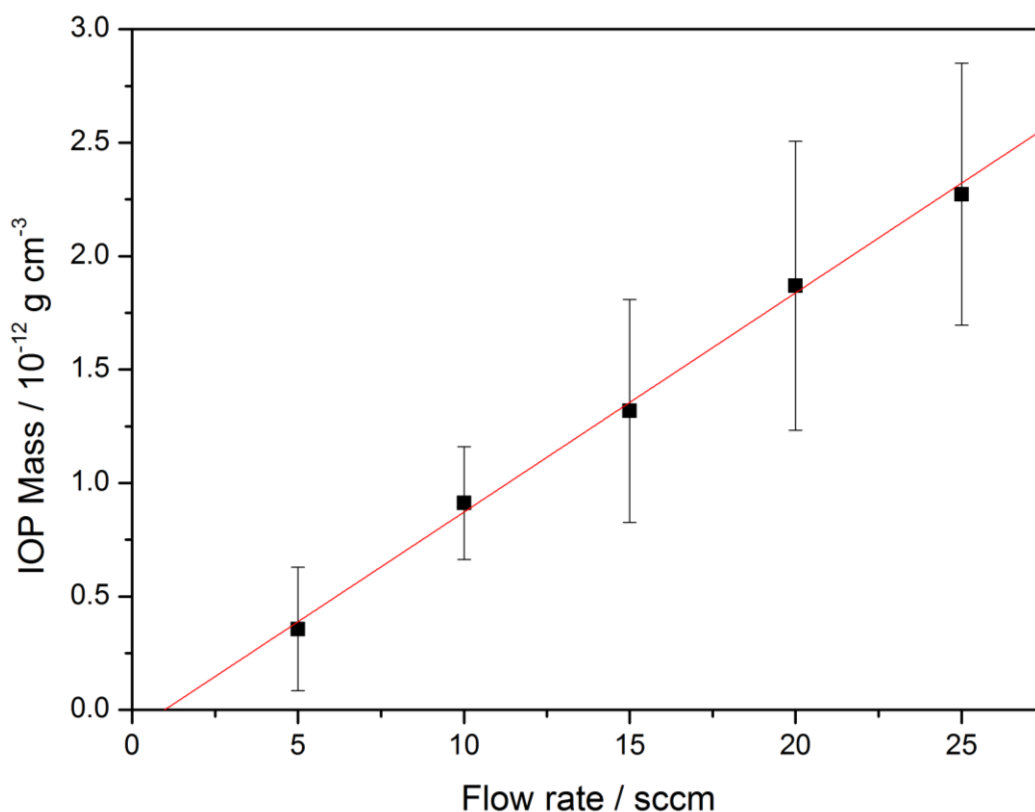
Figure 3.7 Plot of flow rate of N_2 through iodine containing cell and total mass of particles measured by Tapcon showing a linear dependence.

To calculate the efficiency of the Tapcon instrument the vapour pressure of iodine above the iodine crystals needed to be known. Values for the vapour pressure at a range of temperatures were used (Baxter and Grose, 1915; Saiz-Lopez et al., 2004c) to calculate the value for a temperature of 0.4 °C. Using this value the concentration of I_2 in the N_2 flow leaving the cell could be calculated at 1 atm pressure. This flow was then diluted further by the addition of the O_3 and N_2 flows in the IOP generation cell, therefore the concentration of I_2 in the flow entering the TAPCON instrument would be reduced. This fraction of I_2 in the total flow was calculated for each different flow rate through the iodine crystal cell.

Table 3.1 I_2 concentration from vapour pressure at different flow rates of N_2 through the I_2 crystal cell.

Total Flow / sccm	I_2 Flow / sccm	Fraction of I_2 flow	[$I_{2(g)}$] at 0.4°C / molecule cm^{-3}	[$I_{2(g)}$] in flow / molecule cm^{-3}
600	5	0.01	1.11×10^{15}	9.25×10^{12}
600	10	0.02	1.11×10^{15}	1.85×10^{13}
600	15	0.03	1.11×10^{15}	2.77×10^{13}
600	20	0.03	1.11×10^{15}	3.70×10^{13}
600	25	0.04	1.11×10^{15}	4.62×10^{13}

By comparing the amount of I_2 in the flow through the IOP generation cell and the amount of I_2 in the IOPs measured (assuming a composition of I_2O_5 (Saunders and Plane, 2005)), a percentage efficiency could be calculated for each flow rate. This is summarised in the table below. An average efficiency was taken and this correction was applied to all measurements that followed in calculations of the I_2 flux from solution.

Table 3.2 Efficiency of IOP production calculated from IOP mass and vapour pressure of I_2 crystals.

Flow / sccm	Total particles	Total mass / g cm^{-3}	Mass of I / g cm^{-3}	Efficiency %
5	2.49×10^5	3.57×10^{-13}	2.71×10^{-13}	3.48×10^{-2}
10	2.86×10^5	9.12×10^{-13}	6.93×10^{-13}	4.44×10^{-2}
15	2.85×10^5	1.32×10^{-12}	1.00×10^{-12}	4.28×10^{-2}
20	2.86×10^5	1.87×10^{-12}	1.42×10^{-12}	4.56×10^{-2}
25	2.82×10^5	2.27×10^{-12}	1.73×10^{-12}	4.43×10^{-2}
			Average =	**$4.24 \pm 0.43 \times 10^{-2}$**

Additional calibrations were performed for each ozone concentration and light source used in the following experiments, and the different correction factors applied to the individual experiments under those conditions. The effect of relative humidity on the efficiency of the Tapcon system was not investigated, however, this may impact on the efficiency of particle formation, and therefore the fluxes derived, in the temperature dependence experiments. An increase in relative humidity has been shown to decrease particle formation in previous experiments (Saunders et al., 2010), however,

any effect in the current experiments should be minimal due to the dilution of the air flowing from the solution cell prior to photolysis and particle formation. This is discussed further in section 3.3.2.

3.2 KI + O₃ Experiments

A number of experiments have shown that the action of ozone on the surface of solutions containing iodide can lead to the release of iodine molecules to the gas phase (Garland and Curtis, 1981; Sakamoto et al., 2009). A number of measurements of the ozone deposition rate to the sea surface have been performed at various locations around the globe. These range from 0.01 to as high as 0.1 cm s^{-1} (Gallagher et al., 2001; Wesely and Hicks, 2000) and will influence the rate at which I_2 is released from sea water. Laboratory studies have shown that the presence of iodide can cause an increase in the uptake of ozone to the surface of the solution (Magi et al., 1997).

Modelling studies have also shown that this reaction could significantly enhance ozone deposition (Chang et al., 2004; Oh et al., 2008); however, work by Coleman et al. (2010) found that the reaction of ozone with iodide in sea water was not sufficient to explain the observed deposition rates and reactions with organic species must occur to account for the observed difference. However, the reaction of ozone with iodide at the sea surface could provide a significant source of I_2 and HOI which is required to explain observations of IO in Cape Verde (Jones et al., 2010; Mahajan et al., 2010a).

The purpose of the experiments described below was to determine the flux of I_2 from this reaction at ambient concentrations and how factors such as temperature and salinity affect this flux.

3.2.1 Effect of Ozone Concentration

Initial runs were conducted with iodide and ozone both at higher than ambient concentrations; typical concentrations of iodide in seawater range from 0–300 nM. A 1×10^{-5} M solution of iodide was used and ozone was flowed over the solution at varying flow rates. Ozone was generated by photolysis of O_2 at 185 nm using a mercury

UV pen lamp at a quartz cell upstream of the solution cell. A clear particle distribution was observed for all flow rates, with an increase in particle number and mass observed on increasing the flow of ozone over the solution. This can be seen in Figure 3.8.
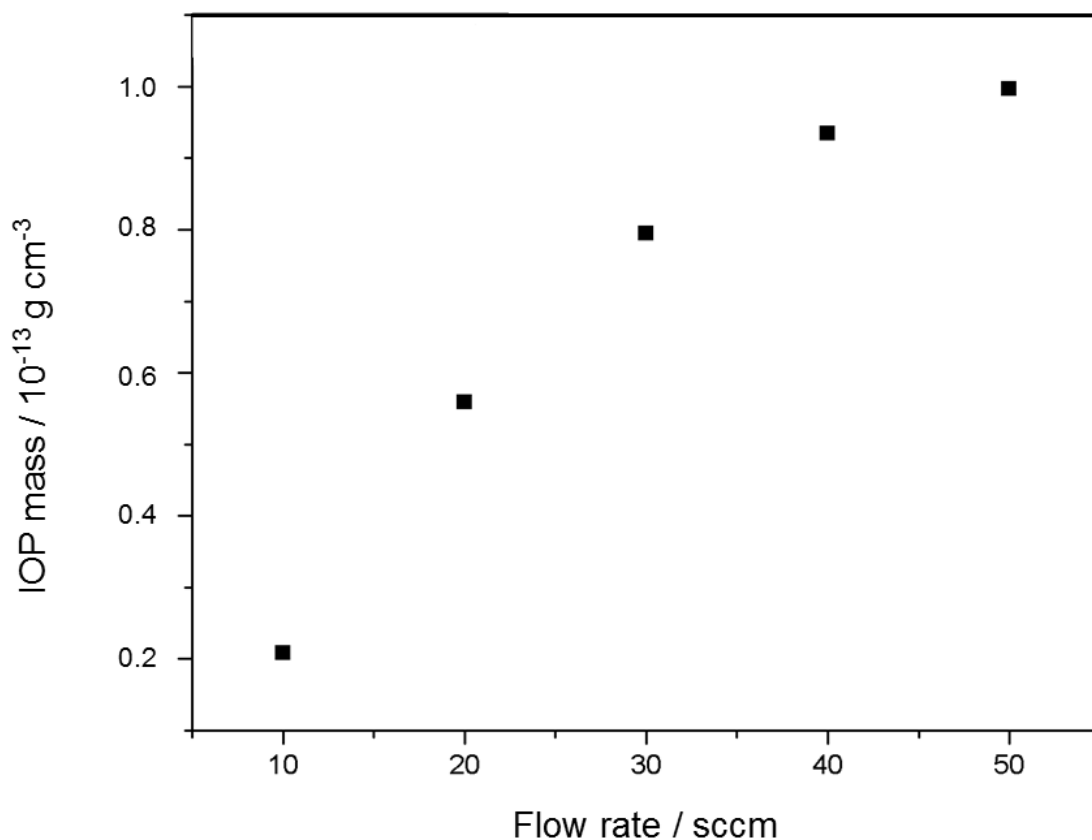
Figure 3.8 Plot showing increase in IOP mass with increasing ozone flow over solution.

The mechanism by which I_2 is released from the iodide solution was described by Sakamoto et al. (2009) and involves the formation of an $IOOO^-$ intermediate at the solution/air interface.

$$I^-_{(aq)} + O_{3(g/interface)} \rightarrow IOOO^-_{(interface)} \qquad \text{(R3.2)}$$

$$IOOO^-_{(interface)} \rightarrow IO^-_{(aq)} + O_{2(aq)} \qquad \text{(R3.3)}$$

$$IO^-_{(aq)} + H^+ \leftrightarrow HOI_{(aq)} \qquad \text{(R3.4)}$$

$$HOI_{(aq)} + I^-_{(aq)} + H^+ \leftrightarrow I_{2(aq)} + H_2O \qquad \text{(R3.5)}$$

$$I_{2(aq)} \rightarrow I_{2(g)} \tag{R3.6}$$

$$I_{2(aq)} + I^-_{(aq)} \leftrightarrow I_3^-_{(aq)} \tag{R3.7}$$

$$HOI/IO^-_{(aq)} + 2O_{3(aq)} \rightarrow IO_3^-_{(aq)} + 2O_2 + H^+ \tag{R3.8}$$
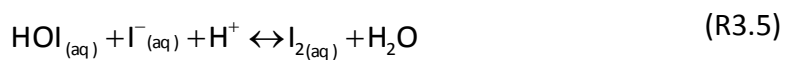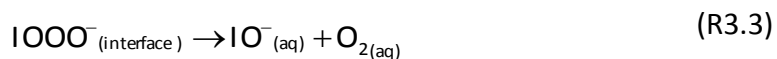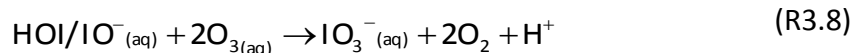
To investigate the effect that ozone concentration had on the mass of IOPs produced, the concentration of ozone was measured at different flow rates and with the mercury pen lamp at increasing distances from the quartz cell. The mercury pen lamp distance was increased until close to ambient levels (78 ppb) were achieved and a clear size distribution of IOPs was still observed (i.e. particles were being produced). The variation of IOP mass with ozone concentration is shown in Figure 3.9.
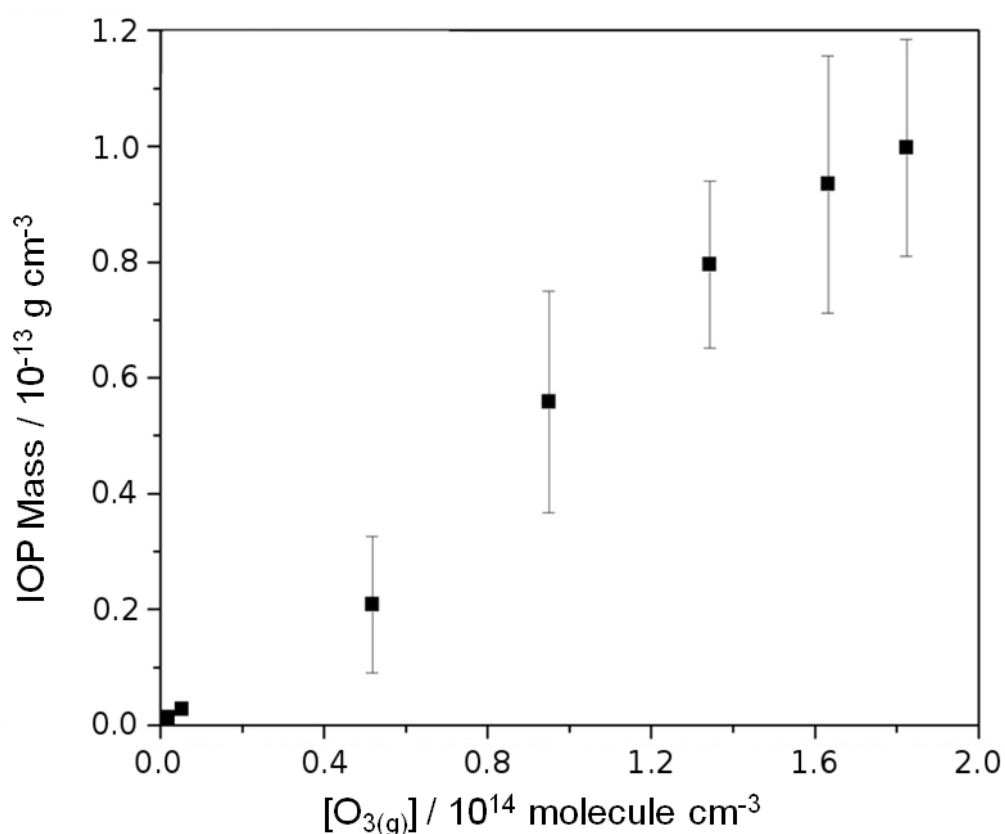
Figure 3.9 Plot showing increased mass of IOPs with increasing ozone concentration at constant iodide concentration (1 x 10⁻⁷ M).

The IOP mass shows a linear dependence on the O_3 concentration as can be seen in the plot above, which is what would be expected given the mechanism of I_2 formation.

O_3 is only involved in the initial formation step where HOI is produced (showing a first order dependence with respect to O_3), and any increase in the O_3 concentration over the solution will result in a corresponding increase in the O_3 in the interfacial layer by virtue of the Henry's law equilibrium (providing the timescale for reaction with iodide is longer than for evasion from solution).

3.2.2 Effect of Iodide Concentration

The next experiments involved reducing the iodide concentration to approximate sea water concentrations, around 100 nM, although this will vary depending on location and factors such as temperature and biological activity (discussed later in Chapter 5). The IOP mass fell with decreasing iodide concentration, with a linear trend when plotted on a log scale (Figure 3.10). This suggests that, in contrast to the first-order kinetics displayed in the O_3 dependence experiments, the overall mechanism displays a more complex I⁻ dependence.
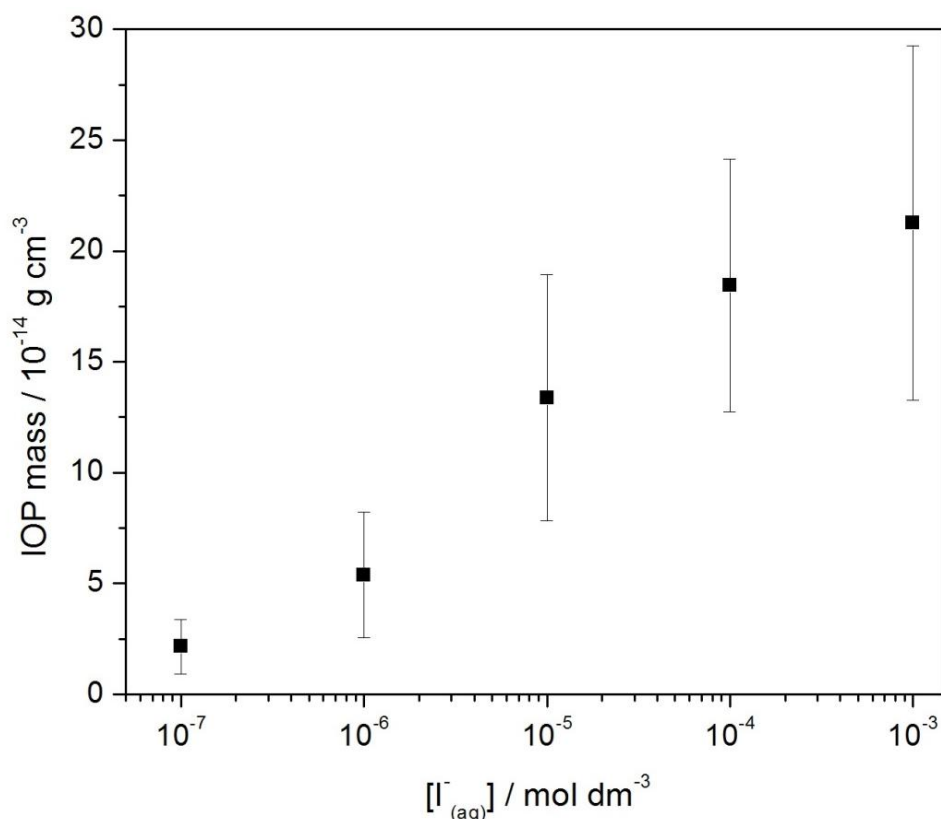
Figure 3.10 Plot of IOP mass vs. [I⁻$_{(aq)}$] showing increasing trend.

There is a possible deviation from linearity at the highest iodide concentrations which could be due to a surface saturation effect.

3.2.3 Effect of Organic Species

The sea surface microlayer is known to contain a large quantity of dissolved organic matter (DOM) which is composed of a number of different organic compounds of both biogenic and anthropogenic origin. The microlayer has an enhanced concentration of DOM compared to bulk seawater (around 40–80 μM (Hansell et al., 2009)), and the composition of this DOM has been the subject of numerous studies, and contains contributions from carbohydrates, proteins, fatty acids and organic carbon, although much of the composition is still unknown (Hunter and Liss, 1977). There are a number of effects that the presence of these compounds may have on the I⁻ + O₃ reaction. The presence of organic compounds is known to enhance the deposition rate of O₃ to surface seawater (Coleman, 2010; Martino et al., 2012), however, these organic compounds may compete with I⁻ for reaction with O₃ if the reactions are fast enough (Hayase et al., 2010; von Gunten, 2003). In addition, the presence of organic films, known to form at the surface of both seawater (Frew, 1997) and marine aerosols (Mochida et al., 2002; Tervahattu et al., 2002), may inhibit the release of the I₂ and HOI produced to the gas phase (Rouviere and Ammann, 2010). A number of studies have found that iodine may be incorporated into organic material (Martino et al., 2009; Reiller et al., 2006; Saunders et al., 2012), possibly through photosynthetic pathways, which is confirmed by the presence of a large organic fraction of iodine in marine aerosols (Baker et al., 2000; Gilfedder et al., 2008). Therefore this could inhibit its release or mean the iodine is released in the form of iodocarbons, the majority of which will be less reactive in the marine boundary layer than the inorganic forms. A number of different organic compounds were considered to investigate their effect on the I₂ flux on addition to the iodide solutions.

The first organic species investigated was humic acid which is not a single compound but contains a number of different organic functional groups formed through the degradation of organic matter. In this case the humic acid was obtained from Sigma

Aldrich and was from a terrestrial source. A small amount was added to a 1×10^{-7} M KI solution which was then stirred overnight and any remaining un-dissolved humic acid filtered off.

Although it was difficult to know the exact amount of humic acid dissolved in the solution, it was possible to estimate the initial dissolved organic content through spectroscopic measurements. Specific UV absorbance (SUVA) values for humic acids have been reported around 5 mg L^{-1} m^{-1} at 254 nm (Weishaar et al., 2003), and spectra showed that the absorption due to humic acid in the solution at 254 nm was around 0.1. This gave a dissolved organic carbon concentration of ~2 mg L^{-1} which was in good agreement with measured values of DOM in shallow seawater (defined as the first 300 m) (Thurman, 1985). The humic material was found to have no significant effect on the resulting I_2 flux compared to the pure iodide solution. This is in agreement with recent work by Hayase et al. (2012) which showed that humic acid had little effect on the concentration of I_2 produced in more concentrated iodide solutions, although fulvic acid was found to have an effect due to more effective proton donation from the carboxylic acid group.

Experiments performed by Hayase et al. (2010) investigated the effect that certain organic compounds have on the iodide plus ozone reaction. They found that phenol and other species containing the phenol functional group had a marked effect on the iodine produced in the gas phase. Working at concentrations which were significantly higher than ambient levels (1 mM phenol), the I_2 and IO produced was around half that of a pure NaI solution. This was attributed to the fast reaction of the phenolate ion with O_3 (1.4×10^9 M^{-1} s^{-1}) which competes with that of I⁻. To determine whether a similar decrease could be detected in the IOP system, ambient levels of phenol (1×10^{-8}–1×10^{-7} M) were added to a 1×10^{-7} M solution of KI. This was found to have no observable effect on the mass of IOPs produced, therefore it was decided to increase the concentration of phenol. Only at a concentration of 1×10^{-3} M phenol (the same concentration used in the Hayase et al. (2010) experiments) was an effect observed. The total particle mass was reduced by around half and a significant reduction in the particle size distribution can be seen in Figure 3.11.
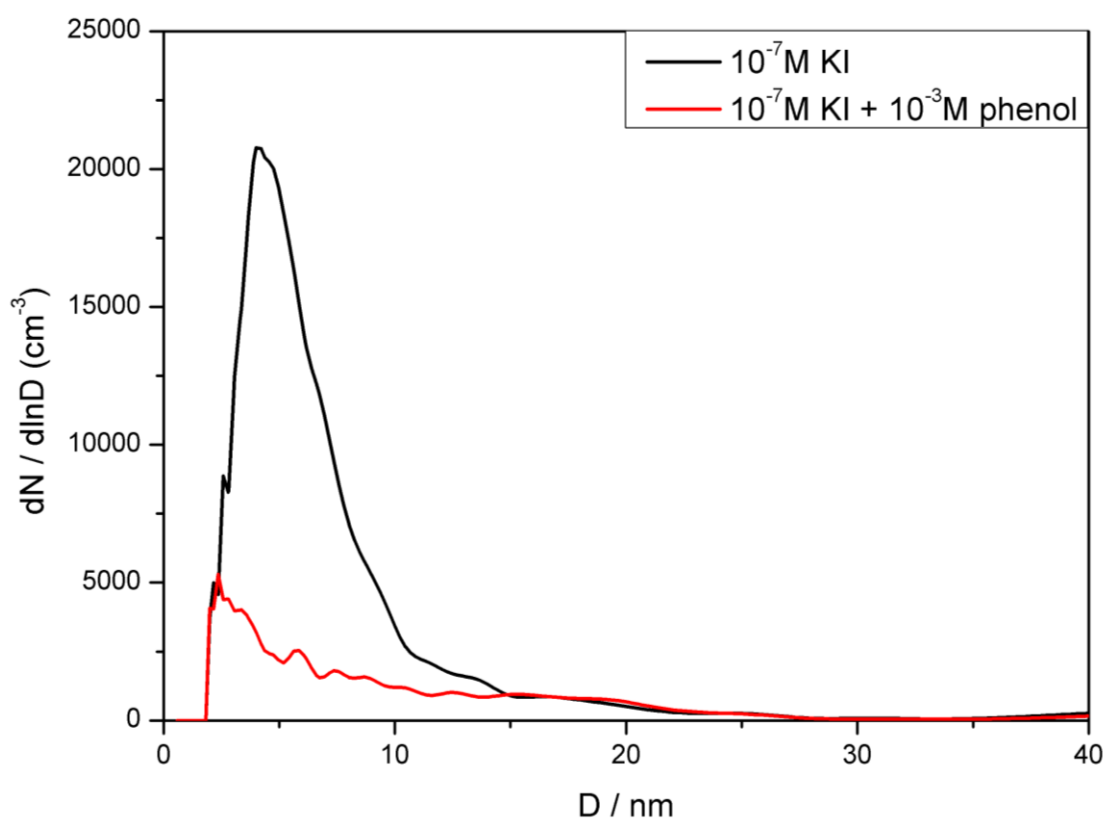
Figure 3.11 Particle distribution for 1 x 10⁻⁷ M KI solution with and without addition of phenol.

This concentration is orders of magnitude higher than that found in sea water, therefore phenolic compounds were not deemed to play an important role in regulating emission of I_2 from the reaction of iodide and ozone.

The final organic compound investigated was sodium dodecyl sulphate (SDS) which is a surfactant compound commonly found in a number of detergents and present at around 10 μg L^{-1} in seawater (Ćosović et al., 1985). SDS was added to a 1 x 10⁻⁷ M KI solution at sufficient concentration to form a monolayer at the solution surface (6.2 x 10⁻³ M) (Hore et al., 2005). However, this amount of SDS was found to have no significant effect on the resulting IOP mass. Studies by Rouviere and Ammann (2010) showed that certain surfactant species could inhibit the release of I_2 from iodide solution reacted with O_3 by forming a barrier to I_2 release. Their work did suggest, however, that chain lengths of > C15 may be necessary for a significant reduction in the I_2 flux to be observed. This is most likely due to the structure of the monolayer formed and how densely the monomers are packed.

In addition to the organic species mentioned above, real seawater samples were also collected to see whether the same mechanism could actually be observed in the environment. The seawater samples were collected from the coast of Scarborough, North Yorkshire in HCl acid-washed, 1 L, high density polyethylene (HDPE) bottles. The samples were then taken back to the laboratory on the same day and stored in a refrigerator at 3 °C. Before adding the seawater samples to the solution cell, the samples were first filtered to remove the larger traces of organic or biological matter. The same procedure that was used for the iodide solutions was employed and an O_3 concentration of 222 ppb was flowed over the seawater surface. The results are shown in Figure 3.12 below.
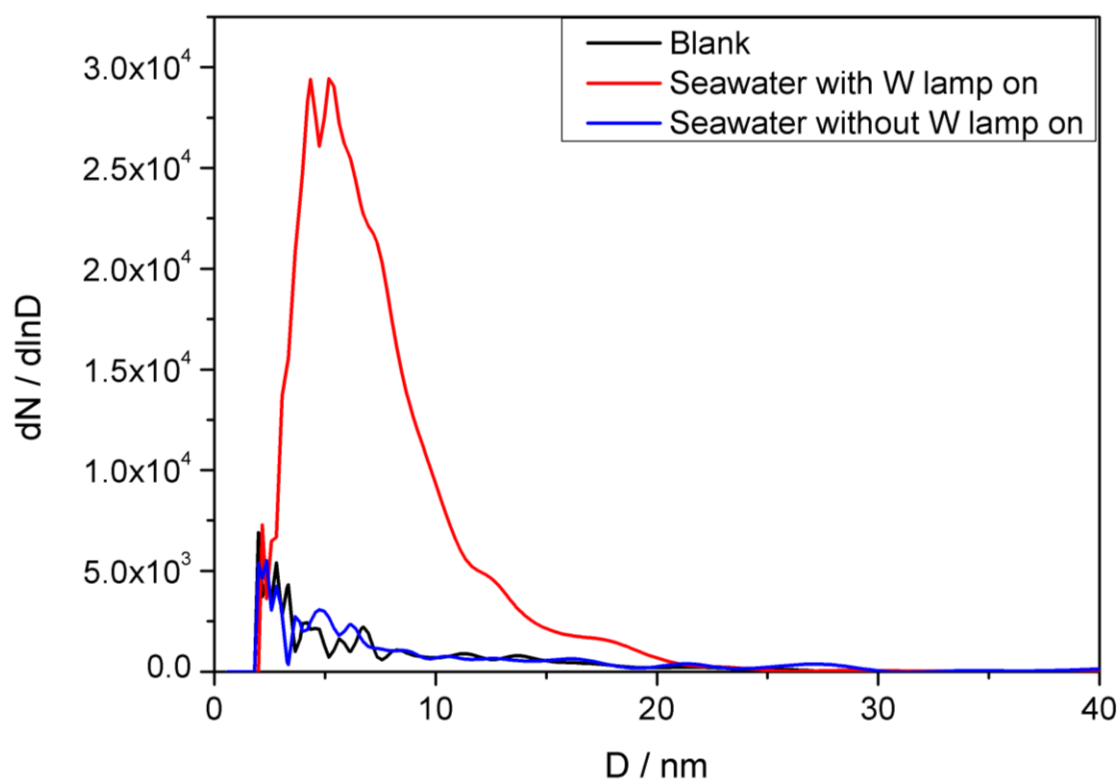
Figure 3.12 IOP distribution from a real seawater sample with (red line) and without (blue line) the W lamp turned on for photolysis of I_2.

A clear distribution of particles is observed showing that this mechanism can occur in real seawater conditions. Unfortunately, it was not possible to verify the amount of iodide in the seawater samples, however, as the samples were obtained from a coastal location it is likely the levels are higher than those in the open ocean.

Also shown is an experiment performed with the tungsten lamp turned off to show that the IOPs observed are formed from the photolysis of I_2 rather than directly from IO released from solution. Previous studies have shown that IO is also released from the reaction of O_3 with iodide in solution as well as I_2 in the ratio 1:100. However, this effect may not be observed in these experiments due to the much lower concentrations used, the detection limit for the set-up and the fact that any IOPs produced in the solution cell would have a longer time to grow and would therefore likely be outside the observable range of the DMA (> 40 nm).

3.2.4 Effect of Mixing

In all other experiments the iodide solutions were unmixed, however, in real seawater it would be expected that there will be increased mixing due to the action of wind and waves at the sea surface. Therefore experiments were conducted using a 1×10^{-7} M KI solution with a magnetic stirrer bar added to the solution cell. The solution was alternately mixed and unmixed by turning on and off the magnetic stirrer plate and the resulting IOP mass calculated. The results of the experiments showed that there was around a factor of two reduction in the IOP mass when the solution was stirred compared to the unstirred solution (IOP mass of 2.44×10^{-15} g cm^{-3} compared to 4.44×10^{-15} g cm^{-3}). This result is due to increased mixing of the I_2 from the surface into the bulk solution. This leads to a decrease in the I_2 at the solution surface resulting in a reduced I_2 flux to the gas phase.

3.2.5 Effect of Salinity

As sea water has a high salinity of around 35 psu (practical salinity units) it was deemed necessary to investigate what effect increasing salinity would have on the reaction of iodide with ozone. Therefore solutions of 1×10^{-5} M KI containing varying concentrations of NaCl from 0.1 to 0.5 M were made up and the IOPs produced from reaction with ozone were measured. This showed an increasing trend with Cl⁻ concentration as can be seen in Figure 3.13.
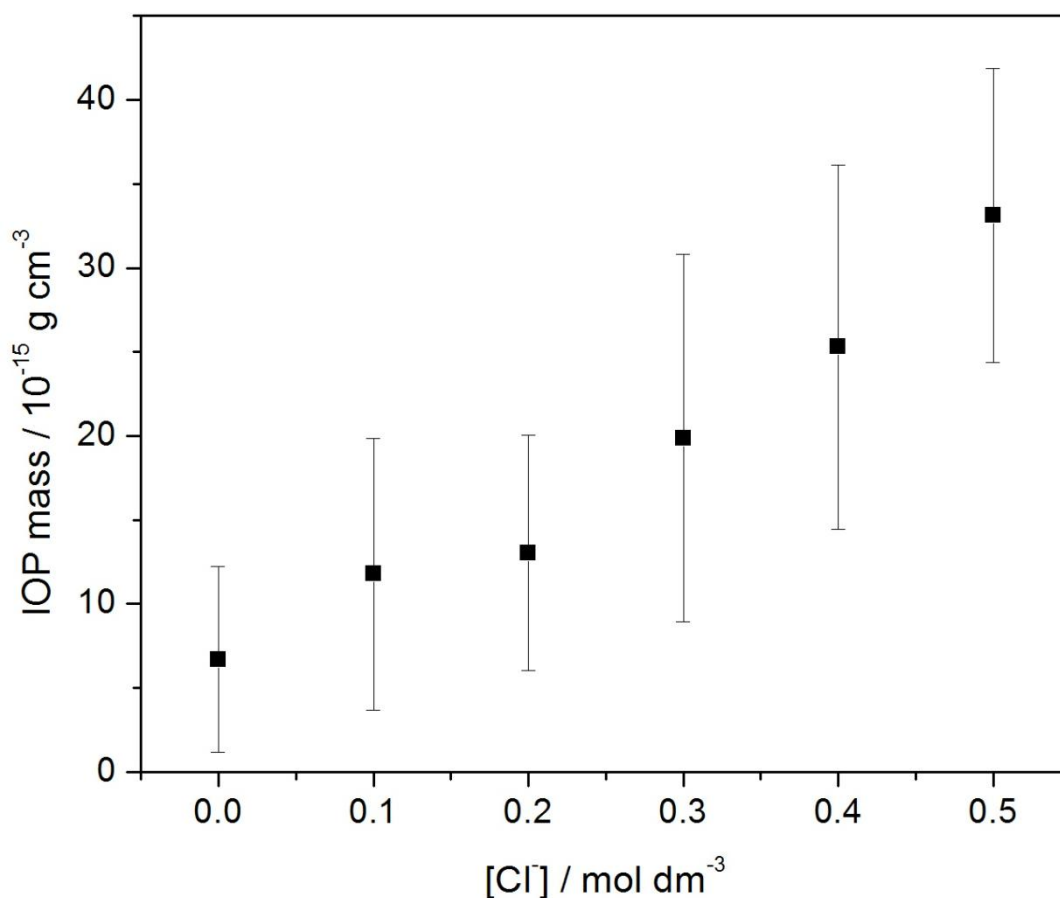
Figure 3.13 Plot showing increase in IOP mass with increasing [Cl⁻]

3.2.6 Effect of Temperature

The temperature of surface sea water varies greatly over the globe and depending on season and changes in climate. Temperatures can range from -2 °C around the poles up to as high as 45 °C in equatorial coastal waters. The effect of temperature on the iodide plus ozone reaction is therefore important to assess how the emission of iodine from this process may vary in different ocean waters.

To investigate the effect of temperature on this reaction a jacketed solution cell was used to allow the circulation of water at a controlled temperature surrounding the solution. The temperature of the water was controlled using a NESLAB Chiller, and the temperature of the solution inside the cell monitored using a thermocouple. The initial measurements were taken at room temperature. The solution was then cooled in approximately 5 °C increments and further measurements taken. A total of 10 scans (3

minutes per scan) were taken at each temperature. The results show an exponential decrease in particle mass as the temperature is lowered.

An Arrhenius plot of the results was produced, which showed a typical linear profile (Figure 3.14).
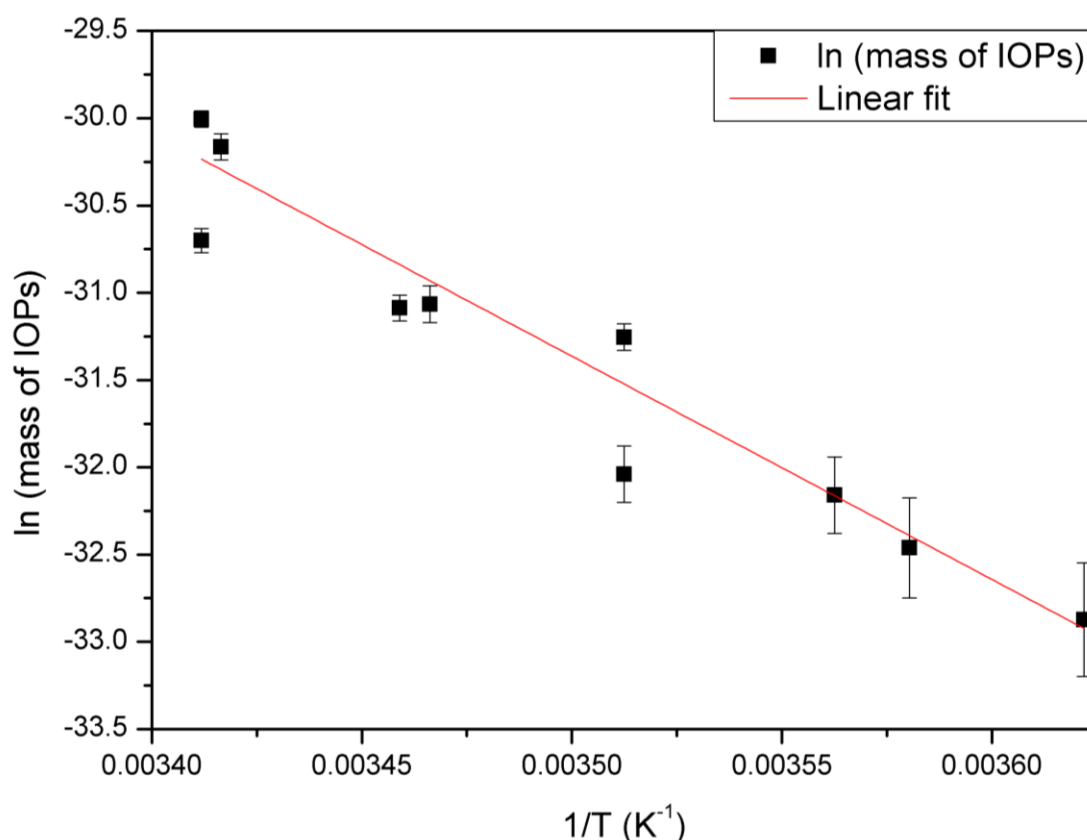
Figure 3.14 Arrhenius plot of ln(mass of I) vs. 1/T for a 1×10^{-7} M KI solution. This represents the temperature dependence for the overall mechanism.

The calculated activation energy of 101 ± 35 kJ mol^{-1} is in good agreement with the previous measurements of Magi et al. (1997) who report an activation energy of 73 ± 30 kJ mol^{-1} for the aqueous phase I⁻ + O₃ reaction. However, it should be noted that the activation energy obtained from the IOP experiments represents the overall mechanism, rather than an elementary process as is the case in the experiments by Magi et al. (1997). The method used in this case measured the disappearance of gaseous O₃ to an aqueous iodide solution using the droplet train technique rather than measuring the products of reaction. However, the Arrhenius expression obtained by

Magi et al. (1997) experiments gave an unphysical pre-exponential factor (1.44 x 10^{22}) around ten orders of magnitude larger than the diffusion limit. The temperature dependence experiments were therefore repeated using the laser set-up described below and the results of these experiments and implications for the results obtained above are discussed in section 3.3.

3.2.7 Measurements in Buffered Solutions

The measurements reported above were all performed using deionised water with a measured pH of around 6. However, seawater has a pH around 8 and this decrease in pH will affect the rate of the I⁻ + O₃ reaction due to the initial reaction involving H^+:

$$O_3 + I^- + H^+ \rightarrow HOI + O_2$$ (R3.9)
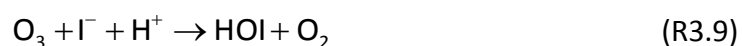
To investigate how changing the pH of the solution would affect the flux of I_2 from solution, experiments were repeated using potassium iodide dissolved in 0.1 M sodium phosphate buffer at pH 8 (made by mixing 0.1 M solutions of sodium phosphate dibasic and sodium phosphate monobasic in appropriate quantities to reach the desired pH). The pH of the solution was checked using pH indicator paper before each experiment.

As a result of the lower emission flux of I_2 from solution at higher pH, the output of the tungsten lamp was increased to 20 V (as opposed to 10 V used previously) and as a result the efficiency of the system was improved by a factor of ten. This allowed detection of IOPs at lower iodide and ozone concentrations.
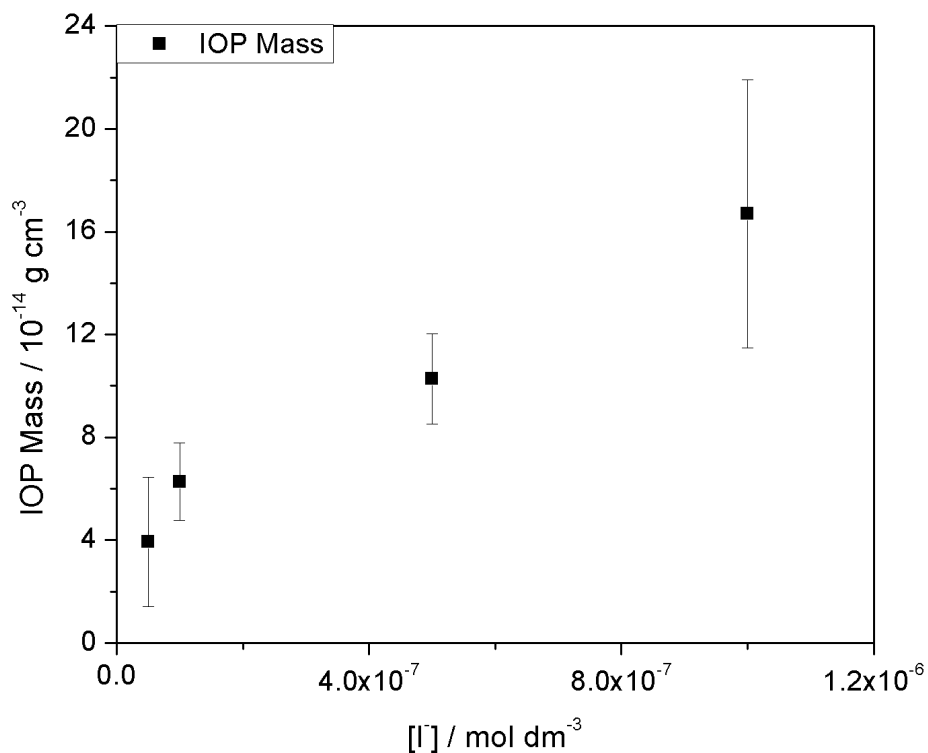
Figure 3.15 IOP mass at different iodide concentrations in pH 8 sodium phosphate buffered solutions.

Figure 3.15 shows the IOP mass as a function of iodide concentration in buffered solution. As can be seen the IOP mass increases with iodide concentration with a tail off at the higher concentrations, as observed in the un-buffered experiments.

The chloride dependence experiments were also repeated and showed a similar increase with increasing chloride concentration, however when in buffered solution this effect was less pronounced. The increase observed in moving from no chloride up to 0.5 M NaCl was a factor of 2.5 compared to 5 observed in the un-buffered experiments.
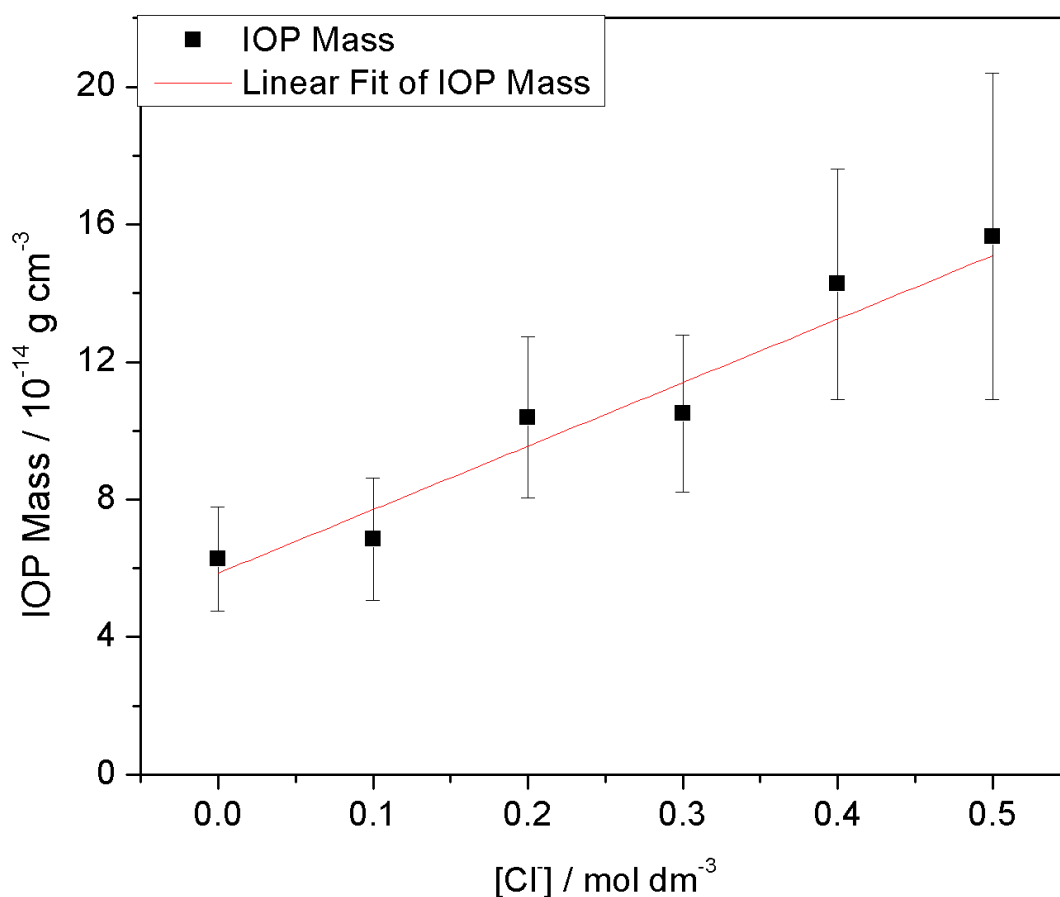
Figure 3.16 IOP mass at different chloride concentrations in pH 8 sodium phosphate buffered solutions.

Although this may seem like a large increase, the changes in salinity observed in real seawater are on a much smaller scale with salinity ranging from around 33 – 37 psu which equates to a chloride concentration of around 0.51 to 0.58 M. As a result, the effect of chloride on the emission of I_2 in seawater, assuming the same trend as observed in these experiments will be around 1 % and therefore negligible.

3.2.8 Measuring the Flux of HOI

The measurement technique described so far is sensitive to detection of I_2 only (with possible contributions from ICl and IBr in experiments using chloride and bromide) due to the light source used and its output in the visible–IR region; the spectrum increases from close to zero at 400 nm to peak at around 600–700 nm. Modelling work performed in York (Lucy Carpenter, University of York, personal communication)

suggested that HOI may also be released by the reaction of I⁻ + O_3 (produced in reaction R3.9) despite its low Henry's law constant, due to a large build up in the interfacial layer.

To detect HOI using the current experimental set-up, a change of light source was required with larger output in the UV due to the peaks in the absorption cross section of HOI at around 340 and 420 nm (see Figure 3.17). For this purpose, the tungsten lamp was exchanged for a 1000 W xenon arc lamp which has increased output in the UV.

To allow selective photolysis of both HOI and I_2, two different band-pass filters were employed: a blue glass band-pass filter (Schott UG-1, transmittance window 270-420 nm, and > 670 nm), and a yellow glass long-pass filter (Schott GG495, transmittance > 480 nm). The transmission spectra of these two filters are shown in Figure 3.17 below, along with the absorption cross sections for HOI and I_2. The photolysis rates of HOI and I_2 through each of the filters were determined by convoluting the transmitted spectral intensity of the Xenon lamp (measured using a grating spectrometer and charge coupled device (CCD) detector) with the respective molecular absorption cross section.
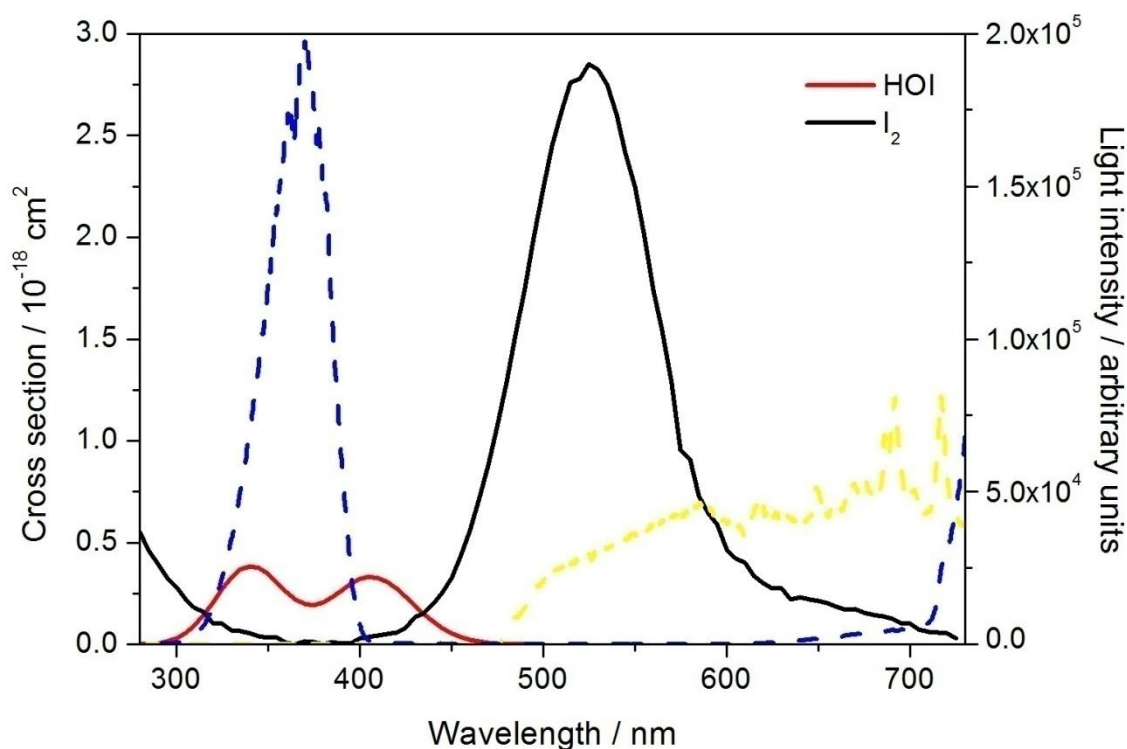
Figure 3.17 Absorption cross-sections of I$_2$ (solid black line) and HOI (solid red line) and the transmission spectra of the xenon light through the blue (blue dashed line) and yellow (yellow dashed line) optical filters.

As can be seen from Figure 3.17, there is still some overlap between the transmission spectrum of the UV filter and the absorption cross section of I$_2$ at the lowest and highest wavelengths and this needs to be taken into account when calculating the IOP mass from each individual species. Due to the order of magnitude larger peak in the I$_2$ absorption cross section compared to HOI this overlap could provide a significant contribution from I$_2$ to the IOP mass in the experiments using this filter. To calculate the relative contributions for each species to the total IOP mass, expressions were derived for the IOP mass produced by photolysis through each filter:

$$M_Y = 2J_Y(I_2)*[I_2] + J_Y(HOI)*[HOI] \tag{3.1}$$

$$M_B = 2J_B(I_2)*[I_2] + J_B(HOI)*[HOI] \tag{3.2}$$

M_Y and M_B represent the observed IOP mass from the experiments using the yellow and blue filters respectively. $J_Y(I_2)$ and $J_Y(HOI)$ are the J values for HOI and I_2 calculated by multiplying the absorption cross section of each species by the emission spectrum of the xenon lamp through the yellow filter, and $J_B(I_2)$ and $J_B(HOI)$ represent the same values calculated using the xenon lamp spectrum through the blue filter.

By assuming that $J_Y(HOI)$ is zero (i.e. there will be no photolysis of HOI using this filter) and combining the two equations, an expression for the ratio of $[HOI]/[I_2]$ was produced:

$$\frac{[HOI]}{[I_2]} = \left(\frac{M_B * 2J_Y(I_2)}{M_Y} \right) - \left(\frac{2J_B(I_2)}{J_B(HOI)} \right) \qquad (3.3)$$

By calculating the I_2 emission using a measured efficiency factor, determined by calibration as previously described, the corresponding HOI emission could also be calculated. As a result of the overlap of the spectra in the HOI experiments and the low IOP masses (close to the detection limit) the errors on the resulting HOI/I_2 ratios are quite large.

The HOI/I_2 ratio as a function of iodide was measured and the results are shown in Figure 3.18.
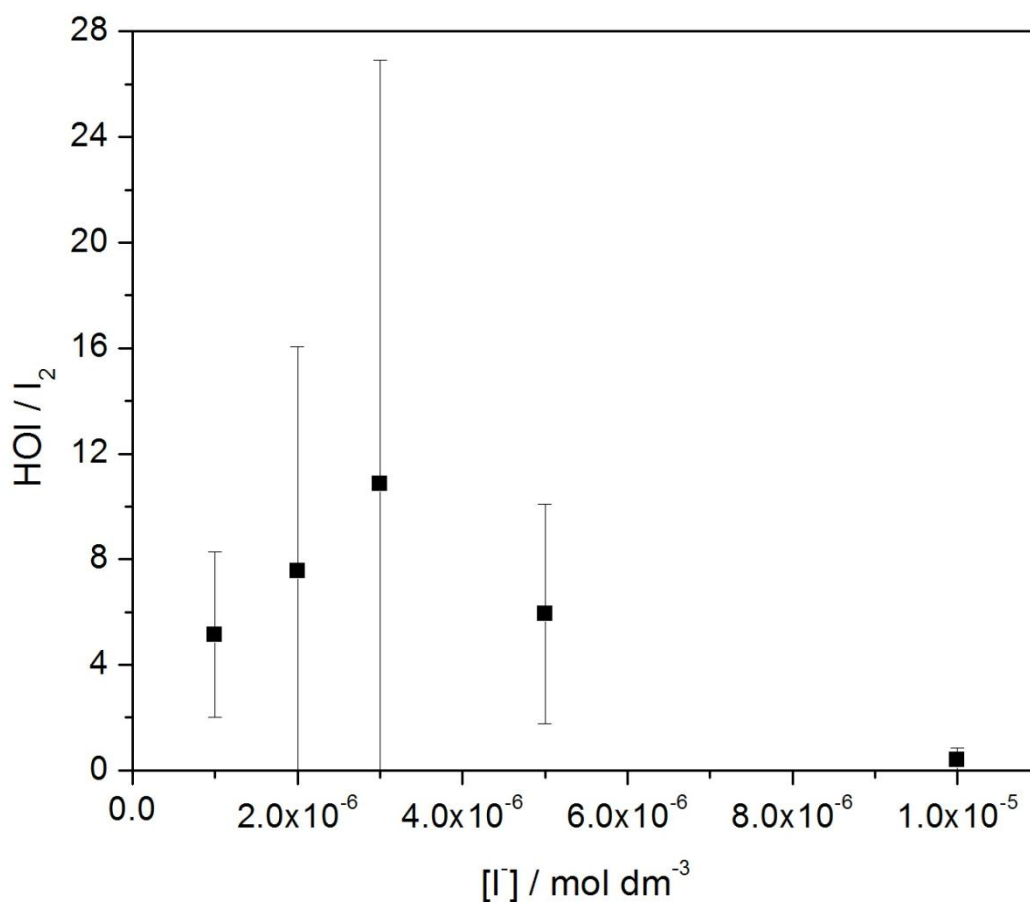
Figure 3.18 HOI/I$_2$ratio at different iodide concentrations.

3.3 Laser Experiments

Due to the unsatisfactory errors on the measurements using selective photolysis described in section 3.2.8, a further technique was employed to try to measure the relative contributions of HOI and I$_2$ to the observed IOP masses. A Nd:YAG (neodymium-doped yttrium aluminium garnet) laser was deemed ideal for selectively photolysing each species as the second and third harmonics at 532 nm and 355 nm coincide with peaks in the I$_2$ and HOI absorption cross-sections, respectively (see Figure 3.17).

The set-up of the laser experiments is shown in Figure 3.19.
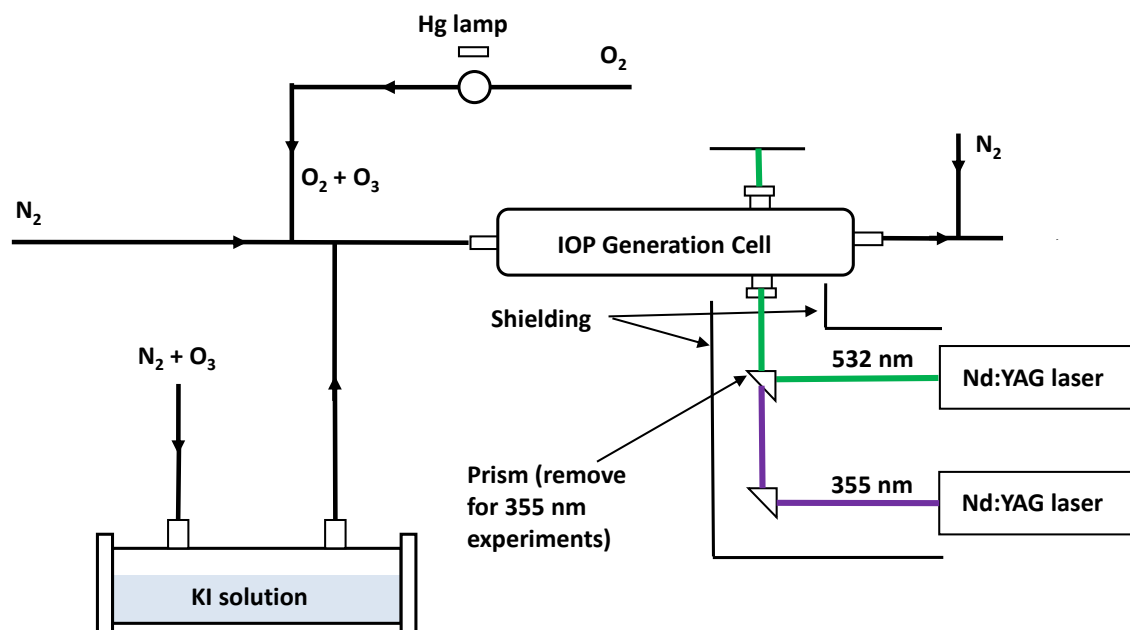
Figure 3.19 Experimental setup for the laser experiments showing the two lasers used. A second laser was used due to its higher power in the UV region for photolysis of HOI and to minimise the time for switching between lasers.

The laser consists of a neodymium doped crystal of yttrium aluminium garnet ($Nd:Y_3Al_5O_{12}$) with typically 1 % of the yttrium ions replaced by neodymium ions. The laser is pumped using xenon flash lamps producing a population inversion in the Neodymium ions. A Q switch inserted into the laser cavity requires maximum population inversion in the neodymium ions before it opens, allowing light into the cavity and depopulating the excited laser medium at maximum population inversion. By increasing the Q switch delay, the laser power could be decreased, should the observed particles extend beyond the size range observable by the nano-DMA (0.6-40 nm).

By frequency doubling and tripling, wavelengths of 532 and 355 nm, respectively, can be achieved. This is a non-linear process whereby photons interacting with a non-linear material "combine" to form new photons with twice or three times the energy of the fundamental photons at 1064 nm.

The mass of IOPs can be said to be a product of the concentration of HOI or I_2 in the gas flow, the cross section at the wavelength used, the fluence of the laser, the number of I atoms produced from photolysis (i.e. one for HOI and two for I_2), and a factor describing the efficiency of particle formation. Assuming that the efficiency of particle formation is the same whether HOI or I_2 is photolysed, this leads to an expression for the ratio of the masses as follows:

$$\frac{M_{I_2}}{M_{HOI}} = \frac{[I_2]}{[HOI]} \times \frac{\sigma_{I_2}}{\sigma_{HOI}} \times \frac{F_{532}}{F_{355}} \times \frac{2}{1}$$
(3.4)

The fluence (F) can be calculated from the laser energy, the wavelength of the laser beam and the diameter of the laser beam at the photolysis cell. The laser power was measured at the beginning and end of each experiment using a laser power meter along with the diameter of the laser spot in the photolysis cell. The number of photons (N) can then be calculated as:

$$N = \frac{E}{hc/\lambda}$$
(3.5)

where E is the measured energy of the laser in J, h is Planck's constant ($6.626 \times 10^{-34} m^2$ kg s^{-1}), c is the speed of light in nm s^{-1} (2.998×10^{17}) and λ is the wavelength of the laser beam in nm. The fluence (in photons/cm^2) is then the number of photons divided by the area of the laser beam (diameter = 0.125 cm).

As h, c and the laser beam diameter remain the same throughout, the fluence term can be calculated as E_{I2}*532/E_{HOI}*355. The ratio [I_2]/[HOI] is then:

$$\frac{[I_2]}{[HOI]} = \frac{M_{I_2}}{M_{HOI}} \bigg/ \left(\frac{\sigma_{I_2}}{\sigma_{HOI}} \times \frac{532 \cdot E_{I_2}}{355 \cdot E_{HOI}} \times 2 \right)$$
(3.6)

3.3.1 Effect of Iodide Concentration on I₂/HOI Ratio

Experiments were conducted using the laser technique described above for a range of iodide concentrations from 1×10^{-5} to 1×10^{-4} mol dm^{-3} and the I₂/HOI ratio calculated for each experiment. Two lasers were set up at the two different wavelengths so that experiments at each wavelength could be conducted sequentially with the minimum amount of time between experiments. All solutions were made up using sodium phosphate buffer at pH 8. As a result of the order of magnitude lower cross section for HOI, the fact that only one I atom is produced per molecule, and the lower laser power at 355 nm, higher O₃ concentrations were used so that the signal was above the detection limit for all iodide concentrations.
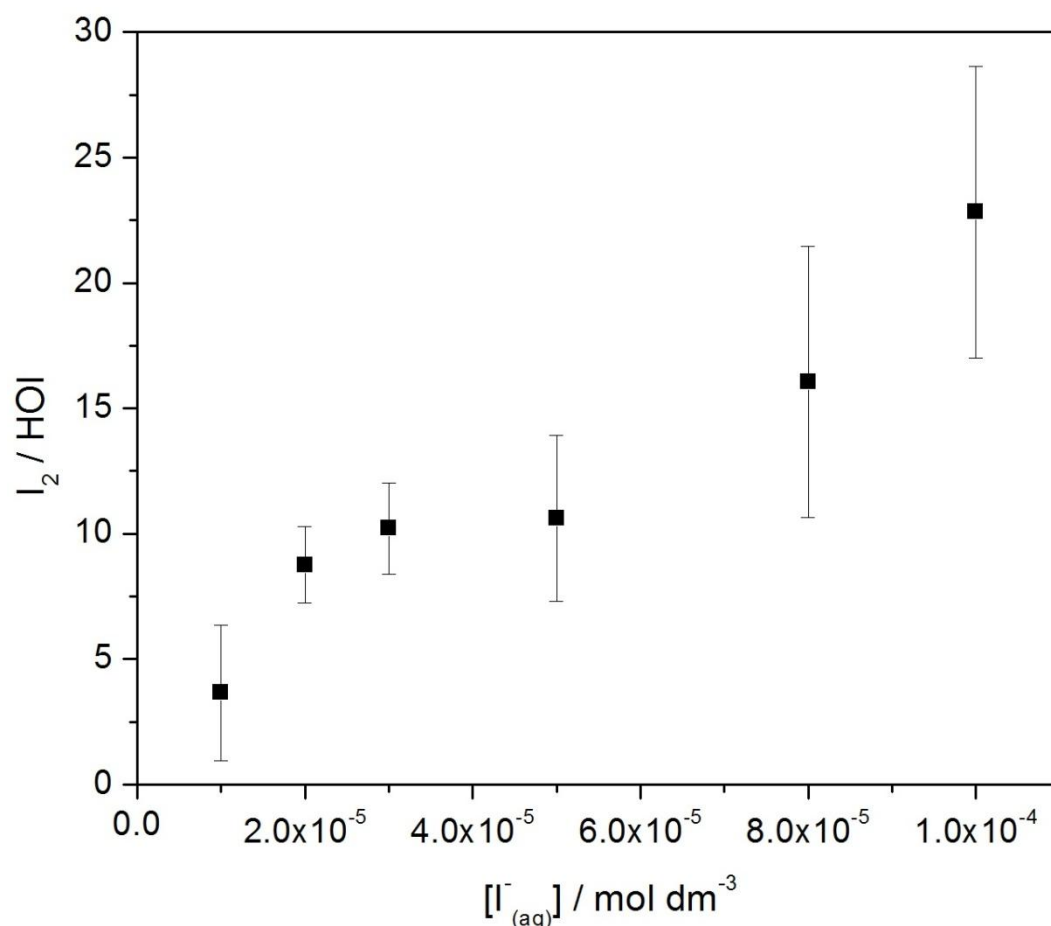
Figure 3.20 I₂/HOI ratio at different iodide concentrations using the laser technique for selective photolysis of HOI and I₂.

The ratio of I_2/HOI increased with increasing iodide concentration, which is to be expected given the mechanism of I_2 and HOI formation, i.e. higher I^- concentrations lead to more I_2 being produced through reaction (R3.5).

3.3.2 Temperature Dependence

The temperature dependence of the I_2/HOI ratio was then studied from 276 to 298 K and the results are shown below using the same laser technique (Figure 3.21). As can be seen the ratio appears to increase as the temperature is decreased but then at the lowest temperature begins to decrease again. A wide range of values was observed at the lowest temperature, however, and this was due to the large variability in the absolute concentrations of I_2 and HOI, suggesting that the measurements at low temperatures are less reliable. The ratio would be expected to show an increase with decreasing temperature due to the greater temperature dependence of the HOI mass transfer compared to I_2 (due to a greater contribution from the temperature dependent Henry's law constant). This is described in greater detail in Chapter 4 when discussing the kinetic model of the interfacial layer.
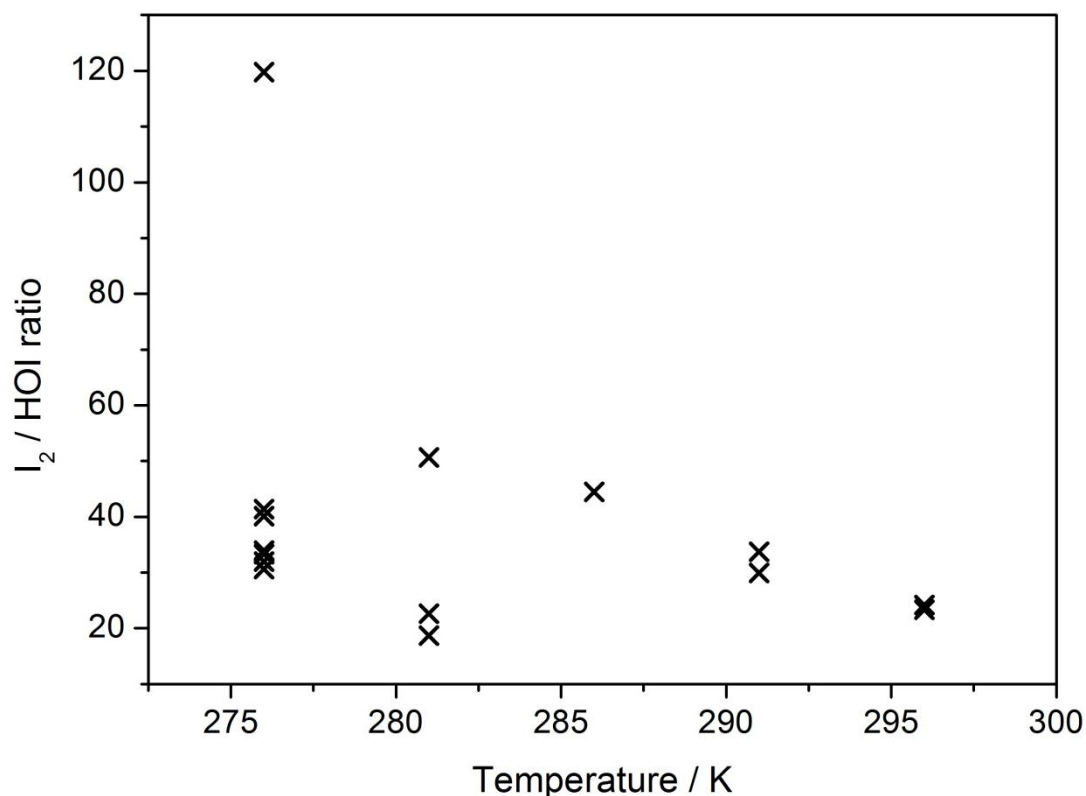
Figure 3.21 Temperature dependence of the I_2/HOI ratio measured using the laser set-up.

Experiments were then conducted on the temperature dependence of I_2 emission using the laser set-up to compare with the previous experiments performed using either the tungsten or xenon lamp to photolyse I_2.

An additional effect observed with the laser temperature dependence experiments was that of ozone. The activation energy for the emission of I_2 varied greatly between experiments and the only difference between the experiments was the amount of O_3. This had to be varied due to the differing efficiencies of the various light sources to ensure that a good signal of IOPs could be observed. The result was that at the highest ozone concentrations, the activation energy for the I_2 emission became negative, and as the ozone concentration decreases, the activation energy becomes more positive.

A summary of the activation energies obtained from all temperature dependence experiments using the three different light sources for I_2 photolysis (tungsten lamp, xenon lamp and YAG laser) are shown below. Figure 3.22 shows the activation energy

plotted against O_3 and this shows a clear decrease in the activation energy as the O_3 concentration is increased.

Table 3.3 Summary of all temperature dependence experiments showing varying ozone and light sources used and resulting activation energy.

Activation energy / kJ mol^{-1}	Light source	[Iodide] / mol dm^{-3}	O$_3$ / ppb	
-84	Tungsten	5.0×10^{-6}	2800	
-79	Tungsten	5.0×10^{-6}	2800	
40	Tungsten	5.0×10^{-6}	900	
-14	laser	5.0×10^{-6}	900	
-13	laser	5.0×10^{-6}	900	
115	Xenon	1.0×10^{-6}	222	with 0.55 M
93	Xenon	1.0×10^{-6}	222	with 0.55 M
101	Xenon	1.0×10^{-6}	222	
Unbuffered solution				
101	Tungsten	1.0×10^{-6}	222	
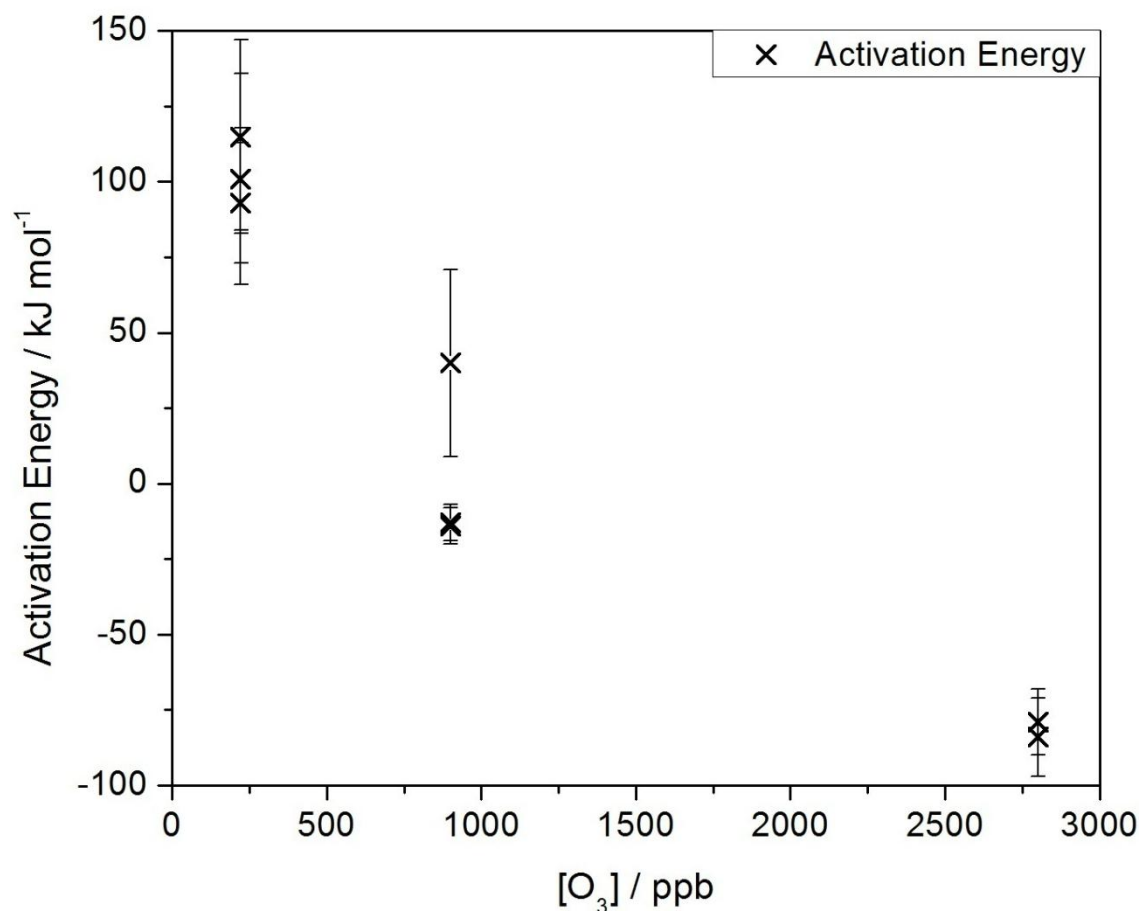
Figure 3.22 Activation energy vs. O_3 for all temperature dependence experiments using different light sources. At higher ozone concentrations a clear decrease in the activation energy is observed.

It was not clear whether this dependence was due to some part of the I⁻ + O_3 mechanism or whether it might be an experimental artefact. One possible explanation could be that IO is being produced in the solution cell at such high ozone concentrations as observed by Sakamoto et al. (2009). This would give the potential for IOP formation in the solution cell which could influence the number and size of the IOPs observed downstream at the Tapcon. The efficiency of IOP formation is also temperature dependent with a negative activation energy so that this process would be more efficient at the lower temperatures which would explain the apparent negative activation energy observed in the experiments at very high O_3.

Humidity is another factor which could influence the temperature dependence observed in these experiments. At high humidities (90 % relative humidity, RH), Saunders et al. (2010) found that the efficiency of IOP production was reduced by

around an order of magnitude compared with that at lower humidities (10 % RH). At higher temperatures the humidity would increase due to the higher vapour pressure of the solution. In the temperature experiments performed above, the humidity in the solution cell would reduce by around 75 % when moving from 298 K down to 276 K. However, this effect should be minimal as the air flow from the solution cell is diluted more than ten times as it enters the photolysis cell, meaning the change in humidity would be around 7.5 %, which would correspond to a change in IOP mass of < 10 %, well within experimental error.

Another problem with the temperature dependence experiments is the very large activation energy observed at low ozone concentrations (222 ppb), despite the agreement with previous observations. Because the pre-exponential factor is around ten orders of magnitude larger than the diffusion limit as mentioned previously, the observed activation energy cannot be applicable to the I$^-$ + O$_3$ reaction. This suggests that the temperature dependence in these experiments arises from some other source.

In the IOP experiments at low ozone where the temperature dependence was measured using either the xenon (for buffered solutions) or tungsten (for non-buffered solutions) lamps there may be an issue with I$_2$ sticking onto the walls of the solution cell. At the colder temperatures this effect would most likely be greater with more I$_2$ sticking to the walls of the cell. At low ozone, there will be a lower I$_2$ flux from solution and therefore any influence of this effect would likely be exaggerated. At higher ozone concentrations the flux of I$_2$ will be much greater and it is likely that the available sites on the solution cell would be filled more quickly. In the low temperature experiments this would lead to the large temperature dependence observed, with the effect being less noticeable as the ozone concentration, and therefore I$_2$ flux, is increased.

An additional complication is the effect of pH, which will vary with temperature. At higher temperatures the pH and therefore the hydrogen ion concentration will be higher (although this effect should be quite small in the buffered solutions). As a result, the hydrogen ion concentration was calculated for each temperature based on the pK_a value of the sodium phosphate buffer solution (6.82) and the observed change with

temperature from the literature (dpK_a/dT = -0.0028 °C⁻¹), according to the following equations:

$$pK_{a,T} = pK_a + \frac{dpK_a}{dT}(T - 298.15)$$
(3.7)

$$pH = pK_a + \log\left([A^-]/[HA]\right)$$
(3.8)

where [A⁻] and [HA] are the concentrations of the dibasic and monobasic forms of sodium phosphate, respectively, in the buffer solution.

To try to relate all the different experiments, the data points were normalised by dividing the observed I₂ flux (after applying the efficiency from calibration with each light source) by the concentration of ozone, iodide and hydrogen ions to get a value for the rate constant for the reaction of I⁻ + O₃. The rate constants were then split into 5 °C bins and an average and standard deviation calculated for each bin. The same process was also applied to the HOI temperature dependence measurements. Arrhenius plots were then created of the calculated rate constants against temperature, as shown in Figure 3.23.
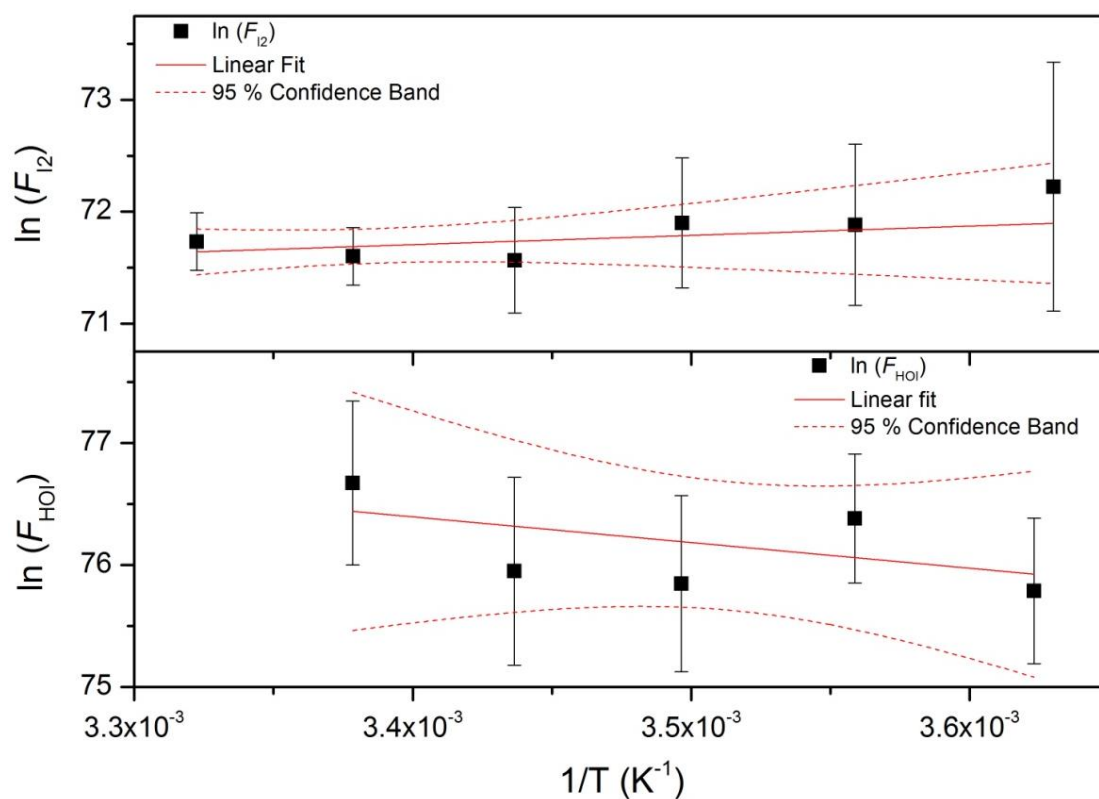
Figure 3.23 Temperature dependence for the flux of I_2 and HOI after normalising for I^-, O_3 and H^+. The solid red line shows a weighted linear fit to the data and the red dashed lines show the 95 % confidence bands.

This shows clearly the greater uncertainty in the results at low temperature compared to those at room temperature. Also plotted are the 95 % confidence intervals for the fit. This means that the activation energy from these experiments for I_2 is -7±18 kJ mol^{-1} and for HOI is 17±50 kJ mol^{-1}. Therefore the conclusion reached is that there is not a large temperature effect for the I_2 and HOI fluxes from the I^- + O_3 reaction. Further discussion of the temperature dependence of this reaction is provided in the context of the kinetic model in Chapter 4 where various sensitivity studies have been conducted. The main conclusions of this chapter and those of Chapters 4, 5 and 6 are provided in Chapter 7.

Chapter 4

Modelling the I⁻ + O₃ Reaction in the Interfacial Layer

This chapter describes the kinetic model of the solution surface used to verify the experimental results of Chapter 3. Ozone, iodide, salinity and temperature are varied in the model and compared with the experimental results for the same parameters and the outcomes are discussed.

4.1 The Sea-Surface Model

To simulate the observations of the experiments described in Chapter 3, a kinetic model, developed by Prof. Lucy Carpenter, University of York, was used. The model consists of a number of chemical reactions involving iodine species in the interfacial layer, including iodine disproportionation, oxidation and reduction. The complete reaction scheme is given in Table 4.1. It uses the commercial software FACSIMILE for integrating the chemical rate equations.

The model assumes that the reaction of I⁻ + O_3 occurs in the interfacial layer, rather than at the surface, and is initiated by accommodation of O_3 and rapid reaction with I⁻ in the surface layer. There is strong experimental evidence that this is the case (Garland et al., 1980; Magi et al., 1997; Rouviere et al., 2010), rather than following the Langmuir-Hinshelwood kinetics indicative of a surface reaction which occurs in many heterogeneous reactions of O_3 with liquid phase substrates (Clifford and Donaldson, 2007). The velocity of ozone deposition in this case is governed by the aqueous phase resistance of the surface layer, along with a smaller contribution from the aerodynamic resistance of the layer of air above the surface.

$$v_D = \frac{1}{\Gamma_a} + \frac{1}{\Gamma_s} \tag{4.1}$$

$$\Gamma_s = \frac{H}{\sqrt{\lambda D}} \tag{4.2}$$

where Γ_a and Γ_s are, respectively, the air and water side resistance, H is the dimensionless gas over liquid form of the Henry's law constant for O_3, D is its molecular diffusivity in water and λ is the integrated chemical reactivity of O_3 in seawater.

The gas phase flux of O_3 into the interfacial layer can be defined as:

$$F_{(O_3)} = v_D [O_{3(g)}] \tag{4.3}$$

so that the change in O_3 concentration in the interfacial layer is:

$$\frac{d[O_{3(\text{int})}]}{dt} = \frac{A}{V} v_D [O_{3(g)}] \tag{4.4}$$

where A is the surface area of solution, V is the volume of the interfacial layer, and A/V is equal to the inverse of the depth of the interfacial layer defined as the reacto-diffusive length, δ.

The model assumes there is no horizontal advection but vertical mixing with the bulk mixed layer occurs at a fixed interfacial layer turnover time. The concentration of [I⁻], [H⁺] and [OH⁻] are fixed for each model run and all iodine species (except IO_3^- and HIO_2, which do not influence gaseous iodine emissions) reach steady state after a few model seconds.

The mass fluxes of I_2 and HOI out of the surface layer are calculated according to the two-resistance model for air water partitioning. In this model, the main body of the two phases is assumed to be well mixed so that turbulent transfer occurs, and the main resistance to transfer occurs at the gas and liquid phase interfacial layers, where

transfer occurs through molecular processes. Using this approach, the flux of a particular species is then given by (Liss and Slater, 1974):

$$F = K_t \left(c_w - c_g \right)$$
(4.5)

$$\frac{1}{K_t} = \frac{1}{K_w} + \frac{1}{HK_a}$$
(4.6)

where c_w and c_g are the respective gas phase and aqueous phase concentrations and K_t, K_w and K_a are, respectively, the total, water-side and air-side mass transfer coefficients. H is the dimensionless gas over liquid form of the Henry's law constant with a defined temperature dependence (von Glasow et al., 2002). The inverse of K_w and K_a are the corresponding water and air-side resistances, respectively.

For soluble molecules such as HOI the air-side resistance term will dominate so that $K_t = HK_a$ whereas in the case of I₂, which is only sparingly soluble, the water-side resistance term dominates, although the air-side resistance can reduce the total mass transfer by several percent.

To calculate the air-side mass transfer coefficient, K_a, for laboratory conditions, an empirical approach is used, based on the dimensionless Sherwood number, S_h, and relevant for indoor or laminar flow environments (Guo and Roache, 2003).

$$K_a = \frac{(S_h D_a)}{L}$$
(4.7)

where D_a is the diffusivity in air and L is the characteristic length calculated from the square root of the source area (the surface area of solution in contact with the air). In this case K_a has units of m h⁻¹. Guo and Roache (2003) found an uncertainty of up to 17 % between experimentally determined and modelled gas-phase transfer coefficients using this approach.

The Sherwood number is a function of the temperature-dependent Schmidt number of the relevant gas in air, Sc_a, and the Reynolds number, R_e (Guo and Roache, 2003).

$$S_h = 0.664 Sc_a^{\frac{1}{3}} R_e^{\frac{1}{2}} \tag{4.8}$$

$$Sc_a = \frac{\mu}{\rho D_a} \tag{4.9}$$

$$R_e = \frac{(Lu\rho)}{\mu} \tag{4.10}$$

where μ is the viscosity of air (g m^{-1} h^{-1}), ρ is the density of air (g m^{-3}) and u is the air velocity (m h^{-1}).

The water-side mass transfer coefficient, K_w, is again calculated using the empirical approach of Guo and Roache (2003):

$$K_w = 2.99 D_w \tag{4.11}$$

where D_w is the diffusion coefficient of the gas in question in water (m^2 h). Here K_w has units of m h^{-1}. The average uncertainty on the calculated liquid-phase transfer coefficients using this approach compared to experimental values was found to be approximately 22 %, and the uncertainty was found to increase as the Henry's law constant decreased (Guo and Roache, 2003).

The standard Henry's law constants used in the model were 3.0 M atm^{-1} for I₂ and 4.5 x 10^2 M atm^{-1} for HOI, with temperature dependences as described in von Glasow et al. (2002). Whilst the Henry's law constant for I₂ has been well established to be around 3 M atm^{-1} (estimates range from 1.1–3.3 M atm^{-1}), that for HOI is much more uncertain with values in the range 4.5 x 10^1–4.5 x 10^4 M atm^{-1} (Sander, 1999). This leads to calculated total mass transfer coefficients for HOI ranging over three orders of magnitude, a large source of uncertainty in the model.

For simulating real seawater conditions the mass transfer coefficients for I₂ and HOI were computed according to the parameterization by Johnson (2010). In this case the air-side mass transfer coefficient is calculated as a function of wind speed u (at 10 m

above the water surface), friction velocity, u_*, the Schmidt number of the gas, and the drag coefficient, C_D:

$$K_a = 1 \times 10^{-3} + \frac{u_*}{13.3 Sc_a^{\frac{1}{2}} + C_D^{-\frac{1}{2}} - 5 + \frac{\ln(Sc_a)}{2\kappa}}$$

(4.12)

where κ is the von Karman constant (taken to be 0.4 in seawater) and u_* and C_D are calculated according to the equations presented in Johnson (2010) for a 10 m wind speed of 7 m s⁻¹:

$$C_D = \left(\frac{u_*}{u}\right)^2$$

(4.13)

$$u_* = u\sqrt{6.1 \times 10^{-4} + 6.3 \times 10^{-5} u}$$

(4.14)

To calculate the water-side transfer coefficient for real seawater conditions the parameterization from Nightingale et al. (2000) was employed:

$$K_w = 0.222(u)^2 + 0.333u$$

(4.15)

The total mass transfer coefficients were then calculated assuming a seawater temperature of 15 °C, an air temperature of 20 °C and a 10 m wind speed of 7 m s⁻¹. All the above model parameters were calculated either off line or directly in the model without being tuned to the experimental results.

The additional reactions used when describing real seawater are included at the bottom of Table 4.1. These include the reactions of O_3, I_2 and HOI with DOM in the sea surface layer and the interhalogen reactions in the presence of Cl⁻ (taken as 0.55 M) and Br⁻ (8.6 x 10⁻⁴ M). The pseudo-first order interfacial loss rate of O_3 to DOM is taken to be 100 s⁻¹, the value suggested by Ganzeveld (2009) for open ocean waters. For I_2/HOI + DOM the value estimated by Truesdale et al. (1995b) is used (5 x 10⁻⁵ s⁻¹). The reaction of HOI with DOM is likely to be faster than that of I_2, however, using a rate

constant 100 times faster than that reported in the table results in only minor reductions in the I_2 and HOI fluxes (0.17 and 0.16 % respectively). Iodate was fixed in the model at 2 x 10^{-7} M, although this had no impact on the resulting inorganic iodine emissions. For each model run the concentrations of I^-, H^+ and OH^- were fixed, and all iodine species reached steady state within a few model seconds.

The model is clearly a simplified approach which does not take into account the potential concentration gradients occurring in the interfacial layer. There will of course be a gradient in the O_3 concentrations: the O_3 will be, by definition, zero at the bottom of the reacto-diffusive layer (the length over which O_3 is removed by reaction with I^- as it diffuses into the bulk solution). There have also been several studies showing that I^- concentrations will be greater at the solution surface (discussed further in section 4.2.3). However, these gradients are effectively accounted for by integrating over the reacto-diffusive length, and average I^- concentrations experienced by O_3 diffusing over this depth will be very close to the bulk I^- concentration.

The rate constants used when comparing the model output with the experimental results have been obtained from numerous experimental and modelling studies on the hydrolysis of molecular iodine in solution. No temperature dependence data was available for these reactions; however, sensitivity studies (discussed in section 4.2.4) showed that the modelled fluxes were not particularly sensitive to temperature dependences in the component reactions.

Although there may be uncertainty over the individual rate constants, the overall model successfully reproduces experimental results of iodine disproportionation over a range of pHs (Carpenter et al., 2013, Supplementary Material). Further experiments on the I^- + O_3 reaction were performed at the University of York using an entirely independent method for HOI and I_2 detection (Carpenter et al., 2013). In those experiments the gas flow was trapped in *n*-hexane with subsequent spectrophotometric detection at 522 nm for I_2 or in phenol red with subsequent detection of iodophenol blue at 591 nm for HOI. The model results compared well with the experimentally determined I_2 and HOI fluxes over a range of iodide concentrations, which provides greater confidence in the proposed mechanism.

Table 4.1 Summary of kinetic data used in the interfacial model.

	Reaction	Rate constant - forward reaction	Rate constant - reverse reaction	Reference
	Reactions included for iodide solutions and seawater:			
R4.1	$O_{3(g)} \rightarrow O_{3(interface)}$	$v_{d,O_3} \times (A/V) \ s^{-1}$		See text
R4.2	$O_{3(interface)} + I^- (+H^+) \rightarrow HOI (+O_2)$	$2.0 \times 10^9 \ M^{-1} s^{-1}$ (pH 8)		(Garland et al., 1980; Magi et al., 1997)
R4.3	$I_2 (+H_2O) \leftrightarrow I_2OH^- + H^+$	$3.2 \ s^{-1}$	$2.0 \times 10^{10} \ M^{-1} s^{-1}$	(Lengyel et al., 1993)
R4.4	$I_2OH^- \rightarrow HOI + I^-$	1.34×10^6 s-1	$4.0 \times 10^8 \ M^{-1} s^{-1}$	(Lengyel et al., 1993)
R4.5	$I_2 + I^- \leftrightarrow I_3^-$	$6.2 \times 10^9 \ M^{-1} s^{-1}$	$8.9 \times 10^6 \ s^{-1}$	Forward: (Lengyel et al., 1993) Reverse: (Palmer et al., 1984)
R4.6	$HOI + HOI \leftrightarrow H^+ + I^- + HIO_2$	$2.5 \times 10^1 \ M^{-1} s^{-1}$	$2.0 \times 10^{10} \ M^{-2} s^{-1}$	Forward: (Schmitz, 2004) Reverse: (Edblom et al., 1987)
R4.7	$I_2 + OH^- \leftrightarrow HOI + I^-$	$7.0 \times 10^4 \ M^{-1} s^{-1}$	$2.1 \times 10^3 \ M^{-1} s^{-1}$	(Sebok-Nagy and Kortvelyesi, 2004)
R4.8	$HOI \leftrightarrow IO^- + H^+$	$1.0 \times 10^{-1} \ s^{-1}$	$1.0 \times 10^{10} \ M^{-1} s^{-1}$	(Wren et al., 1986)
R4.9	$HOI + IO^- \leftrightarrow HIO_2 + I^-$	$1.5 \times 10^1 \ M^{-1} s^{-1}$	Negligible	(Bichsel and von Gunten, 2000)

R4.10	$HIO_2 + HOI \leftrightarrow IO_3^- + I^- + 2H^+$	2.4×10^2 M^{-1} s^{-1}	1.2×10^3 M^{-3} s^{-1}	Forward: (Furrow, 1987) Reverse: (Schmitz, 2000)
R4.11	$H_2OI^+ \leftrightarrow HOI + H^+$	9.0×10^8 s^{-1}	2.0×10^{10} M^{-1} s^{-1}	(Lengyel et al., 1993)
R4.12	$I_2 (+H_2O) \leftrightarrow H_2OI^+ + I^-$	1.2×10^{-1} s^{-1}	1.0×10^{10} M^{-1} s^{-1}	(Lengyel et al., 1993)
R4.13	$HOI + 2O_{3(interface)} \rightarrow IO_3^- + H^+ (+2O_2)$	3.6×10^4 M^{-1} s^{-1}		(Bichsel and von Gunten, 2000)
R4.14	$IO^- + 2O_{3(interface)} \leftrightarrow IO_3^- + 2O_2$	1.6×10^6 M^{-1} s^{-1}		(Bichsel and von Gunten, 2000)
R4.15	$I_2 \rightarrow bulk$	k_{mix}		
R4.16	$HOI \rightarrow bulk$	k_{mix}		
Reactions included only for seawater and chloride dependence experiments				
R4.17	$O_{3(interface)} (+DOM) \rightarrow products$	500 s^{-1} (coastal) 100 s^{-1} (open ocean)		(Ganzeveld, 2009)
R4.18	$I_2 (+DOM) \rightarrow products$	7.0×10^{-3} s^{-1} (coastal) 5.0×10^{-5} s^{-1} (open ocean)		(Truesdale et al., 1995a; Truesdale et al., 1995b)
R4.19	$HOI (+DOM) \rightarrow products$	7.0×10^{-3} s^{-1} (coastal) 5.0×10^{-5} s^{-1} (open ocean)		Assumed analogously to R4.18
R4.20	$HOI + Br^- + H^+ \leftrightarrow IBr (+H_2O)$	4.1×10^{12} M^{-2} s^{-1}		(Faria et al., 1993)

R4.21	$HOI + Cl^- + H^+ \leftrightarrow ICl(+H_2O)$	2.9×10^{10} M^{-2} s^{-1}		(Wang et al., 1989)
R4.22	$I_2 + Br^- \leftrightarrow I^- + IBr$	4.74×10^3 M^{-1} s^{-1}		(Faria et al., 1993)
R4.23	$I_2 + Cl^- \leftrightarrow I_2Cl$	8.33×10^4 M^{-1} s^{-1}		(Margerum et al., 1986)
R4.24	$ICl_2^- \leftrightarrow ICl + Cl^-$	6.0×10^5 s^{-1}		(Margerum et al., 1986)
R4.25	$I^- + ICl \leftrightarrow I_2Cl^-$	1.1×10^9 M^{-1} s^{-1}		(Margerum et al., 1986)

The results of Sakamoto et al. (2009) show that IO is also released as a result of the reaction of I⁻ + O₃, however, due to the very small contribution of this species to the iodine flux of around 1 % compared to I_2 and the lack of any kinetic data, this process was ignored in the model. In addition, photo-oxidation of I⁻ by oxidants such as O_2, IO_3^- and NO_3^- in seawater were also not included due to their negligible rates as reported by Truesdale (2007).

4.2 Comparison of Kinetic Model with Experimental Results

The kinetic model was used to verify that our experimental results make sense in terms of the current understanding of solution phase iodine chemistry and the physical processes governing gas-transfer in the interfacial layer. In order to do this, the parameters which were altered in the original experiments were also varied in the model to test the sensitivity of both the I$_2$ and HOI fluxes to each of these parameters.

4.2.1 Varying Ozone Concentration

The first parameter in the model to be tested against the experimental results was that of ozone. As shown in Figure 4.1, increasing the ozone concentration in the gas phase in the kinetic model leads to a linear response in the resulting I$_2$ and HOI fluxes. This is in good agreement with the experimental results where the response was linear over a wide range of different gaseous ozone concentrations. This response is to be expected given the mechanism of the reaction and emission processes as the stoichiometry of the equation is one-to-one and, due to its low Henry's law constant, the ozone in the interfacial layer will always be the limiting species (assuming concentrations of 1×10^{-7} M iodide or greater) in the I$^-$ + O$_3$ reaction, and ozone does not participate in any of the other solution phase reactions.
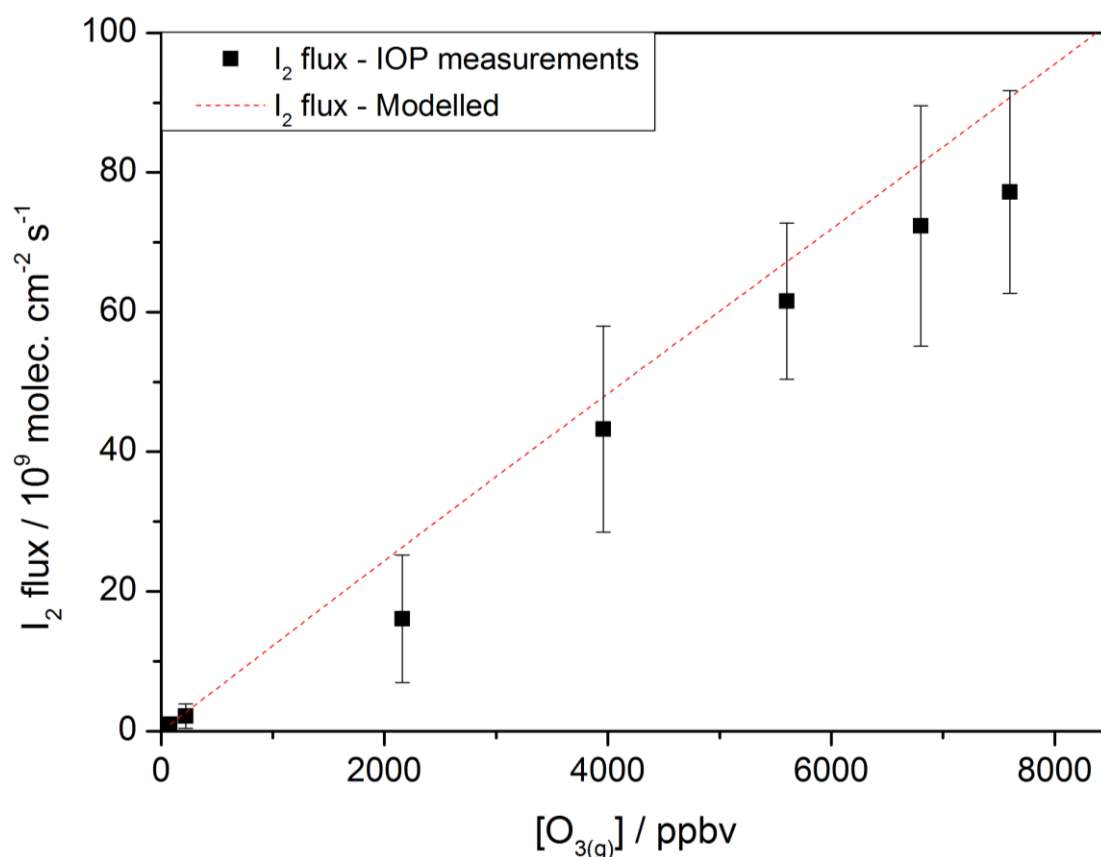
Figure 4.1 Measured (black squares) and modelled (red dashed line) I_2 flux for a range of O_3 concentrations.

4.2.2 Varying Iodide Concentration

The next parameter to test against experimental results was that of the iodide concentration in solution. This was varied from 1×10^{-7} up to 1×10^{-3} M for both model and experiments. The model shows a linear trend in the iodide concentration, whereas there is a levelling out in the experimental results at the higher iodide concentrations (Figure 4.2). This suggests that there is perhaps a surface saturation effect occurring at high iodide concentrations in solution which is not captured by the model. The reason for this increase in the I_2 and HOI fluxes with increasing iodide concentration is due to the decreased surface resistance, meaning a greater concentration of O_3 will be present in the interfacial layer. At these iodide concentrations any O_3 present in the interfacial layer will be immediately scavenged.
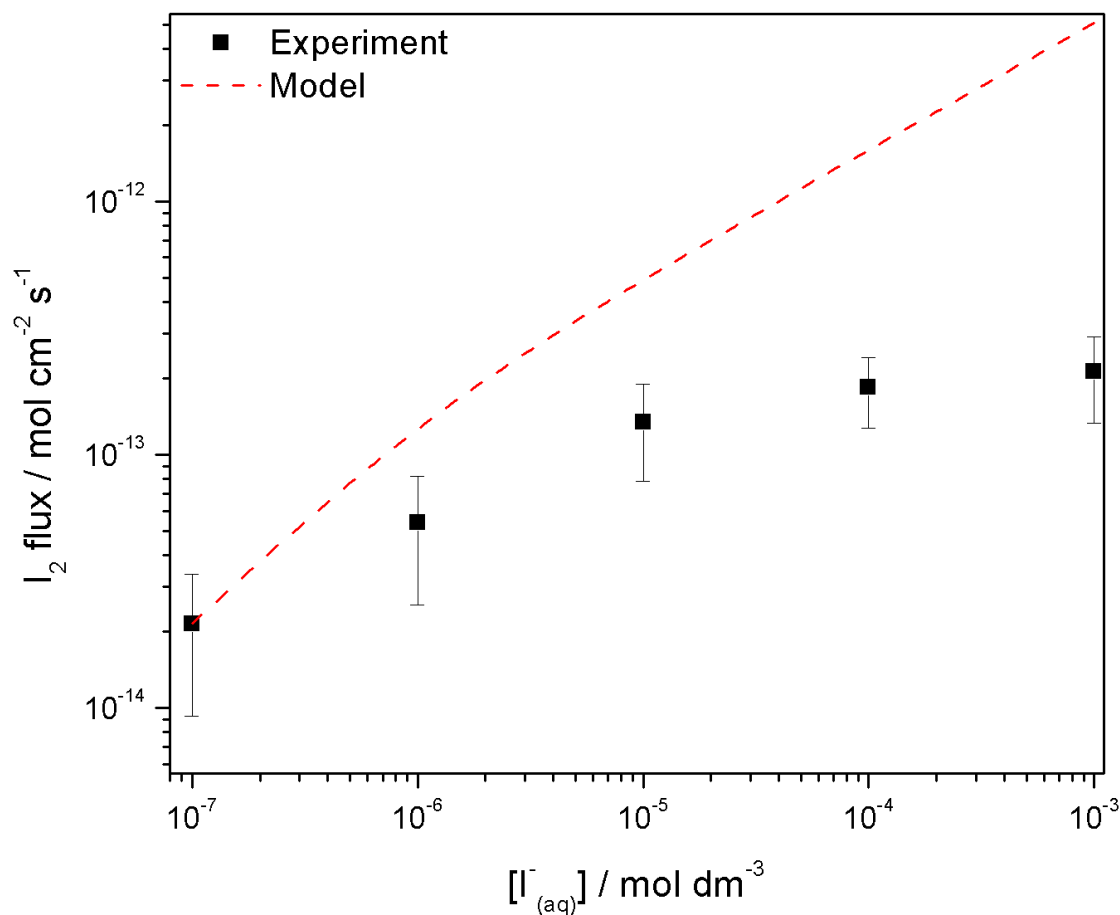
Figure 4.2 Experimental (black squares) and modelled (red dashed line) iodide dependence of the I_2 flux from solution showing the deviation between the two at higher iodide concentrations.

In addition to the increase in the I_2 and HOI fluxes with increasing iodide concentrations, the model also shows clearly the change in the relative contributions of the two species to the overall flux. Figure 4.3 shows the I_2/HOI ratio against iodide concentration, along with the experimentally determined values from the laser experiments reported in Chapter 3; a good agreement between model and experiment is achieved (assuming a room temperature of 22 °C; see section 4.2.4 for further discussion of the temperature dependence).
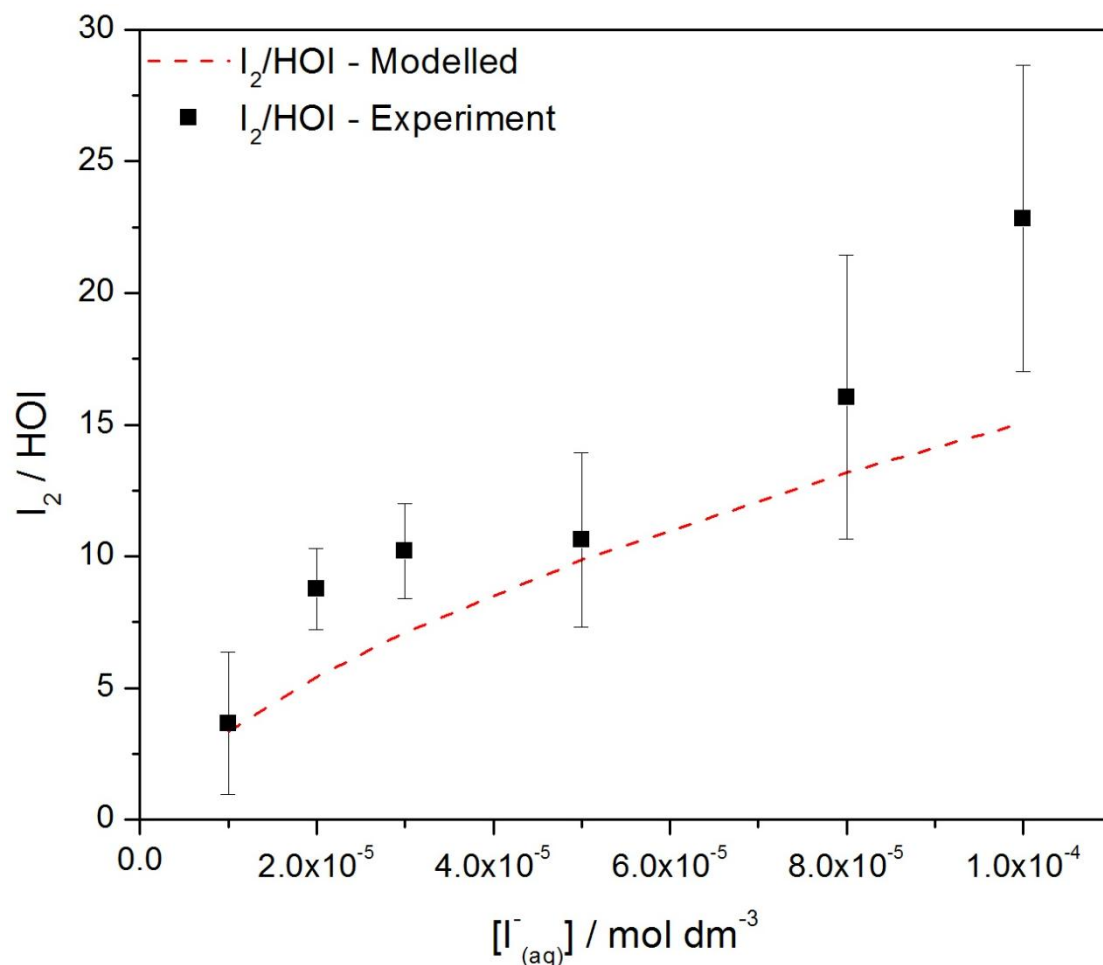
Figure 4.3 Measured (black squares) and modelled (red dashed line) I_2/HOI ratio over a range of iodide concentrations.

4.2.3 Varying Chloride Concentration

The chloride concentration in the model was varied from 0–0.55 M and compared with the experimental results. As expected, the I_2 flux increased with increasing chloride concentration due to the influence of R4.21 and reactions R4.23–25 (Table 4.1) where some HOI is converted to I_2 via ICl. As the concentration of HOI in the interfacial layer is orders of magnitude larger than that of I_2 the corresponding decrease in HOI is negligible so that the HOI flux shows no dependence on the chloride concentration (which was also observed in the laser experiments described in Chapter 3).
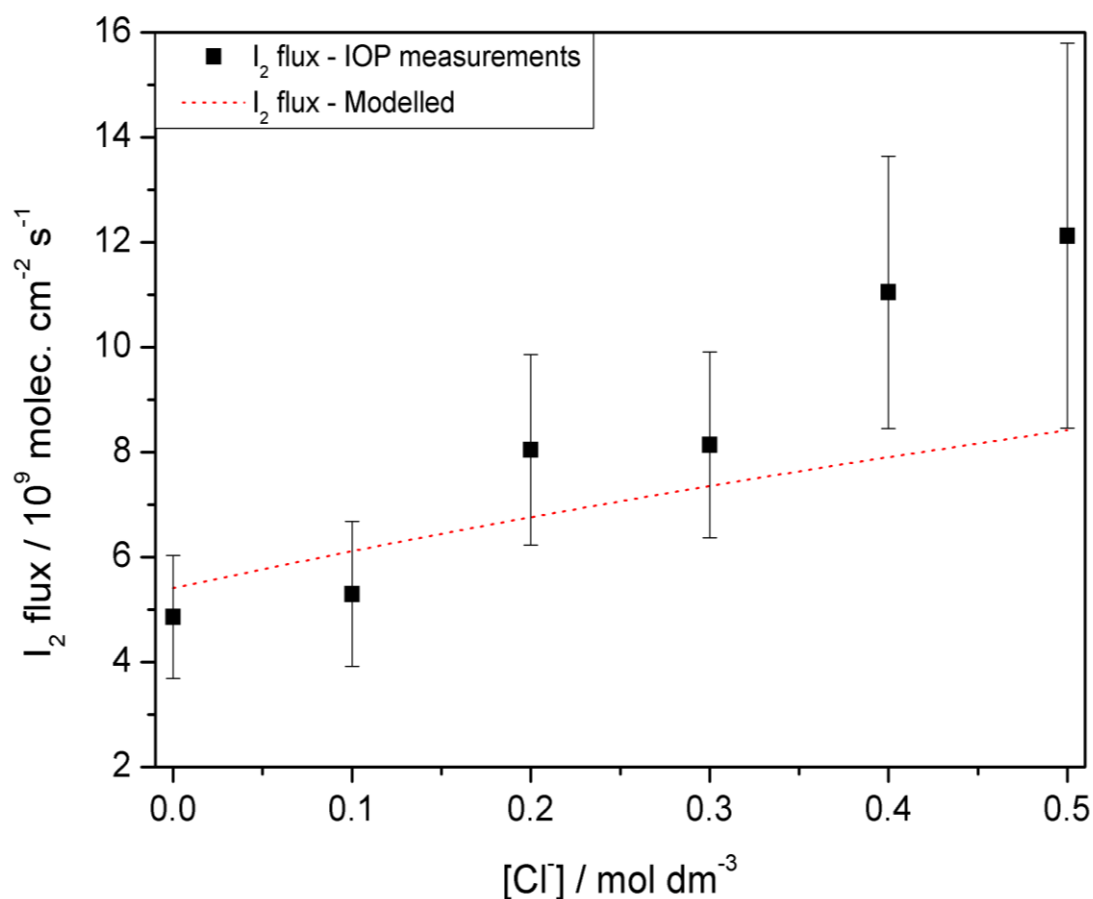
Figure 4.4 Measured (black squares) and modelled (red dashed line) I_2 flux for 1 x 10^{-7} M iodide with varying chloride concentrations.

The observed increase in the I_2 flux from experiments is somewhat greater than the model predicts: a 2.5 fold increase compared to 1.5 in the model results. This could indicate an additional effect of iodide enhancement at the surface of the solution under high chloride conditions.

In fact, there have been a number of studies which have shown that halides are enhanced at the surface of solutions in comparison to the bulk phase. These studies have consisted of both theoretical molecular dynamics simulations and experiments using electron spectroscopy to detect the relevant halide ions (Caleman et al., 2011; Ghosal et al., 2005; Gladich et al., 2011). The physical basis for this effect is due to the relative polarisability of the anions. The larger anions I⁻ and Br⁻ have been found to both show a propensity for the water-air interface of an aqueous solution, whilst Cl⁻, although it is somewhat polarisable, preferentially remains in the bulk solution. The polarisability of the anions increases in the order Cl⁻<Br⁻<I⁻ (3.25, 4.53, 6.90 A) and this

is directly linked to the induced dipole of the specie in question. Molecular dynamics simulations showed that a dipole moment at the interface will position itself so that the positive pole points outward from the interface thereby reducing the electrical potential energy. This reduction is proportional to the dipole moment and therefore the polarisability so that the higher the polarisability the higher the energetic gain from the halide ions remaining at the interface (Gladich et al., 2011). This could mean that the less polarisable chloride ions help to increase this effect and "push" the iodide ions out towards the surface, leading to an enhanced reaction rate at high chloride concentrations.

A further possibility is that the observed increase could be due to contributions from iodide impurities in the NaCl used. Quantitative mass spectrometry was employed to analyse the magnitude of the iodide impurity in the NaCl (performed by Dr Stuart Warriner, University of Leeds). The relative intensity of the iodide mass peak observed in a 0.104 M NaCl solution was found to be less than a sample spiked with 9.9×10^{-9} M KI, therefore, a 0.5 M NaCl solution would contain an iodide impurity of $< 5 \times 10^{-8}$ M. This is a factor of 20 smaller than the 1×10^{-6} M KI solutions employed in the salinity dependence experiments, and therefore rules out this explanation.

4.2.4 Temperature Dependence

The kinetic model contains a number of parameters each with differing temperature dependences which will affect the overall temperature dependence for the fluxes of both HOI and I_2. The various temperature dependent terms in the model are described below along with the physical basis for that dependence.

The transfer coefficients for I_2 and HOI both show a positive temperature dependence arising from the Henry's law term in their calculation (Equation 4.6). As the Henry's law constant characterises the solubility of the species in question, in its gas-over-liquid form it will show a positive temperature dependence, the higher the temperature the greater the solubility.

The diffusion coefficient and Henry's law constant for O_3 both show positive temperature dependences which result in a negative temperature dependence for both the surface resistance and the reacto-diffusive length. This means that at higher temperatures less O_3 will enter the interfacial layer and be available for reaction with I⁻.

In the initial model runs when comparing with the room temperature experimental data, the pH was assumed to be constant (at pH 8) and therefore so was the hydrogen ion concentration. The concentration of hydrogen ions in solution will obviously affect the rate of production of both HOI and I_2 through reaction 2 and the reverse of reactions R4.3, R4.6, R4.8, R4.10 and R4.11 in Table 4.1 (as has been shown by comparing the reduced flux from buffered solutions at pH 8 compared to un-buffered solutions where the *p*H was measured as 5.8) and this concentration will change with a change in temperature. As a result the change in the hydrogen ion concentration with temperature was calculated as described in Chapter 3 and input as a parameter in the kinetic model.

The only aqueous phase reaction in the model for which there was available temperature dependence information was that of the O_3 + I⁻ reaction itself from Magi et al. (1997) and this was used in all the modelling studies when comparing the experiments at room temperature. For all other reactions, no temperature dependence information was available and therefore sensitivity studies were conducted to test whether, should any of these reactions have a significant temperature dependence, this would have a significant effect on the resulting I_2 and HOI fluxes. Those reactions in Table 4.1 which had rate constants $< 10^9$ M^{-1} s^{-1} and therefore most likely to be activation controlled, were tested individually. The reactions used were the forward reactions of R4.3 and R4.6–12, and the reverse reactions of R4.6, R4.7 and R4.10. Using the currently accepted rate constant values as listed in Table 4.1, maximum activation energies were estimated such that the pre-exponential factor for the reaction was not larger than the diffusion limit ($\sim 10^{12}$ M^{-1} s^{-1}). The addition of these activation energies to the majority of the reactions in the chemistry scheme showed no significant effect on the resulting HOI and I_2 fluxes. The only reaction where a significant change in the overall activation energy was observed was the forward reaction 6 where using an activation energy for the reaction of

60 kJ mol^{-1} resulted in an activation energy ~20 kJ mol^{-1} smaller for the resulting I_2 flux compared to when the activation energy of this reaction was set to zero.

The above mentioned model runs used the activation energy from Magi et al. (1997) of ~73 kJ mol^{-1} which gives a rate constant at room temperature which lies within the established range of values from previous experiments of 1–2.5 x 10^9 M^{-1} s^{-1} (Garland et al., 1980; Hu et al., 1995; Liu et al., 2001; Magi et al., 1997). As discussed previously, the published pre-exponential factor is around ten orders of magnitude larger than the diffusion limited rate therefore this activation energy cannot be applicable to this reaction at the rate constants observed. They also show large errors on the results at lower temperatures, in agreement with the lack of reproducibility observed in the experiments described in Chapter 3. Results of the fitting in Chapter 3 suggest this reaction may have a small or negative activation energy, however, it is important to remember that the experimental results give the temperature dependence of the I_2 and HOI fluxes which are both dependent on a number of other temperature dependent processes as mentioned in the section above.

Measurements by Hu et al. (1995) gave a rate coefficient for the I$^-$ + O₃ reaction at 277 K of 4 x 10^9 M^{-1} s^{-1}. Given that previous measurements have established that the rate constant at 298 K lies within the range 1–2.5 x 10^9 M^{-1} s^{-1} this implies that the reaction may in fact have a slightly negative temperature dependence. It should be noted, however, that the measurements of Hu et al. (1995) showed a very large error, which actually encompassed the existing estimates for the room temperature rate constant (and they do not report a room temperature measurement). Therefore the model was run assuming zero activation energy for the O₃ + I$^-$ rate constant.

The iodide and ozone concentrations were then varied to examine how this rate constant affected the temperature dependences of the I_2 and HOI fluxes. The temperature dependence for I_2 and HOI fluxes was dependent on both the iodide and ozone concentrations and the resulting HOI and I_2 flux temperature dependences are reported in Table 4.2 for the range of ozone and iodide concentrations used in the temperature dependence experiments.

Table 4.2 Modelled activation energies for the HOI and I_2 fluxes with different O_3 and I^- concentrations.

[$I^-_{(aq)}$] / mol dm^{-3}	[$O_{3(g)}$] / ppb	E_a (I_2 flux) / kJ mol^{-1}	E_a (HOI flux) / kJ mol^{-1}
1×10^{-6}	222	-5.6	20.3
5×10^{-6}	900	-3.4	24.8
5×10^{-6}	2800	2.0	30.3

The table shows that when increasing the O_3 concentration in the model the activation energy of both the I_2 and HOI fluxes increases. In contrast, increasing the iodide concentration has the opposite effect, causing a decrease in the activation energy of both fluxes.

The model was also run for real seawater conditions, assuming zero activation energy for the I^- + O_3 reaction, an O_3 concentration of 30 ppb (representative of clean marine air), an iodide concentration of 1×10^{-7} M and a wind speed of 7 m s^{-1}. The activation energies obtained for the I_2 and HOI fluxes were -0.2 kJ mol^{-1} and 29 kJ mol^{-1}, respectively. Due to the very minimal apparent temperature dependence, this factor was not considered in the next section when producing a parameterisation of the inorganic iodine flux.

4.3 Parameterisation of the Inorganic Iodine Flux

To derive algorithms describing the relative inorganic iodine fluxes a multiple linear regression model was used. This involved investigating the relationships between each covariate and the response variable (HOI or I_2) as computed by the kinetic model for real seawater conditions. The variables considered were O_3, I^- and wind speed, temperature and salinity were not considered for the reasons discussed above and in Chapter 3. The analysis was carried out as described below by Dr Julie Wilson, University of York.

The ozone concentration was found to have a simple multiplicative effect on both the response variables (HOI and I_2 flux), i.e. increasing the ozone concentration by a factor *k* would cause an increase in the HOI and I_2 flux by the same factor. For this reason the models were initially developed for a constant O_3 and multiplied by the appropriate factor afterwards. The O_3 and wind speed were considered separately for fixed values of the other covariate in each case.

Both the HOI and I_2 fluxes were found to show a clear association with I⁻ and wind speed individually, however, none of these relationships were linear. Therefore, the covariates were transformed by the appropriate function to give a linear relationship with the response variable before fitting the linear regression model. These transformations and corresponding correlations are summarised in Table 4.3 below.

Table 4.3 Transformations for the relevant covariates before fitting in the linear regression model.

Response, y	Covariate, x	Transformation, f(x)
HOI	ws	$1/ws$
	I⁻	$\sqrt{I^-}$
I_2	ws	$ln(ws)$
	I⁻	$\left(I^-\right)^{1.3}$

The linear regression model takes the form:

$$y = \beta_0 + \beta_1 x_1 + \beta_2 x_2 + \beta_3 x_1 x_2 \tag{4.15}$$

where x_1 and x_2 are the transformed covariates and β_i (where $i = 0,..3$) are the coefficients to be determined. For both response variables the intercept was found to be insignificant and therefore β_0 was not included in the fitting procedure.

For I_2 the coefficient of the $[I^-]^{1.3}$ term was not significant, however, the coefficient for the interaction term, $ln(ws) \times [I^-]^{1.3}$ and the ws coefficient were highly significant

(p < 0.0001). The F-statistic for comparison of the two models with and without the $[I^-]^{1.3}$ coefficient showed that the reduced model was preferable. The resulting expression (Equation 4.16) produces a correlation of 0.9991 between calculated (kinetic model) and predicted I_2 emissions.

$$F_{I_2} = \left[O_{3(g)}\right] * \left[I^-_{(aq)}\right]^{1.3} * \left(1.74 \times 10^9 - \left(6.54 \times 10^8 * \ln ws\right)\right) \tag{4.16}$$

The flux is given in nmol m^{-2} day^{-1} with [$O_{3(g)}$] in ppb, [$I^-_{(aq)}$] in mol dm^{-3} and wind speed in m s^{-1}.

For HOI the coefficients of both covariates and of the interaction term were all highly significant. The expression produced (Equation 4.17) gives a correlation of 0.9986 between the calculated and predicted HOI emissions.

$$F_{HOI} = \left[O_{3(g)}\right] * \left(4.15 \times 10^5 * \left(\frac{\sqrt{\left[I^-_{(aq)}\right]}}{ws}\right) - \left(\frac{20.6}{ws}\right) - 23600 * \sqrt{\left[I^-_{(aq)}\right]}\right) \tag{4.17}$$

Both these expressions were employed for use in the 1-D model THAMO to link inorganic iodine emissions from seawater to measurements of IO and IO$_x$ over the oceans and results suggested that these equations may only be applicable when the wind speeds are higher than 2 m s^{-1}. This work is described in Chapters 5 and 6.

Chapter 5

Iodine in the Remote Tropical MBL

As part of the PhD project, field measurements have been performed using long-path (LP) and multi-axis (MAX) differential optical absorption spectroscopy (DOAS) on the Galapagos Islands in the Eastern Pacific ocean as part of the Climate and HAlogen Reactivity tropical EXperiment (CHARLEX) field campaign. The theoretical basis of the LP-DOAS and MAX-DOAS techniques is discussed below in section 5.1, along with a description of the instrument and the experimental set-up. The motivations for, and results of, the CHARLEX field campaign are then discussed in section 5.2.

5.1 Experimental Techniques

5.1.1 Differential Optical Absorption Spectroscopy

Differential optical absorption spectroscopy (DOAS) has been used for many years as a valuable technique for taking atmospheric measurements. It has many advantages for measuring trace gases in the atmosphere, one of which being that it can retrieve concentrations without affecting the chemical behaviour of the species being studied, which is particularly useful when studying highly reactive species such as free radicals (Stutz and Platt, 1997).

DOAS relies on using the narrow band absorption structure of the species being measured, which is characteristic of an individual molecule and can therefore be used as a fingerprint. The technique is capable of measuring multiple species with a single instrument, valuable in field campaigns in remote locations. DOAS can also detect unsuspected species in the atmosphere which may be revealed in the residual structure after spectral de-convolution (Plane and Nien, 1992).

Measurements can be performed continuously and with a high time resolution of typically a few minutes, giving insight into the chemical interactions between species (Plane and Nien, 1992; Stutz and Platt, 1996).

5.1.2 Physical Basis of DOAS

The basis of the DOAS technique is the Beer-Lambert law which details the exponential relationship between the intensity of light passing through a sample and the concentration of the absorbing species:

$$I_{tr}(\lambda) = I_0(\lambda) \exp\left(-\int_0^1 \sum_{i=1}^n \sigma_i(\lambda, P, T) c_i dl \right) \tag{5.1}$$

where I_{tr} is the intensity of light transmitted through the sample at wavelength λ, I_0 is the intensity of the incident light, l is the path length of light, c_i is the concentration of the absorbing species i and σ_i is its absorption cross section at pressure P and temperature T.

Taking the natural logarithm of $I_0(\lambda)/I_{tr}(\lambda)$ then gives the optical density (OD) which is the sum of the optical densities of the n absorbing species at the wavelength λ:

$$OD(\lambda) = ln\left(\frac{I_0(\lambda)}{I_{tr}(\lambda)} \right) = \sum_{i=1}^n OD_i(\lambda) = \sum_{i=1}^n \int_0^l \sigma_i(\lambda) c_i dl \tag{5.2}$$

Converting to concentrations gives:

$$\bar{c}_i = \frac{OD_i(\lambda)}{\sigma_i(\lambda) l} \tag{5.3}$$

This is the average concentration of the species i over the path length l.

However, the Beer-Lambert law is an over simplification when considering absorption in the atmosphere. This is because in the atmosphere, light is also extinguished through elastic scattering by air molecules and aerosols. These scattering processes are described by the Rayleigh and Mie extinction coefficients, ε_R and ε_M, respectively. Although they are not absorption processes, they can be treated as such in the case of DOAS as they scatter light out of the path of the beam from the DOAS instrument (Platt, 1994).

The Rayleigh extinction coefficient ε_R describes the elastic scattering of light by particles which are smaller than the wavelength of the incident light:

$$\varepsilon_R(\lambda) = \sigma_R \lambda^{-4} c_{air} \tag{5.4}$$

where σ_R is 4.4×10^{-16} cm^2 nm^4 for air and c_{air} is the concentration of air in molecules cm^{-3}. It is clear from Equation 5.4 that Rayleigh scattering is strongly dependent on the wavelength of light, so that for instance, light intensity at $\lambda = 300$ nm will be reduced by around 12 % per km of light path compared to only 1 % at 600 nm. This is one of the reasons that make DOAS measurements in the UV region challenging in the MBL.

The Mie extinction coefficient defines the scattering of light by particles which are larger than the wavelength of the incident light, such as aerosols:

$$\varepsilon_M(\lambda) = \varepsilon_M \lambda^{-n} \tag{5.5}$$

where n (which varies between 1 and 4) and ε_M depend on the chemical composition and size distribution of aerosol.

Including these processes in Equation 5.1 and averaging over the optical path length, l, leads to:

$$I_{tr}(\lambda) = I_0(\lambda) exp\left(-l\left(\sum_{i=1}^{n} \sigma_i(\lambda)\bar{c}_i + \bar{\varepsilon}_R(\lambda) + \bar{\varepsilon}_M(\lambda)\right)\right) \tag{5.6}$$

In the atmosphere, the Beer-Lambert law cannot be applied directly as most molecular species are present continuously and extinction by Rayleigh and Mie scattering always occur, therefore I_0 cannot be obtained free from extinction. The differential absorption is used instead, providing the absorbing species has a highly structured absorption spectrum within a narrow wavelength range. This structure can be used as a fingerprint for the species, appearing in the atmospheric spectrum.

The differential absorption cross-section, σ_i' is defined as the difference between the absolute cross-section, σ_i, and the broad trend, σ_i^s, which varies slowly with wavelength (Plane and Saiz-Lopez, 2006; Platt, 1994).

$$\sigma_i(\lambda) = \sigma_i'(\lambda) + \sigma_i^s(\lambda) \tag{5.7}$$

This is shown in Figure 5.1 for the case of NO_2, showing the absolute cross section, the broad trend of the spectrum and finally the differential cross-section, over a wavelength range of 40 nm, typical of that used by DOAS instruments (Plane and Saiz-Lopez, 2006). A 3rd order polynomial is employed to describe the slowly varying component of the absorption cross section for the case of NO_2; the degree of the polynomial used will depend on the species and wavelength region of interest.
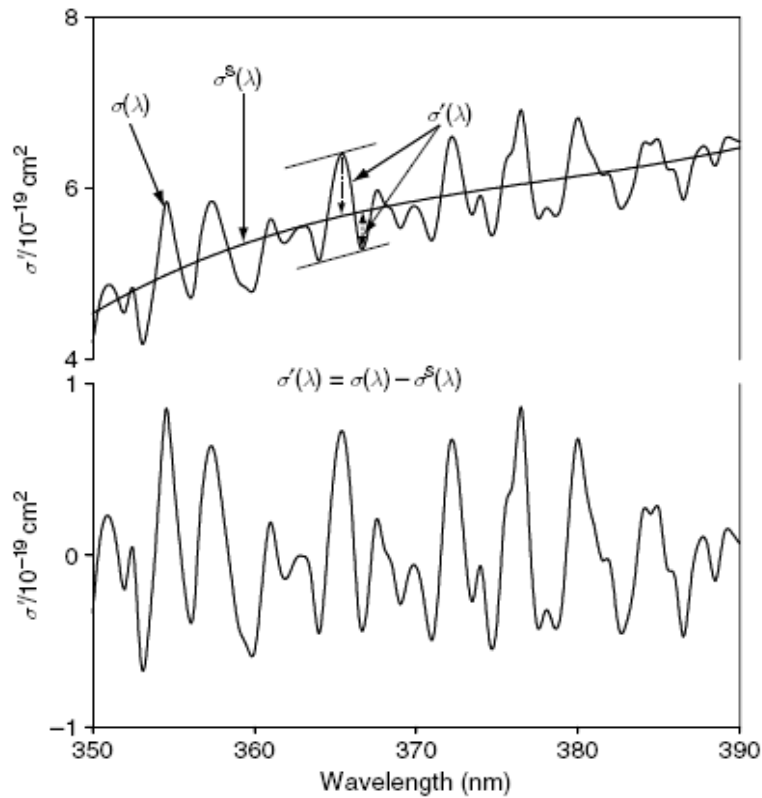
Figure 5.1 Absolute and differential absorption cross-sections for NO_2 showing the 3rd order polynomial fitted to the absorption cross section (Plane and Saiz-Lopez, 2006).

Substituting this into Equation 5.6 and taking into account instrument related factors $F_{ins}(\lambda)$, which includes the wavelength dependence of the optical transmission within the spectrometer and the quantum efficiency of the detector, gives:

$$I_{tr}(\lambda) = I_0(\lambda) exp\left(-l\left(\sum_{i=1}^{n}\sigma_i^{'}(\lambda)\bar{c}_i\right)\right) exp\left(-l\left(\sum_{i=1}^{n}\sigma_i^{s}(\lambda)\bar{c}_i + \bar{\varepsilon}_R(\lambda) + \bar{\varepsilon}_M(\lambda)\right)\right) F_{ins}(\lambda) \quad (5.8)$$

This equation can be considered in two parts: the first exponential factor describes the narrow band absorption features; the second exponential factor and the instrumental factor explain the broad band features (Plane and Saiz-Lopez, 2006; Platt, 1994). The intensity measured in the absence of differential absorption can then be defined as:

$$I_{tr}(\lambda) = I_0^{'}(\lambda) exp\left(-l\left(\sum_{i=1}^{n}\sigma_i^{'}(\lambda)\bar{c}_i\right)\right) \quad (5.9)$$

where the optical density is given by:

$$OD_i'(\lambda) = \ln\left(\frac{I_0'(\lambda)}{I_{tr}'(\lambda)}\right) = l\sum_{i=1}^{n}\sigma_i'(\lambda)\bar{c}_i \qquad (5.10)$$

And finally converting to concentrations (as for Equation 5.3) yields:

$$\bar{c}_i = \frac{OD_i'(\lambda)}{\sigma_i'(\lambda)l} \qquad (5.11)$$

5.1.3 The LP-DOAS Instrument

The basic components of the long-path DOAS instrument involve a transmitter, usually a high pressure Xe lamp, a receiver which is coupled to a spectrometer and a detector where the dispersed spectrum is recorded. In early DOAS instruments the transmitter and receiver were placed at opposite ends of the light path and a slotted disc scanning device along with a photomultiplier tube was used as the detector (Platt et al., 1979). Developments in the design of LP-DOAS instruments have involved placing the transmitter and receiver in the same location and folding the light path using a reflector and using photodiode array (PDA) or charge coupled devices (CCD) in place of photomultiplier tubes. A description of a typical DOAS instrument is described below and a schematic diagram of the setup is shown in Figure 5.2.

The long-path DOAS instrument uses a Xe Arc lamp as the light source which is projected over the given path length through a Newtonian telescope. The advantages of using a xenon lamp include the relatively high intensity in the UV wavelength region (allowing measurements of species such as BrO) and the small arc size, allowing easier focusing onto the optic fibre (Plane and Nien, 1992). This light source is generally positionedat the focal point of a spherical or parabolic mirror to provide a highly collimated beam. The light is then reflected back to the telescope by a corner-cube array of mirrors, positioned several kilometres away. The corner-cube array uses internal reflections to reflect the light back to the spectrometer with high accuracy. In

addition to this it has a large acceptance angle (~20°) so that it does not need to be pointed accurately at the source (Plane and Saiz-Lopez, 2006; Platt, 1994).

A number of advantages are achieved from folding the light path and housing the receiver and transmitter in the same location. Firstly, in the processing of the atmospheric spectrum, a spectrum of the lamp is required which is unattenuated by transmission through the atmosphere. This can easily be achieved if the light source and spectrometer are housed in the same location. Secondly, folding the light path gives double the path length and reduces complications which could arise from inhomogeneous air masses over long distances. Thirdly, folding the light beam means that light losses from divergence of the light beam are significantly reduced as the reflected light converges back to the source. In addition to this, housing the transmitter and receiver in the same location is preferable when taking measurements in remote locations as only one power source is required (Plane and Nien, 1992; Plane and Saiz-Lopez, 2006).

The received light is then focused onto a quartz optic fibre bundle and the light dispersed through a 0.5 m Czerny-Turner spectrometer through a 1200 or 600 mm^{-1} grating. This gives a resolution of 0.2–0.4 nm. An advantage in using a CCD is that CCD chips can have high quantum efficiencies in the near-UV, extremely useful for wavelengths < 400 nm. This is achieved through application of a suitable surface coating (e.g. Lumogen) which improves the quantum efficiency in the region below 400 nm (without this coating the quantum efficiency falls to zero at 350 nm). The CCD is also cooled to -70 °C using a multistage Peltier thermoelectric cooling system to minimise the dark current within the device and improve signal to noise. The signal from the CCD is then detected by the computer.

In addition to these components, stepper motors can be used to shutter-off light so that scattered light spectra can be recorded and also to obtain unattenuated lamp spectra. Filter wheels are also used with neutral density filters to attenuate the light entering the spectrometer so that the CCD is not saturated (Plane and Saiz-Lopez, 2006).
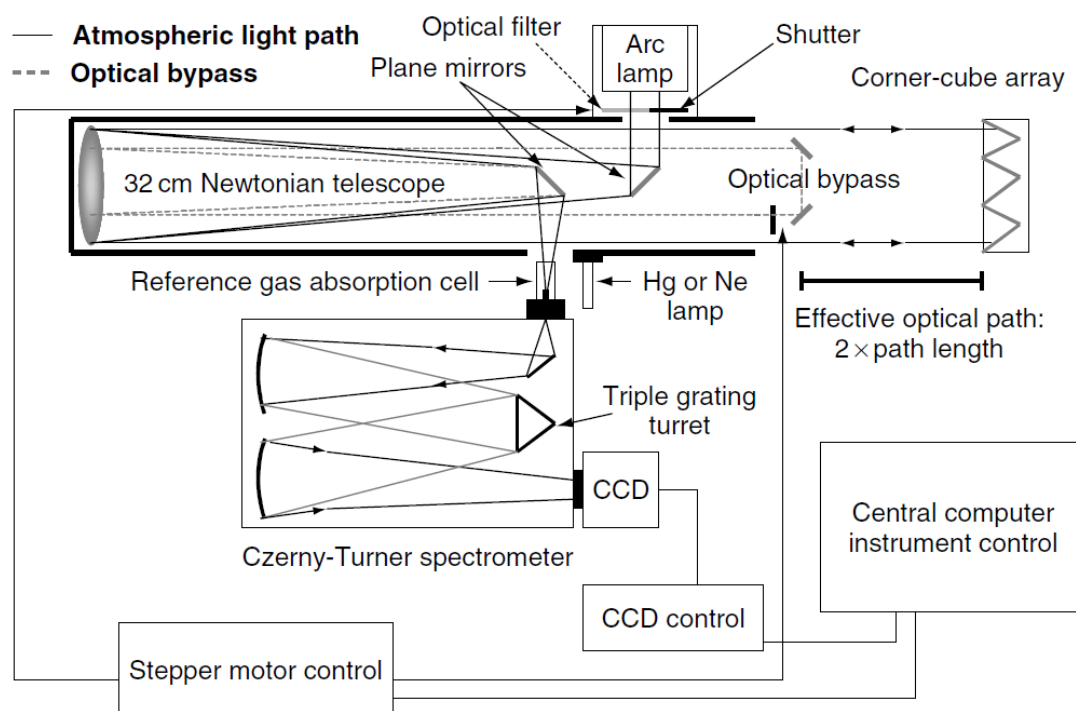
Figure 5.2 Schematic diagram of the LP-DOAS instrument (Plane and Saiz-Lopez, 2006).

5.1.4 Analysis of Halogen Measurements

There have been a number of field campaigns involving measurement of halogen species using LP-DOAS, in a variety of locations, covering polar, mid-latitude and tropical environments (e.g. Friess et al., 2011; Honninger et al., 2004b; Huang et al., 2010; Mahajan et al., 2009b; Peters et al., 2005; Read et al., 2008; Saiz-Lopez and Plane, 2004a; Saiz-Lopez et al., 2007b; Stutz et al., 2011). The halogen species that have been successfully measured during these campaigns are I_2, IO, OIO, and BrO and concentrations for all are typically several parts per trillion. These species do not all absorb in the same spectral region and therefore simultaneous measurements are not possible using this technique.

BrO is measured in the near-UV region of the spectrum from 324–357 nm, IO in the visible at 425–445 nm and I_2 and OIO are measured in the region 535–575 nm (Gomez Martin et al., 2005; Mahajan, 2009; Saiz-Lopez et al., 2004c; Wilmouth et al., 1999). The absorption cross sections of each of these species and others commonly measured using LP-DOAS are given in Figure 5.3.
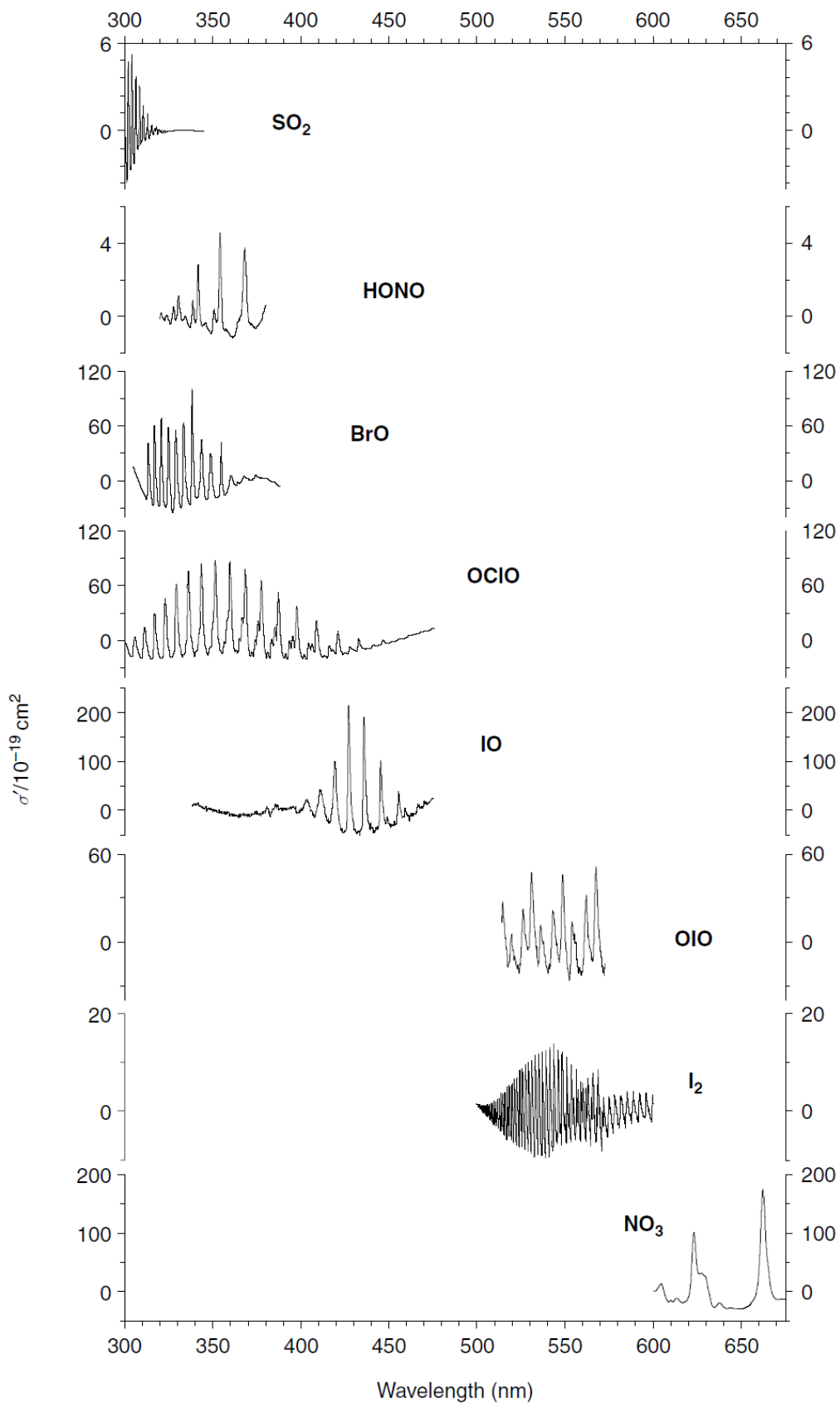
Figure 5.3 Differential absorption cross sections for species commonly measured using LP-DOAS (Plane and Saiz-Lopez, 2006).

The instrument will be set up to focus on a specific region of the spectrum dependent upon the species of interest. Spectra are recorded every 30 s, and consist of three components: the atmospheric spectrum (A), scattered light spectrum (S) and lamp spectrum (L) which are differentiated using three separate measurements every 10 s (A+L+S, A+S and S). Each of these measurements is a single spectrum, which is comprised of contributions from the individual A, L and S spectra.

For the concentrations of species to be retrieved, a spectral de-convolution procedure must be followed. The first step involves producing processed spectra (I_{pr}) using the formula:

$$I_{pr} = \frac{AS - S}{ALS - AS}$$

(5.12)

In this way the Xe lamp spectral features are removed from the spectrum before analysis (Plane and Saiz-Lopez, 2006).

The spectra are then converted to optical densities using a Fourier transform and filter procedure. A smoothed spectrum is obtained using a fast Fourier transform (FFT) and high-pass frequency filter and a low-pass filter FFT analysis gives the overall trend of the processed spectrum. The differential optical density is then given by the logarithm of the broad trend spectrum divided by the smoothed spectrum (Plane and Nien, 1992). The variation of wavelength of the attenuation in intensity caused by Mie and Rayleigh scattering is largely removed by employing this process. The optical density spectrum is then given by the sum of the contributions from n individual absorbers at each wavelength. To this, a first order polynomial is added, optimised during the fitting procedure, which accounts for any residual off-sets:

$$OD'(\lambda) = \ln\left(\frac{I_0'(\lambda)}{I_{pr}'(\lambda)}\right) = l\sum_{i=1}^{n} \sigma_i'(\lambda)\bar{c}_i + \alpha\lambda + \beta$$

(5.13)

Dependent upon the region of interest, there will be several species with strong absorption features that should be considered; for the 425–445 nm range the important species are IO, NO_2 and H_2O. Reference differential absorption cross sections for these species must first be converted to optical densities using the same FFT, low and high-pass filter procedure as employed for the processed spectra. The OD′ is measured over a large number of wavelengths in a multiplexing detector leading to 1024 simultaneous equations for the i unknown concentrations $\bar{c}_i$ (Plane and Nien, 1992). However, the unknowns in the equation are the n molecular concentrations $\bar{c}_i$ and the parameters α and β, and this means there are usually fewer than ten unknowns in total. The solution to Equation 5.13 is therefore greatly over-determined. The solution to this is to use a least squares fitting routine using singular value decomposition (Press et al., 1986) where the reference optical density spectra are fitted simultaneously to the processed OD′ leaving a featureless residual spectrum. Also included in the analysis procedure is the ability to stretch or shift the reference spectra with respect to wavelength to correct for differences in the wavelength calibration between the DOAS spectrometer and the literature cross-sections.

The errors on the retrieved concentrations and the detection limits of the DOAS instrument will depend on a number of factors such as the size and structure of the differential absorption cross sections, the number of absorbers, the optical path length and the intensity of the light signal transmitted through the atmosphere. A chi-squared significance analysis gives a measure of the goodness of fit of the de-convolution routine:

$$\chi^2 = \frac{\sum\limits_{\lambda_1}^{\lambda_2}\left(OD'(\lambda) - l\sum\limits_{i=1}^{n}\sigma_i'(\lambda)\bar{c}_i + \alpha\lambda + \beta\right)^2}{m-1} \qquad (5.14)$$

where m is the number of wavelength intervals between λ_1 and λ_2 (i.e. the number of elements of the detector). The smaller the χ^2, the better the fit, and the less structure in the residual spectrum (which is assumed to be random). The statistical standard errors on the retrieved concentrations are calculated directly from the singular value decomposition routine (Press et al., 1986) and are weighted by the χ^2 distribution and the $m-n$ degrees of freedom of the system. This 1σ statistical error is normally an underestimation of the overall error as it does not account for systematic errors such as those in the absolute absorption cross section of the reference spectra and the errors in the length of the optical path.

In some instances, consistent structures can be observed in successive residual spectra and this can be for a number of reasons, including the presence of an unknown absorbing molecular species (although this is rare) or incorrect matching of the reference and atmospheric spectra. Another cause can be incomplete removal of lamp spectral features due to variations in the spectral output across the Xe arc (this can often be improved by fitting the lamp spectrum as another absorber in the fitting routine). One way to remove consistent structures in a sequence of residual spectra is to average them to give an "instrumental reference" spectrum which can be fitted in the de-convolution routine along with the other molecular absorbers (Allan et al., 2000). This will often lead to reduced errors and detection limits for trace absorbing species without significantly affecting the retrieved concentrations.

The minimum detectable OD' can be estimated from the root mean square of the residual (Equation 5.15 below) and the detection limit for each individual species can then be estimated using Equation 5.11.

$$OD'_{min} = \sqrt{\frac{\chi^2}{m-1}} \qquad (5.15)$$

The detection limit will depend on the conditions affecting the light transmission through the atmosphere and scattered sunlight such as precipitation, cloud and

time of day. This is because χ^2 varies inversely with the light intensity transmitted through the atmosphere and is proportional to the level of scattered sunlight (Plane and Saiz-Lopez, 2006).

5.1.5 The MAX-DOAS Instrument

Multi-axis DOAS is based on the same principles as the LP-DOAS technique, however, in this case rather than an artificial light source, scattered-sunlight is used. There are numerous so-called "passive" DOAS techniques which use scattered sunlight, as well as stellar and lunar light, on various different measurement platforms including ground-based, aircraft, balloon-borne and satellite measurements (Brewer et al., 1973; Burrows et al., 1995; Pfeilsticker and Platt, 1994; Pommereau and Piquard, 1994; Roscoe et al., 1994; Solomon et al., 1987; Wagner et al., 2000). Figure 5.4 shows the viewing geometry for both a zenith-sky instrument, used extensively for measuring O_3 and NO_2 in the stratosphere (e.g. Roscoe et al., 1999), and that of a multi-axis instrument.
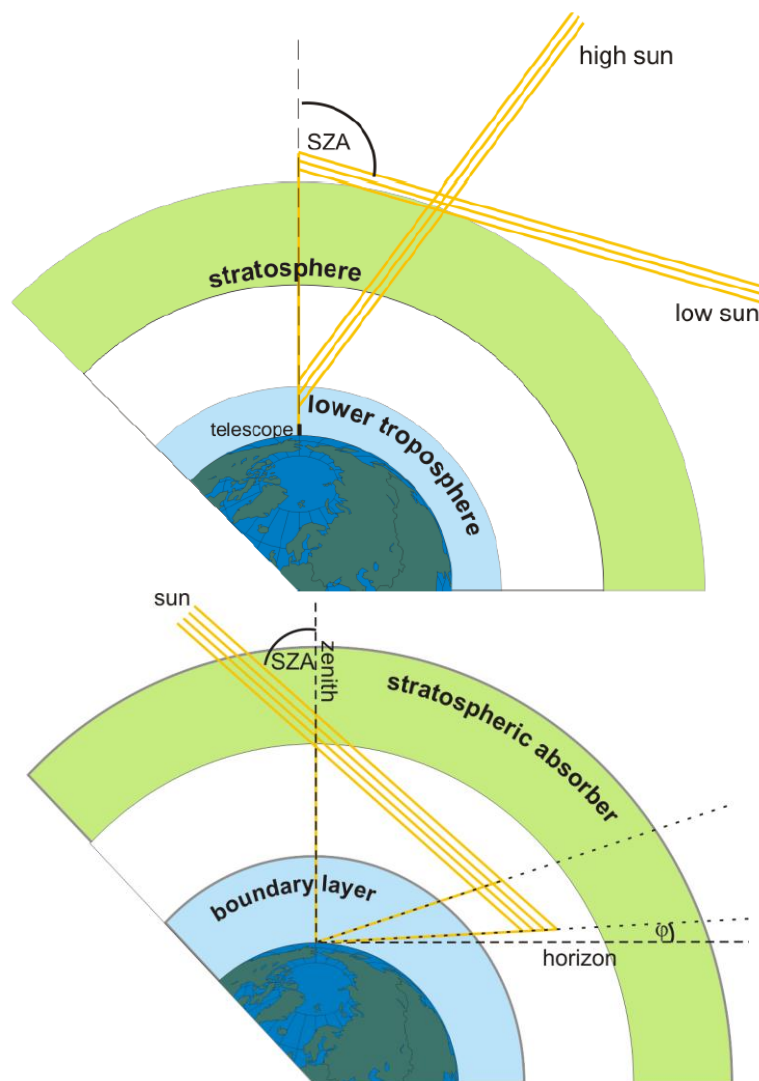
Figure 5.4 Diagram showing the zenith-sky and multi-axis viewing geometries (Oetjen, 2009).

This demonstrates the path of a single photon through the atmosphere whereas, in reality, the signal recorded by the instrument is due to a large number of photons all having taken differing paths through the atmosphere. The viewing geometry can be described using three different angles: the solar zenith angle (SZA); the elevation angle of the telescope relative to the horizon; and the solar azimuth angle (SAA) which is the angle between the viewing direction of the telescope and the position of the sun when both are projected to the plane of the surface level.

Zenith measurements can be reasonably approximated by considering single scattering as photons are scattered only once above the instrument's line of sight, having passed a great distance through the stratosphere before this (Solomon et al., 1987). This

height is dependent on the scattering probability which is proportional to the light intensity multiplied by the density of scatterers. To a first approximation the density of scatterers can be described by the air density which decreases exponentially with height. Therefore light intensity decreases moving closer to the surface as it is attenuated by scattering processes in the lower layers of the atmosphere (Solomon et al., 1987).

This gives a most probable height for scattering which will change with SZA; as the sun sets the light intensity at the surface decreases to an even greater extent meaning the most probable scattering height will be shifted upwards. The light path through the troposphere remains almost constant, independent of SZA. This means zenith measurements have a much greater sensitivity to stratospheric absorbers (Brewer et al., 1973).

The MAX-DOAS instrument achieves greater sensitivity to tropospheric absorbers by positioning the telescope viewing angle closer to the horizon compared to zenith measurements. This has allowed a large number of different tropospheric trace species to be measured using the MAX-DOAS technique, including IO, OIO, I_2, BrO, ClO, O_3, HCHO and CHOCHO.

In the case of MAX-DOAS measurements, by measuring light at several different elevation angles as well as at the zenith (as shown in Figure 5.5), profile information about the trace gas absorbers can be obtained (Honninger and Platt, 2002). The stratospheric light path remains fairly constant for all elevation angle measurements. Unlike zenith sky measurements the sensitivity of the off-axis measurement is strongly dependent upon the aerosol load of the atmosphere. The accurate interpretation of the light path therefore requires consideration of multiple scattering of photons, which is where radiative transfer modelling is employed to understand all possible photon paths (Marquard et al., 2000).
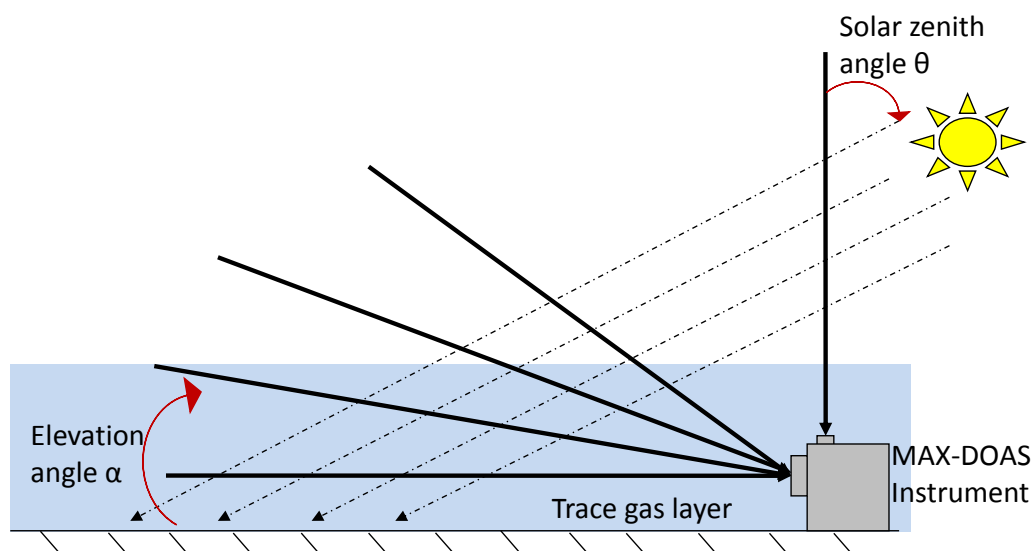
Figure 5.5 Schematic diagram of the MAX-DOAS instrument set-up showing different elevation angles (α) passing through the trace gas layer and the solar zenith angle (θ) which is a function of the time of day. Figure adapated from Honninger and Platt (2002).

For scattered sunlight DOAS the Beer-Lambert law needs to be modified to take into account the source of light being outside the Earth's atmosphere (Solomon et al., 1987).

$$I_{tr}(\lambda) = I_0(\lambda) exp(-\sigma(\lambda) SCD)$$
(5.16)

The SCD is the slant column density which is integrated along the path that solar photons take through the atmosphere. The optical density is then given by:

$$OD(\lambda) = ln\left(\frac{I_0(\lambda)}{I_{tr}(\lambda)}\right) = \sum_{i=1}^{n} OD_i(\lambda) = \sum_{i=1}^{n} \sigma_i(\lambda) SCD_i$$
(5.17)

where n is the number of species present in the light path which absorb at wavelength, λ.

As in the case of the LP-DOAS technique, the photons passing through the atmosphere are subject to Rayleigh and Mie scattering, and so wavelength dependent extinction coefficients are included as described previously (section 5.1.2).

The unattenuated I_0 spectrum, which in the case of the LP-DOAS analysis is accounted for by dividing by the lamp spectrum, cannot be obtained directly and an alternative method must be employed to account for this. Ideally, an extra-terrestrial spectrum recorded using the same instrument would be used, however, this is clearly not possible and using a spectrum recorded by, for instance, a satellite instrument would introduce additional uncertainty due to instrumental variations. Therefore the solar spectrum when the solar zenith angle (SZA) is at a minimum (i.e. local noon) is used, as this represents the point at which the slant column is at a minimum and includes as little absorption as possible from the Earth's atmosphere (Noxon, 1975, 1976). This process removes the highly structured Fraunhofer lines in the solar spectrum which account for much of the observed absorption (~30 %) so that the much smaller molecular absorptions can be discerned (Plane and Saiz-Lopez, 2006).

Another effect which needs to be taken into account when analysing the MAX-DOAS spectra is the so-called "Ring effect" (Grainger and Ring, 1962). This comes from the partial filling in of the Fraunhofer lines as sunlight passes through the atmosphere, most likely due to Raman scattering (Fish and Jones, 1995; Sioris and Evans, 1999; Vountas et al., 1998), resulting in reduced optical densities of the Fraunhofer lines. The Ring effect needs to be accounted for as it can represent a change in optical density an order of magnitude larger than the absorption of atmospheric trace gases. This is usually achieved using an artificially generated Ring spectrum (Chance and Spurr, 1997) fitted as another absorber in the analysis routine. Another complicating factor in the analysis of MAX-DOAS spectra is the effect of clouds which increase the optical path length of the solar photons and can also increase the Ring effect (de Beek et al., 2001).

After accounting for these various effects and calculating the contribution of the individual absorbers, a SCD for each species is obtained. However, a more useful quantity is the vertical column density (VCD), and conversion is achieved through calculation of an air mass factor (AMF) (Perliski and Solomon, 1993; Solomon et al., 1987). The VCD is then given by:

$$VCD = \frac{SCD}{AMF} \qquad (5.18)$$

The AMF is dependent on the radiative transfer of the atmosphere and is calculated using radiative transfer models as mentioned previously, which take into account wavelength-dependent Rayleigh and Mie scattering effects, temperature and pressure profiles as well as SZA and the azimuth angle of the receiving telescope (Marquard et al., 2000; von Friedeburg et al., 2002). This determines the altitude at which significant light scattering occurs for the SZA (θ) and elevation angle (α) used. For a stratospheric absorber there will be a strong dependence of the AMF on θ, whereas a boundary layer absorber will have a much smaller dependence on θ and a strong dependence on α.

This can be explained with reference to Figure 5.6, which shows the scattering geometries for an absorber in the stratosphere (A) and in the boundary layer (B). For single scattering occurring below the trace gas layer (as in the case of a stratospheric absorber) the AMF can be estimated as $1/\cos\theta$. In the case of the boundary layer absorber, scattering occurs above the trace gas layer and the AMF can be approximated as $1/\sin\alpha$. In the case of a molecule being present in both the stratosphere and troposphere, the SCD will clearly contain contributions from both regions. However, for a fixed θ, the slope of a plot of SCD against AMF ($1/\sin\alpha$) will give an estimate of the vertical column below the scattering altitude (i.e. in the troposphere), whereas the intercept will give an estimate of the stratospheric component (Honninger and Platt, 2002).
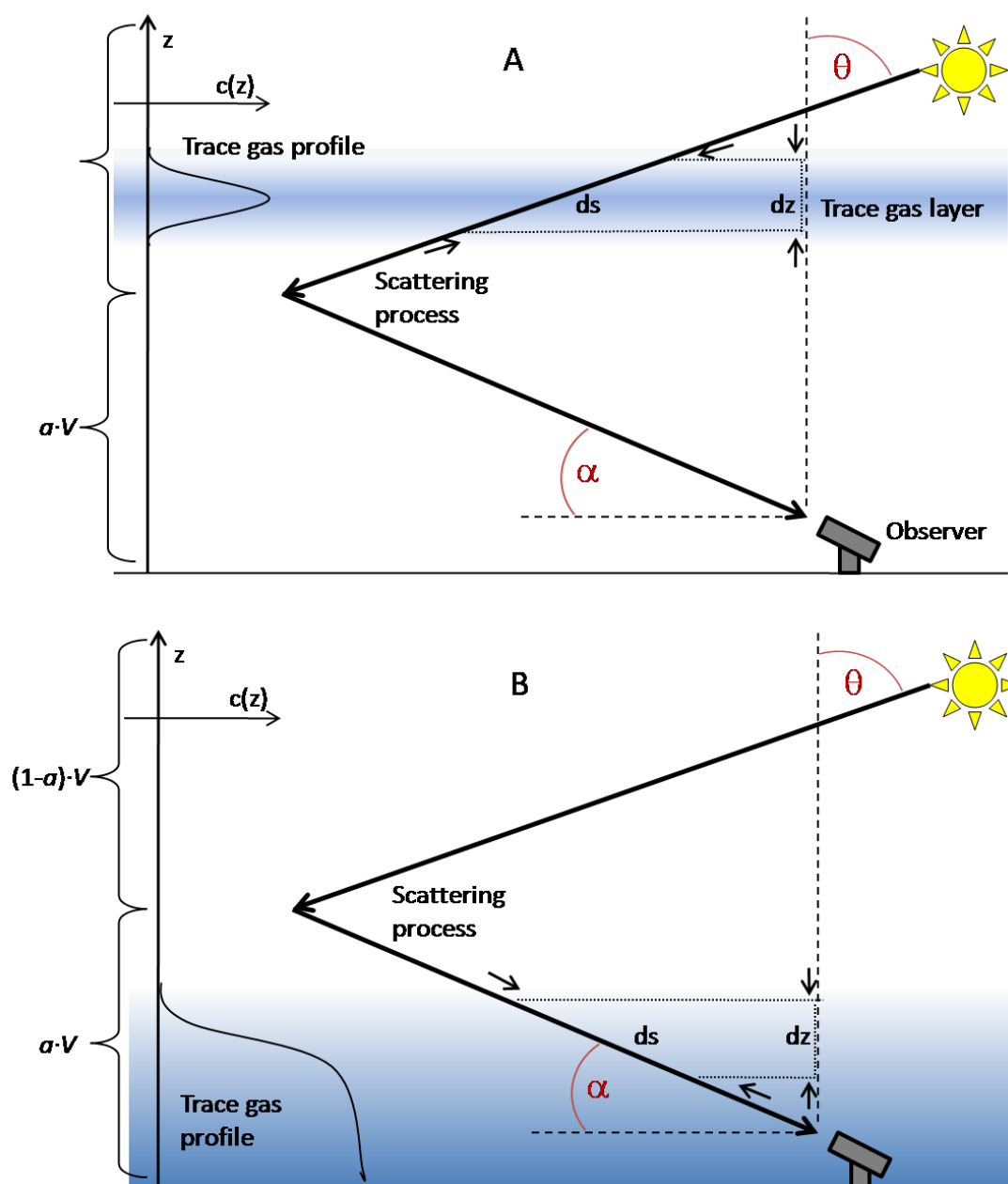
Figure 5.6 Diagram showing the single scattering for an off-axis viewing geometry for a trace species absorbing in the stratosphere (A) and in the boundary layer (B). The measured SCD (along ds) is converted to a VCD (along dz) by applying an AMF. Figure adapted from Honninger and Platt (Honninger and Platt, 2002)

5.1.6 Recent Developments in DOAS Measurements

A number of recent developments to the DOAS technique have arisen through the necessity to measure species in a variety of locations, including ship-borne and air-borne measurements in remote locations. This has led to the development of more

portable instruments which require lower power compared to traditional DOAS techniques.

One such technique is that of Cavity Enhanced DOAS (CE-DOAS), based on the principles of Cavity Ring-Down Spectroscopy (CRDS), using two highly reflective mirrors to increase the path length inside the cavity and therefore obtain increased sensitivity to atmospheric trace species (Meinen et al., 2010; Platt et al., 2009; Thalman and Volkamer, 2010). Using broadband light sources such as light emitting diodes (LEDs) (as opposed to e.g. Xe arc lamps used in LP-DOAS) means that the power required is significantly reduced, and the LED colour can be tuned to the specific wavelength range of interest. As with other DOAS techniques, the instrument is also inherently calibrated and therefore the frequent calibrations required in other cavity-enhanced absorption spectroscopy (CEAS) techniques are not needed so that sampling is not compromised (Thalman and Volkamer, 2010). In addition, the ability to make in situ measurements, rather than averaging over a large distance gives greater information on the spatial distribution of halogens.

Portability has been improved by the development of mini-DOAS instruments which have been developed for use in measuring networks of species such as NH_3 (Volten et al., 2012), and on aircraft platforms for measurements of BrO, IO, O_3 and HONO (Prados-Roman et al., 2011). It has also been suggested they may be used for making flux measurements by arranging two or more instruments in a gradient set-up (Volten et al., 2012). As well as being smaller than traditional instruments, they also have reduced costs and handling complexity (with increased automation) making them ideal for deployment in remote, unmanned locations (Carlson et al., 2010).

In addition, the use of instruments on mobile platforms requires some compensation for pitch and roll in both aircraft and ship based measurements which has lead to the development of motion compensation systems for the telescopes of MAX-DOAS instruments, including angle sensors with feedback loops to correct the telescope angle in real time (Baidar et al., 2013) . As well as developments in instrumentation, measurements of trace gas species from mobile platforms have also necessitated adaptations to the analysis technique due to the rapidly changing air masses

encountered (Wagner et al., 2010) and lack of a priori information on vertical profiles for species like BrO and IO (Prados-Roman et al., 2011).

In addition, the increasing need for spatial information of chemical species, particularly in terms of possible pollutants, has led to extensions of the DOAS technique to acquire a 2D or even 3D picture of the relevant species. These techniques include imaging DOAS (IDOAS) which has been employed to measure NO_2 plumes from industrial activities (Heue et al., 2008; Lee et al., 2009a) and volcanic gas emissions (Louban et al., 2009), and Hemispheric Scanning Imaging DOAS (HSI-DOAS) where a 360° rotating head unit allows scanning of entire hemispheres of the surrounding skyline (Graves et al., 2013). A further challenge for the continuing use of DOAS instruments in the field is to achieve even better detection limits as the species of interest are often in minute trace quantities (<pptv levels). There has been progress in this area through limiting the effects of detector non-linearity noise and small temperature fluctuations which can cause variations in optical resolution (Coburn et al., 2011).

A description of the specific set-up of both the LP-DOAS and MAX-DOAS instruments deployed during the CHARLEX field campaign is provided in the next section.

5.2 CHARLEX Field Campaign

Satellite measurements have indicated that elevated levels of IO can be observed around the Galapagos Islands, with the largest mixing ratios observed outside the polar regions (Schonhardt et al., 2008). This is believed to be due to increased biological activity in the waters surrounding the islands from nearby deep water kelp forests (Thiel et al., 2007). However, on averaging the data over several years (2004–2009) it is found that the peak disappears around Galapagos (Schönhardt, 2009); this may be due to a seasonal effect and despite the IO being under the detection limit it could still have a significant impact on O_3. Ozonesonde data from the Southern Hemisphere Additional Ozonesondes (SHADOZ) experiment (Solomon et al., 2005) also shows frequent reduced ozone episodes in the boundary layer across a number of sites in the Pacific ocean, indicating a possible link to halogen emissions .

In addition, in tropical coastal regions it is known that deep convection occurs which could transport species such as CH_3I through the free troposphere and possibly to the stratosphere (Butler et al., 2007). This means the reactive species emitted at these sites may have a larger impact on the chemistry occurring higher in the atmosphere than at other locations such as the Arctic where zenith sky measurements estimate an IO concentration in the stratosphere of up to 0.8 pptv (Wittrock et al., 2000).

To verify the high satellite measurements of IO and to address the impact that these iodine emissions may have on the local ozone concentrations a field campaign was conducted on the island of Isabela, Galapagos. The Climate and Halogen Reactivity tropical EXperiment (CHARLEX) had several aims to better understand halogen chemistry in remote tropical environments, these were:

1) to validate the high satellite measurements of IO observed around the Galapagos Islands

2) to explain the extremely low surface O_3 measurements observed during the SHADOZ experiments at San Cristobal Island

3) to characterise the role of halogen species in the remote tropical marine boundary layer

4) to determine whether the levels of IO observed were sufficient to lead to particle formation and the subsequent formation of CCN.

To achieve these aims a number of different measurement techniques were employed to observe a range of halogen species including I, IO, OIO, I_2 and BrO. In addition, a suite of instruments was used to make complimentary measurements of NO_x, O_3, particles, RGM and meteorological conditions such as wind speed and temperature.

5.2.1 Site Description and Meteorology

The CHARLEX campaign is an ongoing campaign on the Galapagos Islands in the tropical Pacific Ocean. The campaign can be split into two, with the first campaign which ran from September 2010 to May 2011 involving a suite of instruments, including both the LP and MAX-DOAS instruments at Puerto Villamil on the Island of Isabela (0°57'27.37"S, 90°57'55.55"W), which is the largest island of the Galapagos archipelago. The second part of the campaign which ran from June 2011 until present took place at the INAMHI meteorological station in Puerto Baquerizo Moreno on the island of San Cristobal (0°54'14.53"S, 89°36'50.92"W), the eastern-most island of the archipelago, with semi autonomous MAX-DOAS, ozone monitor and aerosol instruments.
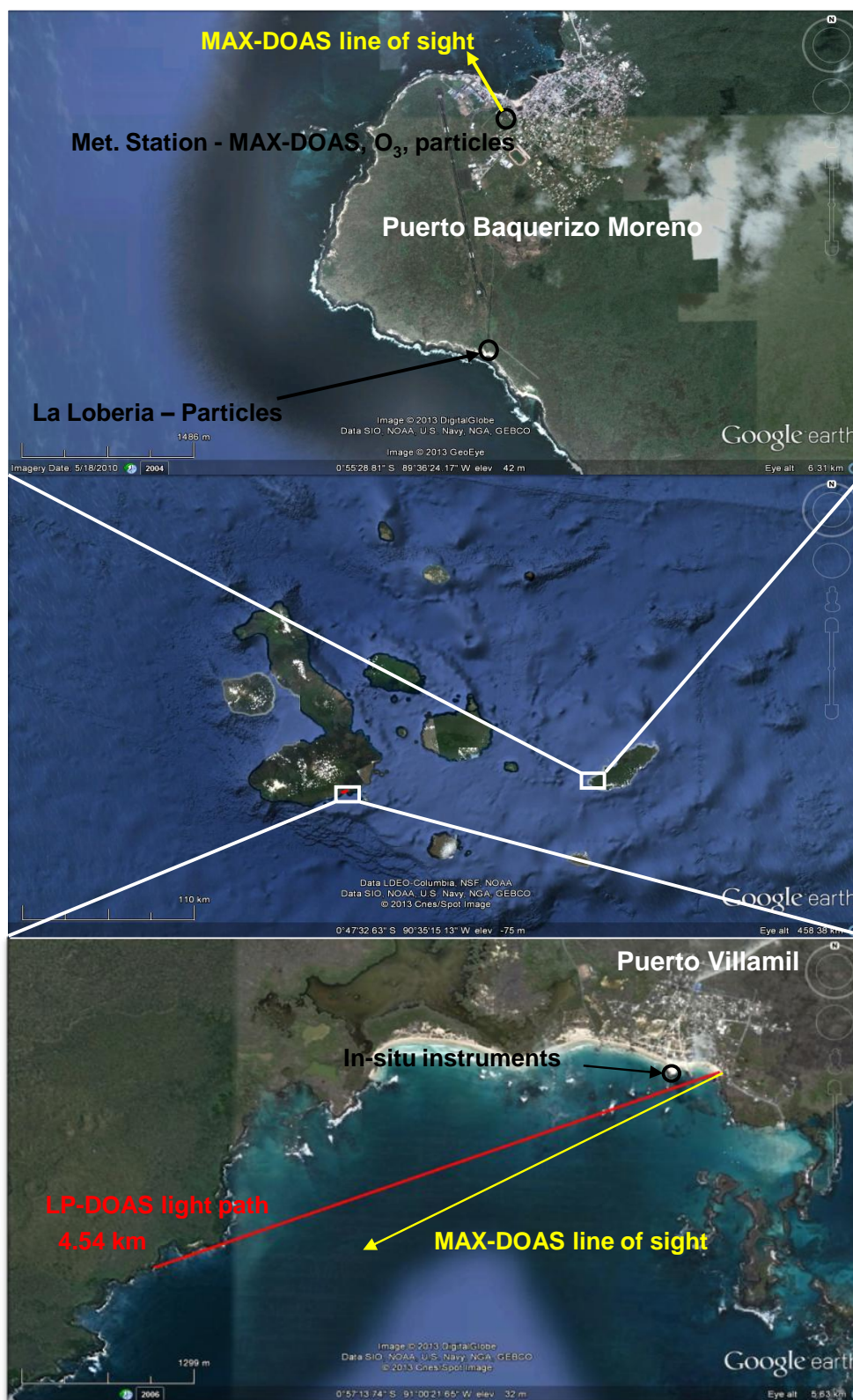
Figure 5.7 Satelite image of the two measurement sites (Google Earth). The middle panel shows the position of the measurement sites within the Galapagos archipelago. The top panel shows the site of the Met station in San Cristobal where the MAX-DOAS and particle instruments were located and La Loberia where additional particle measurements were performed. The bottom panel shows the measurement site at Isabela with the LP-DOAS light path and MAX-DOAS line of sight. The group of islets known as the Tintoreras are also visible to the bottom right.

The Galapagos archipelago is a range of volcanic islands in the equatorial Pacific almost 1000 km west of the coast of Ecuador. The surrounding ocean is subject to large seasonal variability in both sea surface temperature (SST) and salinity, and shows highly temporally variable areas of heightened primary productivity. This arises due to the position of the Galapagos Archipelago at the intersection of several different current systems. The islands are bisected by the Equatorial Front which divides the warmer tropical waters in the North from the cooler temperate waters in the south (Pak and Zaneveld, 1974). There are three major currents which influence the waters surrounding the islands: the cool Humboldt current from the south; the North Equatorial Countercurrent (NECC) from the North; and the westward-flowing South Equatorial Current (SEC) (Kessler, 2006). The SEC is influenced by both the Humboldt and NECC at different times of year depending on the position of the inter-tropical convergence zone (ITCZ). During May–December (cold season) the ITCZ is north of the equator and the Humboldt Current is the major contributor to SEC influence. From December-May (warm season) the ITCZ shifts south so that the SEC is pushed towards the NECC and North Easterly trade winds become dominant (Schaeffer et al., 2008). There is an additional influence from the eastward flowing Equatorial Undercurrent (EUC) which collides into the Archipelago, upwelling cold nutrient rich waters to the warmer tropical surface waters (Steger et al., 1998).

The island coastal shelves are relatively shallow, with a gradual incline with lava flows forming protrusions and shallow bays around the islands. These waters do not however contain any large beds of iodine emitting macroalgal species. The waters around the Galapagos Islands are home to deep-water tropical kelp forests (Graham et al., 2007) which increase with depths > 60 m. These kelp beds could act as a source of iodine species to the ocean surface.

The air masses arriving at the island are predominantly south-easterly trade winds, which have spent a considerable time over the ocean and therefore can be considered clean, with little influence from terrestrial sources. Figure 5.8 shows the back trajectories of air masses arriving at the Galapagos during the entire measurement period. The back trajectories are classified according to the contribution from different oceanic regions (as indicated on the figure). These are defined roughly according to: in

the Southern Hemisphere their primary productivity; in the Northern Hemisphere their proximity to land masses. The trajectories show that 60–89 % of the time the air masses pass over low Chl-*a* regions in the open ocean.
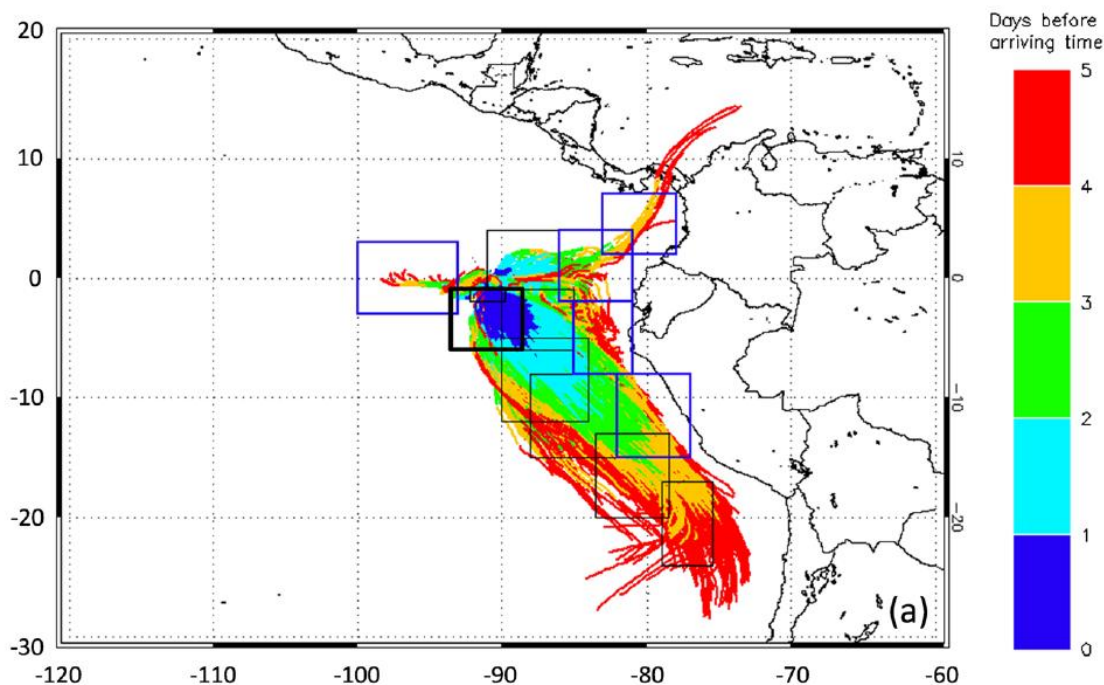
Figure 5.8 Hysplit five day back trajectories for the entire measurement period: the bold outlined black box represents the region used for comparing Moderate Resolution Imaging Spectroradiometer (MODIS) chlorophyll-*a* (Chl-*a*), chromophoric dissolved organic matter (CDOM) and sea surface temperature (SST) data to the reactive iodine observations. The colours are indicative of the number of days before the air mass arrived at the measurement site (Gómez Martín et al., 2013).

The wind vectors observed are consistent with the expected patterns for the Eastern Equatorial Pacific (Hayes et al., 1989; Wallace et al., 1989) with weaker meridional components during the warm season, leading to negative (i.e. northerly) meridional components in March 2011. The weakening of the meridional component implies that the air masses pass closer to, and spend more time around the upwelling region along the Peruvian coast and also around the Galapagos archipelago itself, reaching the islands from the east rather than the south (as observed during the cold season).

At San Cristobal the observed wind speeds are stronger than at Isabela with a daytime average of 3.7 m s^{-1} compared to 1.7 m s^{-1}. The zonal wind at Isabela is also more variable with both positive (westerly) and negative (easterly) values, whereas at San Cristobal the zonal component is fairly consistently negative. The observations at

San Cristobal are in agreement with buoy wind measurements previously conducted in the region (Hayes et al., 1989; Wallace et al., 1989). The greater variability at Isabela is indicative of the surface winds being partially blocked or slowed down by the presence of the group of islets (known as the Tintoreras) to the south of the measurement site.

Throughout both campaigns the SST can be described as either La Niña or ENSO (El-Niño-Southern Oscillation) neutral with the greatest temperature anomalies occurring in the 2010 cold season (SST anomalies up to -2 °C). There was then a transition to ENSO neutral conditions during the 2011 warm season followed by moderate La Niña conditions in the 2011 cold season (SST anomalies < -1.2 °C). The warm season of 2012 saw a return to ENSO neutral conditions. The air temperature recorded at both Isabela and San Cristobal for 2010 and 2011 was within ±1 °C of the average except during the 2010 cold season where the temperature anomaly reached below -1.5 °C.

5.2.2 Instrumentation

The LP-DOAS instrument ran from September 2010 to March 2011 and was housed in an air-conditioned room in Puerto Villamil, Isabela. It consisted of a Newtonian telescope containing a 450 W xenon arc lamp and the transmitting and receiving optics. The light beam extended 4.54 km to the West where a retro-reflector was positioned, on the other side of Villamil bay to fold the light path back to the telescope. This gave a total optical path length of 9.08 km. The height of the light beam above the ocean ranged from around 1 m at high tide at the instrument site up to around 5 m where the retro-reflector was situated.

The instrument uses a 0.5 m Czerny-Turner spectrometer with a 1200 groove mm^{-1} grating coupled to a cooled (-70 °C) CCD camera, giving a spectral resolution of 0.25 nm at full-width half-maximum (FWHM) and covering a spectral range of around 40 nm. The recorded differential spectra were then averaged for 30 minutes to improve the signal-to-noise ratio and then converted to optical densities. The contributions from individual absorbing species were then calculated using multivariate fitting of a

library of reference absorption cross sections, degraded to the resolution of the spectrometer and taking into account stretching and shifting effects of the instrument.

Throughout the campaign, the measurements were alternated between four different spectral regions to probe a number of reactive halogen species. The reference spectra fitted in the 425–440 nm region were IO (Gómez Martín, 2005), NO_2 (Vandaele et al., 1998), H_2O (Rothman et al., 2003) and glyoxal (Volkamer et al., 2005). For the 530-570 nm region the species fitted were I_2 (Saiz-Lopez et al., 2004c) and OIO (Spietz et al., 2005).

During the first part of the campaign, the MAX-DOAS scanning telescope was situated on the terrace of the laboratory at a height of around 3 m above sea level and around 15 m away from the mean tide level. The telescope pointed in a westerly direction, almost parallel to the light beam of the LP-DOAS instrument. At the site in San Cristobal the instrument is located at around 5 m on the roof of a building around 160 m from the coastline. The telescope points NNW but does not overlook the seaport.

The MAX-DOAS telescope consists of a 2.5 cm diameter quartz lens set at 7.5 cm focal length from a fibre optic bundle giving a 1° field of view. The telescope is mounted on a stepper motor allowing spectra to be recorded at 19 discreet elevation angles between -5° and 90°. The optic fibre was then connected to a spectrometer (Princeton Instruments SP500i) positioned inside the temperature-stabilized laboratory with 1200 grooves mm^{-1} grating and CCD camera (Princeton Instruments Pixis 400B) giving a spectral resolution of 0.25 nm FWHM and a 40 nm spectral range. Spectra were recorded at 10 s exposure time for each elevation angle. The spectral range was extended to 80 nm when the instrument was moved to the San Cristobal site and the number of discreet elevation angles was reduced to six (from 0° to 90°). The exposure time was increased to 30 s per elevation angle giving a better signal-to-noise ratio. Finally, one hour averaging at each elevation angle was employed to further improve signal-to-noise.

The measurements also alternated between different spectral windows to allow retrieval of different trace species. For the retrieval of IO, the reference spectra as indicated above for the LP-DOAS measurements were fitted along with O_3 (recorded at

223 K) (Bogumil et al., 2003) and a Ring spectrum (Chance and Spurr, 1997). These were fitted simultaneously using the commercial QDOAS software (Fayt and van Roozendael, 2011) together with a 3rd order polynomial to take into account broadband extinction processes, and a linear intensity offset to allow for possible instrumental stray light. The window region chosen for spectral deconvolution was 416–440 nm and the zenith spectrum recorded for each scan was used as a reference.

In addition to the two DOAS instruments measuring iodine species, another technique, resonance and off-resonance fluorescence by lamp excitation (ROFLEX), was used to measure atomic and molecular iodine. This technique is described in detail in Gomez Martin et al. (2011). Briefly, the instrument works by pumping ambient air at a rate of 7000 cm^3 min^{-1} through a 0.8 mm pinhole and through a low pressure chamber. Iodine atoms in the airflow are then excited by vacuum UV radiation at 178.276 and 183.038 nm by a radiofrequency discharge iodine lamp. Resonance fluorescence is then collected orthogonally by a photon counting module. Background measurements are made by drawing the airflow into an iodine trap for a set time before entering the fluorescence chamber. The iodine trap consists of a blackened glass tube where the I atoms are scavenged by excess O_3. The instrument was calibrated by concurrently measuring I_2 off-resonance fluorescence by the ROFLEX instrument and absorption by incoherent broadband cavity enhanced absorption spectroscopy (IBBCEAS), combined with photolysis of known amounts of molecular iodine to generate atomic I.

The ROFLEX instrument was located less than 30 m from the high tide line throughout October 2010 and around 1 m above sea-level. In February 2011 the ROFLEX was located with the rest of the in situ instruments on a nearby pier, closer to the sea but around 5 m above sea level. The detection limit of the instrument for atomic iodine was found to be 1.1 pptv for one hour averaging during October 2010, increasing to 1.9 pptv during February 2011.

Air samples were taken at the coast of Isabela during May and June 2011 for halocarbon analysis using GC-MS. Samples were collected in 3.2 L silicocans and transported to University of East Anglia for analysis. Iodocarbons were monitored

using the m/z 127 peak for iodinated compounds with typically better than 5 % precision.

During the second half of the campaign at San Cristobal, ambient aerosol particle size distributions were measured using a scanning mobility particle sizer (SMPS) consisting of a neutralizer and differential mobility analyser. An ultrafine concentration particle counter (UCPC) was used to count particles, and this set-up allowed particles with sizes in the range 9–483 nm to be measured. A second UCPC instrument was employed to measure particles with diameters greater than 3 nm and by subtracting these measurements from those of the SMPS, particles in the size range 3–9 nm could be evaluated. The instruments were deployed from 21st July – 11th August for the UCPC and 30th July – 5th August for the SMPS instrument, both being housed in the same laboratory as the MAX-DOAS instrument. The instruments could not be deployed during the 9 month campaign in Isabela due to logistical reasons.

Two ozone monitors (2BT 202 and 205) and a NO$_x$ analyser (Teledyne 200EU) were situated on the second floor of a cabin, on the end of a pier pointing South, allowing air to be sampled directly off the ocean. The Teflon inlet tubing for the ozone and NO$_x$ instruments was guided using a pole pointing south so that the air sampled was around 2 m away from the walls of the cabin and around 5 m above sea level. The detection limits for these instruments were 2 ppbv and 50 pptv, respectively.

A weather station (WeatherLink Vantage) measuring temperature, relative humidity (RH %), wind speed and direction, and rainfall, and a global radiometer (Kipp and Zonen CPM11) were also situated on the same pole as the inlet tubing for the NO$_x$ and ozone instruments at Isabela. At San Cristobal, the existing weather station provided the relevant meteorological measurements; surface and sonde measurements suggested that the weather conditions at both sites were very similar.

5.2.3 Observations of Reactive Iodine Species

5.2.3.1 IO

Measurements of IO were recorded as mentioned previously by both the LP and MAX-DOAS instruments. The differential SCDs (dSCD) obtained from the MAX-DOAS analysis routine (Figure 5.9) had typical detection limits in the range 5×10^{12} to 1×10^{13} molecule cm^{-2} with a root mean squared (RMS) of $2.5–5 \times 10^{-4}$. Before converting dSCDs into volume mixing ratios (VMRs), filters were applied to remove data from SZA > 60° (to avoid influence of higher atmospheric layers), RMS > 4×10^{-4} and data recorded under cloudy conditions, estimated using a cloud filter (Sinreich, 2010) which uses the ratio of radiation fluxes at the edges of the spectral window. Only data from clear sky conditions were used for further analysis.
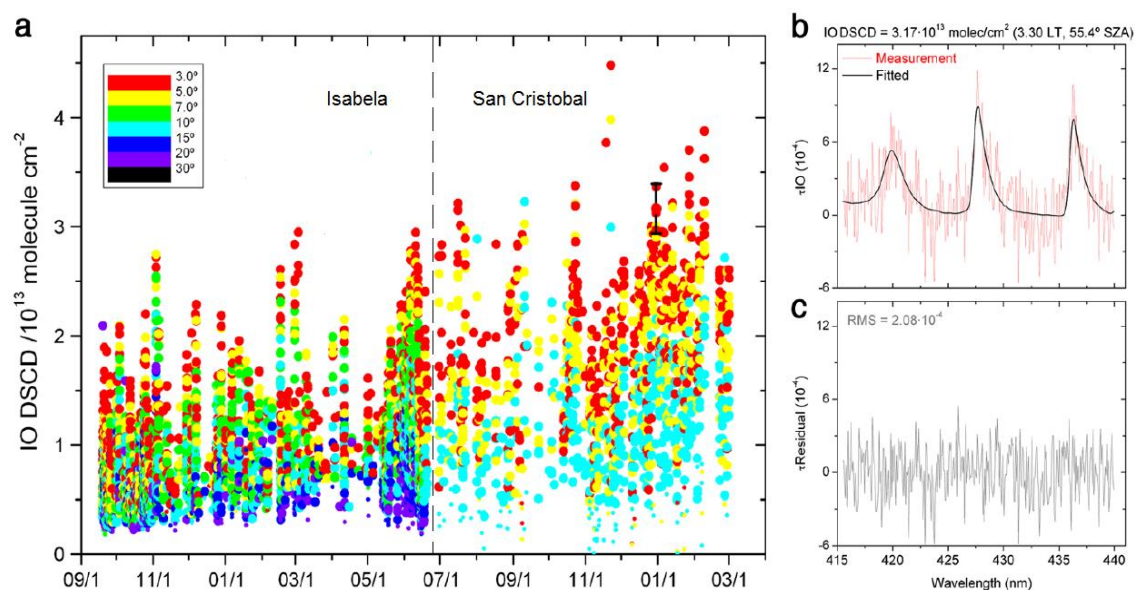
Figure 5.9 a) MAX-DOAS IO dSCDs at different elevation angles. b) An example spectral fit for IO. c) Example residual spectrum after all other absorbers have been fitted out (Gomez Martin et al. 2013).

For selected days when there were three or more viewing angles after filtering, to convert the filtered dSCDs into VMRs the so-called O_4 method was employed which has been used by a number of groups (Sinreich, 2010; Wagner et al., 2004) in addition to the NIMO fully spherical Monte Carlo radiative transfer model (RTM) (Hay et al., 2012). The procedure involves estimating an aerosol profile to reproduce the observed O_4 dSCDs, whose vertical distribution is known through forward modelling using the

RTM. O_4 dSCDs act as good proxies for the average effective path lengths of observed photons in the boundary layer due to their known vertical distribution which decreases in proportion to the square of the pressure. Aerosol profiles with varying optical depths and shapes were prescribed and the profile parameters were floated to achieve the best fit between the forward modelled and the observed O_4 dSCDs.

Aerosol profiles were only available for days when spectra were recorded in the UV as the 360 nm O_4 band was used. Therefore, for days when IO was measured the aerosol profile for either the previous or following day was used in the RTM for retrieval of the IO vertical profile by optimal estimation (Rodgers, 2000). This method requires an *a priori* profile for IO, which was assumed to decrease linearly from 0.4 pptv at the surface to 0 pptv at 4 km with a vertical resolution of 50 m and an error of 80 % at each level. A shortened light path due to aerosols meant that there was no available information from the 1° elevation angle and therefore a reduced sensitivity of the optimal estimation to the first 200 m of the boundary layer. With the available viewing angles, a more accurate estimation of the VMRs was achieved for a layer of 1000 m compared to 200 m. The closeness of most IO dSCDs to the detection limit and poor sampling of elevation angles means the quality of the data is insufficient for obtaining reliable vertical profiles.

A second more straight forward method was also used for the retrieval of IO VMRs from the observed dSCDs for the entire measurement period. This method used the 3° viewing angle dSCDs scaled with the simultaneously measured O_4 dSCDs to account for light path changes due to differences in aerosol loading. The upper altitude was defined by the mean last scattering altitude for photons reaching the detector and this provides an averaged VMR inside the layer with no vertical profile information. A further correction is required to account for the more rapidly decreasing IO profile with altitude. Correction factors were applied to remove the contribution of O_4 to the O_4 dSCDs from above the mean last scattering altitude (1200 m). This was achieved by using the single scattering geometrical approximation to calculate relative path lengths above and below 1200 m for each SZA. The O_4 derived path lengths were then calculated by dividing the O_4 dSCDs by the average O_2 squared concentration (2.4×10^{37} molecules^2 cm^{-6} from PTU sonde measurements) up to 1200 m.

The two methods gave IO VMRs which agreed within 25 % for O_4 derived path lengths shorter than 19 km, corresponding to a last scattering altitude of 1000 m based on the single scattering geometrical approach. For last scattering altitudes > 1000 m the O_4 scaled VMRs are systematically lower than those from the optimal estimation as a result of overestimation of the light path due to the differing profiles of O_4 and IO. Extremely high errors in the optimal estimation method result from the high errors on the IO *apriori* profile required to optimize the residual RMS of the forward model fit to the measurements. Due to the high dSCD errors and the lack of profile information from the lowest elevation angles the retrieval errors are only slightly reduced compared to the *apriori*. The errors on the O_4 method are somewhat harder to estimate due to the differences in the O_4 and IO profile shapes being unknown. The estimated errors arise from the range of the last scattering altitude from the different aerosol profiles in the O_4 forward modelling fits to the measurements. This gives an uncertainty in the mean O_4 extinction coefficient along the light path which is combined with the propagated errors from the O_4 and IO dSCDs to give the errors in the final IO VMRs.

The average 2σ detection limit with the LP-DOAS instrument over the entire campaign was 0.9 pptv which corresponds to a root mean squared residual of 2×10^{-4} and IO was not observed above this limit over the duration of the campaign at Isabela. For the derived VMRs from the MAX-DOAS instrument during the same period, 99 % were also under this limit. Comparison of the LP and MAX-DOAS instruments must be treated with caution, however, as the MAX-DOAS VMRs are averaged over a height of 1000 m whereas the LP-DOAS instrument measurements were sampled at 1–5 m above the ocean surface. The highest VMRs from the MAX-DOAS measurements were found for the lowest single scattering heights (average of 600 m) and shortest O_4 path lengths (average of 11 km). This implies that most of the IO is contained in the lowermost part of the MBL.

The atomic I was below the detection limit of the ROFLEX instrument (1.1 pptv) in October 2010 and February 2011 (1.9 pptv). The absolute mixing ratios of atomic I can be reasonably estimated by using a box model constrained by standard HO_x and NO_x chemistry. For low NO_x conditions (20 pptv for open ocean conditions (Lee et al., 2010))

the IO to I ratio calculated at noon is found to follow the linear relationship $IO/I = 0.13 \times [O_3]$ where the O_3 mixing ratio is in ppbv. The calculated I atom concentrations using this relationship are consistent with the detection limits of the ROFLEX instrument. The low O_3 concentrations result in I atom mixing ratios which are comparable to or even larger than the IO mixing ratios. To directly link these species to oceanic iodine sources, the variable IO_x is used, which represents the sum of the measured IO and modelled I atom mixing ratios. IO_x rather than IO is used as this allows potential links between variables to be elucidated without being obscured by the partitioning between I and IO, which is essentially dependent on O_3 and radiation.

Unfortunately, measurements of other reactive iodine species such as OIO and I_2, targeted by twilight and night-time measurements with the LP-DOAS instrument, could not be observed above the detection limits (2.2 and 10 pptv respectively).

5.2.3.2 Halocarbons

Halocarbons can act as important sources of reactive iodine to the marine boundary layer in coastal regions, however, they are not believed to be the major source in the remote ocean, where inorganic precursors have been found to contribute over 50 % to the production of IO (Mahajan et al., 2010a). However, in tropical locations where deep upwelling regions occur, the transport of the longer lived halocarbons (as opposed to inorganic halogenated species) could provide a source of halogens to the upper troposphere–lower stratosphere (UTLS) region.

One such compound is CH_3I which has a lifetime at the equator of approximately two days and therefore is not considered to be a major contributor to reactive iodine in the MBL. However, it can be transported up to the UTLS region where it becomes the major contributor to IO_x (Ordonez et al., 2012; Saiz-Lopez et al., 2012).

Samples of CH_3I were taken during May and June 2011 at the site in Isabela and mixing ratios were found to vary between 0.6 to 5.4 pptv with an average during that period of 1.83 ± 1.05 pptv (1σ standard deviation). These are significantly higher than those reported in a previous campaign at San Cristobal in 2004 (Yokouchi et al., 2008) where mixing ratios were found to vary from 0.53–2.55 pptv with a yearly average of

1.13±0.37 pptv (the average for May–June 2004 was 1.2 pptv). The earlier measurements are in good agreement with the open ocean measurements recorded during the HaloCAST-P cruise whilst crossing the equator in April 2010 (Mahajan et al., 2012). There is only one previous study which reports open ocean CH_3I measurements, where mixing ratios of up to 3 pptv were observed in the South Atlantic near the coast of Argentina (Arnold et al., 2010; Lai et al., 2011). These high values were attributed to increased phytoplankton activity and high Chl-*a* concentrations.

Previous studies have suggested a correlation between gaseous CH_3I with SST and Chl-*a*. However, the differences in SST (~2°C warmer) and Chl-*a* (~20 % lower in 2011) based on MODIS-A measurements south of Galapagos in May-June 2004 and 2011 do not agree with the linear relationships of CH_3I with these variables previously reported. Furthermore, no significant correlation is observed in the CHARLEX data set between CH_3I and open ocean Chl-*a* or exposure to Chl-*a*.

All these factors suggest a localised source of CH_3I. There is no significant correlation observed between CH_3I and wind speed or tidal height therefore influence of a local terrestrial or intertidal source can be rejected. An interesting feature in the MODIS-A Chl-*a* data shows periodically enhanced biological activity in a narrow strip (~10 km wide) along the Southern coast of Isabela with an average Chl-*a* concentration of 0.4 ± 0.2 mg m^{-3} and a maximum of 1.6 mg m^{-3} during the CHARLEX campaign. Indeed, this could be observed at times along the beach at Puerto Villamil, where significant green algal deposits would appear at the tide lines. The Chl-*a* fields around San Cristobal are shown to be much weaker and therefore the increased CH_3I observed at Isabela compared to CH_3I could be attributed to this increased biological activity.

Unfortunately, due to the long time elapsed between sample collection and analysis (around 4–5 months) it was not possible to obtain mixing ratios for the more photo-labile halocarbon species such as CH_2I_2.

5.2.4 Ancillary Measurements

Ozone VMRs observed during both campaigns were generally low (< 32 ppbv) which was to be expected for such a remote marine location. The seasonal cycle of ozone can be seen to be driven by SST; evaporation of H_2O from the ocean reacts with O^1D to reduce ozone production. The lowest VMRs are observed in the warm season, when the water vapour also peaks, with values of a few ppb and sometimes even below the detection limit (DL) of the ozone monitor.

Daily O_3 does not show a photolytic profile as has been observed during previous campaigns over the open ocean (e.g. Read et al., 2008), except for limited depletion in October 2010 (2.5 ppbv) plus night time depletion due to NO in January-April 2011 and 2012. This phenomenon is isolated to the more populous islands where there are increased emissions of NO_x due to activities such as fishing, tourism, shipping and local fossil fuel plants. During warm season nights NO_x is emitted into slow moving air masses with negative meridional component (i.e. flowing from north to south) which reach the detector depleted in O_3. In the morning NO_2 photolysis initiates O_3 production but simultaneously wind strength increases from the south bringing fresh open ocean air. Therefore the O_3 measurements were filtered by setting NO_x and wind speed thresholds (200 ppt, 1 ms^{-1}) to remove these localised effects.

The particle measurements recorded at the meteorological station Puerto Baquerizo are typical of a background rural site. The instrument was located away from local influences - roads were located 160 and 400 m away downwind of the measurement site. However, particles related to rural activities during daylight hours (i.e. 6.00–18.00 local time) could contribute to the observed background aerosol levels. New particle formation events were observed at this site with the peaks in particle concentration at 3500 cm^{-3} (3–9 nm) and 5000 cm^{-3} (< 3 nm) coinciding with winds arriving from the South East. These winds travel over a densely wooded part of the island and therefore the particle bursts are thought to be associated with secondary organic aerosol (SOA) formation from organic compounds released by vegetation. Particle concentrations were much smaller when the air was arriving from the south and south-west, passing over a much more barren strip of land. Particle measurements at La Loberia, sampling

oceanic air, showed no evidence of new particle formation, with average total particle numbers of 400-500 cm^{-3}, typical of a coastal clean environment (Brechtel et al., 1998; Heintzenberg et al., 2000). The particle concentrations were found to be independent of solar radiation, wind direction and all other meteorological variables. This adds to the evidence that the observed new particle formation events at the meteorological station were caused by SOA. Previous modelling work (Mahajan et al., 2010a) suggested that IO mixing ratios of around 10 pptv would be required to produce new particles of 20 nm diameter (large enough that they would be likely to survive to form CCN), whereas the MAX-DOAS observations reported here are more than an order of magnitude smaller than this, and therefore halogen driven new particle formation will not be important at this location.
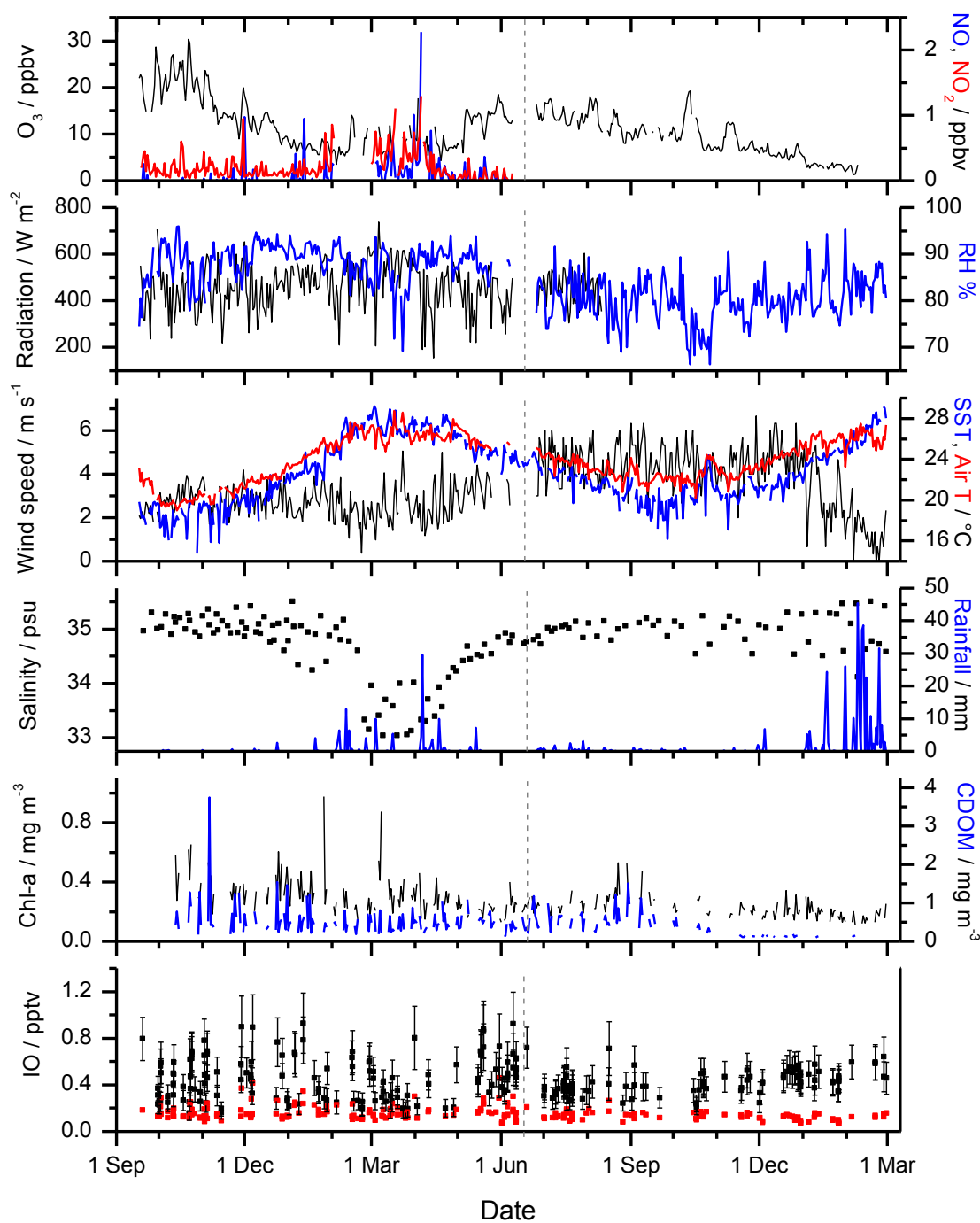
Figure 5.10 Full time series of daily averaged data over entire measurement period. From top to bottom: a) O_3, NO and NO_2 mixing ratios from in situ instruments; b) average global radiation and relative humidity; c) wind speed, MODIS-A sea surface temperature and in situ air temperature; d) salinity (from ARGO floats) and in situ accumulated rainfall; e) MODIS-A sea surface Chl-*a* and CDOM; f) MAX-DOAS IO quality filtered VMRs (assuming a height of 1000 m) with detection limits in red. The data before the dashed lines were collected at the measurement site on Isabela Island and those after are from San Cristobal.

5.2.5 Correlation of IO_x Measurements with Oceanic Variables

Due to the sparseness of the MAX-DOAS data after quality and cloud filtering, the measurements cannot be used to make conclusions on the daily or weekly variability of IO. However, the data are sufficient for investigating the monthly and seasonal variability of reactive iodine mixing ratios and the influence of ocean variables. The MAX-DOAS data should not be influenced by local effects such as the shielding of wind speed at Puerto Villamil due to the presence of the small islets. As a consequence of the cloud filtering of the MAX-DOAS data, correlations will only reflect measurements recorded during clear sky conditions, therefore any variations in ocean variables occurring during cloudy sky conditions will not be reflected in the correlations obtained. However, the sampling of measurements was found to be fairly homogeneous over the course of the campaign at both measurement sites, even after filtering.

A correlation analysis was carried out between the reactive iodine mixing ratio time series and available in situ and satellite data. It should be noted that the I atom data used in the correlation analyses were calculated via IO_x concentrations, inferred from the MAX-DOAS IO data using the relationship previously described by Mahajan et al. (2012). Time series of Chl-*a* CDOM and SST were averaged in a box defined by the coordinates 5.97–0.97^o S x 93.48–88.48^o W where most of the one day long back trajectories were contained. A larger box was used for the salinity data to account for the poorer sampling available from the ARGO drifting floats.

5.2.5.1 Shorter-term Variability

To remove any influence of the short term variability in contiguous data points and seasonal variability a Fast Fourier Transform (FFT) band-pass filter was applied with higher and lower cut off frequencies of 0.2 and 0.0167 day^{-1}, respectively. Pearson correlation coefficients were then calculated for the filtered data for the entire measurement period and for each measurement site separately. The only significant correlation of the high-pass filtered entire data series was with satellite SST (R = 0.3,

p = 0.001) and air temperature, with a similar but less significant correlation also observed for I atoms and IO_x.

Looking at each site separately, this picture changes completely. At the Isabela measurement site using the IO measurements, no significant correlations are observed, whereas the IO data from San Cristobal shows significant correlation with SST (R = 0.48, p = 0.001) and with air temperature (R = 0.51, p < 0.001). This correlation is also strong for the high-pass filtered I atom and IO_x data. The larger variability of the IO data from Isabela may be due to more variable mixing in the boundary layer or to intermittent emissions of very short lived iodocarbons from periodic episodes of increased biological activity in the narrow strip south of the island, as mentioned in the previous section.

There is a distinct lack of correlation between the observed IO_x and exposure to Chl-*a*, which is consistent with the minor contribution of CH_3I to IO_x as estimated previously. However, the Chl-*a* fields south of Galapagos are fairly homogeneous along the track of the air mass trajectories and only show an obvious enhancement at more than six days upwind of the Archipelago.

5.2.5.2 Longer-term Variability

For analysing any month to month or seasonal patterns, the low-pass FFT filter (as defined above) was applied to the daily averaged time series. Once the IO mixing ratios were smoothed in this way an anti-correlation with radiation (R = -0.65, p < 0.001) and Chl-*a* (R = -0.35, p < 0.001) was determined, whereas a positive correlation was observed for salinity (R = 0.50, p < 0.001). I and IO_x were found to be anti-correlated to O_3, which dominates the variability of these species over that of IO itself, and follow the seasonal cycle of O_3 with a 180° phase shift. No strong correlation was observed for either relative humidity or SST. I atoms were shown to be weakly correlated to radiation (R = 0.31, p = 0.003) in contrast to IO, and there was anti-correlation of I and IO_x with Chl-*a* and CDOM.

Looking at the Isabela data separately an anti-correlation of IO_x with the O_3 cycle can be observed and a correlation with relative humidity and wind direction. The IO

correlation with salinity and anti-correlation with radiation and Chl-*a* becomes stronger, and a strong correlation with wind speed becomes apparent (R = 0.74, p < 0.001). There is also a distinct negative correlation of IO with SST.

Using only the San Cristobal data there is an even stronger anti-correlation of IO with O_3 (R = -0.83, p < 0.001). I and IO can be seen to grow in parallel along with a continuous decrease in the O_3. They show a positive correlation with SST and a negative correlation with Chl-*a* and CDOM. Radiation data was not available for this period of the campaign and there is no significant change in salinity during this time.
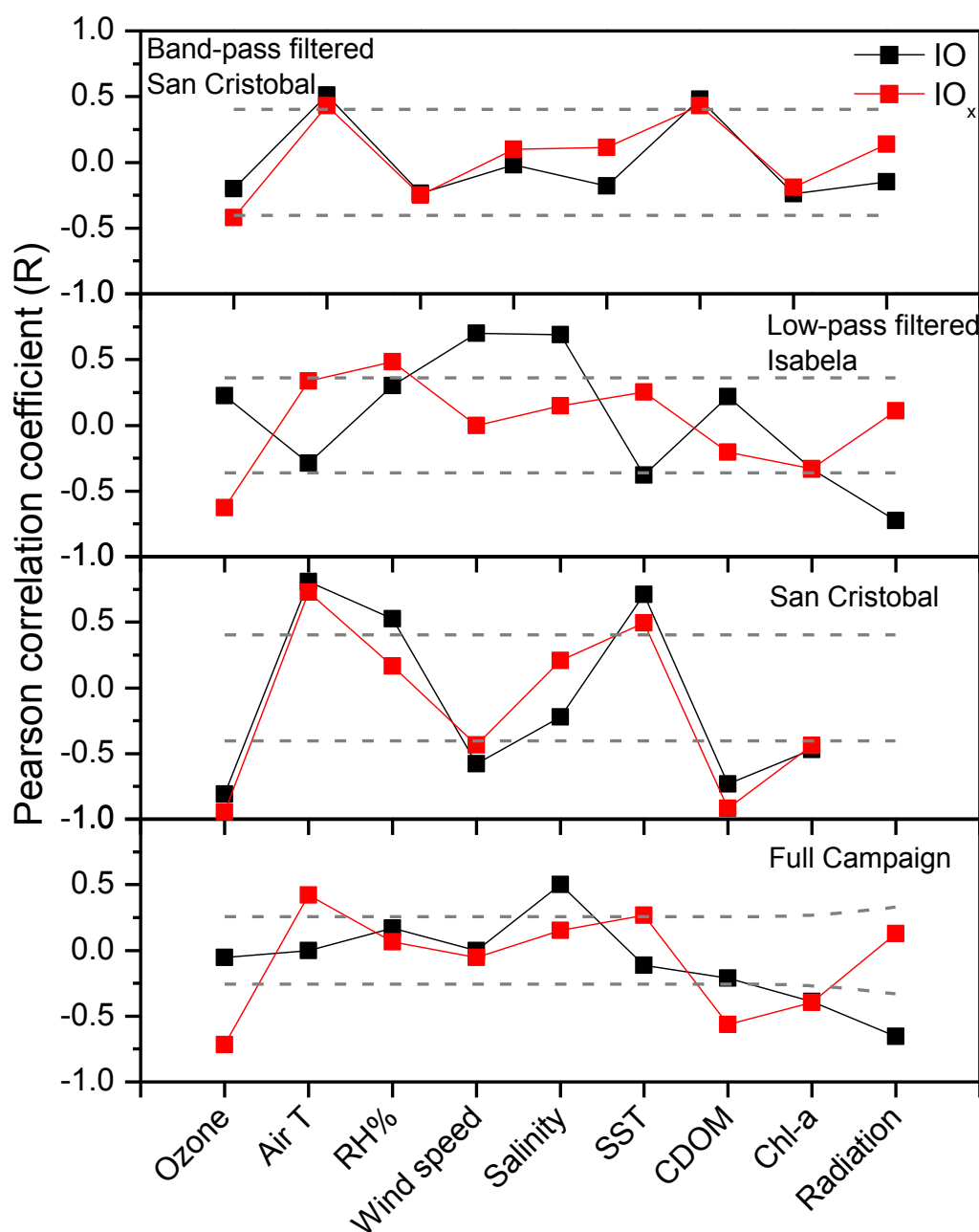
Figure 5.11 Pearson correlation coefficients for IO (black) and IO$_x$ (red) VMRs with meteorological and ocean physical variables. From top to bottom: band-pass filtered data for San Cristobal only; low-pass filtered data for Isabela only; low-pass filtered data for San Cristobal only; low-pass filtered full data set. The grey dashed lines show the 99 % confidence intervals on the correlations.

5.2.5.3 Mechanism of Iodine Emission

As a consequence of the many mutual correlations between different variables, conclusions about the mechanisms of reactive iodine emissions are difficult to make. The differences observed between the two measurement sites, especially with regards

to SST and salinity indicate that there are multiple factors influencing the emission rate. Several mechanisms have been proposed for the release of reactive iodine compounds into the MBL from surface seawater as discussed in Chapter 2 and include production of iodinated hydrocarbons by marine organisms such as phytoplankton or alternatively abiotic sources including photochemical production or, as discussed in Chapter 3, the reaction of O_3 deposited to the sea surface with iodide in the surface layer to release I_2 and HOI.

At San Cristobal, the positive correlation of IO and IO_x with SST could be a consequence of increased sea-air emission of reactive iodine precursors or an increased rate of production in the ocean surface. The decoupling of the IO and IO_x seasonal trend to that of SST at Isabela where no correlation is observed for IO_x and a negative correlation is observed for IO could be due to changes in salinity and/or radiation. The minimum in IO observed during February–April 2011 coincides with a minimum in both salinity and radiation. Higher radiation would result in a shift of the I/IO balance towards I and an increased rate of formation of IO_x from photolysis of reactive iodine precursors and also possibly the production rates of those precursors.

To best describe the seasonal trends in the IO_x data, the SST and salinity data must be combined. A multiple linear regression of the low-pass filtered IO_x mixing ratios against SST and salinity gives a much improved correlation ($R^2 = 0.34$) compared to each of the variables individually ($R^2 = 0.01$ for SST and $R^2 = 0.03$ for salinity). Corresponding expressions for the resulting IO_x from changes in these two variables can then be defined as 0.075 ± 0.010 pptv $°C^{-1}$ for SST and 0.40 ± 0.05 pptv psu^{-1} for salinity. The average monthly IO and IO_x for the whole campaign are compared with those of SST (from satellite data) and salinity (ARGO floats) in Figure 5.12.
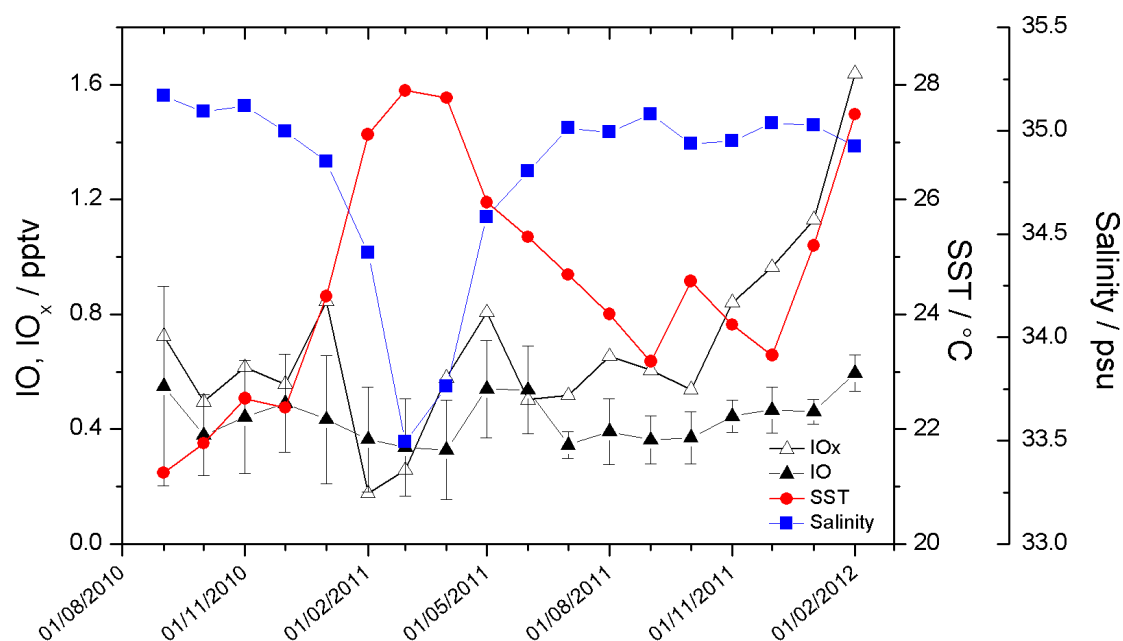
Figure 5.12 Monthly averaged MAX-DOAS IO VMRs (solid black triangles) and IOx derived from expression in Mahajan et al. (2012) (open black triangles). Monthly averaged MODIS-A SST (red circles) and salinity (blue squares) for the region to the south of Galapagos as indicated by the bold black outlined box in Figure 5.8.

The salinity in the waters surrounding the Galapagos is influenced by the various movements of currents converging at this point in the ocean (described in section 5.2.1, previously). A shift in the ITCZ downwards during the warm season (January–June) results in lower salinity waters surrounding the Galapagos islands due to a shut-down of the equatorial upwelling and water being advected southwards from the less saline Northern Hemisphere (Donguy and Henin, 1980; Pak and Zaneveld, 1974). In addition, the increased rainfall associated with this shift in ITCZ during the warm season results in dilution at the ocean surface (Donguy and Henin, 1980). The cessation of the equatorial upwelling would be expected to enhance the reduction of Iodate to iodide close to the surface and hence increase the emission of reactive iodine to the MBL, causing a negative correlation between IO_x and salinity (Truesdale et al., 2000; Truesdale and Bailey, 2002).

However, the decrease in salinity due to advection of Northern Hemispheric waters may also be indicative of reduced iodide availability in the surface waters. This decrease in iodide could explain the decrease in IO_x observed, as the reaction of O_3

deposited to the ocean surface with iodide in the surface layer acts as a source of reactive iodine (in the form of I_2 and HOI) to the atmosphere. Currently, measurements of iodide in surface oceans are fairly sparse and the only measurements available in this region are those of Elderfield and Truesdale (1980) recorded during a ship cruise in 1976. These data show nearly a factor of two higher iodide concentrations in the waters of the Peruvian upwelling region compared to those surrounding the Galapagos Islands during the warm season.

The anti-correlation observed for IO and IO_x with Chl-*a* and CDOM suggests an inhibiting role of biological activity, although this may be due to its association with the upwelling of cold waters and therefore is anti-correlated to SST seasonally. In any case, an emission mechanism which is dependent upon the availability of Chl-*a* is unlikely to be operating in this region, which points to the greater importance of the inorganic I^- + O_3 reaction in supplying reactive iodine species to the atmosphere. Another possible reason for the negative correlation of IO and IO_x with Chl-*a* and CDOM is the possibility of organic films forming on the surface of the ocean (associated with biological activity) which may inhibit the release of reactive iodine species from the sea surface layer to the atmosphere (Rouviere and Ammann, 2010).

5.2.6 Comparison with Satellite and Previous Open Ocean Data

The IO measurements at Galapagos are consistent with those measured during the HaloCAST-P cruise which took place in March/April 2010 with the cruise track running from Punta Arenas in southern Chile, North to Seattle, USA (Mahajan et al., 2012). These measurements are consistent with the observations of low iodine loading in the marine boundary layer of the Pacific ocean and also show a correlation with SST and salinity (albeit with a very small slope) and an anti-correlation with Chl-*a*, again backing up the suggestion of an "inorganic" mechanism playing the major role in reactive iodine emissions over the ocean. At the equatorial crossing point during the cruise the IO mixing ratio, assuming a 1000 m layer height, was 0.4±0.2 pptv (IO_x = 0.7±0.2 pptv) which compares well with the monthly average for April observed in Galapagos of 0.33±0.17 pptv (IO_x = 0.7±0.4 pptv) and the maximum during this period of 0.57 pptv

(IO_x = 1–2 pptv). Both salinity and SST were higher during the HaloCAST-P measurement period in April 2010 compared to the Galapagos in April 2011 which may explain the slightly higher mixing ratios observed.

By merging the IO_x daily averages observed during the HaloCAST-P cruise and the monthly averages from Galapagos, a strong linear correlation is found between the IO_x and SST (R^2 = 0.60, p < 0.001) and between SST and IO itself. The addition of a salinity term to the correlation analysis does not improve the fitting of the IO and IO_x data. The link between the SST and reactive iodine loading, however may not be a direct effect such as an increase in the rate of emission or production of reactive iodine precursors, but could be related to the change in iodide in the surface waters. As shown in Figure 5.13 the iodide shows a gradual increase when moving from the mid-latitudes towards the equator in the Pacific Ocean which correlates well with the observations of IO and IO_x. An increase in iodide has been shown to lead to increased emissions of both I_2 and HOI into the gas phase, which would lead to increased IO and IO_x following photolysis during daylight hours. Further modelling of this mechanism is discussed in Chapter 6.

As well as the ship-based measurements, ground-based measurements at Cape Verde in the tropical Atlantic ocean have also been performed using the same LP-DOAS and MAX-DOAS instruments as used in the Galapagos campaign (Read et al., 2008) and showed somewhat higher IO mixing ratios of 1.4±0.8 pptv, in contrast to the observations in Galapagos where IO was not observed by the LP-DOAS instrument above the detection limit of 0.9 pptv. The observations during the Cape Verde campaign which ran from November 2006 to June 2007 did not show any seasonal variability over and above the instrument uncertainty. In this region, higher mixing ratios of O_3 will result in most of the IO_x being in the form of IO. The SST range observed during the November 2006 – June 2007 period was narrower (19–24 °C) than that during the Galapagos measurement period (19–28 °C) and the salinity at this time was higher at 36.4 psu. This may explain the higher and more constant IO_x values observed.

A further ship-based campaign was conducted in the Western Pacific during October 2009 as part of the TransBromSonne cruise from Tomakomai, Japan to Townsville, Australia, where measurements of IO were recorded using the MAX-DOAS technique (Großmann et al., 2012). A similar latitudinal distribution is observed as seen in the Eastern Pacific cruise with higher mixing ratios of IO observed closer to the equator (up to 2.2 pptv) and lower values (around 1 pptv) observed in the mid latitudes. In addition, the retrieved profiles suggested that the majority of the IO was contained in the lowest part of the marine boundary layer (< 300 m altitude). As was concluded during the Cape Verde and Eastern Pacific campaigns, the observed IO mixing ratios cannot be explained using the concurrent iodocarbon fluxes measured during the campaign, and an additional reactive iodine flux was required to model the observations. Attempting to convert the IO observations into IO_x using the same principle as employed previously for the Eastern Pacific data set is not so straight forward as the reported ozone measurements are much lower.

Earlier campaigns in Tenerife and Tasmania (Allan et al., 2000) (representative of open ocean sites) are also in agreement with the observations in Galapagos. The measurements in Tenerife gave an average IO mixing ratio of 1.23 pptv, whereas the detection limit for the open ocean measurements in Tasmania (a location with colder ocean waters) gave an upper limit for IO of 0.38 pptv.

Satellite measurements of IO retrieved from the SCIAMACHY satellite instrument have been reported (Schonhardt et al., 2008) from 2005 with monthly average IO columns of up to 8×10^{12} cm^{-2} observed (detection limit 3–7 $\times 10^{12}$ cm^{-2}). However, the retrieval of these columns was highly sensitive to the fit settings due to the poor signal to noise ratio of the spectra, and the authors advise caution when using the data. Subsequent publications show a time series of IO columns retrieved from 2005 to 2007 where the data is spatially averaged (5°N–10°S, 80°W–100°W) plus the daily averaged IO columns. The average IO column for this time period is around 3×10^{12} cm^{-2} with a standard deviation of 4×10^{12} cm^{-2} and a maximum of 8×10^{12} cm^{-2}. The monthly averages range from around 2–4 $\times 10^{12}$ cm^{-2} with no significant seasonal variation discernible from the data. Assuming a unit air mass factor so that the slant column is equal to the vertical column density and using a box profile height of 1 km the average slant columns of

3×10^{12} cm^{-2} convert to a mixing ratio of 1.4 pptv. This is around a factor of two higher than the highest IO mixing ratios recorded in Galapagos, and around a factor of three higher than the monthly averaged IO.

In addition to this, as the IO most likely shows a decreasing vertical profile moving upwards through the boundary layer, the actual surface mixing ratios would be much larger than 1.4 pptv, and well above the detection limit of 0.9 pptv for the LP-DOAS instrument. The spatial distribution of the IO measurements from the satellite also does not match those of the HaloCAST-P cruise and so it can be concluded that the field measurements of IO are not consistent with those of the satellite. It should be noted, however, that the satellite measurements would be sensitive to any IO which may be located higher up in the free troposphere. Recent airborne MAX-DOAS observations of IO in the free troposphere over the Pacific ocean around Hawaii found that up to two-thirds of the observed VCDs arose from IO above the MBL (~800 m) (Dix et al., 2013). In addition, MAX-DOAS measurements at a mountain site in Tenerife also showed elevated levels of IO in the free troposphere (0.2–0.4 pptv), possibly associated with Saharan dust input (Puentedura et al., 2012).

5.2.7 Link to I⁻ in Surface Seawater

Due to the link between the surface iodide concentrations and measured IO$_x$ observed during the CHARLEX campaign, further investigation into this correlation was then carried out. There have been a number of studies where surface sea water iodide concentrations have been measured, and these findings are summarised in Figure 5.13 (courtesy of Rosie Chance, University of York). As can be seen, the surface iodide concentrations show a clear latitudinal distribution with higher concentrations at the tropics and in coastal regions and lower concentrations at mid and high latitudes (especially in the Southern Hemisphere) with concentrations ranging from 0 up to around 300 nM.
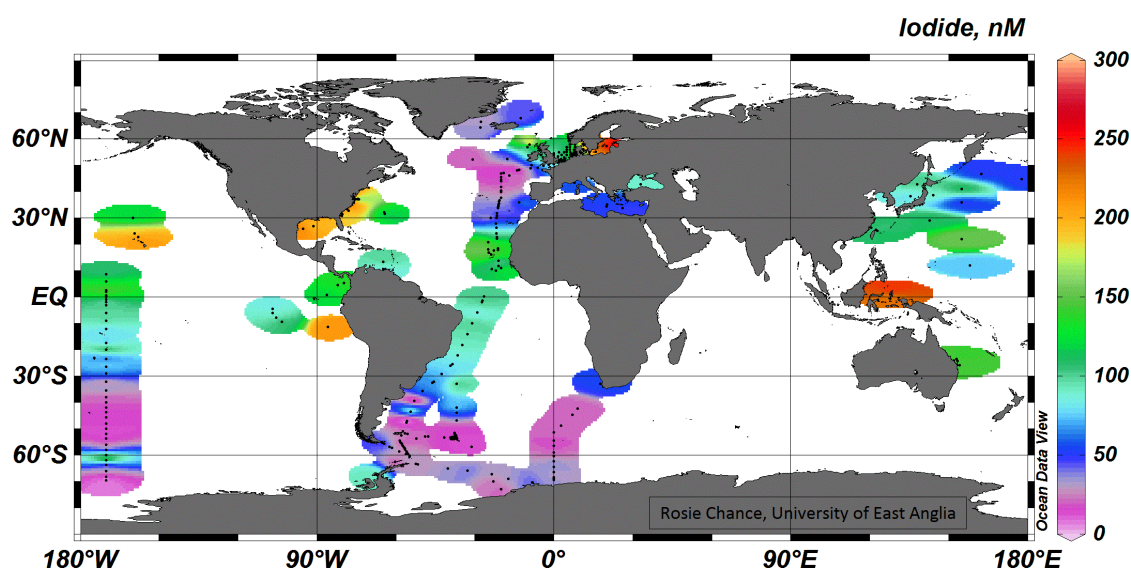
Figure 5.13 Global surface seawater iodide concentrations in nM. Black dots show the actual point of measurements with the colours derived from simple interpolations using Ocean Data View (courtesy of Rosie Chance, University of York, 2012).

Measurements of IO recorded at open ocean locations including those during the HaloCAST-P cruise and CHARLEX campaigns and previous measurements from campaigns in Cape Verde (Read et al., 2008), Tenerife (Allan et al., 2000) and Tasmania (Allan et al., 2000) were plotted against surface seawater concentrations of iodide recorded during cruises in the Atlantic (Truesdale et al., 2000) and Pacific (Huang et al., 2005; Nakayama et al., 1989; Tsunogai and Henmi, 1971). The IO_x concentrations were also computed based on the expression derived by Mahajan et al. (2012) for the IO/I ratio and the measured O_3 where available.
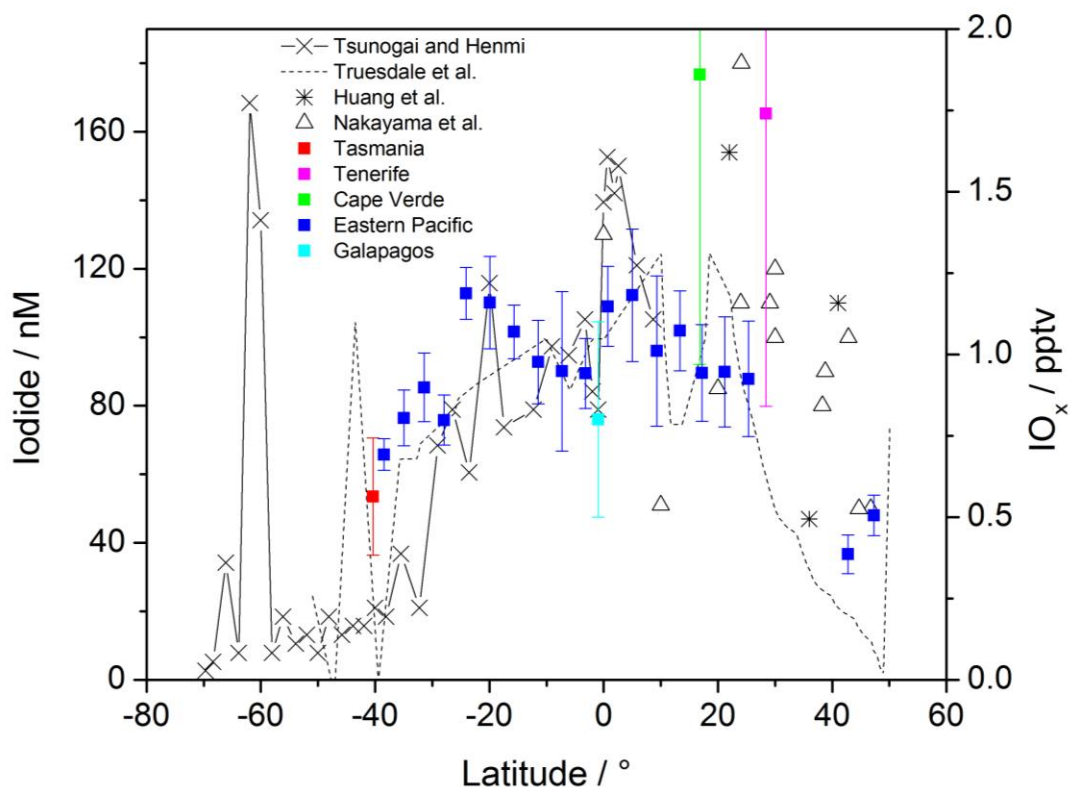
Figure 5.14 Iodide (nM) from both the Atlantic (Truesdale et al., 2000) and Pacific (Huang et al., 2005; Nakayama et al., 1989; Tsunogai and Henmi, 1971) and IO_x (pptv) from the HaloCAST-P cruise and previous DOAS measurements in open ocean locations plotted against latitude.

The observed IO and IO_x measurements appear to match well with the measurements of iodide in both the Atlantic and Pacific surface waters suggesting that the $I^- + O_3$ mechanism may be the most significant source of reactive iodine over the oceans. Correlation coefficients were calculated between the HaloCAST-P cruise and the Pacific iodide data from Tsunogai and Henmi (1971) with a significant R = 0.67 and using the Atlantic iodide data the correlation is even stronger with R = 0.78. The correlation plots are shown in Figure 5.15.
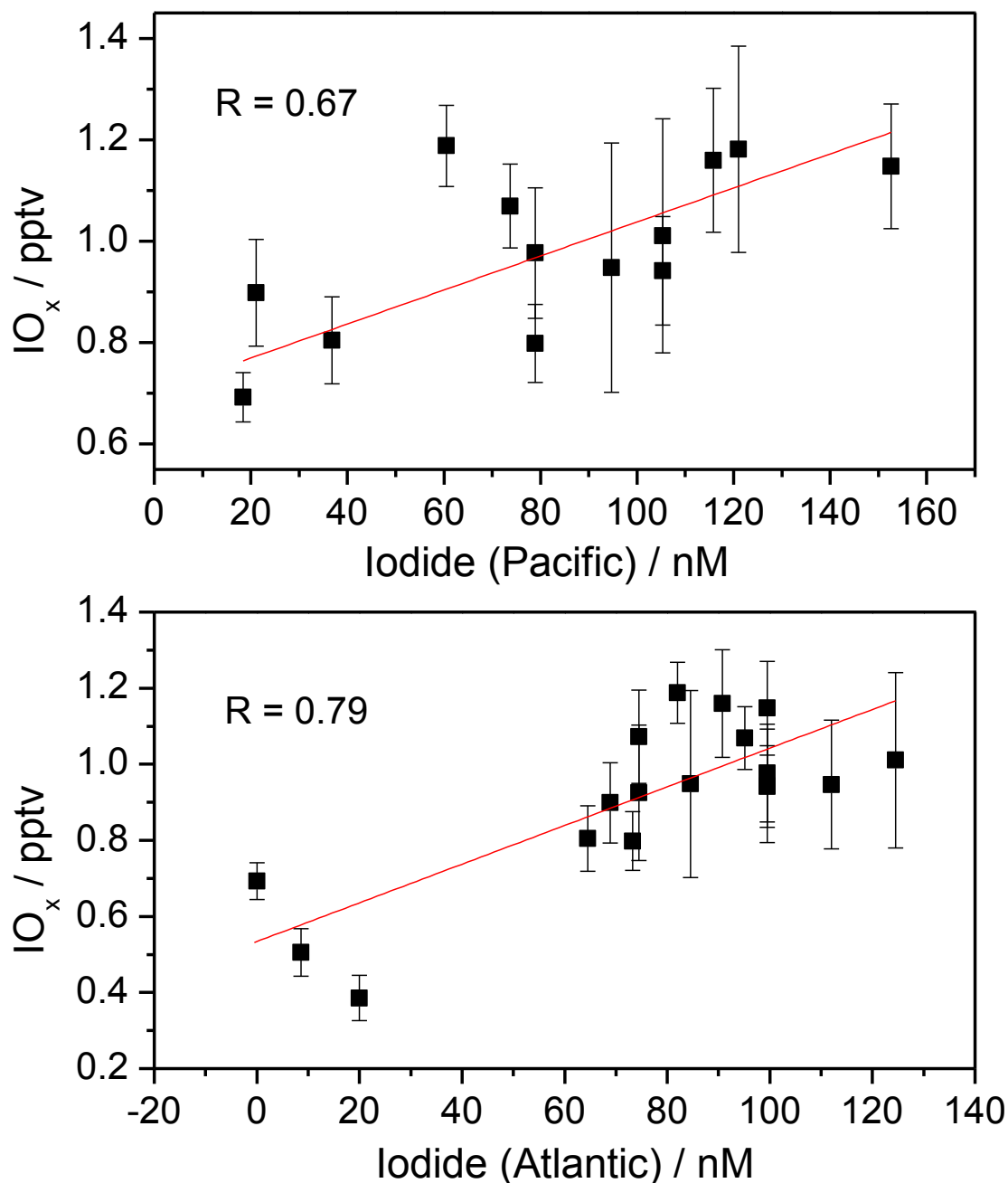
Figure 5.15 Correlation plots for IO_x from the HaloCAST-P cruise and iodide measurements from a) the Pacific (Tsunogai et al. 1971) and b) the Atlantic (Truesdale 2000).

Using the surface iodide measurements, along with SST and salinity measurements, a multiple linear regression analysis was performed on the IO_x HaloCAST-P data. This gave an R^2 value of 0.81 (R value of 0.91) for the multiple linear regression, compared to individual R^2 values of 0.69, 0.41 and 0.61 for SST, salinity and iodide respectively and coefficients of 0.038 pptv $°C^{-1}$, 0.026 pptv psu^{-1} and 9.5 x 10^{-4} pptv nM^{-1}.

Further discussion and modelling of this mechanism using the 1D chemistry-transport model THAMO and the flux expressions derived for I_2 and HOI from Chapter 4 is presented in Chapter 6. The model results are compared with the available field measurements from open ocean locations and the atmospheric impacts are discussed.

Chapter 6

Modelling the Inorganic Iodine Flux

To link the experimental measurements of the inorganic iodine flux to field measurements of reactive iodine species in the marine boundary layer, the 1-D chemistry-transport model THAMO was employed. In the first part of the chapter the model itself is described, including recent updates to the iodine oxide particle growth scheme, and the derivation of the parameterised I_2 and HOI fluxes. The model is then used to explain the variability in observations of IO and IO_x over the oceans in relation to the flux of inorganic iodine.

6.1 The Tropospheric HAlogen chemistry MOdel – THAMO

The Tropospheric HAlogen chemistry MOdel (THAMO) was first developed by Saiz-Lopez et al. (2008) to interpret field measurements of halogen species in the coastal Antarctic boundary layer. The model was later developed to include a full description of iodine oxide particle formation and has been used to validate results from several field campaigns in a range of environments including tropical, mid-latitude and polar locations (Gómez Martín et al., 2013; Mahajan et al., 2009b; Mahajan, 2010; Mahajan et al., 2010b; Saiz-Lopez et al., 2008). The model utilises a multistep implicit explicit (MIE) integration routine (Jacobson, 2005) coupled to a vertical diffusion routine (Shimazaki, 1985) and a dynamic particle production and growth code (Jacobson, 2005).

There are four main components to the model:

1. A chemical scheme that includes photochemical, gas phase and uptake reactions using the MIE procedure.

2. A 1-D transport module using vertical eddy diffusion

3. A radiation scheme that calculates solar irradiation as a function of altitude, wavelength and solar zenith angle (SZA).

4. A particle formation and growth module.

Each of these components is described in detail in the following sections.

6.1.1 The Chemistry Scheme

The MIE routine is a positive-definite, mass conserving, unconditionally stable iterative technique. It achieves this through use of the explicit forward Euler (mass conserving but positive-definite only for short time steps) and implicit backward Euler (positive-definite but not mass conserving) schemes without the need for much more computer time. Concentrations of chemical species are estimated using the iterative backward Euler and are applied to reaction rates in the forward Euler scheme. Upon iteration, the forward Euler converges to the backward Euler; as the backward Euler is always positive then the forward Euler will converge to a positive value and upon iteration with the backward Euler will produce values which are mass conserving. A convergence factor defines the number of consecutive iterations required so that both forward and backward Euler estimates are positive; in the case of THAMO this has a value of 20 and gives an error of < 1 %.

The continuity equations for describing the concentration N_i of a species i at time t and altitude z is given by Equation 6.1:

$$\frac{\partial N_i}{\partial t} = P_i - L_i - \frac{\partial \phi_i}{\partial z} \qquad (6.1)$$

where P_i and L_i are, respectively, the production and loss rates for the backward Euler scheme and ϕ_i is the vertical flux of species i due to eddy diffusion.

The equations are solved using an integration time step of 2 minutes which is a compromise between computational efficiency and compliance with the Courant-Levy criterion (Courant et al., 1928). The model consists of 200 stacked boxes, representing

a boundary layer height of 1 km in the tropics with 5 m resolution. At the lower boundary, deposition of species i may occur, or a flux of i into the bottom box.

The chemical production and loss rates for a trace gas species i are given by:

$$P_i = \sum_{l=1}^{N_{prod,i}} k_{j,k}(l,i) N_j N_k + \sum_{l=1}^{N_{phot,i}} J_m N_m \qquad (6.2)$$

$$L_i = \sum_{l=1}^{N_{loss,i}} k_{i,j}(l,i) N_j + \sum_{l=1}^{N_{phot,i}} J_i \qquad (6.3)$$

The production and loss terms are calculated at every iterative time step in the MIE routine.

The full chemistry scheme for iodine chemistry as described in Mahajan (2009) is employed. These reactions are used to calculate the production and loss rates as described above.

In addition to the gas phase reactions, THAMO also treats heterogeneous chemical processes through uptake onto aqueous aerosol. Because the modelling studies are conducted for the marine boundary layer this is assumed to be sea-salt aerosol. Uptake and hydrolysis of HOX, $XONO_2$ and XNO_2 onto sea salt aerosol gives $HOX_{(aq)}$ as described in Chapter 2. The $HOX_{(aq)}$ is then processed to produce XY via reaction with Y^- and this takes around 10–15 minutes in fresh sea-salt aerosol (McFiggans et al., 2000). Due to the low solubility of XY it is rapidly released into the gas phase and hence, it is assumed that uptake of inorganic iodine species onto aerosols is the rate-limiting step in these recycling reactions (McFiggans et al., 2000). There is a depletion of Y^- in aged aerosol, leading to a lengthened processing time, however, their increased acidity due to HNO_3, H_2SO_4 and SO_2 uptake will increase the processing rate (von Glasow et al., 2002).

The aqueous phase chemistry in the bulk phase of the aerosol is not treated explicitly in THAMO. In the model it is assumed that the rate limiting step for halogen heterogeneous recycling on aerosol is the first order rate of uptake using uptake

coefficients for each of the relevant gaseous species. The total uptake is then computed using the volumetric aerosol surface area (ASA) and a free molecular transfer approximation (Fuchs, 1964). The ASA used in the model is taken from field observations for the respective field campaigns and for simplicities sake, the ASA and humidity are considered to be constant in each of the vertical levels of the model.

In addition to uptake on aerosol, dry deposition to the ocean surface is included in the lowermost box and is applied to most of the soluble halogen species as well as nitrogen oxides and O_3. The dry deposition flux (F_d) for each individual species, i, is given by Equation 6.4:

$$F_d = V_{di} N_i \tag{6.4}$$

where V_{di} is the deposition velocity and N_i is the concentration of species i. For the sake of simplicity the ocean is taken to be a flat surface.

6.1.2 Vertical Transport

The vertical flux due to eddy diffusion (the final term in Equation 6.1) is defined as:

$$\phi_i = K_z \left(\frac{\partial n_i}{\partial t} + \left(\frac{1}{T} \frac{\partial T}{\partial z} + \frac{1}{\overline{H}} \right) n_i \right) \tag{6.5}$$

where T is the temperature at altitude z, $\overline{H}$ is the scale height of the atmosphere (as defined in Chapter 1) and K_z is the eddy diffusion coefficient which is a function of time t and height z. At the surface turbulence is predominantly generated by wind shear and can be described by Monin-Obhukov similarity theory. From this a function for the eddy diffusion coefficient can be derived (Stull, 1988):

$$K_z(z,t) = \kappa z u_*(t) \tag{6.6}$$

where κ is the von Karman constant (0.4) and $u_*(t)$ is the surface friction velocity. In the case of the stable BL, the surface friction velocity can be described to a good approximation by:

$$\frac{\kappa U_z}{u_*} = ln\left(\frac{z}{z_0}\right)$$

(6.7)

where U_z is the wind speed at height z and z_0 is the surface roughness length. The value for surface roughness length for the open ocean is taken from Jacobson (2005). One problem with K_z defined as in Equation 6.6 is that it is linearly dependent on z and therefore tends to zero at the surface. This implies that a gas released at a height $z = 0$ would never diffuse upwards which is clearly unrealistic. Therefore, for modelling purposes a surface condition is assumed such that this form of K_z is only valid for $z > z_0$ (Stull, 1988). Because the BL is a well mixed region of the atmosphere, photolysis rates, ASA and relative humidity were all considered to be constant with height.

6.1.3 Radiation Scheme

Photolysis rates for all chemical species in the model are calculated on-line using an explicit two-stream radiation scheme described by Thompson (1984). The photolysis rate J of a species i by a pathway I is defined as:

$$J_i^I = \int_{\lambda_1}^{\lambda_2} d\lambda F_{total}(\lambda)\sigma_i(\lambda,T)\Phi_i^I(\lambda,T)$$

(6.8)

where σ is the absorption cross section of species i at a wavelength λ and temperature T, Φ is the quantum yield or probability that molecule i will decompose via pathway I on absorption of light at wavelength λ and $F_{total}(\lambda)$ is the solar flux at wavelength λ. Due to the abundance of measurements of absorption cross sections and quantum yields for tropospheric trace gas species, the calculation of photolysis rates in the model reduces to calculating the UV-visible solar flux under relevant atmospheric conditions. The irradiation reaching the Earth's surface is computed after photons have been attenuated through 50 layers of 1 km each in the atmosphere as a function

of SZA, time of year and location. These layers are considered to be cloud free and the total overhead O_3 column abundance is used to filter the UV radiation reaching the surface.

The photolysis rates for individual species are then calculated by including albedo measurements from an actinic flux spectrometer co-located with the DOAS instruments.

6.1.4 Particle Formation and Growth

The final part of the model is the particle formation and growth scheme. As described in Chapter 2 there have been numerous measurements of particle bursts linked to increased emissions of reactive iodine species in coastal locations and in Antarctica. The exact mechanism of IOP formation, their growth behaviour in the presence of condensable vapours and their precise chemical composition are still uncertain, however, there have been a number of recent advances in this field.

Work by Saunders and Plane (2005) suggested that the most probable form of IOPs is I_2O_5 and the original particle scheme considered that particles were formed from polymerisation of I_2O_5 via the formation pathway described in Saunders and Plane (2005). This pathway involved the oxidation of I_2O_3 and I_2O_4 by O_3, however, although theoretical calculations indicate that these reactions are exothermic, they had not been studied experimentally. Here, it was assumed that the rate of I_2O_5 formation in the particle was the same as Saunders and Plane (2005), albeit in the gas phase. Once formed, the concentration was no longer calculated explicitly and subsequent evolution was described using a dynamic aerosol module. However, there have been more recent studies that have shown that I_2O_5 does not form in the gas phase, and its presence in IOPs may be due to condensation of other iodine oxides followed by formation of I_2O_5 in the particle phase: the work of Gómez Martín et al. (2013) suggests that the mechanism most likely proceeds from formation and dimerisation of I_2O_4 in the gas phase.

The aerosol module in THAMO is semi-implicit, volume conserving and uses a sectional approach to consider the two methods of particle growth: coagulation and condensation. Coagulation reduces the number of particles but conserves the particle volume whereas condensation results in an increase in the total particle volume but conserves the number. In the remote MBL condensation should be the more important form of particle growth as these regions will have a low initial I_2O_5 concentration for coagulation to occur.

The aerosol distribution is divided into 30 individual bins (N_B) where the bin spacing is determined by a volume ratio (V_{rat}) of 1.5. The first bin is assumed to be made up of I_2O_5 monomers and is coupled to the I_2O_5 in the gas phase to simplify the mechanism rather than using rearrangement of I_2O_4 dimers in the aerosol phase and subsequent release of I_2. The volume of the first bin is calculated using the known mass of I_2O_5 and the density of bulk I_2O_5, 4980 kg m^{-3}(Saunders and Plane, 2006). For the second bin onwards the centre volume for each bin is defined by the volume ratio:

$$V_i = V_{rat} \cdot V_{i-1}$$
(6.9)

There is assumed to be no thermodynamic barrier to homogeneous nucleation as single I_2O_5 molecules are used as the monomer and subsequent growth in the aerosol phase contains any multiple of I_2O_5 leading to compact polymers. In fact, fractal geometry plays a large role for particle diameters > 6–7 nm (Saunders and Plane, 2006), however, if particles deliquesce before they grow to this size, the fractal effect can be ignored because particles will be spherical.

To calculate changes in distribution resulting from the collision and coalescence of particles from smaller bins (resulting in fewer, larger particles) the semi-implicit, volume conserving technique described in Jacobson (2005) is employed. In this method for each collision between a particle in bin i and a particle in bin j an intermediate volume $V_{i,j}$ can be defined:

$$V_{i,j} = \upsilon_i + \upsilon_j$$
(6.10)

where υ_i and υ_j are the respective volumes of each particle in bin i and j. The fraction partitioned into the adjacent larger bins around bin k is determined by:

$$f_{i,j,k} = \begin{cases} \left(\dfrac{\upsilon_{k+1} - V_{ij}}{\upsilon_{k+1} - \upsilon_k}\right)\dfrac{\upsilon_k}{V_{ij}} & \upsilon \le V_{ij} < \upsilon_{k+1} & k < N_B \\[2em] 1 - f_{i,j,k-1} & \upsilon_{k-1} < V_{ij} < \upsilon_k & k > 1 \\[2em] 1 & V_{ij} \ge \upsilon_k & k = N_B \\[2em] 0 & others \end{cases} \qquad (6.11)$$

The total volume, V, in each bin k at time t is then given by:

$$V_{k,t} = \frac{V_{k,t-h} + h \displaystyle\sum_{j=1}^{k}\left(\sum_{i=1}^{k-1} f_{i,j,k}\beta_{i,j}V_{i,t}n_{j,t-h}\right)}{1 + h \displaystyle\sum_{j=1}^{N_B}\left(1 - f_{i,j,k}\right)\beta_{k,j}n_{j,t-h}} \qquad (6.12)$$

where h is the time step and n_i is the number of particles in bin i. This equation again is solved using a MIE routine in order to use the larger two minute time step as described previously. The total number of particles in each bin can be calculated easily using the section model, as the volume of all particles in a given bin is the same:

$$n_k = \frac{V_k}{\upsilon_k} \qquad (6.13)$$

The term β in Equation 6.12 is the coagulation rate coefficient (or kernel) and its value is calculated using Fuch's interpolation formula for the transition regime (Knudsen number, K_n ~1). The collision kernel for particles in bin i with bin j is given by:

$$\beta_{i,j} = \frac{4\pi\left(r_i + r_j\right)\left(D_{p,i} + D_{p,j}\right)}{\dfrac{r_i + r_j}{r_i + r_j + \sqrt{\delta_i^2 + \delta_j^2}} + \dfrac{4\left(D_{p,i} + D_{p,j}\right)}{\sqrt{\overline{v}_{p,i}^2 + \overline{v}_{p,j}^2} + \left(r_i + r_j\right)}} \qquad (6.14)$$

where r_i is the radius of the particles in bin i, δ_i is the mean distance from the centre of a sphere that a particle leaving its surface reaches when travelling one mean free path ($\lambda_{p,i}$). $D_{p,i}$ is the diffusion coefficient and $v_{p,i}$ is the thermal speed of the particle in air. These values can be calculated from the well known expressions below:

$$\delta_i = \frac{\left(2r_i + \lambda_{p,i}\right)^3 - \left(4r_i^2 + \lambda_{p,i}^2\right)^{3/2}}{6r_i\lambda_{p,i}} - 2r_i \qquad (6.15)$$

$$\lambda_{p,i} = \frac{8D_{p,i}}{\pi\overline{v}_{p,i}} \qquad (6.16)$$

$$\overline{v}_{p,i} = \sqrt{\frac{8k_BT}{\pi\overline{M}_{p,i}}} \qquad (6.17)$$

where k_B is Boltzmann's constant (1.38 x 10^{-23} J K^{-1} molecule^{-1}), T is the temperature and $M_{p,i}$ is the mass of one particle in bin i.

$$D_{p,i} = \frac{k_BT}{6\pi r_i\eta_a}G_i \qquad (6.18)$$

η_a is the viscosity of air given by Sutherland's expression (List, 1984):

$$\eta_a \approx 1.8325\times10^{-5}\left(\frac{416.16}{T+120}\right)\left(\frac{T}{296.16}\right)^{1.5} \qquad (6.19)$$

G_i is Cunningham's slip-flow correction (Cunningham, 1910) calculated using the estimation of Knudsen and Weber (1911) and coefficients from Kasten (1968).

$$G_i = 1 + K_{n(a,i)}\left(1.249 + 0.42e^{\left(-0.87 / K_{n(a,i)}\right)}\right) \tag{6.20}$$

$K_{n(a,i)}$ is the Knudsen number for air which can be calculated from the mean free path and the radius of particle i:

$$K_{n(a,i)} = \frac{\lambda_a}{r_i} \tag{6.21}$$

At high Knudsen numbers (i.e. smaller particles) Equation 6.14 simplifies to give Equation 6.22, and is valid for the first few bins in THAMO.

$$\beta_{i,j} = \pi\left(r_i + r_j\right)^2 \sqrt{\overline{v}_{p,i}^2 + \overline{v}_{p,j}^2} \tag{6.22}$$

In the MBL, there are a number of other gaseous vapours such as water and acids at pph and ppt levels which could contribute to particle growth. These condensable vapours could play an important role in the growth of new particles into CCN. Work by Saunders et al. (2010) showed that there was an increase in the size and number of IOPs in the presence of H_2SO_4. In THAMO it is assumed that once particles grow to 1-2 nm in radius they will deliquesce and subsequent growth is determined by condensation of H_2O and acids. This can be considered the critical radius which is defined as the size above which there will be spontaneous growth of the particle. At smaller sizes the Kelvin effect plays an important role in decreasing the vapour pressure of the particle so that growth will not occur.

Chemical transformations within the aerosol phase are still highly uncertain and for simplicity's sake, in THAMO it is assumed that the effects of individual components on the vapour pressure are independent of each other. At larger sizes this should not make a big difference due to the dilution of I_2O_5. For instance, when a 1 nm particle grows to 10 nm, I_2O_5 will make up ~0.005 % of the weight due to the condensed H_2O. This number would clearly be lower if the density of the condensed vapour is higher than H_2O.

The amount of water condensed will depend on the relative humidity and weight percentage of I_2O_5 within the new particle. I_2O_5 clusters deliquesce at around 80 % relative humidity therefore growth from condensation can occur above this threshold (Kumar et al., 2010). The growth of the particles is then controlled by the vapour pressure of the particle; once the vapour pressure of the aerosol is greater than that of the atmosphere, growth will stop. The growth is constrained using the water activity of the particle where the growth of the particle (assuming it is composed of I_2O_5 and H_2O only) ceases if the H2O is greater than 30 % of the weight at 80 % relative humidity. This means that a 1 nm particle only grows to 1.44 nm before the vapour pressure becomes too high (this number will be larger at higher humidities). In the MBL particles are certainly not just I_2O_5 and H_2O and contain a large number of condensable acids including H_2SO_4, HNO_3, organic acids etc. These acids will condense at a rate than can be calculated using the free molecular transfer approximation (Fuchs, 1964):

$$\frac{\upsilon_{cond,i}}{dt} = 4\pi r_i^2 \gamma_{acid} \upsilon_{acid} n_{acid} \frac{1}{4} \sqrt{\frac{8k_B T}{\pi M_{acid}}}$$
(6.23)

where γ_{acid} is the uptake coefficient, υ_{acid} is the volume of one molecule, n_{acid} is the concentration and M_{acid} is the mass in kg. The condensation of acids onto particles will lower the vapour pressure and therefore allows the particle to take up more H_2O. Therefore it can be said that the I_2O_5 polymers act as nuclei, while the uptake of H_2O and growth are controlled by condensation of acids. In THAMO it is assumed that the uptake of H_2O is not rate limiting in the MBL and the main condensing acids are taken to be H_2SO_4 and HNO_3. The water activities of H_2SO_4 and HNO_3 have been measured in previous studies and particle growth will cease at < 27 % weight of H_2SO_4 (Giauque et al., 1960) or 23.7 % weight of HNO_3 (Tang et al., 1988) assuming 80 % relative humidity. As mentioned previously the contributions of each species are considered independent so that each will control the growth rate individually. The uptake of I_2O_5 may also contribute by condensing onto existing particles, however, its contribution in the MBL is likely to be minimal.

The final aspect to consider in modelling particle growth is the loss of new particles onto pre-existing sea-salt aerosol. The heterogeneous loss rate can be calculated using the measured ASA from:

$$k_{het} = ASA\gamma_i\upsilon_i n_i \frac{1}{4}\sqrt{\frac{8k_B T}{\pi M_i}} \qquad (6.24)$$

where γ_i is unknown but assumed to be large (0.5) and the same for all small IOPs, υ_i is the volume of the particle, n_i is the concentration and M_i is the mass of one particle in bin i. This channel is considered to be the largest loss of IOPs in the MBL.

In addition to the aerosol processes mentioned above, recycling of I_2 out of the aerosol was also considered. Iodate will accumulate in aerosol due to the uptake of I_2O_3, I_2O_4 and I_2O_5 vapours and recent work by Saunders et al. (2012) on the reduction of iodate to iodide, showed that, in the presence of humic acid and light at wavelengths < 310 nm, iodate is reduced to iodide, with a rate of 1.2×10^{-5} s^{-1}. Through spectroscopic measurements, it was found that a significant proportion of the iodide produced is organically bound (~80 %). The remaining 20 % will rapidly react with O_3 deposited to the particle surface with an efficiency of around 2×10^{-7} for every O_3 collision with the surface of a 1×10^{-7} M iodide solution. Assuming a typical O_3 concentration of 20 ppb in the MBL, the lifetime of iodide in aerosol is only around 1 s.

In THAMO it is assumed that the aerosol particles contain a high loading of humic acid so that the laboratory determined photochemical loss rate of iodate to iodide was applied during daylight hours. The iodide produced is assumed to be immediately recycled back to the gas phase as I_2 due to O_3 uptake. The levels of iodide reported in aerosol are at odds with this assessment, however, it is important to note that these measurements are ex situ and analysis is often performed weeks or months after the aerosol are filtered out of the atmosphere. Therefore, in dark, O_3-less conditions it is likely that I$^-$ may be regenerated from the soluble organic fraction or via disproportionation; this can only be verified by fast, in situ aerosol iodide analysis which has, to date, not been performed.

6.2 Deriving an SST-dependent Inorganic Iodine Flux

In Chapter 4, expressions for the flux of I_2 and HOI from the sea surface were produced as a function of gaseous O_3, aqueous I^- and wind speed. Although there have been a number of field measurements of I^- in surface seawater – as indicated by Figure 5.13 in Chapter 5 - these measurements generally do not coincide geographically with measurements of reactive iodine species in the overlying MBL. This presents a problem for modelling the effect of this additional iodine flux, especially for global modelling purposes. There appears to be no clear link between iodide and chemical parameters such as nitrate or phosphate concentration or with biological markers such as Chl-*a* and CDOM. However, the map indicates a strong latitudinal dependence which matches well with observed variability in SST, albeit with further local phenomena overlaid.

Figure 6.1 below shows a correlation plot of measured sea surface iodide against SST from field campaigns in the Atlantic and Pacific where concurrent measurements were available. When plotted in Arrhenius form, an activation energy of ~76 kJ mol^{-1} is obtained. This activation energy may be indicative of a threshold for iodide production through biological processes, so that at higher temperatures IO_3^- is converted to I^- by phytoplankton in the surface ocean.
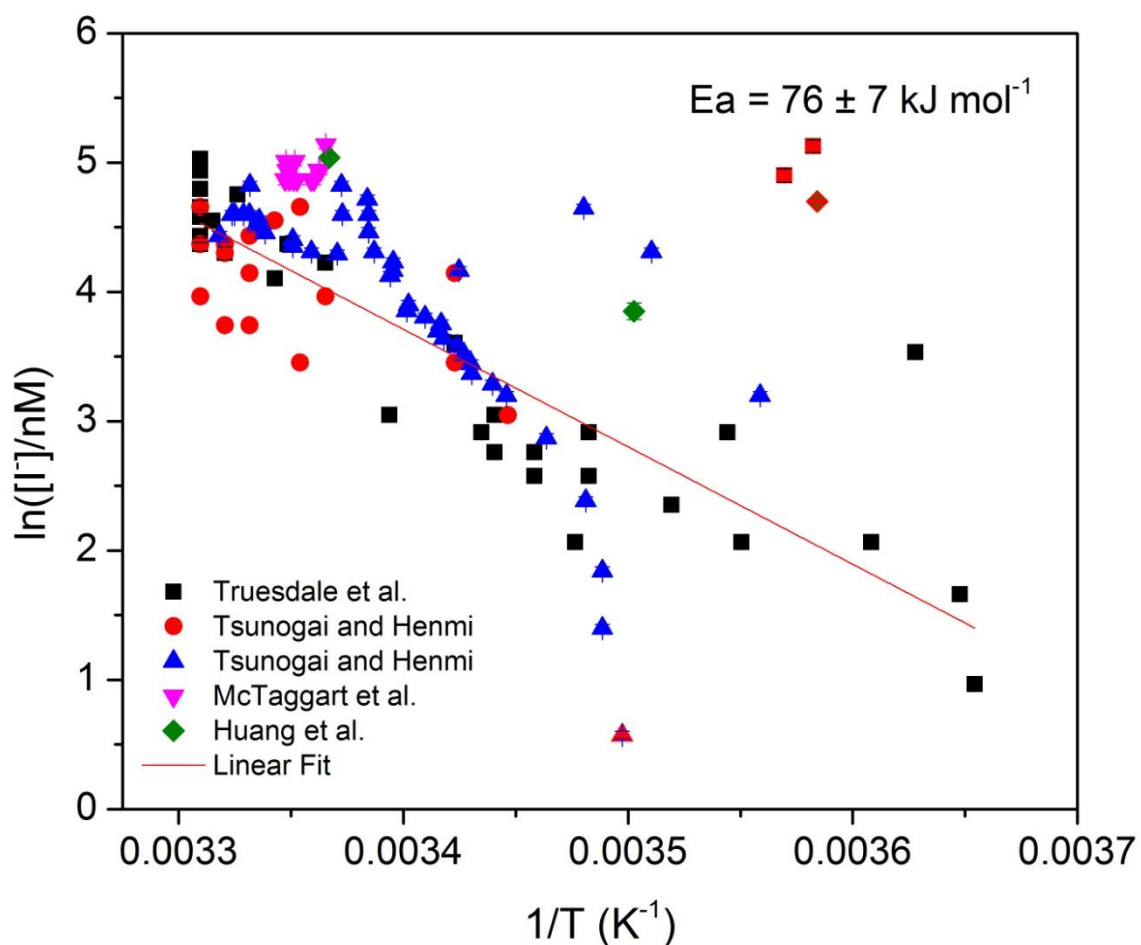
Figure 6.1 Arrhenius plot of SST and sea surface iodide concentrations for ship-based campaigns in the Atlantic and Pacific oceans (Huang et al., 2005; McTaggart et al., 1994; Truesdale et al., 2000; Tsunogai and Henmi, 1971). The three red squares in the top right of the plot were omitted from the regression analysis as they correspond to a high iodide episode at low latitudes during the Atlantic cruise (Truesdale et al., 2000).

From this plot, an Arrhenius type expression can be derived to describe the sea surface iodide concentration with respect to SST:

$$\left[I^-\right] = 1.07 \times 10^{15} * \exp\left(\frac{-9141}{SST}\right) \tag{6.25}$$

where [I⁻] is in nM and SST is in K.

This Arrhenius expression is then used in place of the iodide terms in the HOI and I$_2$ flux expressions derived in Chapter 4.

6.3 Modelling Field Measurements of IO and IO$_x$

6.3.1 Cape Verde

There have been a number of field measurements of IO and IO$_x$ in the MBL over the open oceans and in this section, the results from two campaigns are used to test the derived flux expressions. The first of these is the ground-based campaign on the Cape Verde islands in the tropical Atlantic Ocean during 2006-2007, where measurements of IO were recorded using the LP-DOAS instrument described in Chapter 5. The flux expressions are input into THAMO and typical measured values for temperature (296 K), wind speed (7 m s^{-1}) and O$_3$ (30 ppb) are used.

The K$_z$ profile was constructed using wind speed measurements at Cape Verde at three different heights (4, 10 and 30 m). Aircraft measurements at Cape Verde showed that there was a distinct temperature inversion at around 1 km altitude which shows that the BL is decoupled from the free troposphere at this site. Therefore the K$_z$ profile was assumed to increase up to 30 m (where it peaked at 3 x 10^4 cm s^{-1}) and then decrease monotonically to 2 cm^2 s^{-1} at the top of the BL (1 km). A plot of the K$_z$ profile is shown in Figure 6.2.
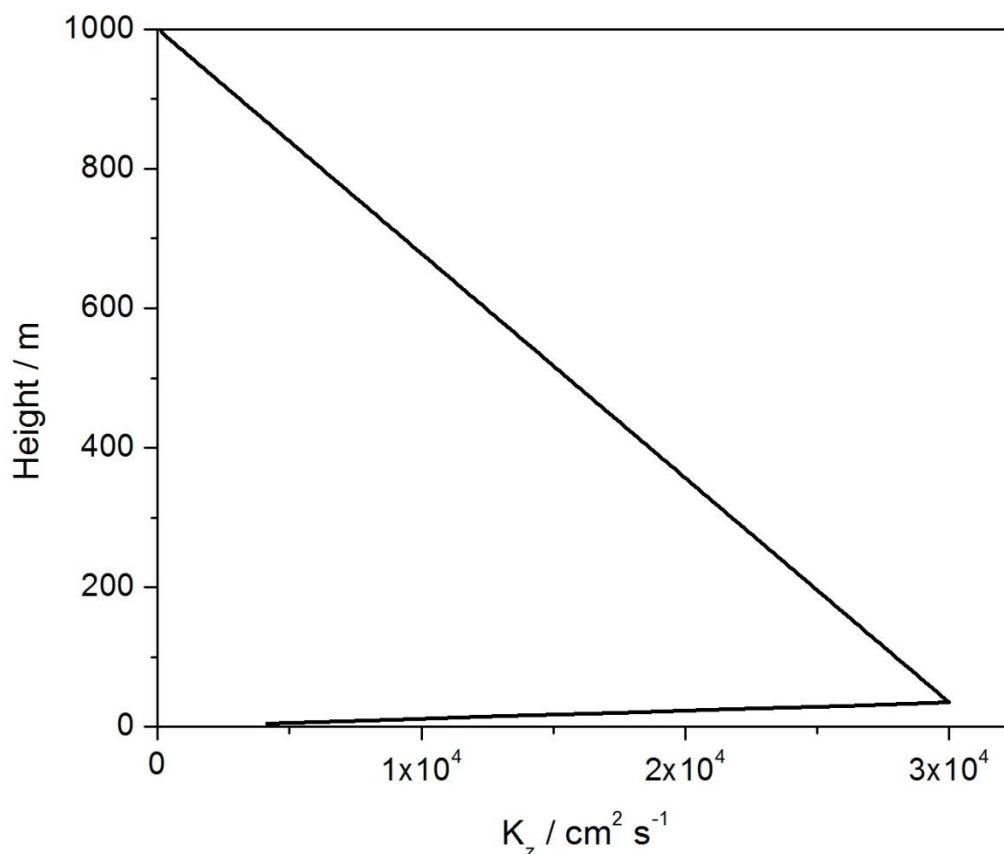
Figure 6.2 K_z profile used for modelling the iodine chemistry at Cape Verde.

The model is constrained using typical measured mixing ratios of a number of species: $[NO_x]$ = 25 ppt, $[CO]$ = 110 ppb, $[DMS]$ = 30 ppt, $[CH_4]$ = 1820 ppb, [ethane] = 925 ppt, $[CH_3CHO]$ = 970 ppt, HCHO = 500 ppt, isoprene = 10 ppt, propane = 60 ppt, propene = 20 ppt (Carpenter et al., 2010; Lee et al., 2009b; Mahajan et al., 2010c; Read et al., 2008; Read et al., 2009). The average background aerosol surface area was taken to be 1×10^{-6} cm^2 cm^{-3} based on measurements recorded at the site (Allan et al., 2009). The modelled HO_x was in agreement with the measured values at Cape Verde (Whalley et al., 2010). The iodocarbon fluxes (cm^{-2} s^{-1}) measured during the campaign were also included: CH_2I_2 = 1.3×10^7, CH_2IBr = 7.6×10^6, CH_2ICl = 1.2×10^7, CH_3I = 3.38×10^7, C_2H_5I = 2.86×10^6, C_3H_7I = 6.27×10^5 (Jones et al., 2010).

The HOI and I_2 fluxes calculated by THAMO were 1.74×10^8 and 7.76×10^6 cm^{-2} s^{-1}, and the corresponding surface seawater concentrations for HOI and I_2 were 5.89×10^{-9} and 6.77×10^{-12} M, respectively. The model was initially run by considering the fluxes as

purely evasive terms, and subsequently by considering equilibration with their surface atmospheric concentrations where the flux was calculated as:

$$Flux_{equil.} = K_t - \left(\left[\text{HOI} \, or \, \text{I}_{2(sea)} \right] - \frac{\left[\text{HOI} \, or \, \text{I}_{2(g)} \right]}{H} \right) \qquad (6.26)$$

The Henry's law constants (Sander, 1999), which are temperature dependent, and transfer coefficients, which depend on both wind speed and temperature, were calculated in THAMO according to the equations in Chapter 4.

Figure 6.3 shows the measured (annual average) and modelled IO diurnal profile. The dashed line shows the modelled IO if only iodocarbons are included, the solid black line shows the modelled IO when both iodocarbons and the inorganic iodine fluxes are included, and the solid red line shows the modelled IO when both iodocarbons and the equilibrated inorganic iodine fluxes are included. It is clear from the plot that when only iodocarbons are considered the IO is under-predicted by ~63 %. In the case of the purely evasive inorganic iodine fluxes, the IO is over-predicted by around 60 %. A good agreement with the measured IO mixing ratios is achieved, however, when the equilibrated inorganic iodine fluxes are included.
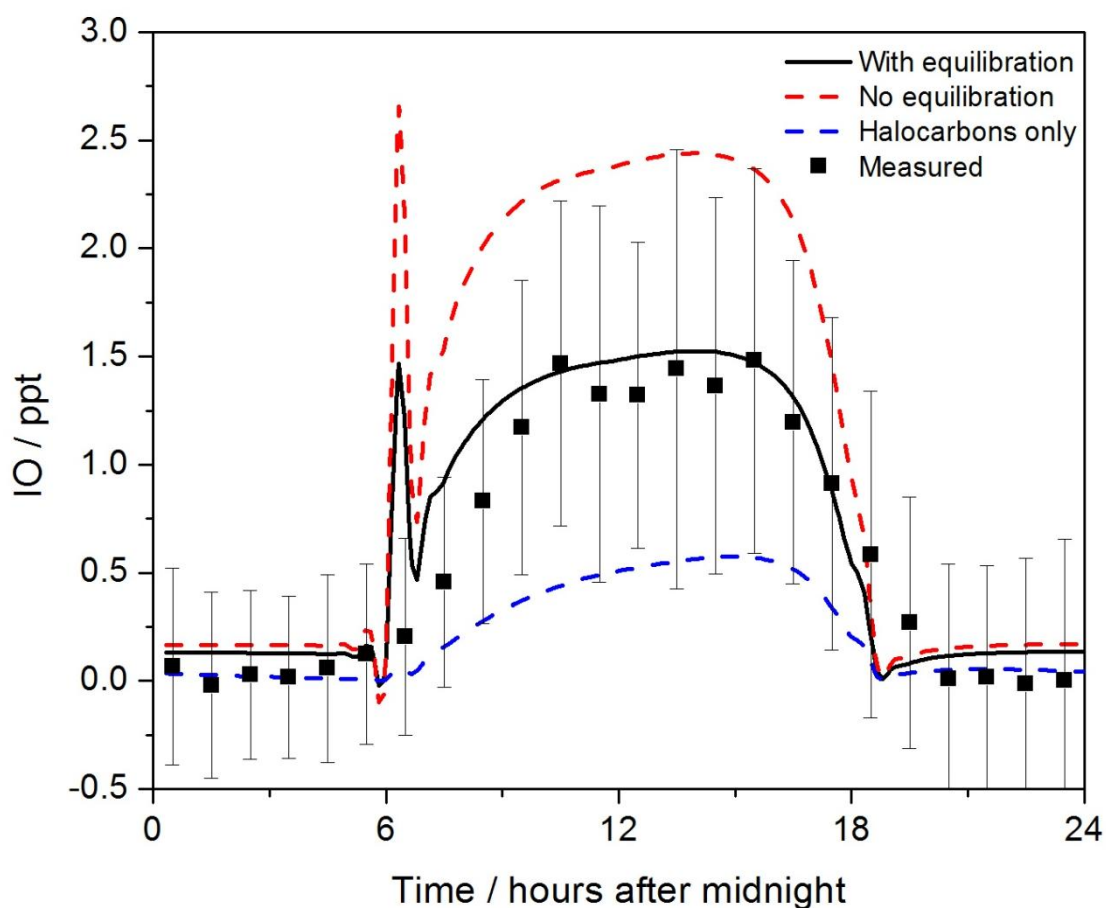
Figure 6.3 The modelled diurnal IO profile at 5 m above the ocean surface, produced from combined emissions of halocarbons, HOI and I_2 equilibrated with atmospheric concentrations (black solid line), without equilibration (red dashed line) and from halocarbon emissions only (blue dashed line). The black squares show the annual average IO measured using the LP-DOAS instrument and associated standard deviations.

It should be noted that the large peak in IO observed around sunrise in the model is due to the rapid photolysis of I_2 which has built up overnight. This feature has, as yet, not been observed in field observations. However, the timescale for this is on the order of around 20 minutes in the model and the DOAS spectra were averaged over an hour to improve signal to noise ratio for the Cape Verde measurements, which may explain why this predicted effect is not seen in the measurements.

Figure 6.4 shows the diurnal profile for the equilibrated HOI and I_2 fluxes for the conditions mentioned above. The gas phase chemistry of iodine and HO_x causes a build up of HOI in the atmosphere above the sea surface during the day causing the HOI flux to be suppressed. At night, the HOI is converted to I_2 and IBr by heterogeneous chemistry on sea salt aerosol and so the sea-air flux of HOI increases to approximately

twice that of the daytime flux. The I_2 flux, on the other hand, shows the opposite behaviour: during the day I_2 is rapidly photolysed meaning that a relatively large I_2 flux is maintained, whereas at night the build up of I_2 causes the flux to reduce to zero.
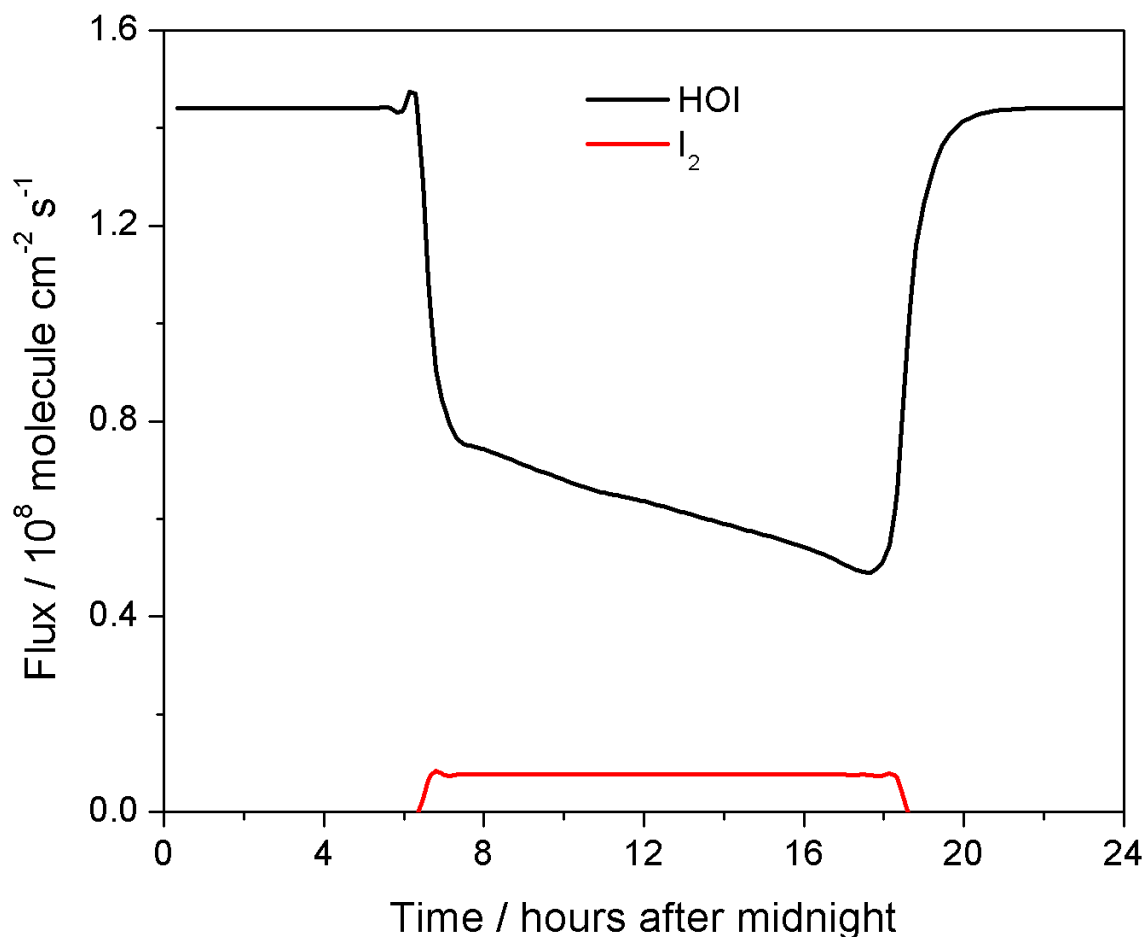
Figure 6.4 Diurnal profiles for the HOI and I_2 emission fluxes showing the effect of equilibration with atmospheric concentrations above the surface.

The time-height profiles for IO, OIO, HOI and I_2 are shown in Figure 6.5 for a diurnal cycle. The IO is only present at significant levels during the daytime and extends from the surface up to around 300 m where the levels drop to around 50 % of the near surface values. The IO then disappears at sunset as photolysis is switched off and therefore there is no possibility for reaction of $I + O_3$. OIO is also only present at significant levels during daytime although the mixing ratios remain relatively low throughout the day. The HOI is present during the day due to HO_x chemistry (reactions R6.1 and R6.2) and increases as sunset approaches due to the decrease in photolysis rate.

$$IO + HO_2 \rightarrow HOI + O_2 \qquad\qquad R6.1$$

$$HOI + h\nu \rightarrow I + OH \qquad\qquad R6.2$$
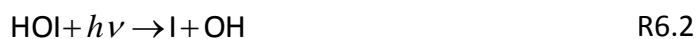
During the night any HOI which evades from the sea surface will react rapidly on sea-salt aerosol and therefore the mixing ratio remains low. The I_2 shows daytime levels which are very low due to its rapid photolysis rate. The mixing ratios then increase following sunset but begin to decrease throughout the night due to its reaction with NO_3.
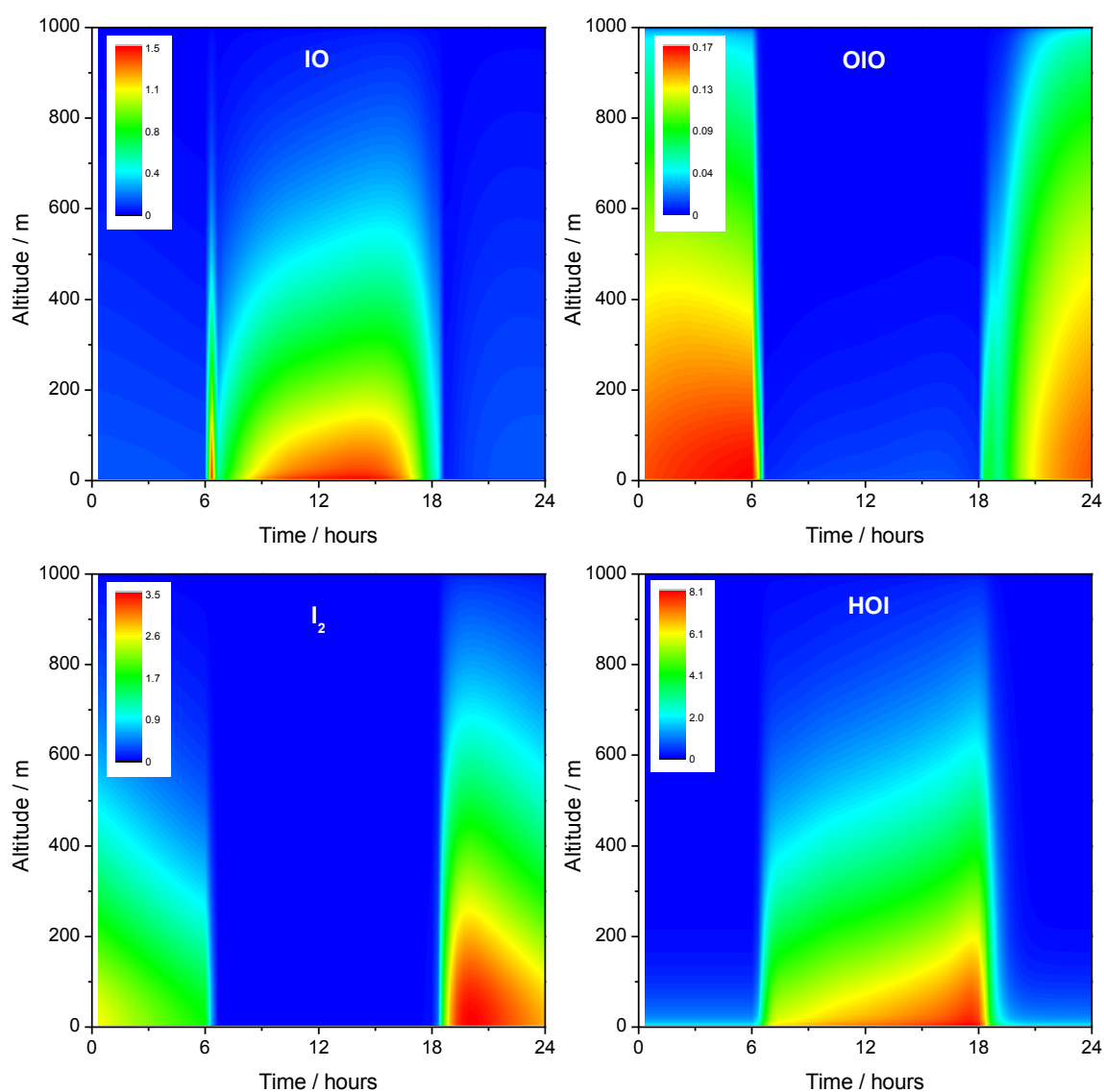
Figure 6.5 Modelled IO, OIO, I_2 and HOI mixing ratios (pptv) for Cape Verde in the 1 km boundary layer where the total iodine flux includes the contributions from both halocarbon and equilibrated inorganic iodine fluxes.

The presence of significant concentrations of HOI could also lead to changes in OH through HO_x chemistry (via R6.1 and R6.2), leading to changes in the oxidative capacity of the marine boundary layer.

To investigate the contribution of this additional HOI to the OH concentration, the model was run assuming that all the inorganic iodine emission was in the form of I_2; the calculated HOI flux in the model was halved (to take into account that only one I atom is liberated on photolysis of HOI) and added to the calculated I_2 flux. The resulting IO concentrations were then compared to the previous model runs where both fluxes were included. The OH produced when the inorganic iodine flux was assumed to be solely due to I_2 was only around 2 % lower than when HOI was also included, therefore it is unlikely that the additional HOI produced from this mechanism will have a significant impact on the OH concentrations in the MBL.

6.3.2 Eastern Pacific

Using the new expressions, the HOI and I_2 fluxes for each of the measurement points in the HaloCAST-P cruise were calculated from the on board measurements of SST, wind speed and the modelled O_3 from the global model CAM-Chem (Mahajan et al., 2012; data provided by Juan Carlos Gómez Martín). The total inorganic I flux is then calculated as the HOI flux plus twice the I_2 flux (owing to the two I atoms produced from photolysis of I_2). This is then plotted against the measured IO_x from the MAX-DOAS instrument and the correlation plot is shown in Figure 6.6.
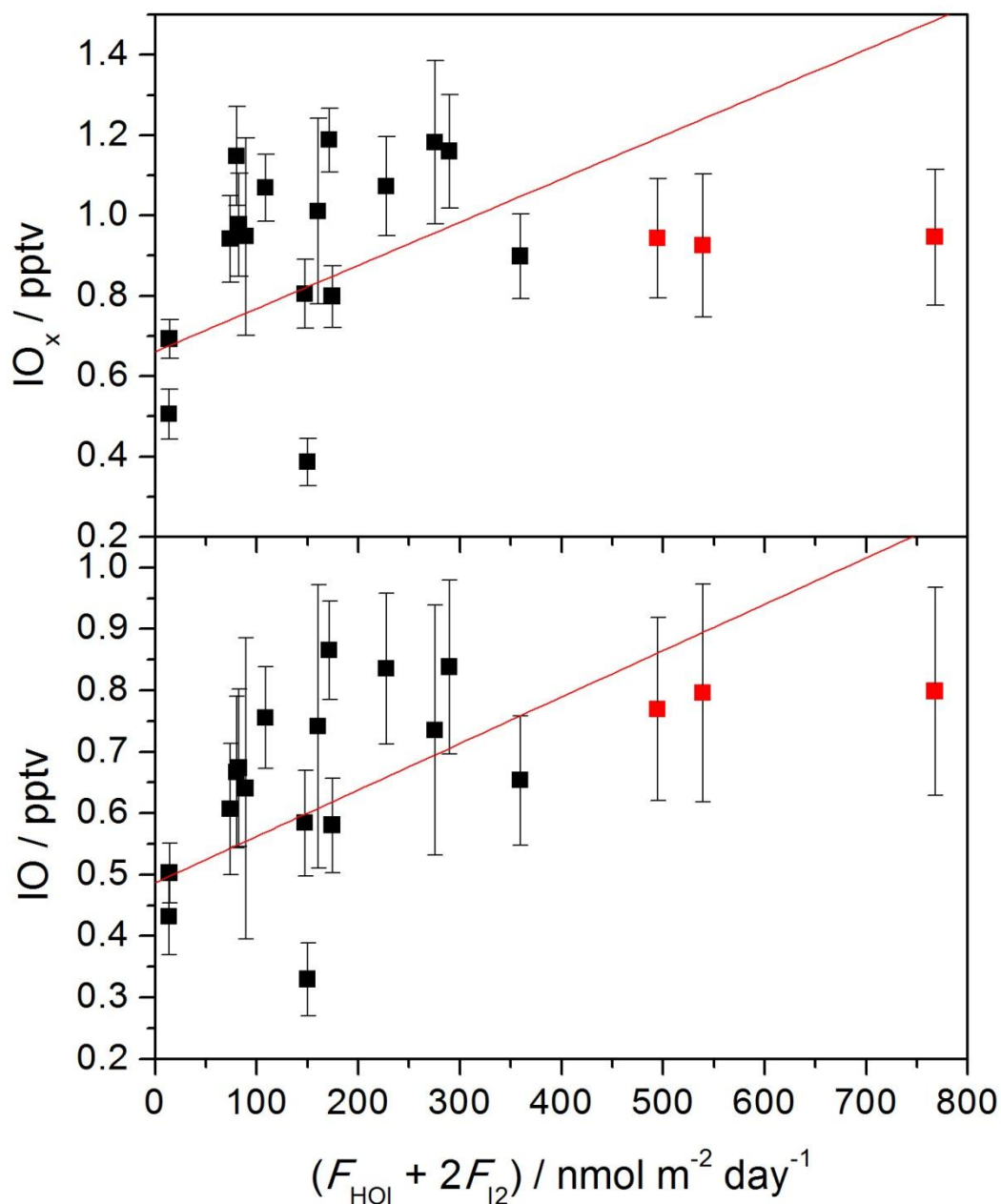
Figure 6.6 Measured IO$_x$ (top panel) and IO (bottom panel) during the HaloCAST-P cruise versus predicted inorganic iodine flux (HOI + 2I$_2$). The red lines show a straight line fit of the data and a significant intercept is observed for both. The points highlighted in red were excluded from the linear regression analysis.

Before fitting a straight line to the data, three of the points at very high O$_3$ were omitted as these points coincided with the cruise ship passing over the equatorial front. In this region the O$_3$ is particularly sensitive to changes in SST and humidity which in turn depend on seasonal cycles such as El Niño or La Niña. As a result the high O$_3$ output from CAM-Chem may not be representative of the actual O$_3$ during the

Thompson cruise. The correlation coefficients obtained from this fit were $R^2 = 0.10$ ($p = 0.13$) for IO_x and $R^2 = 0.15$ ($p = 0.09$) for IO.

Another interesting feature of the correlation plot is the significant intercept of 0.66±0.08 ppt obtained for the IO_x plot (0.48±0.08 ppt for IO). This intercept may indicate the contribution of halocarbons to the measured IO_x in the absence of the inorganic iodine flux. The modelling work performed by Mahajan et al. (2012) suggested that around 20 % of the IO_x could be explained by the observed emissions of CH_3I, and there are likely other iodocarbon species which will also contribute. THAMO was run with the HOI and I_2 fluxes turned off and the halocarbon fluxes were adjusted so that the resulting daytime IO_x was ~0.66 ppt. In fact, using the average CH_3I flux measured during the campaign (4.17 x 10^6 molecule cm^{-2} s^{-1}), and the average measurements from the Cape Verde campaign for the other halocarbons (Mahajan et al. 2010), gave IO_x in agreement with this value. This halocarbon flux was then fixed for further THAMO model runs.

The HOI and I_2 flux expressions, Equations 4.16 and 4.17 (using the Arrhenius SST expression (Equation 6.25) in place of I^-), were in-put into THAMO and all the points of the Thompson cruise were modelled. The measured O_3, wind speed and SST were used and a separate K_z profile was produced for each point based on the measured wind speed.

The IO and IO_x output from the model were then plotted against the HOI and I_2 fluxes along with the measured IO and IO_x. The IO and IO_x was computed by averaging over the first 200 m of the model (first 40 boxes) using only the daylight measurements. This was done because the mixing ratios were calculated assuming a 200 m box profile from the MAX-DOAS slant columns and for quality control, only daylight data with SZA < 60° was used. Figure 6.7 below shows the modelled and measured IO and IO_x with the model output for the same conditions.
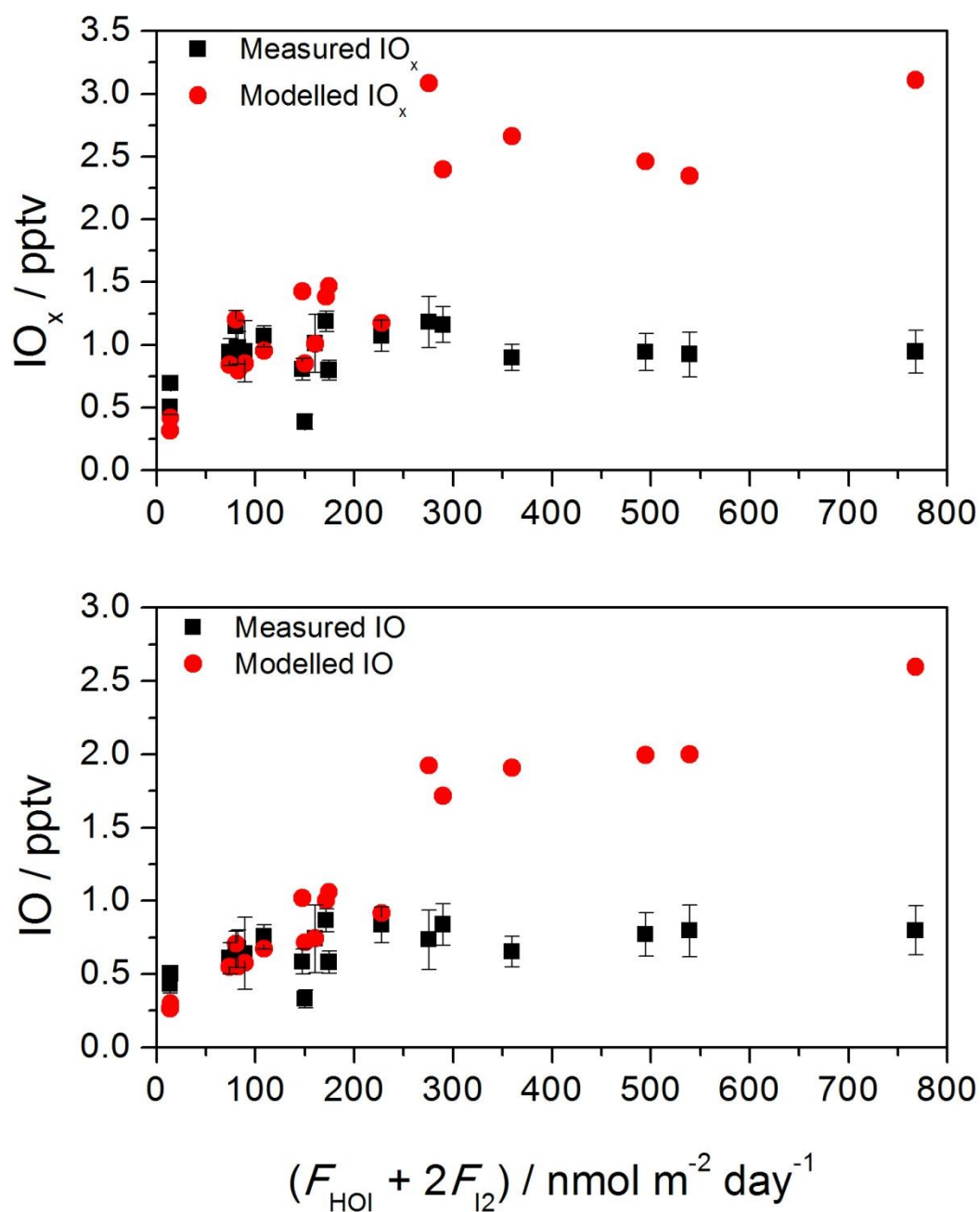
Figure 6.7 Measured (black squares) and modelled (red circles) IO and IO_x against predicted total inorganic iodine flux from the parameterised expressions.

There is good agreement for the points with lower computed HOI and I_2 fluxes, however, there is a large disagreement as the HOI and I_2 flux increases, with the IO and IO_x being over-predicted by more than a factor of three. This is largely due to the high O_3 and low wind speeds for the highest three points which result in the very high predicted fluxes. As mentioned previously the high O_3 from the CAM-Chem output may not accurately represent the O_3 during the Thompson cruise. Therefore, the

model was re-run for the highest three points, varying the O_3 concentration until the resulting IO matched the measured mixing ratios. The IO was used to match the observations as the IO_x measurements were derived from the O_3 mixing ratios predicted by CAM-Chem.

The O_3 had to be reduced to 2 ppb before the observations could be matched. Although such low concentrations have been observed previously over the open ocean, these are much lower than even the lowest O_3 mixing ratios calculated during the cruise.

An additional possible reason for the lower measured IO compared to the predicted values could be due to the very low wind speeds meaning there is much less mixing just above the surface of the ocean. This could mean that any I_2 and HOI emitted into the bottom box would build up to levels that would suppress further emission due to equilibration. In addition, increased mixing ratios of I_2 and HOI in the bottom box during daylight hours could lead to sufficient IO concentrations for IOP formation to occur. As IOP formation is treated as a sink for IO in the model, this would reduce the overall IO levels over the first 200 m. A further physical effect of reduced wind speeds over the ocean is the possibility for organic films to form at the surface, inhibiting the release of I_2 and HOI from the sea to the gas phase. For these reasons, the K_z profile for the highest points was adjusted so that the K_z values in the first five boxes (first 25 m) were reduced by a factor of two to test whether this would lower the mixing ratio.

Using the reduced K_z in the first five boxes, the resulting daytime average IO mixing ratio over the first 200 m for the highest point was 2.46 ppt, still three times higher than the observed mixing ratio (~0.8 ppt). The K_z profile was then adjusted so that the K_z value in the first box (5 m above the ocean surface) was an order of magnitude smaller than that calculated, however, the reduction was even smaller in this case (2.58 ppt IO).

A further possible explanation for the lower observed IO and IO_x in this region could be due to iodide becoming depleted in the top layer of the ocean. At the highest calculated HOI and I_2 fluxes, over the course of 24 hours, the iodide would be depleted in a layer at the surface down to around 8 mm. Using the diffusion coefficient for

iodide of 2×10^{-5} cm^2 s^{-1} (Friedman and Kennedy, 1955) it would take around 3 hours for the iodide in this layer to be replenished from below. Hence, this explanation appears to be unlikely.

Another reason for the discrepancy could be the change in organoiodine flux throughout the campaign. During the latter half of the campaign the measured CH$_3$I flux was lower than during the first half of the campaign and there is some evidence for a correlation between IO and the CH$_3$I flux (although this is only significant at the 95 % confidence level and not at 99 %). Reducing the CH$_3$I flux from 4.17×10^6 cm^{-2} s^{-1}, (the average flux observed during the whole campaign) to 1.5×10^6 cm^{-2} s^{-1} (the flux observed at the highest modelled point), the daytime average IO mixing ratio was 2.58 ppt, so only a small reduction compared to the previously modelled result. Assuming that the other halocarbons in the model are reduced by the same factor, the resulting IO mixing ratio was 2.49 pptv. This demonstrates that the halocarbon flux is only playing a minor role in the overall contribution to the observed IO mixing ratios. Variations in the halocarbon fluxes could be one of the explanations for the higher IO mixing ratios observed in the Western Pacific (Großmann et al., 2013), even at low O$_3$ concentrations, where their contribution would become more important; despite CH$_3$I emissions being nearly an order of magnitude smaller than the Cape Verde observations, the shorter lived CH$_2$ICl and CH$_2$I$_2$ fluxes were much larger (3.8×10^7 and 2.3×10^7 cm^{-2} s^{-1}, respectively).

The other reason that the observations may not match for these data points is down to uncertainty in the parameterisation of the iodide concentration based on SST measurements. As mentioned in section 6.2, the general trend of the sea surface iodide was to follow the changes in SST, however, there are a number of local phenomena which do not conform to this pattern. If the iodide around the ITCZ was much lower than indicated by the SST measurements this would again lead to a reduced HOI and I$_2$ flux, and therefore lower IO and IO$_x$ as observed in the cruise data. Seasonal variations in ocean currents could cause fluctuations in sea surface salinity, and therefore also in iodide, as was observed in the case of the Galapagos IO$_x$ data in Chapter 5.

6.3.3 Sensitivity Studies

Sensitivity studies were conducted to investigate the effect of the three variables (O_3, wind speed, SST) in the parameterised flux expressions on the modelled IO and IO_x mixing ratios over the first 200 m. The results of these investigations are shown in Figure 6.8.

As expected, there is a clear increase in IO with an increase in O_3, however, this increase is not reflected in the IO_x mixing ratios. At lower O_3 concentrations the majority of the IO_x will be in the form of I rather than IO. As the O_3 increases, the IO_x ratio will shift towards IO and at the highest O_3 concentrations this IO is converted to I_2O_5 and further to IOPs. This acts as a sink for IO in the model and therefore reduces the total IO_x at higher O_3 concentrations.

The increase in the IO and IO_x with SST can be attributed to two factors: the first is that an increase in SST leads to a greater predicted sea surface iodide concentration from the Arrhenius expression described previously; the second is that the higher temperature leads to larger transfer coefficients (K_t) for both HOI and I_2 leading to a greater inorganic iodine flux.
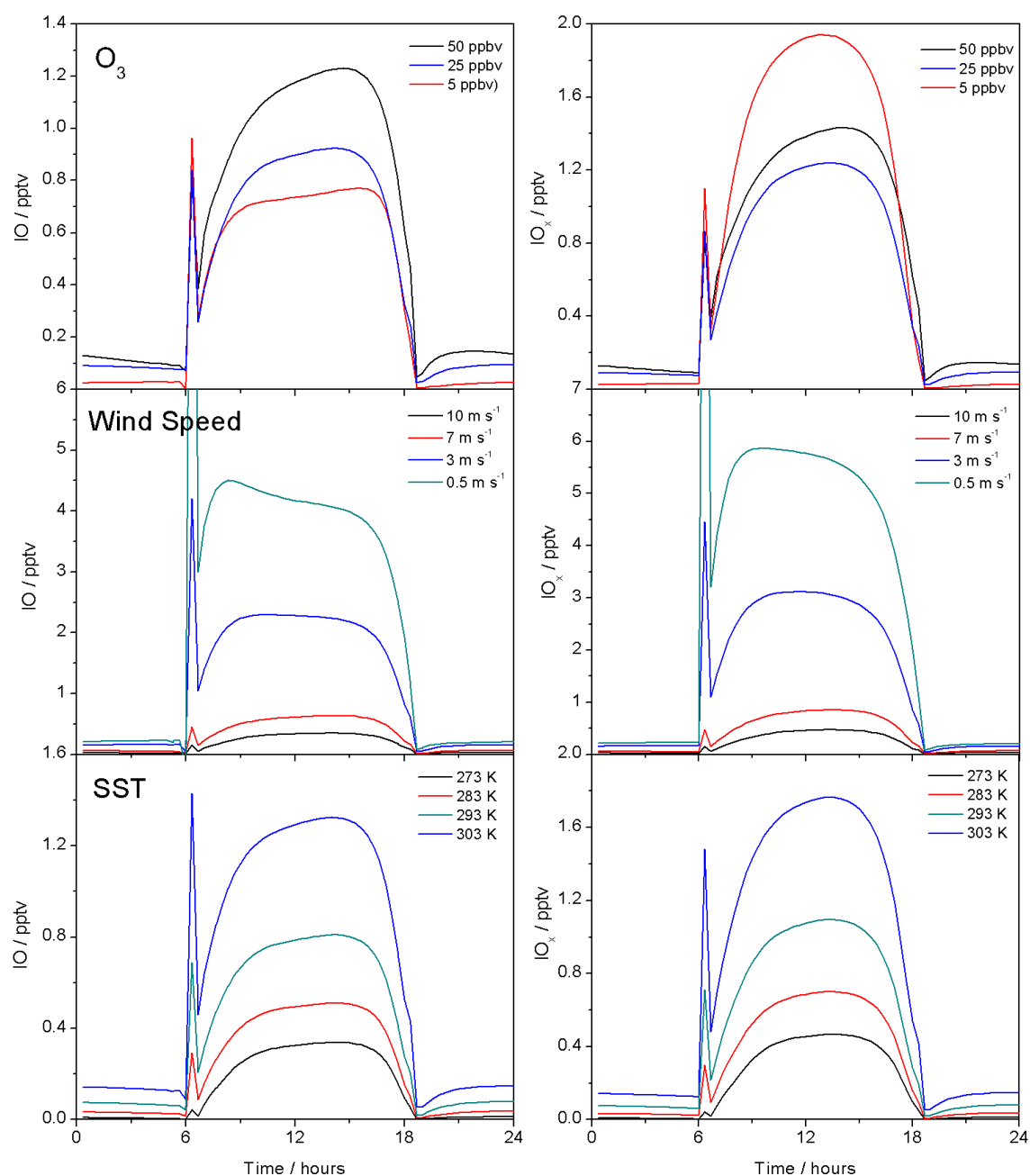
Figure 6.8 Modelled diurnal profiles of IO and IO$_x$ as a function of O$_3$ (top panels), wind speed (central panels) and SST (bottom panels).

A clear dependence on wind speed is demonstrated, however, the effect becomes quite extreme when a wind speed of 0.5 m s^{-1} is used. The resulting IO and IO$_x$ mixing ratios are clearly unrealistic for remote ocean conditions and a limiting factor must come into play at these very low wind speeds. Comparing the wind speed dependence of the HOI and I$_2$ flux expressions with the output from the kinetic model, there is a clear divergence at wind speeds lower than 2 m s^{-1} (Figure 6.9).
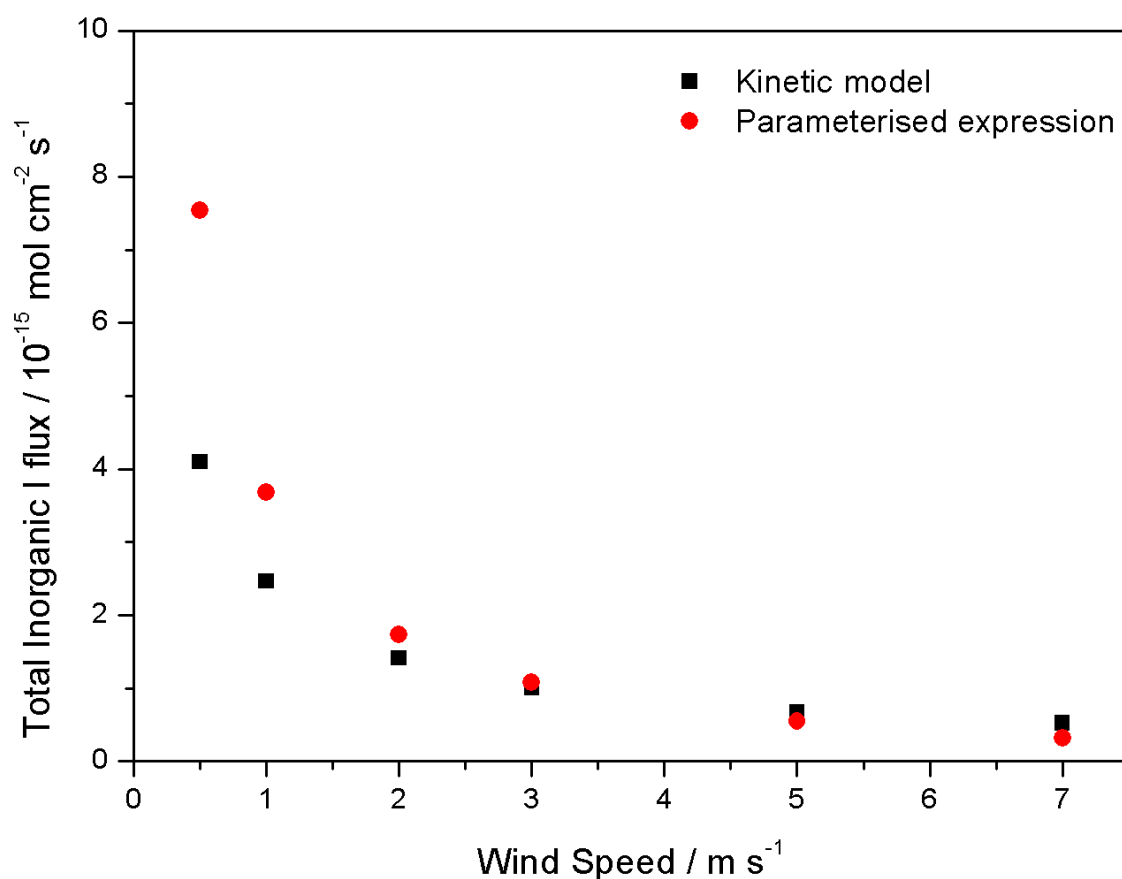
Figure 6.9 Total inorganic iodine flux (HOI + 2I_2) predicted by the kinetic model (black squares) and the parameterised flux expressions (red circles).

Some adaptation of the expressions may therefore be required for very calm conditions when wind speeds drop close to zero. As mentioned previously, one possibility at these very low wind speeds is that this gives the chance for organic films to form on the still surface waters. Organic films are well known to inhibit sea-air transfer of a number of species (e.g. Frew, 1997; Frew et al., 2004; Goldman et al., 1988) and this may suppress the HOI and I_2 emissions.

Another important feature that is shown in Figure 6.8 is the presence of IO at night. The production of IO at night in the model occurs through the reaction of I_2 with NO_3 (R6.3) giving I atoms. The atoms can then react further with NO_3 (R6.4) or with O_3 (R6.5) to produce IO.

$$I_2 + NO_3 \rightarrow I + INO_3 \qquad \text{(R6.3)}$$

$$I + NO_3 \rightarrow IO + NO_2 \tag{R6.4}$$

$$I + O_3 \rightarrow IO + O_2 \tag{R6.5}$$

Under the very clean conditions encountered in the remote oceans the amount of night time IO produced is minimal due to the very low NO_x concentrations. However, in more polluted environments, with higher NO_x concentrations, this reaction may become more important and could act as a significant night time source of IO. In addition to this, there is the possibility that HOI may also react with NO_3 to produce IO directly via reaction R6.6.

$$HOI + NO_3 \rightarrow IO + HNO_3 \tag{R6.6}$$
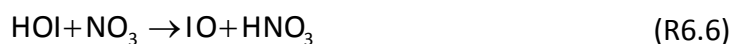
In more polluted areas, the concentration of O_3 will also be higher, with transport of polluted air from the continents in the Northern Hemisphere over the ocean giving rise to O_3 concentrations which can exceed 100 ppb (Logan, 1985; Vingarzan, 2004). These increased O_3 concentrations will lead to higher emissions of HOI and I_2 to the gas phase due to the linear relationship between O_3 and the HOI and I_2 fluxes from the parameterised expressions. This in turn will lead to more reactive iodine, which will cause O_3 destruction through the catalytic cycles described in Chapter 2. This could be increasingly important in coastal regions where the sea surface emissions may help to limit the amount of O_3 over the surface of the open ocean.

Chapter 7

Conclusions and Further Work

This work describes experimental results from laboratory measurements of the I_2 and HOI fluxes produced from the reaction of O_3 and I^-, kinetic modelling to verify the experimental results, field measurements of reactive iodine species in the remote MBL and finally 1-D modelling work to link the experimentally determined fluxes to the field measurements. The main conclusions from chapters 3, 4, 5 and 6 are discussed below, along with suggestions for further work to improve the understanding of iodine chemistry in the MBL.

In Chapter 3, a number of different parameters were investigated for their influence on the I_2 and HOI fluxes produced from the reaction of I^- + O_3. The I_2 and HOI fluxes were found to increase with increasing O_3 concentration and showed a linear response over the range of O_3 concentrations investigated. Increasing iodide concentration also resulted in an increase in the HOI and I_2 fluxes although there was some deviation from linearity at the highest iodide concentrations which may be indicative of a surface saturation effect.

Salinity was found to have a positive influence on the I_2 flux, with around a 2.5 fold increase moving from 0 to 0.5 M Cl^-, but had no significant effect on the HOI flux. However, this effect was deemed negligible over the range of salinity observed in real seawater. Mixing was found to be an important parameter in determining the I_2 and HOI fluxes, with an increase in mixing causing a decrease in the fluxes, due to mixing of I_2 from the surface into the bulk solution.

None of the three organic species investigated in this work were found to have a significant effect on the HOI and I_2 concentrations when using realistic seawater concentrations. An effect of organic surfactants cannot be ruled out, however, given previous experimental results, as longer chain hydrocarbons may cause a greater

effect and are likely to be present in the highly heterogeneous organic surface films found in seawater.

Initial results from the temperature dependence experiments suggested that the reaction had a large, positive activation energy ~100 kJ mol^{-1} in agreement with previous studies (within experimental error). However, given the unphysical nature of the reported pre-exponential factor, and the poor reproducibility of observations at low temperatures, further experiments suggested that the temperature dependence is most likely minimal, both for HOI and I_2. Combining the measurements under all experimental conditions and normalising for $[O_3]$, $[I^-]$ and $[H^+]$, the activation energies obtained for the HOI and I_2 fluxes were 17±50 and -7±18 kJ mol^{-1}, respectively.

In Chapter 4 a kinetic model of the interfacial layer was found to reproduce the experimental observations well under most of the conditions studied with a few exceptions. There was some deviation at higher iodide concentrations, with the model predicting much higher emissions for I_2, and this was considered to be a result of a surface saturation effect occurring in the experiments and not considered in the model. However, these discrepancies arose at much higher concentrations than observed in real seawater.

The model under-predicted the effect of salinity on the I_2 flux slightly when compared to the experimental results. This could be due to a surface enhancement effect whereby the preference of iodide to remain at the surface of solution is enhanced by the presence of the larger chloride ions. The temperature dependence in the model was found to be in good agreement with the results of the combined temperature dependence experiments and the modelled activation energies were 29 and -0.2 kJ mol^{-1} for HOI and I_2, respectively.

The results of the experiments were then used to produce parameterised expressions for both the HOI and I_2 fluxes, as a function of $[O_3]$, $[I^-]$ and wind speed. The resulting fluxes were found to be in excellent agreement with the modelled results, apart from at very low wind speeds, where the 1/ws term in each of the expressions caused an over-prediction in both fluxes.

The results of the CHARLEX field campaign in Chapter 5 suggest that IO and IO_x in the Eastern Pacific MBL are consistently low and are inconsistent with previous satellite measurements in the region, however, the possibility that there are higher concentrations of IO_x in the free troposphere cannot be ruled out.

The iodine emissions were found to be dependent on multiple factors. The anti-correlation with Chl-*a* and CDOM suggests that biological activity is unlikely to play a major role, and in fact may have an inhibitory effect. This could be due to surfactant effects or additional reactions of organics with iodine species in surface seawater. There was a strong seasonal cycle observed which correlated well with SST and salinity, and it seems most likely that an abiotic mechanism is responsible for the iodine emissions.This seasonal cycle may not be directly linked the temperature and salinity variations, but could actually indicate changes in the sea surface iodide concentration. This would lead to variations in the inorganic source from the mechanism described in Chapter 3.

Based on model calculations, the organoiodine flux contribution (in the form of CH_3I) to the IO_x mixing ratios was found to be small, but significant, at around 30 %, suggesting that the inorganic source will be a major contributor to the overall iodine flux from the ocean to the atmosphere, although other organoiodine species will also likely play a role.

Photolytic O_3 loss and particle formation were not observed due to the low concentrations of halogens observed during the campaign. The maximum O_3 loss attributable to halogen chemistry was modelled at around 30 %. The absence of particle formation observed during the CHARLEX campaign and the Cape Verde campaign described in Chapter 6 and this leads to the conclusion that it is unlikely that iodine oxide particle formation is important over the open oceans.

In Chapter 6 the 1-D chemistry transport model THAMO was used to test the parameterised expressions for predicting IO concentrations measured during field campaigns in Cape Verde and the Eastern Pacific. The model was found to produce good agreement with the yearly averaged diurnal profile of IO measured in Cape Verde and the results showed a number of interesting features.

Because measurements of iodide in surface seawater are quite sparse it was deemed necessary to produce a more useful parameterisation for use in global models. The surface iodide concentration was found to show a good correlation with sea surface temperature and an Arrhenius type fit was produced which matched the overall trend well. The Arrhenius expression was then used in THAMO to predict the iodide concentration for each of the points in the HaloCAST-P cruise.

The model was able to reproduce the observed IO for the higher wind speeds, however, there was a significant over-prediction at lower wind speeds, due to the very high inorganic iodine fluxes predicted by the parameterised expressions. In addition, the O_3 concentration was not measured during the cruise and O_3 data were derived from the CAMChem global model. The very high O_3 concentrations predicted for the latter part of the campaign coincided with the ship track passing through the ITCZ. The O_3 concentrations in this region are known to vary greatly depending on the season and year due to sea surface temperature variations and the very large O_3 concentrations predicted may not accurately reflect the O_3 during the campaign. To best match the result an O_3 concentration of 2 ppb was required.

Sensitivity studies showed that, as expected, the modelled IO mixing ratios increased with increasing O_3 concentration. However, this increase was not observed in the IO_x; at the lower O_3 concentrations the IO_x will be mostly in the form of I, but as the O_3 concentration increases the ratio will shift towards IO and the formation of I_2O_5 leading to a lower total IO_x mixing ratio. Increasing SST in the model resulted in an increase in both the IO and IO_x mixing ratios as a consequence of two factors, the increase in the predicted sea surface I$^-$ from the Arrhenius expression and the larger K_t coefficients for both HOI and I_2 at higher temperatures, both of which will lead to higher predicted fluxes. The IO and IO_x concentrations both decreased with increasing wind speed as a result of the increased mixing of I_2 and HOI from the surface to bulk seawater. However, there was a significant over-prediction by the model at very low wind speeds due to the 1/ws term in the parameterised expressions, which suggests that a further limiting factor may be necessary when modelling iodine chemistry under very still conditions.

The results presented in this thesis demonstrate that there is a ubiquitous inorganic source of iodine over the open ocean, but that the overall levels of reactive iodine species, such as IO, may be lower than previous results suggested. The levels of reactive iodine observed are not capable of sustaining IOP production, and new particle formation will most likely be confined to coastal locations with exposed algal beds. The impact on ozone will also be smaller than previously predicted, but still significant.

This thesis has addressed several aspects of iodine chemistry occurring over the remote oceans, however, there are still a number of outstanding questions. Further work in all three branches of atmospheric chemistry (laboratory work, field measurements and modelling) is necessary before we can fully assess the impact of iodine chemistry on a global scale. In terms of laboratory work, further experiments on the role of organics and organic films, possibly using real seawater samples, would be beneficial to ascertain whether these can have an inhibitory effect which may be important under low wind speed conditions.

Concurrent measurements of reactive iodine species in the air and iodide in surface seawater using ship-based measurements would help to remove some of the uncertainties related to the iodide-SST parameterisation. Improving the detection limits of the available instruments for reactive iodine measurements would also be beneficial, particularly for night-time measurements of I_2 which would help to verify that this inorganic mechanism is functioning in dark conditions. In addition, field measurements in more polluted locations, such as off the coasts of North America and China, would be useful to determine whether this additional mechanism, which will increase in the presence of increased O_3 concentrations, could help to limit the concentrations of O_3 in these regions.

Finally, use of the parameterised expressions derived in this thesis in global models will help our understanding of iodine chemistry in the MBL and higher up in the free troposphere. By combining the global model results with the increasing number of measurements of reactive iodine species over the open oceans, these expressions may

be further refined to improve our predictions of how the impact of iodine on tropospheric chemistry might change with a changing climate.

Bibliography

Abrahamsson, K., Lorén, A., Wulff, A., and Wängberg, S.-Å.: Air–sea exchange of halocarbons: the influence of diurnal and regional variations and distribution of pigments, Deep Sea Research Part II: Topical Studies in Oceanography, 51, 2789-2805, 2004.

Aiuppa, A., Federico, C., Franco, A., Giudice, G., Gurrieri, S., Inguaggiato, S., Liuzzo, M., McGonigle, A. J. S., and Valenza, M.: Emission of bromine and iodine from Mount Etna volcano, Geochem. Geophys. Geosyst., 6, 2005.

Aiuppa, A., Baker, D. R., and Webster, J. D.: Halogens in volcanic systems, Chem. Geol., 263, 1-18, 2009.

Alicke, B., Hebestreit, K., Stutz, J., and Platt, U.: Iodine oxide in the marine boundary layer, Nature, 397, 572-573, 1999.

Allan, B. J., McFiggans, G., Plane, J. M. C., and Coe, H.: Observations of iodine monoxide in the remote marine boundary layer, J. Geophys. Res.-Atmos., 105, 14363-14369, 2000.

Allan, B. J., Plane, J. M. C., and McFiggans, G.: Observations of OIO in the remote marine boundary layer, Geophys. Res. Lett., 28, 1945-1948, 2001.

Allan, J. D., Topping, D. O., Good, N., Irwin, M., Flynn, M., Williams, P. I., Coe, H., Baker, A. R., Martino, M., Niedermeier, N., Wiedensohler, A., Lehmann, S., Müller, K., Herrmann, H., and McFiggans, G.: Composition and properties of atmospheric particles in the eastern Atlantic and impacts on gas phase uptake rates, Atmos. Chem. Phys., 9, 9299-9314, 2009.

Andreae, M. O., and Crutzen, P. J.: Atmospheric aerosols: Biogeochemical sources and role in atmospheric chemistry, Science, 276, 1052-1058, 1997.

Archer, S. D., Goldson, L. E., Liddicoat, M. I., Cummings, D. G., and Nightingale, P. D.: Marked seasonality in the concentrations and sea-to-air flux of volatile iodocarbon compounds in the western English Channel, J. Geophys. Res.-Oceans, 112, 2007.

Arnold, S. R., Spracklen, D. V., Gebhardt, S., Custer, T., Williams, J., Peeken, I., and Alvain, S.: Relationships between atmospheric organic compounds and air-mass exposure to marine biology, Environ. Chem., 7, 232-241, 2010.

Ashu-Ayem, E. R., Nitschke, U., Monahan, C., Chen, J., Darby, S. B., Smith, P. D., O'Dowd, C. D., Stengel, D. B., and Venables, D. S.: Coastal Iodine Emissions. 1. Release of I_2 by Laminaria digitata in Chamber Experiments, Environ. Sci. Technol., 46, 10413-10421, 2012.

Ayers, G. P., Gillett, R. W., Cainey, J. M., and Dick, A. L.: Chloride and bromide loss from sea-salt particles in southern ocean air, J. Atmos. Chem., 33, 299-319, 1999.

Baidar, S., Oetjen, H., Coburn, S., Dix, B., Ortega, I., Sinreich, R., and Volkamer, R.: The CU Airborne MAX-DOAS instrument: vertical profiling of aerosol extinction and trace gases, Atmos. Meas. Tech., 6, 719-739, 2013.

Baker, A. R., Thompson, D., Campos, M., Parry, S. J., and Jickells, T. D.: Iodine concentration and availability in atmospheric aerosol, Atmos. Environ., 34, 4331-4336, 2000.

Baker, A. R.: Marine Aerosol Iodine Chemistry: The Importance of Soluble Organic Iodine, Environ. Chem., 2, 295-298, 2005.

Bale, C. S. E., Ingham, T., Commane, R., Heard, D. E., and Bloss, W. J.: Novel measurements of atmospheric iodine species by resonance fluorescence, J. Atmos. Chem., 60, 51-70, 2008.

Ball, S. M., Hollingsworth, A. M., Humbles, J., Leblanc, C., Potin, P., and McFiggans, G.: Spectroscopic studies of molecular iodine emitted into the gas phase by seaweed, Atmos. Chem. Phys., 10, 6237-6254, 2010.

Barrie, L. A., Bottenheim, J. W., Schnell, R. C., Crutzen, P. J., and Rasmussen, R. A.: Ozone destruction and photochemical reactions at polar sunrise in the lower Arctic atmosphere, Nature, 334, 138-141, 1988.

Baxter, G. P., and Grose, M. R.: The vapor pressure of iodine between 50 degrees and 95 degrees, J. Am. Chem. Soc., 37, 1061-1072, 1915.

Behnke, W., Kruger, H. U., Scheer, V., and Zetzsch, C.: Formation of atomic Cl from sea spray via photolysis of nitryl chloride - determination of the sticking coefficient of N_2O_5 on NaCl aerosol, J. Aerosol. Sci., 22, S609-S612, 1991.

Berner, A., A. C. Lindner, G. P. Reischl & W. Winklmayr: Operating Instructions - Electrical Mobility Spectrometer EMS VIE-10, in, tapcon & analysesysteme GmbH, 2006.

Bichsel, Y., and von Gunten, U.: Hypoiodous acid: Kinetics of the buffer-catalyzed disproportionation, Water Res., 34, 3197-3203, 2000.

Bitter, M., Ball, S. M., Povey, I. M., and Jones, R. L.: A broadband cavity ringdown spectrometer for in-situ measurements of atmospheric trace gases, Atmos. Chem. Phys., 5, 2547-2560, 2005.

Bloss, W. J., Lee, J. D., Johnson, G. P., Sommariva, R., Heard, D. E., Saiz-Lopez, A., Plane, J. M. C., McFiggans, G., Coe, H., Flynn, M., Williams, P., Rickard, A. R., and Fleming, Z. L.: Impact of halogen monoxide chemistry upon boundary layer OH and HO_2 concentrations at a coastal site, Geophys. Res. Lett., 32, 2005.

Bobrowski, N., Honninger, G., Galle, B., and Platt, U.: Detection of bromine monoxide in a volcanic plume, Nature, 423, 273-276, 2003.

Bobrowski, N., and Platt, U.: SO_2/BrO ratios studied in five volcanic plumes, J. Volcanol. Geotherm. Res., 166, 147-160, 2007.

Bobrowski, N., von Glasow, R., Aiuppa, A., Inguaggiato, S., Louban, I., Ibrahim, O. W., and Platt, U.: Reactive halogen chemistry in volcanic plumes, J. Geophys. Res.-Atmos., 112, 2007.

Bogumil, K., Orphal, J., Homann, T., Voigt, S., Spietz, P., Fleischmann, O. C., Vogel, A., Hartmann, M., Kromminga, H., Bovensmann, H., Frerick, J., and Burrows, J. P.: Measurements of molecular absorption spectra with the SCIAMACHY pre-flight model: instrument characterization and reference data for atmospheric remote-sensing in the 230-2380 nm region, J. Photochem. Photobiol. A-Chem., 157, 167-184, 2003.

Brechtel, F. J., Kreidenweis, S. M., and Swan, H. B.: Air mass characteristics, aerosol particle number concentrations, and number size distributions at Macquarie Island

during the First Aerosol Characterization Experiment (ACE 1), Journal of Geophysical Research: Atmospheres, 103, 16351-16367, 1998.

Brewer, A. W., McElroy, C. T., and Kerr, J. B.: Nitrogen dioxide concentrations in the atmosphere, Nature, 246, 129-133, 1973.

Burrows, J. P., Holzle, E., Goede, A. P. H., Visser, H., and Fricke, W.: SCIAMACHY - SCanning Imaging Absorption spectroMeter for Atmospheric CHartographY, Acta Astronaut., 35, 445-451, 1995.

Butler, J. H., King, D. B., Lobert, J. M., Montzka, S. A., Yvon-Lewis, S. A., Hall, B. D., Warwick, N. J., Mondeel, D. J., Aydin, M., and Elkins, J. W.: Oceanic distributions and emissions of short-lived halocarbons, Glob. Biogeochem. Cycle, 21, 2007.

Butz, A., Bosch, H., Camy-Peyret, C., Chipperfield, M. P., Dorf, M., Kreycy, S., Kritten, L., Prados-Roman, C., Schwarzle, J., and Pfeilsticker, K.: Constraints on inorganic gaseous iodine in the tropical upper troposphere and stratosphere inferred from balloon-borne solar occultation observations, Atmos. Chem. Phys., 9, 7229-7242, 2009.

Caleman, C., Hub, J. S., van Maaren, P. J., and van der Spoel, D.: Atomistic simulation of ion solvation in water explains surface preference of halides, Proceedings of the National Academy of Sciences of the United States of America, 108, 6838-6842, 2011.

Carlson, D., Donohoue, D., Platt, U., and Simpson, W. R.: A low power automated MAX-DOAS instrument for the Arctic and other remote unmanned locations, Atmos. Meas. Tech., 3, 429-439, 2010.

Carpenter, L. J., Sturges, W. T., Penkett, S. A., Liss, P. S., Alicke, B., Hebestreit, K., and Platt, U.: Short-lived alkyl iodides and bromides at Mace Head, Ireland: Links to biogenic sources and halogen oxide production, J. Geophys. Res.-Atmos., 104, 1679-1689, 1999.

Carpenter, L. J.: Iodine in the marine boundary layer, Chem. Rev., 103, 4953-4962, 2003.

Carpenter, L. J., Liss, P. S., and Penkett, S. A.: Marine organohalogens in the atmosphere over the Atlantic and Southern Oceans, J. Geophys. Res.-Atmos., 108, 2003.

Carpenter, L. J., Fleming, Z. L., Read, K. A., Lee, J. D., Moller, S. J., Hopkins, J. R., Purvis, R. M., Lewis, A. C., Müller, K., Heinold, B., Herrmann, H., Fomba, K. W., Pinxteren, D., Müller, C., Tegen, I., Wiedensohler, A., Müller, T., Niedermeier, N., Achterberg, E. P., Patey, M. D., Kozlova, E. A., Heimann, M., Heard, D. E., Plane, J. M. C., Mahajan, A., Oetjen, H., Ingham, T., Stone, D., Whalley, L. K., Evans, M. J., Pilling, M. J., Leigh, R. J., Monks, P. S., Karunaharan, A., Vaughan, S., Arnold, S. R., Tschritter, J., Pöhler, D., Frieß, U., Holla, R., Mendes, L. M., Lopez, H., Faria, B., Manning, A. J., and Wallace, D. W. R.: Seasonal characteristics of tropical marine boundary layer air measured at the Cape Verde Atmospheric Observatory, J. Atmos. Chem., 67, 87-140, 2010.

Chance, K. V., and Spurr, R. J. D.: Ring effect studies: Rayleigh scattering, including molecular parameters for rotational Raman scattering, and the Fraunhofer spectrum, Appl. Optics, 36, 5224-5230, 1997.

Chang, W. N., Heikes, B. G., and Lee, M. H.: Ozone deposition to the sea surface: chemical enhancement and wind speed dependence, Atmos. Environ., 38, 1053-1059, 2004.

Chapman, S.: A theory of upper-atmospheric ozone, Memoirs of the Royal Meteorological Society, 3, 103-125, 1930.

Clifford, D., and Donaldson, D. J.: Direct experimental evidence for a heterogeneous reaction of ozone with bromide at the air-aqueous interface, J. Phys. Chem. A, 111, 9809-9814, 2007.

Coburn, S., Dix, B., Sinreich, R., and Volkamer, R.: Development and characterization of the CU ground MAX-DOAS instrument: lowering RMS noise and first measurements of BrO, IO, and CHOCHO near Pensacola, FL, Atmos. Meas. Tech. Discuss., 4, 247-284, 2011.

Coleman, L., S. Varghese, O. P. Tripathi, S. G. Jennings, and C. D. O'Dowd: Regional-Scale Ozone Deposition to North-East Atlantic Waters, Advances in Meteorology, 2010.

Commane, R., Seitz, K., Bale, C. S. E., Bloss, W. J., Buxmann, J., Ingham, T., Platt, U., Pohler, D., and Heard, D. E.: Iodine monoxide at a clean marine coastal site:

observations of high frequency variations and inhomogeneous distributions, Atmos. Chem. Phys., 11, 6721-6733, 2011.

Corrigan, A. L., Hanley, S. W., and Haan, D. O.: Uptake of glyoxal by organic and inorganic aerosol, Environ. Sci. Technol., 42, 4428-4433, 2008.

Ćosović, B., Žutić, V., Vojvodić, V., and Pleše, T.: Determination of surfactant activity and anionic detergents in seawater and sea surface microlayer in the Mediterranean, Mar. Chem., 17, 127-139, 1985.

Courant, R., Friedrichs, K., and Lewy, H.: On the Partial Difference Equations of Mathematical Physics, Mathematische Annalen, 100, 32-74, 1928.

Cox, R. A., Bloss, W. J., Jones, R. L., and Rowley, D. M.: OIO and the atmospheric cycle of iodine, Geophys. Res. Lett., 26, 1857-1860, 1999.

Cunningham, E.: On the Velocity of Steady Fall of Spherical Particles through Fluid Medium, Proceedings of the Royal Society of London. Series A, 83, 357-365, 1910.

Davis, D., Crawford, J., Liu, S., McKeen, S., Bandy, A., Thornton, D., Rowland, F., and Blake, D.: Potential impact of iodine on tropospheric levels of ozone and other critical oxidants, J. Geophys. Res.-Atmos., 101, 2135-2147, 1996.

de Beek, R., Vountas, M., Rozanov, V. V., Richter, A., and Burrows, J. P.: The Ring Effect in the cloudy atmosphere, Geophys. Res. Lett., 28, 721-724, 2001.

Dix, B., Baidar, S., Bresch, J. F., Hall, S. R., Schmidt, K. S., Wang, S., and Volkamer, R.: Detection of iodine monoxide in the tropical free troposphere, Proceedings of the National Academy of Sciences of the United States of America, 110, 2035-2040, 2013.

Donguy, J. R., and Henin, C.: Surface conditions in the eastern equatorial Pacific related to the intertropical convergence zone of the winds, Deep-Sea Research Part a-Oceanographic Research Papers, 27, 693-714, 1980.

Dorf, M., Butz, A., Camy-Peyret, C., Chipperfield, M. P., Kritten, L., and Pfeilsticker, K.: Bromine in the tropical troposphere and stratosphere as derived from balloon-borne BrO observations, Atmos. Chem. Phys., 8, 7265-7271, 2008.

Edblom, E. C., Gyorgyi, L., Orban, M., and Epstein, I. R.: Systematic design of chemical oscillators. 40. A mechanism for dynamical behavior in the Landolt reaction with ferrocyanide, J. Am. Chem. Soc., 109, 4876-4880, 1987.

Elderfield, H., and Truesdale, V. W.: On the biophilic nature of iodine in seawater, Earth Planet. Sci. Lett., 50, 105-114, 1980.

Faria, R. D., Lengyel, I., Epstein, I. R., and Kustin, K.: Combined mechanism explaining nonlinear dynamics in bromine (III) and bromine (V) oxidations of iodide ion, J. Phys. Chem., 97, 1164-1171, 1993.

Fayt, C., and van Roozendael, M.: QDOAS 1.00. Software User Manual, in, 2011.

Fickert, S., Adams, J. W., and Crowley, J. N.: Activation of Br_2 and BrCl via uptake of HOBr onto aqueous salt solutions, J. Geophys. Res.-Atmos., 104, 23719-23727, 1999.

Finley, B. D., and Saltzman, E. S.: Observations of Cl_2, Br_2, and I_2 in coastal marine air, Journal of Geophysical Research: Atmospheres, 113, D21301, 2008.

Fish, D. J., and Jones, R. L.: Rotational Raman scattering and the Ring effect in zenith-sky spectra, Geophys. Res. Lett., 22, 811-814, 1995.

Flagan, R. C.: Differential Mobility Analysis of Aerosols: A Tutorial, KONA Powder Part. J., 26, 254-268, 2008.

Forster, P. M., and Ramaswamy, V.: Changes in Atmospheric Constituents and in Radiative Forcing, in: Climate Change 2007: The Physical Science Basis. Contribution of Working Group I to the Fourth Assessment Report of the Intergovernmental Panel on Climate Change, edited by: S. Solomon, D. Q., M. Manning, Z. Chen, M. Marquis, K.B. Averyt, M. Tignor, H.L. Miller, Cambridge University Press, 2007.

Frew, N. M.: The role of organic films in air-sea gas exchange, in: The Sea Surface and Global Change, edited by: Liss, P. S., and Duce, R. A., Cambridge University Press, Cambridge, 121-172, 1997.

Frew, N. M., Bock, E. J., Schimpf, U., Hara, T., Haußecker, H., Edson, J. B., McGillis, W. R., Nelson, R. K., McKenna, S. P., Uz, B. M., and Jähne, B.: Air-sea gas transfer: Its dependence on wind stress, small-scale roughness, and surface films, Journal of Geophysical Research: Oceans, 109, C08S17, 2004.

Friedman, A. M., and Kennedy, J. W.: The self-diffusion coefficients of potassium, cesium, iodide and chloride ions in aqueous solutions, J. Am. Chem. Soc., 77, 4499-4501, 1955.

Frieß, U., Wagner, T., Pundt, I., Pfeilsticker, K., and Platt, U.: Spectroscopic measurements of tropospheric iodine oxide at Neumayer Station, Antarctica, Geophys. Res. Lett., 28, 1941-1944, 2001.

Frieß, U., Deutschmann, T., Gilfedder, B. S., Weller, R., and Platt, U.: Iodine monoxide in the Antarctic snowpack, Atmos. Chem. Phys., 10, 2439-2456, 2010.

Frieß, U., Chipperfield, M. P., Harder, H., Otten, C., Platt, U., Pyle, J., Wagner, T., and Pfeilsticker, K.: Intercomparison of measured and modelled BrO slant column amounts for the Arctic winter and spring 1994/95, Geophys. Res. Lett., 26, 1861-1864, 1999.

Frieß, U., Sihler, H., Sander, R., Pohler, D., Yilmaz, S., and Platt, U.: The vertical distribution of BrO and aerosols in the Arctic: Measurements by active and passive differential optical absorption spectroscopy, J. Geophys. Res.-Atmos., 116, 2011.

Fuchs, N. A.: The mechanics of aerosols, Pergamon Press, New York, 1964.

Fumagalli, I., Gimeno, B. S., Velissariou, D., De Temmerman, L., and Mills, G.: Evidence of ozone-induced adverse effects on crops in the Mediterranean region, Atmos. Environ., 35, 2583-2587, 2001.

Furneaux, K. L., Whalley, L. K., Heard, D. E., Atkinson, H. M., Bloss, W. J., Flynn, M. J., Gallagher, M. W., Ingham, T., Kramer, L., Lee, J. D., Leigh, R., McFiggans, G. B., Mahajan, A. S., Monks, P. S., Oetjen, H., Plane, J. M. C., and Whitehead, J. D.: Measurements of iodine monoxide at a semi polluted coastal location, Atmos. Chem. Phys., 10, 3645-3663, 2010.

Furrow, S.: Reactions of iodine intermediates in iodate hydrogen-peroxide oscillators, J. Phys. Chem., 91, 2129-2135, 1987.

Gallagher, M. W., Beswick, K. M., and Coe, H.: Ozone deposition to coastal waters, Q. J. R. Meteorol. Soc., 127, 539-558, 2001.

Ganzeveld, L.: Atmosphere-ocean ozone exchange: A global modeling study of biogeochemical, atmospheric, and waterside turbulence dependencies, Glob. Biogeochem. Cycles, 23, GB4021, 2009.

Garland, J. A., Elzerman, A. W., and Penkett, S. A.: The mechanism for dry deposition of ozone to seawater surfaces, Journal of Geophysical Research-Oceans and Atmospheres, 85, 7488-7492, 1980.

Garland, J. A., and Curtis, H.: Emission of iodine from the sea-surface in the presence of ozone, Journal of Geophysical Research-Oceans and Atmospheres, 86, 3183-3186, 1981.

Ghosal, S., Hemminger, J. C., Bluhm, H., Mun, B. S., Hebenstreit, E. L. D., Ketteler, G., Ogletree, D. F., Requejo, F. G., and Salmeron, M.: Electron spectroscopy of aqueous solution interfaces reveals surface enhancement of halides, Science, 307, 563-566, 2005.

Giauque, W. F., Hornung, E. W., Kunzler, J. E., and Rubin, T. R.: The Thermodynamic Properties of Aqueous Sulfuric Acid Solutions and Hydrates from 15 to 300°K.1, J. Am. Chem. Soc., 82, 62-70, 1960.

Gilfedder, B. S., Petri, M., and Biester, H.: Iodine and bromine speciation in snow and the effect of orographically induced precipitation, Atmos. Chem. Phys., 7, 2661-2669, 2007a.

Gilfedder, B. S., Petri, M., and Biester, H.: Iodine speciation in rain and snow: Implications for the atmospheric iodine sink, J. Geophys. Res.-Atmos., 112, 2007b.

Gilfedder, B. S., Lai, S. C., Petri, M., Biester, H., and Hoffmann, T.: Iodine speciation in rain, snow and aerosols, Atmos. Chem. Phys., 8, 6069-6084, 2008.

Gilfedder, B. S., Chance, R., Dettmann, U., Lai, S. C., and Baker, A. R.: Determination of total and non-water soluble iodine in atmospheric aerosols by thermal extraction and spectrometric detection (TESI), Anal. Bioanal. Chem., 398, 519-526, 2010.

Gladich, I., Shepson, P. B., Carignano, M. A., and Szleifer, I.: Halide Affinity for the Water-Air Interface in Aqueous Solutions of Mixtures of Sodium Salts, J. Phys. Chem. A, 115, 5895-5899, 2011.

Goldman, J. C., Dennett, M. R., and Frew, N. M.: Surfactant effects on air-sea gas exchange under turbulent conditions, Deep Sea Research Part A. Oceanographic Research Papers, 35, 1953-1970, 1988.

Gómez Martín, J. C., Spietz, P., and Burrows, J. P.: Spectroscopic studies of the I_2/O_3 photochemistry - Part 1: Determination of the absolute absorption cross sections of iodine oxides of atmospheric relevance, J. Photochem. Photobiol. A-Chem., 176, 15-38, 2005.

Gómez Martín, J. C., Ashworth, S. H., Mahajan, A. S., and Plane, J. M. C.: Photochemistry of OIO: Laboratory study and atmospheric implications, Geophys. Res. Lett., 36, L09802, 2009.

Gómez Martín, J. C., Blahins, J., Gross, U., Ingham, T., Goddard, A., Mahajan, A. S., Ubelis, A., and Saiz-Lopez, A.: In situ detection of atomic and molecular iodine using Resonance and Off-Resonance Fluorescence by Lamp Excitation: ROFLEX, Atmos. Meas. Tech., 4, 29-45, 2011.

Gómez Martín, J. C., Mahajan, A. S., Hay, T. D., Prados-Román, C., Ordóñez, C., MacDonald, S. M., Plane, J. M. C., Sorribas, M., Gil, M., Paredes Mora, J. F., Agama Reyes, M. V., Oram, D. E., Leedham, E., and Saiz-Lopez, A.: Iodine chemistry in the eastern Pacific marine boundary layer, Journal of Geophysical Research: Atmospheres, 118, 887-904, 2013.

Gómez Martín, J. C., Galvez, O., Baeza-Romero, M. T., Ingham, T., Plane, J. M. C., and Blitz, M. A.: On the mechanism of iodine oxide particle formation, Phys. Chem. Chem. Phys., 2013.

Goodsite, M. E., Plane, J. M. C., and Skov, H.: A theoretical study of the oxidation of Hg^0 to $HgBr_2$ in the troposphere, Environ. Sci. Technol., 38, 1772-1776, 2004.

Graham, M. H., Kinlan, B. P., Druehl, L. D., Garske, L. E., and Banks, S.: Deep-water kelp refugia as potential hotspots of tropical marine diversity and productivity, Proceedings of the National Academy of Sciences of the United States of America, 104, 16576-16580, 2007.

Grainger, J. F., and Ring, J.: Anomalous Fraunhofer line profiles, Nature, 193, 762-&, 1962.

Graves, R., Leigh, R. J., Anand, J., McNally, M., Lawrence, J., and Monks, P. S.: A Tale of Two Cities - HSI-DOAS Measurements of Air Quality, in, EGU General Assembly, Vienna, Austria, 2013.

Groβmann, K., Frieβ, U., Peters, E., Wittrock, F., Lampel, J., Yilmaz, S., Tschritter, J., Sommariva, R., von Glasow, R., Quack, B., Kruger, K., Pfeilsticker, K., and Platt, U.: Iodine monoxide in the Western Pacific marine boundary layer, Atmospheric Chemistry and Physics Discussions, 12, 27475-27519, 2012.

Groβmann, K., Frieβ, U., Peters, E., Wittrock, F., Lampel, J., Yilmaz, S., Tschritter, J., Sommariva, R., von Glasow, R., Quack, B., Krüger, K., Pfeilsticker, K., and Platt, U.: Iodine monoxide in the Western Pacific marine boundary layer, Atmos. Chem. Phys., 13, 3363-3378, 2013.

Guenther, A., Hewitt, C. N., Erickson, D., Fall, R., Geron, C., Graedel, T., Harley, P., Klinger, L., Lerdau, M., McKay, W. A., Pierce, T., Scholes, B., Steinbrecher, R., Tallamraju, R., Taylor, J., and Zimmerman, P.: A global model of natural volatile organic compound emissions, J. Geophys. Res.-Atmos., 100, 8873-8892, 1995.

Guo, Z., and Roache, N. F.: Overall mass transfer coefficient for pollutant emissions from small water pools under simulated indoor environmental conditions, Ann. Occup. Hyg., 47, 279-286, 2003.

Hansell, D. A., Carlson, C. A., Repeta, D. J., and Schlitzer, R.: Dissolved organic matter in the ocean: A controversy stimulates new insights, Oceanography, 22, 202-211, 2009.

Hausmann, M., and Platt, U.: Spectroscopic measurement of bromine oxide and ozone in the high Arctic during Polar Sunrise Experiment 1992, Journal of Geophysical Research: Atmospheres, 99, 25399-25413, 1994.

Hay, T. D., Bodeker, G. E., Kreher, K., Schofield, R., Liley, J. B., Scherer, M., and McDonald, A. J.: The NIMO Monte Carlo model for box-air-mass factor and radiance calculations, Journal of Quantitative Spectroscopy and Radiative Transfer, 113, 721-738, 2012.

Hayase, S., Yabushita, A., Kawasaki, M., Enami, S., Hoffmann, M. R., and Colussi, A. J.: Heterogeneous Reaction of Gaseous Ozone with Aqueous Iodide in the Presence of Aqueous Organic Species, J. Phys. Chem. A, 114, 6016-6021, 2010.

Hayase, S., Yabushita, A., and Kawasaki, M.: Iodine Emission in the Presence of Humic Substances at the Water's Surface, J. Phys. Chem. A, 116, 5779-5783, 2012.

Hayes, S. P., McPhaden, M. J., and Wallace, J. M.: The influence of sea-surface temperature on surface wind in the eastern equatorial Pacific - weekly to monthly variability, J. Clim., 2, 1500-1506, 1989.

Heintzenberg, J., Covert, D. C., and Van Dingenen, R.: Size distribution and chemical composition of marine aerosols: a compilation and review, Tellus B, 52, 1104-1122, 2000.

Heue, K. P., Wagner, T., Broccardo, S. P., Walter, D., Piketh, S. J., Ross, K. E., Beirle, S., and Platt, U.: Direct observation of two dimensional trace gas distributions with an airborne Imaging DOAS instrument, Atmos. Chem. Phys., 8, 6707-6717, 2008.

Hill, V. L., and Manley, S. L.: Release of reactive bromine and iodine from diatoms and its possible role in halogen transfer in polar and tropical oceans, Limnology and Oceanography, 54, 812-822, 2009.

Honninger, G., and Platt, U.: Observations of BrO and its vertical distribution during surface ozone depletion at Alert, Atmos. Environ., 36, 2481-2489, 2002.

Honninger, G., Bobrowski, N., Palenque, E. R., Torrez, R., and Platt, U.: Reactive bromine and sulfur emissions at Salar de Uyuni, Bolivia, Geophys. Res. Lett., 31, 2004a.

Honninger, G., Leser, H., Sebastian, O., and Platt, U.: Ground-based measurements of halogen oxides at the Hudson Bay by active longpath DOAS and passive MAX-DOAS, Geophys. Res. Lett., 31, 2004b.

Hore, D. K., Beaman, D. K., and Richmond, G. L.: Surfactant headgroup orientation at the air/water interface, J. Am. Chem. Soc., 127, 9356-9357, 2005.

Hu, J. H., Shi, Q., Davidovits, P., Worsnop, D. R., Zahniser, M. S., and Kolb, C. E.: Reactive Uptake of $Cl_{2(g)}$ and $Br_{2(g)}$ by Aqueous Surfaces as a Function of Br^- and I^- Ion

Concentration: The Effect of Chemical Reaction at the Interface, The Journal of Physical Chemistry, 99, 8768-8776, 1995.

Huang, R. J., Seitz, K., Buxmann, J., Pohler, D., Hornsby, K. E., Carpenter, L. J., Platt, U., and Hoffmann, T.: In situ measurements of molecular iodine in the marine boundary layer: the link to macroalgae and the implications for O_3, IO, OIO and NO(x), Atmos. Chem. Phys., 10, 4823-4833, 2010.

Huang, R. J., Thorenz, U. R., Kundel, M., Venables, D. S., Ceburnis, D., Ho, K. F., Chen, J., Vogel, A. L., Küpper, F. C., Smyth, P. P. A., Nitschke, U., Stengel, D. B., Berresheim, H., O'Dowd, C. D., and Hoffmann, T.: The seaweeds Fucus vesiculosus and Ascophyllum nodosum are significant contributors to coastal iodine emissions, Atmos. Chem. Phys., 13, 5255-5264, 2013.

Huang, Z., Ito, K., Morita, I., Yokota, K., Fukushi, K., Timerbaev, A. R., Watanabe, S., and Hirokawa, T.: Sensitive monitoring of iodine species in sea water using capillary electrophoresis: vertical profiles of dissolved iodine in the Pacific Ocean, J. Environ. Monit., 7, 804-808, 2005.

Hunter, K. A., and Liss, P. S.: Input of organic material to oceans: air-sea interactions and organic chemical composition of the sea-surface, Mar. Chem., 5, 361-379, 1977.

Jacob, D. J.: Introduction to Atmospheric Chemistry, Princeton University Press, Princeton, New Jersey, USA, 1999.

Jacobson, M. Z.: Fundamentals of Atmospheric Modeling, Second ed., Cambridge University Press, New York, 2005.

Jickells, T. D., Boyd, S. S., and Knap, A. H.: Iodine cycling in the Sargasso Sea and the Bermuda inshore waters, Mar. Chem., 24, 61-82, 1988.

Jickells, T. D., An, Z. S., Andersen, K. K., Baker, A. R., Bergametti, G., Brooks, N., Cao, J. J., Boyd, P. W., Duce, R. A., Hunter, K. A., Kawahata, H., Kubilay, N., laRoche, J., Liss, P. S., Mahowald, N., Prospero, J. M., Ridgwell, A. J., Tegen, I., and Torres, R.: Global iron connections between desert dust, ocean biogeochemistry, and climate, Science, 308, 67-71, 2005.

Johnson, M. T.: A numerical scheme to calculate temperature and salinity dependent air-water transfer velocities for any gas, Ocean Sci., 6, 913-932, 2010.

Jones, C. E., Hornsby, K. E., Dunk, R. M., Leigh, R. J., and Carpenter, L. J.: Coastal measurements of short-lived reactive iodocarbons and bromocarbons at Roscoff, Brittany during the RHaMBLe campaign, Atmos. Chem. Phys., 9, 8757-8769, 2009.

Jones, C. E., Hornsby, K. E., Sommariva, R., Dunk, R. M., Von Glasow, R., McFiggans, G., and Carpenter, L. J.: Quantifying the contribution of marine organic gases to atmospheric iodine, Geophys. Res. Lett., 37, 2010.

Kampa, M., and Castanas, E.: Human health effects of air pollution, Environmental Pollution, 151, 362-367, 2008.

Karlsson, A., Auer, N., Schulz-Bull, D., and Abrahamsson, K.: Cyanobacterial blooms in the Baltic — A source of halocarbons, Mar. Chem., 110, 129-139, 2008.

Kasten, F.: Falling Speed of Aerosol Particles, Journal of Applied Meteorology, 7, 944-947, 1968.

Keene, W. C., Khalil, M. A. K., Erickson, D. J., McCulloch, A., Graedel, T. E., Lobert, J. M., Aucott, M. L., Gong, S. L., Harper, D. B., Kleiman, G., Midgley, P., Moore, R. M., Seuzaret, C., Sturges, W. T., Benkovitz, C. M., Koropalov, V., Barrie, L. A., and Li, Y. F.: Composite global emissions of reactive chlorine from anthropogenic and natural sources: Reactive Chlorine Emissions Inventory, J. Geophys. Res.-Atmos., 104, 8429-8440, 1999.

Keppler, F., Eiden, R., Niedan, V., Pracht, J., and Scholer, H. F.: Halocarbons produced by natural oxidation processes during degradation of organic matter, Nature, 403, 298-301, 2000.

Kern, C., Sihler, H., Vogel, L., Rivera, C., Herrera, M., and Platt, U.: Halogen oxide measurements at Masaya Volcano, Nicaragua using active long path differential optical absorption spectroscopy, Bull. Volcanol., 71, 659-670, 2009.

Kessler, W. S.: The circulation of the eastern tropical Pacific: A review, Progress in Oceanography, 69, 181-217, 2006.

Knudsen, M., and Weber, S.: Luftwiderstand gegen die langsame Bewegung kleiner Kugeln, Annalen der Physik, 341, 981-994, 1911.

Knutson, E. O., and Whitby, K. T.: Aerosol classification by electric mobility: apparatus, theory, and applications, J. Aerosol. Sci., 6, 443-451, 1975.

Krol, M., and Lelieveld, J.: Can the variability in tropospheric OH be deduced from measurements of 1,1,1-trichloroethane (methyl chloroform)?, J. Geophys. Res.-Atmos., 108, 11, 2003.

Kumar, R., Saunders, R. W., Mahajan, A. S., Plane, J. M. C., and Murray, B. J.: Physical properties of iodate solutions and the deliquescence of crystalline I_2O_5 and HIO_3, Atmos. Chem. Phys., 10, 12251-12260, 2010.

Küpper, F. C., Carpenter, L. J., McFiggans, G. B., Palmer, C. J., Waite, T. J., Boneberg, E.-M., Woitsch, S., Weiller, M., Abela, R., Grolimund, D., Potin, P., Butler, A., Luther, G. W., Kroneck, P. M. H., Meyer-Klaucke, W., and Feiters, M. C.: Iodide accumulation provides kelp with an inorganic antioxidant impacting atmospheric chemistry, Proceedings of the National Academy of Sciences, 105, 6954-6958, 2008.

Lai, S. C., Hoffmann, T., and Xie, Z. Q.: Iodine speciation in marine aerosols along a 30,000 km round-trip cruise path from Shanghai, China to Prydz Bay, Antarctica, Geophys. Res. Lett., 35, 2008.

Lai, S. C., Williams, J., Arnold, S. R., Atlas, E. L., Gebhardt, S., and Hoffmann, T.: Iodine containing species in the remote marine boundary layer: A link to oceanic phytoplankton, Geophys. Res. Lett., 38, 2011.

Lee, C., Kim, Y. J., Tanimoto, H., Bobrowski, N., Platt, U., Mori, T., Yamamoto, K., and Hong, C. S.: High ClO and ozone depletion observed in the plume of Sakurajima volcano, Japan, Geophys. Res. Lett., 32, 2005a.

Lee, H., Kim, Y. J., Jung, J., Lee, C., Heue, K. P., Platt, U., Hu, M., and Zhu, T.: Spatial and temporal variations in NO_2 distributions over Beijing, China measured by imaging differential optical absorption spectroscopy, J. Environ. Manage., 90, 1814-1823, 2009a.

Lee, H. M., Kim, C. S., Shimada, M., and Okuyama, K.: Bipolar diffusion charging for aerosol nanoparticle measurement using a soft X-ray charger, J. Aerosol. Sci., 36, 813-829, 2005b.

Lee, J. D., Moller, S. J., Read, K. A., Lewis, A. C., Mendes, L., and Carpenter, L. J.: Year-round measurements of nitrogen oxides and ozone in the tropical North Atlantic marine boundary layer, Journal of Geophysical Research: Atmospheres, 114, D21302, 2009b.

Lee, J. D., McFiggans, G., Allan, J. D., Baker, A. R., Ball, S. M., Benton, A. K., Carpenter, L. J., Commane, R., Finley, B. D., Evans, M., Fuentes, E., Furneaux, K., Goddard, A., Good, N., Hamilton, J. F., Heard, D. E., Herrmann, H., Hollingsworth, A., Hopkins, J. R., Ingham, T., Irwin, M., Jones, C. E., Jones, R. L., Keene, W. C., Lawler, M. J., Lehmann, S., Lewis, A. C., Long, M. S., Mahajan, A., Methven, J., Moller, S. J., Müller, K., Müller, T., Niedermeier, N., O'Doherty, S., Oetjen, H., Plane, J. M. C., Pszenny, A. A. P., Read, K. A., Saiz-Lopez, A., Saltzman, E. S., Sander, R., von Glasow, R., Whalley, L., Wiedensohler, A., and Young, D.: Reactive Halogens in the Marine Boundary Layer (RHaMBLe): the tropical North Atlantic experiments, Atmos. Chem. Phys., 10, 1031-1055, 2010.

Leigh, R. J., Ball, S. M., Whitehead, J., Leblanc, C., Shillings, A. J. L., Mahajan, A. S., Oetjen, H., Lee, J. D., Jones, C. E., Dorsey, J. R., Gallagher, M., Jones, R. L., Plane, J. M. C., Potin, P., and McFiggans, G.: Measurements and modelling of molecular iodine emissions, transport and photodestruction in the coastal region around Roscoff, Atmos. Chem. Phys., 10, 11823-11838, 2010.

Lengyel, I., Epstein, I. R., and Kustin, K.: Kinetics of iodine hydrolysis, Inorganic Chemistry, 32, 5880-5882, 1993.

Liss, P. S., and Slater, P. G.: Flux of gases across the air-sea interface, Nature, 247, 181-184, 1974.

Liu, Q., Schurter, L. M., Muller, C. E., Aloisio, S., Francisco, J. S., and Margerum, D. W.: Kinetics and mechanisms of aqueous ozone reactions with bromide, sulfite, hydrogen sulfite, iodide, and nitrite ions, Inorganic Chemistry, 40, 4436-4442, 2001.

Logan, J. A.: Tropospheric ozone: Seasonal behavior, trends, and anthropogenic influence, Journal of Geophysical Research: Atmospheres, 90, 10463-10482, 1985.

Louban, I., Bobrowski, N., Rouwet, D., Inguaggiato, S., and Platt, U.: Imaging DOAS for volcanological applications, Bull. Volcanol., 71, 753-765, 2009.

Magi, L., Schweitzer, F., Pallares, C., Cherif, S., Mirabel, P., and George, C.: Investigation of the uptake rate of ozone and methyl hydroperoxide by water surfaces, J. Phys. Chem. A, 101, 4943-4949, 1997.

Mahajan, A. S.: Reactive halogen species in the marine boundary layer, PhD, University of Leeds, 2009.

Mahajan, A. S., Oetjen, H., Lee, J. D., Saiz-Lopez, A., McFiggans, G. B., and Plane, J. M. C.: High bromine oxide concentrations in the semi-polluted boundary layer, Atmos. Environ., 43, 3811-3818, 2009a.

Mahajan, A. S., Oetjen, H., Saiz-Lopez, A., Lee, J. D., McFiggans, G. B., and Plane, J. M. C.: Reactive iodine species in a semi-polluted environment, Geophys. Res. Lett., 36, 2009b.

Mahajan, A. S., Plane, J. M. C., Oetjen, H., Mendes, L., Saunders, R. W., Saiz-Lopez, A., Jones, C. E., Carpenter, L. J., and McFiggans, G. B.: Measurement and modelling of tropospheric reactive halogen species over the tropical Atlantic Ocean, Atmos. Chem. Phys., 10, 4611-4624, 2010a.

Mahajan, A. S., Shaw, M., Oetjen, H., Hornsby, K. E., Carpenter, L. J., Kaleschke, L., Tian-Kunze, X., Lee, J. D., Moller, S. J., Edwards, P., Commane, R., Ingham, T., Heard, D. E., and Plane, J. M. C.: Evidence of reactive iodine chemistry in the Arctic boundary layer, J. Geophys. Res.-Atmos., 115, 11, 2010b.

Mahajan, A. S., Whalley, L. K., Kozlova, E., Oetjen, H., Mendez, L., Furneaux, K. L., Goddard, A., Heard, D. E., Plane, J. M. C., and Saiz-Lopez, A.: DOAS observations of formaldehyde and its impact on the HO_x balance in the tropical Atlantic marine boundary layer, J. Atmos. Chem., 66, 167-178, 2010c.

Mahajan, A. S., Sorribas, M., Gómez Martín, J. C., MacDonald, S. M., Gil, M., Plane, J. M. C., and Saiz-Lopez, A.: Concurrent observations of atomic iodine, molecular iodine and ultrafine particles in a coastal environment, Atmos. Chem. Phys., 11, 2545-2555, 2011.

Mahajan, A. S., Martin, J. C. G., Hay, T. D., Royer, S. J., Yvon-Lewis, S., Liu, Y., Hu, L., Prados-Roman, C., Ordonez, C., Plane, J. M. C., and Saiz-Lopez, A.: Latitudinal distribution of reactive iodine in the Eastern Pacific and its link to open ocean sources, Atmos. Chem. Phys., 12, 11609-11617, 2012.

Margerum, D. W., Dickson, P. N., Nagy, J. C., Kumar, K., Bowers, C. P., and Fogelman, K. D.: Kinetics of the iodine monochloride reaction with iodide measured by the pulsed-accelerated-flow method, Inorganic Chemistry, 25, 4900-4904, 1986.

Marquard, L. C., Wagner, T., and Platt, U.: Improved air mass factor concepts for scattered radiation differential optical absorption spectroscopy of atmospheric species, J. Geophys. Res.-Atmos., 105, 1315-1327, 2000.

Martinez, M., Arnold, T., and Perner, D.: The role of bromine and chlorine chemistry for arctic ozone depletion events in Ny-Ålesund and comparison with model calculations, Ann. Geophys., 17, 941-956, 1999.

Martino, M., Liss, P. S., and Plane, J. M. C.: The photolysis of dihalomethanes in surface seawater, Environ. Sci. Technol., 39, 7097-7101, 2005.

Martino, M., Mills, G. P., Woeltjen, J., and Liss, P. S.: A new source of volatile organoiodine compounds in surface seawater, Geophys. Res. Lett., 36, 2009.

Martino, M., Leze, B., Baker, A. R., and Liss, P. S.: Chemical controls on ozone deposition to water, Geophys. Res. Lett., 39, 2012.

Matveev, V., Peleg, M., Rosen, D., Tov-Alper, D. S., Hebestreit, K., Stutz, J., Platt, U., Blake, D., and Luria, M.: Bromine oxide - ozone interaction over the Dead Sea, J. Geophys. Res.-Atmos., 106, 10375-10387, 2001.

McFiggans, G., Plane, J. M. C., Allan, B. J., Carpenter, L. J., Coe, H., and O'Dowd, C.: A modeling study of iodine chemistry in the marine boundary layer, Journal of Geophysical Research: Atmospheres, 105, 14371-14385, 2000.

McFiggans, G., Cox, R. A., Mossinger, J. C., Allan, B. J., and Plane, J. M. C.: Active chlorine release from marine aerosols: Roles for reactive iodine and nitrogen species, J. Geophys. Res.-Atmos., 107, 2002.

McFiggans, G., Coe, H., Burgess, R., Allan, J., Cubison, M., Alfarra, M. R., Saunders, R., Saiz-Lopez, A., Plane, J. M. C., Wevill, D. J., Carpenter, L. J., Rickard, A. R., and Monks, P. S.: Direct evidence for coastal iodine particles from Laminaria macroalgae - linkage to emissions of molecular iodine, Atmos. Chem. Phys., 4, 701-713, 2004.

McTaggart, A. R., Butler, E. C. V., Haddad, P. R., and Middleton, J. H.: Iodide and iodate concentrations in eastern Australian subtropical waters, with iodide by ion chromatography, Mar. Chem., 47, 159-172, 1994.

Meinen, J., Thieser, J., Platt, U., and Leisner, T.: Technical Note: Using a high finesse optical resonator to provide a long light path for differential optical absorption spectroscopy: CE-DOAS, Atmos. Chem. Phys., 10, 3901-3914, 2010.

Mochida, M., Kitamori, Y., Kawamura, K., Nojiri, Y., and Suzuki, K.: Fatty acids in the marine atmosphere: Factors governing their concentrations and evaluation of organic films on sea-salt particles, J. Geophys. Res.-Atmos., 107, 2002.

Moore, R. M., Webb, M., Tokarczyk, R., and Wever, R.: Bromoperoxidase and iodoperoxidase enzymes and production of halogenated methanes in marine diatom cultures, Journal of Geophysical Research: Oceans, 101, 20899-20908, 1996.

Nakayama, E., Kimoto, T., Isshiki, K., Sohrin, Y., and Okazaki, S.: Determination and distribution of iodide- and total-iodine in the North Pacific Ocean - by using a new automated electrochemical method, Mar. Chem., 27, 105-116, 1989.

Nightingale, P. D., Malin, G., Law, C. S., Watson, A. J., Liss, P. S., Liddicoat, M. I., Boutin, J., and Upstill-Goddard, R. C.: In situ evaluation of air-sea gas exchange parameterizations using novel conservative and volatile tracers, Glob. Biogeochem. Cycle, 14, 373-387, 2000.

Nitschke, U., Ruth, A. A., Dixneuf, S., and Stengel, D. B.: Molecular iodine emission rates and photosynthetic performance of different thallus parts of Laminaria digitata (Phaeophyceae) during emersion, Planta, 233, 737-748, 2011.

Noxon, J. F.: Nitrogen dioxide in the Stratosphere and Troposphere measured by ground-based absorption spectroscopy, Science, 189, 547-549, 1975.

Noxon, J. F.: Atmospheric nitrogen-fixation by lightning, Geophys. Res. Lett., 3, 463-465, 1976.

O'Dowd, C. D., Jimenez, J. L., Bahreini, R., Flagan, R. C., Seinfeld, J. H., Hameri, K., Pirjola, L., Kulmala, M., Jennings, S. G., and Hoffmann, T.: Marine aerosol formation from biogenic iodine emissions, Nature, 417, 632-636, 2002.

Oetjen, H.: Measurements of halogen oxides by scattered sunlight differential optical absorption spectroscopy, PhD, University of Bremen, 2009.

Oh, I. B., Byun, D. W., Kim, H. C., Kim, S., and Cameron, B.: Modeling the effect of iodide distribution on ozone deposition to seawater surface, Atmos. Environ., 42, 4453-4466, 2008.

Ordonez, C., Lamarque, J. F., Tilmes, S., Kinnison, D. E., Atlas, E. L., Blake, D. R., Santos, G. S., Brasseur, G., and Saiz-Lopez, A.: Bromine and iodine chemistry in a global chemistry-climate model: description and evaluation of very short-lived oceanic sources, Atmos. Chem. Phys., 12, 1423-1447, 2012.

Pak, H., and Zaneveld, J. R.: Equatorial front in the Eastern Pacific Ocean, J. Phys. Oceanogr., 4, 570-578, 1974.

Palmer, C. J., Anders, T. L., Carpenter, L. J., Küpper, F. C., and McFiggans, G. B.: Iodine and Halocarbon Response of Laminaria digitata to Oxidative Stress and Links to Atmospheric New Particle Production, Environ. Chem., 2, 282-290, 2005.

Palmer, D. A., Ramette, R. W., and Mesmer, R. E.: Triiodide ion formation equilibrium and activity coefficients in aqueous solution, Journal of Solution Chemistry, 13, 673-683, 1984.

Pechtl, S., Schmitz, G., and von Glasow, R.: Modelling iodide – iodate speciation in atmospheric aerosol: Contributions of inorganic and organic iodine chemistry, Atmos. Chem. Phys., 7, 1381-1393, 2007.

Pedersen, M., Collen, J., Abrahamsson, K., and Ekdahl, A.: Production of halocarbons from seaweeds: An oxidative stress reaction?, Sci. Mar., 60, 257-263, 1996.

Perliski, L. M., and Solomon, S.: On the evaluation of air mass factors for atmospheric near-ultraviolet and visible absorption spectroscopy, J. Geophys. Res.-Atmos., 98, 10363-10374, 1993.

Peters, C., Pechtl, S., Stutz, J., Hebestreit, K., Honninger, G., Heumann, K. G., Schwarz, A., Winterlik, J., and Platt, U.: Reactive and organic halogen species in three different European coastal environments, Atmos. Chem. Phys., 5, 3357-3375, 2005.

Pfeilsticker, K., and Platt, U.: Airborne measurements during the Arctic Stratospheric Experiment - Observation of O_3 and NO_2, Geophys. Res. Lett., 21, 1375-1378, 1994.

Plane, J. M. C., and Nien, C. F.: Differential optical absorption spectrometer for measuring atmospheric trace gases, Rev. Sci. Instrum., 63, 1867-1876, 1992.

Plane, J. M. C., and Saiz-Lopez, A.: Differential Optical Absorption Spectroscopy, in: Analytical Techniques for Atmospheric Measurement, edited by: Heard, D. E., Blackwell Publishing, Oxford, 2006.

Platt, U., Perner, D., and Patz, H. W.: Simultaneous measurement of atmospheric CH_2O, O_3, and NO_2 by differential optical absorption, Journal of Geophysical Research-Oceans and Atmospheres, 84, 6329-6335, 1979.

Platt, U.: Differential optical absorption spectroscopy (DOAS), in: Air monitoring by spectroscopy techniques, edited by: Sigrist, M. W., John Wiley, London, 27-83, 1994.

Platt, U., Meinen, J., Pohler, D., and Leisner, T.: Broadband Cavity Enhanced Differential Optical Absorption Spectroscopy (CE-DOAS) - applicability and corrections, Atmos. Meas. Tech., 2, 713-723, 2009.

Pommereau, J. P., and Piquard, J.: Ozone and nitrogen dioxide vertical distributions by UV-Visible solar occultation from balloons, Geophys. Res. Lett., 21, 1227-1230, 1994.

Poschl, U.: Atmospheric aerosols: Composition, transformation, climate and health effects, Angew. Chem.-Int. Edit., 44, 7520-7540, 2005.

Prados-Roman, C., Butz, A., Deutschmann, T., Dorf, M., Kritten, L., Minikin, A., Platt, U., Schlager, H., Sihler, H., Theys, N., Van Roozendael, M., Wagner, T., and Pfeilsticker, K.: Airborne DOAS limb measurements of tropospheric trace gas profiles: case studies on the profile retrieval of O-4 and BrO, Atmos. Meas. Tech., 4, 1241-1260, 2011.

Press, W. H., Flannery, T. S., and Vetterlinng, W. T.: Numerical recipes: The art of scientific computing, University Press, Cambridge, 1986.

Prinn, R. G., Huang, J., Weiss, R. F., Cunnold, D. M., Fraser, P. J., Simmonds, P. G., McCulloch, A., Harth, C., Salameh, P., O'Doherty, S., Wang, R. H. J., Porter, L., and Miller, B. R.: Evidence for substantial variations of atmospheric hydroxyl radicals in the past two decades, Science, 292, 1882-1888, 2001.

Puentedura, O., Gil, M., Saiz-Lopez, A., Hay, T., Navarro-Comas, M., Gomez-Pelaez, A., Cuevas, E., Iglesias, J., and Gomez, L.: Iodine monoxide in the north subtropical free troposphere, Atmos. Chem. Phys., 12, 4909-4921, 2012.

Read, K. A., Mahajan, A. S., Carpenter, L. J., Evans, M. J., Faria, B. V. E., Heard, D. E., Hopkins, J. R., Lee, J. D., Moller, S. J., Lewis, A. C., Mendes, L., McQuaid, J. B., Oetjen, H., Saiz-Lopez, A., Pilling, M. J., and Plane, J. M. C.: Extensive halogen-mediated ozone destruction over the tropical Atlantic Ocean, Nature, 453, 1232-1235, 2008.

Read, K. A., Lee, J. D., Lewis, A. C., Moller, S. J., Mendes, L., and Carpenter, L. J.: Intra-annual cycles of NMVOC in the tropical marine boundary layer and their use for interpreting seasonal variability in CO, Journal of Geophysical Research: Atmospheres, 114, D21303, 2009.

Reiller, P., Mercier-Bion, F., Gimenez, N., Barre, N., and Miserque, F.: Iodination of humic acid samples from different origins, Radiochim. Acta, 94, 739-745, 2006.

Reischl, G. P.: Measurement of ambient aerosols by the differential mobility analyzer method - Concepts and realization criteria for the size range between 2 nm and 500 nm, Aerosol Sci. Technol., 14, 5-24, 1991.

Reischl, G. P., Makela, J. M., Karch, R., and Necid, J.: Bipolar charging of ultrafine particles in the size range below 10 nm, J. Aerosol. Sci., 27, 931-949, 1996.

Roberts, J. M., Osthoff, H. D., Brown, S. S., Ravishankara, A. R., Coffman, D., Quinn, P., and Bates, T.: Laboratory studies of products of N_2O_5 uptake on Cl^- containing substrates, Geophys. Res. Lett., 36, L20808, 2009.

Rodgers, C. D.: Inverse Methods for Atmospheric Sounding: Theory and Practice, 1st ed ed., World Scientific Publishing, Singapore, 2000.

Roscoe, H. K., Freshwater, R. A., Wolfenden, R., Jones, R. L., Fish, D. J., Harries, J. E., South, A. M., and Oldham, D. J.: Using stars for remote sensing of the Earth's stratosphere, Appl. Optics, 33, 7126-7131, 1994.

Roscoe, H. K., Johnston, P. V., Van Roozendael, M., Richter, A., Sarkissian, A., Roscoe, J., Preston, K. E., Lambert, J. C., Hermans, C., Decuyper, W., Dzienus, S., Winterrath, T., Burrows, J., Goutail, F., Pommereau, J. P., D'Almeida, E., Hottier, J., Coureul, C., Didier, R., Pundt, I., Bartlett, L. M., McElroy, C. T., Kerr, J. E., Elokhov, A., Giovanelli, G., Ravegnani, F., Premuda, M., Kostadinov, I., Erle, F., Wagner, T., Pfeilsticker, K., Kenntner, M., Marquard, L. C., Gil, M., Puentedura, O., Yela, M., Arlander, D. W., Hoiskar, B. A. K., Tellefsen, C. W., Tornkvist, K. K., Heese, B., Jones, R. L., Aliwell, S. R., and Freshwater, R. A.: Slant column measurements of O_3 and NO_2 during the NDSC intercomparison of zenith-sky UV-visible spectrometers in June 1996, J. Atmos. Chem., 32, 281-314, 1999.

Rothman, L. S., Barbe, A., Benner, D. C., Brown, L. R., Camy-Peyret, C., Carleer, M. R., Chance, K., Clerbaux, C., Dana, V., Devi, V. M., Fayt, A., Flaud, J. M., Gamache, R. R., Goldman, A., Jacquemart, D., Jucks, K. W., Lafferty, W. J., Mandin, J. Y., Massie, S. T., Nemtchinov, V., Newnham, D. A., Perrin, A., Rinsland, C. P., Schroeder, J., Smith, K. M., Smith, M. A. H., Tang, K., Toth, R. A., Vander Auwera, J., Varanasi, P., and Yoshino, K.: The HITRAN molecular spectroscopic database: edition of 2000 including updates through 2001, J. Quant. Spectrosc. Radiat. Transf., 82, 5-44, 2003.

Rouviere, A., and Ammann, M.: The effect of fatty acid surfactants on the uptake of ozone to aqueous halogenide particles, Atmos. Chem. Phys., 10, 11489-11500, 2010.

Rouviere, A., Sosedova, Y., and Ammann, M.: Uptake of Ozone to Deliquesced KI and Mixed KI/NaCl Aerosol Particles, J. Phys. Chem. A, 114, 7085-7093, 2010.

Roy, R.: Short-term variability in halocarbons in relation to phytoplankton pigments in coastal waters of the central eastern Arabian Sea, Estuarine, Coastal and Shelf Science, 88, 311-321, 2010.

Saiz-Lopez, A., and Plane, J. M. C.: Novel iodine chemistry in the marine boundary layer, Geophys. Res. Lett., 31, 2004a.

Saiz-Lopez, A., and Plane, J. M. C.: Recent applications of differential optical absorption spectroscopy: Halogen chemistry in the lower troposphere, J. Phys. IV, 121, 223-238, 2004b.

Saiz-Lopez, A., Saunders, R. W., Joseph, D. M., Ashworth, S. H., and Plane, J. M. C.: Absolute absorption cross-section and photolysis rate of I_2, Atmos. Chem. Phys., 4, 1443-1450, 2004c.

Saiz-Lopez, A., Shillito, J. A., Coe, H., and Plane, J. M. C.: Measurements and modelling of I_2, IO, OIO, BrO and NO_3 in the mid-latitude marine boundary layer, Atmos. Chem. Phys., 6, 1513-1528, 2006.

Saiz-Lopez, A., Chance, K., Liu, X., Kurosu, T. P., and Sander, S. P.: First observations of iodine oxide from space, Geophys. Res. Lett., 34, 2007a.

Saiz-Lopez, A., Mahajan, A. S., Salmon, R. A., Bauguitte, S. J.-B., Jones, A. E., Roscoe, H. K., and Plane, J. M. C.: Boundary Layer Halogens in Coastal Antarctica, Science, 317, 348-351, 2007b.

Saiz-Lopez, A., Mahajan, A. S., Salmon, R. A., Bauguitte, S. J. B., Jones, A. E., Roscoe, H. K., and Plane, J. M. C.: Boundary layer halogens in coastal Antarctica, Science, 317, 348-351, 2007c.

Saiz-Lopez, A., Plane, J. M. C., Mahajan, A. S., Anderson, P. S., Bauguitte, S. J. B., Jones, A. E., Roscoe, H. K., Salmon, R. A., Bloss, W. J., Lee, J. D., and Heard, D. E.: On the vertical distribution of boundary layer halogens over coastal Antarctica: implications for O_3, HO_x, NO_x and the Hg lifetime, Atmos. Chem. Phys., 8, 887-900, 2008.

Saiz-Lopez, A., Plane, J. M. C., Baker, A. R., Carpenter, L. J., von Glasow, R., Gómez Martín, J. C., McFiggans, G., and Saunders, R. W.: Atmospheric Chemistry of Iodine, Chem. Rev., 112, 1773-1804, 2011.

Saiz-Lopez, A., Lamarque, J. F., Kinnison, D. E., Tilmes, S., Ordonez, C., Orlando, J. J., Conley, A. J., Plane, J. M. C., Mahajan, A. S., Santos, G. S., Atlas, E. L., Blake, D. R., Sander, S. P., Schauffler, S., Thompson, A. M., and Brasseur, G.: Estimating the climate significance of halogen-driven ozone loss in the tropical marine troposphere, Atmos. Chem. Phys., 12, 3939-3949, 2012.

Sakamoto, Y., Yabushita, A., Kawasaki, M., and Enami, S.: Direct emission of I_2 molecule and IO radical from the heterogeneous reactions of gaseous ozone with aqueous potassium iodide solution, J. Phys. Chem. A, 113, 7707-7713, 2009.

Sander, R.: Compilation of Henry's Law Constants for Inorganic and Organic Species of Potential Importance in Environmental Chemistry, in, www.mcph-mainz.mpg.de/~sander/res/henry.html, 1999.

Saunders, R. W., and Plane, J. M. C.: Formation pathways and composition of iodine oxide ultra-fine particles, Environ. Chem., 2, 299-303, 2005.

Saunders, R. W., and Plane, J. M. C.: Fractal growth modelling of I_2O_5 nanoparticles, J. Aerosol. Sci., 37, 1737-1749, 2006.

Saunders, R. W., Kumar, R., Martin, J. C. G., Mahajan, A. S., Murray, B. J., and Plane, J. M. C.: Studies of the Formation and Growth of Aerosol from Molecular Iodine Precursor, Z. Phys. Chemie-Int. J. Res. Phys. Chem. Chem. Phys., 224, 1095-1117, 2010.

Saunders, R. W., Kumar, R., MacDonald, S. M., and Plane, J. M. C.: Insights into the Photochemical Transformation of Iodine in Aqueous Systems: Humic Acid Photosensitized Reduction of Iodate, Environ. Sci. Technol., 46, 11854-11861, 2012.

Schaeffer, B. A., Morrison, J. M., Kamykowski, D., Feldman, G. C., Xie, L., Liu, Y. Y., Sweet, W., McCulloch, A., and Banks, S.: Phytoplankton biomass distribution and identification of productive habitats within the Galapagos Marine Reserve by MODIS, a surface acquisition system, and in-situ measurements, Remote Sens. Environ., 112, 3044-3054, 2008.

Schmitz, G.: Kinetics and mechanism of the iodate-iodide reaction and other related reactions, Phys. Chem. Chem. Phys., 1, 1909-1914, 1999.

Schmitz, G.: Kinetics of the Dushman reaction at low I^- concentrations, Phys. Chem. Chem. Phys., 2, 4041-4044, 2000.

Schmitz, G.: Inorganic reactions of iodine(+1) in acidic solutions, Int. J. Chem. Kinet., 36, 480-493, 2004.

Schönhardt, A., Richter, A., Wittrock, F., Kirk, H., Oetjen, H., Roscoe, H. K., and Burrows, J. P.: Observations of iodine monoxide columns from satellite, Atmos. Chem. Phys., 8, 637-653, 2008.

Schönhardt, A.: DOAS measurements of iodine monoxide from satellite, PhD, University of Bremen, Bremen, Germany, 2009.

Schroeder, W. H., and Munthe, J.: Atmospheric mercury - An overview, Atmos. Environ., 32, 809-822, 1998.

Sebok-Nagy, K., and Kortvelyesi, T.: Kinetics and mechanism of the hydrolytic disproportionation of iodine, Int. J. Chem. Kinet., 36, 596-602, 2004.

Seinfeld, J. H., Pandis, S.N.: Atmospheric Chemistry and Physics: from air pollution to climate change, 2 ed., John Wiley & Sons, Hoboken, New Jersey, 2006.

Seitz, K., Buxmann, J., Pohler, D., Sommer, T., Tschritter, J., Neary, T., O'Dowd, C., and Platt, U.: The spatial distribution of the reactive iodine species IO from simultaneous active and passive DOAS observations, Atmos. Chem. Phys., 10, 2117-2128, 2010.

Seto, F. Y. B., and Duce, R. A.: Laboratory study of iodine enrichment on atmospheric sea-salt particles produced by bubbles, Journal of Geophysical Research, 77, 5339-&, 1972.

Shimazaki, T.: Minor Constituents in the Middle Atmosphere, Terra Scientific Publishing Company, Tokyo, 1985.

Simpson, W. R., von Glasow, R., Riedel, K., Anderson, P., Ariya, P., Bottenheim, J., Burrows, J., Carpenter, L. J., Friess, U., Goodsite, M. E., Heard, D., Hutterli, M., Jacobi, H. W., Kaleschke, L., Neff, B., Plane, J., Platt, U., Richter, A., Roscoe, H., Sander, R., Shepson, P., Sodeau, J., Steffen, A., Wagner, T., and Wolff, E.: Halogens and their role in polar boundary-layer ozone depletion, Atmos. Chem. Phys., 7, 4375-4418, 2007.

Sinreich, R., S. Coburn, B. Dix, and R. Volkamer: Ship-based detection of glyoxal over the remote tropical Pacific Ocean, Atmos. Chem. Phys., 10, 11359-11371, 2010.

Sioris, C. E., and Evans, W. F. J.: Filling in of Fraunhofer and gas-absorption lines in sky spectra as caused by rotational Raman scattering, Appl. Optics, 38, 2706-2713, 1999.

Sive, B. C., Varner, R. K., Mao, H., Blake, D. R., Wingenter, O. W., and Talbot, R.: A large terrestrial source of methyl iodide, Geophys. Res. Lett., 34, 2007.

Smythe-Wright, D., Boswell, S. M., Breithaupt, P., Davidson, R. D., Dimmer, C. H., and Eiras Diaz, L. B.: Methyl iodide production in the ocean: Implications for climate change, Glob. Biogeochem. Cycle, 20, GB3003, 2006.

Smythe-Wright, D., Peckett, C., Boswell, S., and Harrison, R.: Controls on the production of organohalogens by phytoplankton: Effect of nitrate concentration and grazing, Journal of Geophysical Research: Biogeosciences, 115, G03020, 2010.

Solomon, S., Schmeltekopf, A. L., and Sanders, R. W.: On the interpretation of zenith sky absorption measurements, J. Geophys. Res.-Atmos., 92, 8311-8319, 1987.

Solomon, S., Thompson, D. W. J., Portmann, R. W., Oltmans, S. J., and Thompson, A. M.: On the distribution and variability of ozone in the tropical upper troposphere: Implications for tropical deep convection and chemical-dynamical coupling, Geophys. Res. Lett., 32, 2005.

Spietz, P., Martin, J. C. G., and Burrows, J. P.: Spectroscopic studies of the I_2/O_3 photochemistry - Part 2. Improved spectra of iodine oxides and analysis of the IO absorption spectrum, J. Photochem. Photobiol. A-Chem., 176, 50-67, 2005.

Spokes, L. J., and Liss, P. S.: Photochemically induced redox reactions in seawater .2. Nitrogen and iodine, Mar. Chem., 54, 1-10, 1996.

Steger, J. M., Collins, C. A., and Chu, P. C.: Circulation in the Archipielago de Colon (Galapagos Islands), November, 1993, Deep-Sea Res. Part II-Top. Stud. Oceanogr., 45, 1093-1114, 1998.

Stull, R. B.: An Introduction to Boundary Layer Meteorology, Kluwer Academic Publishers, Dordrecht, 1988.

Stutz, J., and Platt, U.: Numerical analysis and estimation of the statistical error of differential optical absorption spectroscopy measurements with least-squares methods, Appl. Optics, 35, 6041-6053, 1996.

Stutz, J., and Platt, U.: Improving long-path differential optical absorption spectroscopy with a quartz-fiber mode mixer, Appl. Optics, 36, 1105-1115, 1997.

Stutz, J., Ackermann, R., Fast, J. D., and Barrie, L.: Atmospheric reactive chlorine and bromine at the Great Salt Lake, Utah, Geophys. Res. Lett., 29, 2002.

Stutz, J., Pikelnaya, O., Hurlock, S. C., Trick, S., Pechtl, S., and von Glasow, R.: Daytime OIO in the Gulf of Maine, Geophys. Res. Lett., 34, L22816, 2007.

Stutz, J., Thomas, J. L., Hurlock, S. C., Schneider, M., von Glasow, R., Piot, M., Gorham, K., Burkhart, J. F., Ziemba, L., Dibb, J. E., and Lefer, B. L.: Longpath DOAS observations of surface BrO at Summit, Greenland, Atmos. Chem. Phys., 11, 9899-9910, 2011.

Tang, I. N., Munkelwitz, H. R., and Lee, J. H.: Vapor-liquid equilibrium measurements for dilute nitric acid solutions, Atmospheric Environment (1967), 22, 2579-2585, 1988.

Tanner, R. L., and Meng, Z.: Seasonal variations in ambient atmospheric levels of formaldehyde and acetaldehyde, Environ. Sci. Technol., 18, 723-726, 1984.

Tegtmeier, S., Krüger, K., Quack, B., Atlas, E., Blake, D. R., Boenisch, H., Engel, A., Hepach, H., Hossaini, R., Navarro, M. A., Raimund, S., Sala, S., Shi, Q., and Ziska, F.: The contribution of oceanic methyl iodide to stratospheric iodine, Atmos. Chem. Phys. Discuss., 13, 11427-11471, 2013.

Tervahattu, H., Juhanoja, J., and Kupiainen, K.: Identification of an organic coating on marine aerosol particles by TOF-SIMS, J. Geophys. Res.-Atmos., 107, 2002.

Thalman, R., and Volkamer, R.: Inherent calibration of a blue LED-CE-DOAS instrument to measure iodine oxide, glyoxal, methyl glyoxal, nitrogen dioxide, water vapour and aerosol extinction in open cavity mode, Atmos. Meas. Tech., 3, 1797-1814, 2010.

Thiel, M., Macaya, E. C., Acuna, E., Arntz, W. E., Bastias, H., Brokordt, K., Camus, P. A., Castilla, J. C., Castro, L. R., Cortes, M., Dumont, C. P., Escribano, R., Fernandez, M., Gajardo, J. A., Gaymer, C. F., Gomez, I., Gonzalez, A. E., Gonzalez, H. E., Haye, P. A., Illanes, J. E., Iriarte, J. L., Lancellotti, D. A., Luna-Jorquerai, G., Luxoroi, C., Manriquez, P. H., Marin, V., Munoz, P., Navarrete, S. A., Perez, E., Poulin, E., Sellanes, J., Sepulveda, H. H., Stotz, W., Tala, F., Thomas, A., Vargas, C. A., Vasquez, J. A., and Vega, J. M. A.: The Humboldt Current System of northern and central Chile, in: Oceanography and Marine Biology, Vol 45, Oceanography and Marine Biology, Crc Press-Taylor & Francis Group, Boca Raton, 195-344, 2007.

Thompson, A. M.: The effect of clouds on photolysis rates and ozone formation in the unpolluted troposphere, J. Geophys. Res.-Atmos., 89, 1341-1349, 1984.

Thurman, E. M.: Developments in Biogeochemistry: Organic Geochemistry of Natural Waters, Thurman, E. M. Developments in Biogeochemistry: Organic Geochemistry of Natural Waters. Xii+497p. Kluwer Academic Publishers Warehouse: Fitchburg, Mass., USA; Martinus Nijhoff/Dr W. Junk Publishers: Dordrecht, Netherlands; Boston, Mass., USA, XII+497P pp., 1985.

Tokarczyk, R., and Moore, R. M.: Production of volatile organohalogens by phytoplankton cultures, Geophys. Res. Lett., 21, 285-288, 1994.

Truesdale, V. W., Canosamas, C. E., and Luther, G. W.: Disproportionation and reduction of molecular iodine added to seawater, Mar. Chem., 51, 55-60, 1995a.

Truesdale, V. W., Luther, G. W., and Canosa-Mas, C. E.: Molecular iodine reduction in seawater: An improved rate equation considering organic compounds, Mar. Chem., 48, 143-150, 1995b.

Truesdale, V. W., Bale, A. J., and Woodward, E. M. S.: The meridional distribution of dissolved iodine in near-surface waters of the Atlantic Ocean, Progress in Oceanography, 45, 387-400, 2000.

Truesdale, V. W., and Bailey, G. W.: Iodine distribution in the Southern Benguela system during an upwelling episode, Continental Shelf Research, 22, 39-49, 2002.

Truesdale, V. W.: On the feasibility of some photochemical reactions of iodide in seawater, Mar. Chem., 104, 266-281, 2007.

Tsukada, H., Hara, H., Iwashima, K., and Yamagata, N.: The iodine content of atmospheric aerosols as determined by the use of a fluorophore filter for collection, Bulletin of the Chemical Society of Japan, 60, 3195-3198, 1987.

Tsunogai, S., and Henmi, T.: Iodine in the surface water of the ocean, Journal of the Oceanographical Society of Japan, 27, 67-72, 1971.

Vandaele, A. C., Hermans, C., Simon, P. C., Carleer, M., Colin, R., Fally, S., Merienne, M. F., Jenouvrier, A., and Coquart, B.: Measurements of the NO_2 absorption cross-section

from 42 000 cm^{-1} to 10 000 cm^{-1} (238-1000 nm) at 220 K and 294 K, Journal of Quantitative Spectroscopy & Radiative Transfer, 59, 171-184, 1998.

Vingarzan, R.: A review of surface ozone background levels and trends, Atmos. Environ., 38, 3431-3442, 2004.

Vogt, R., Sander, R., von Glasow, R., and Crutzen, P. J.: Iodine chemistry and its role in halogen activation and ozone loss in the marine boundary layer: A model study, J. Atmos. Chem., 32, 375-395, 1999.

Volkamer, R., Spietz, P., Burrows, J., and Platt, U.: High-resolution absorption cross-section of glyoxal in the UV-vis and IR spectral ranges, J. Photochem. Photobiol. A-Chem., 172, 35-46, 2005.

Volten, H., Bergwerff, J. B., Haaima, M., Lolkema, D. E., Berkhout, A. J. C., van der Hoff, G. R., Potma, C. J. M., Kruit, R. J. W., van Pul, W. A. J., and Swart, D. P. J.: Two instruments based on differential optical absorption spectroscopy (DOAS) to measure accurate ammonia concentrations in the atmosphere, Atmos. Meas. Tech., 5, 413-427, 2012.

von Friedeburg, C., Wagner, T., Geyer, A., Kaiser, N., Vogel, B., Vogel, H., and Platt, U.: Derivation of tropospheric NO_3 profiles using off-axis differential optical absorption spectroscopy measurements during sunrise and comparison with simulations, J. Geophys. Res.-Atmos., 107, 2002.

von Glasow, R., Sander, R., Bott, A., and Crutzen, P. J.: Modeling halogen chemistry in the marine boundary layer - 1. Cloud-free MBL, J. Geophys. Res.-Atmos., 107, 2002.

von Glasow, R., and Crutzen, P. J.: 4.02 - Tropospheric Halogen Chemistry, in: Treatise on Geochemistry, edited by: Editors-in-Chief: Heinrich, D. H., and Karl, K. T., Pergamon, Oxford, 1-67, 2003.

von Glasow, R., and Crutzen, P. J.: Model study of multiphase DMS oxidation with a focus on halogens, Atmos. Chem. Phys., 4, 589-608, 2004.

von Glasow, R.: Atmospheric chemistry: Sun, sea and ozone destruction, Nature, 453, 1195-1196, 2008.

von Gunten, U.: Ozonation of drinking water: Part I. Oxidation kinetics and product formation, Water Res., 37, 1443-1467, 2003.

Vountas, M., Rozanov, V. V., and Burrows, J. P.: Ring effect: Impact of rotational Raman scattering on radiative transfer in earth's atmosphere, J. Quant. Spectrosc. Radiat. Transf., 60, 943-961, 1998.

Wada, R., Beames, J. M., and Orr-Ewing, A. J.: Measurement of IO radical concentrations in the marine boundary layer using a cavity ring-down spectrometer, J. Atmos. Chem., 58, 69-87, 2007.

Wagner, T., and Platt, U.: Satellite mapping of enhanced BrO concentrations in the troposphere, Nature, 395, 486-490, 1998.

Wagner, T., Otten, C., Pfeilsticker, K., Pundt, I., and Platt, U.: DOAS moonlight observation of atmospheric NO_3 in the Arctic winter, Geophys. Res. Lett., 27, 3441-3444, 2000.

Wagner, T., Leue, C., Wenig, M., Pfeilsticker, K., and Platt, U.: Spatial and temporal distribution of enhanced boundary layer BrO concentrations measured by the GOME instrument aboard ERS-2, J. Geophys. Res.-Atmos., 106, 24225-24235, 2001.

Wagner, T., Dix, B., Friedeburg, C. v., Frieß, U., Sanghavi, S., Sinreich, R., and Platt, U.: MAX-DOAS O_4 measurements: A new technique to derive information on atmospheric aerosols—Principles and information content, Journal of Geophysical Research: Atmospheres, 109, D22205, 2004.

Wagner, T., Ibrahim, O., Sinreich, R., Friess, U., von Glasow, R., and Platt, U.: Enhanced tropospheric BrO over Antarctic sea ice in mid winter observed by MAX-DOAS on board the research vessel Polarstern, Atmos. Chem. Phys., 7, 3129-3142, 2007.

Wagner, T., Ibrahim, O., Shaiganfar, R., and Platt, U.: Mobile MAX-DOAS observations of tropospheric trace gases, Atmos. Meas. Tech., 3, 129-140, 2010.

Wallace, J. M., Mitchell, T. P., and Deser, C.: The influence of sea-surface temperature on surface wind in the eastern equatorial Pacific: Seasonal and interannual variability, J. Clim., 2, 1492-1499, 1989.

Wayne, R. P., Barnes, I., Biggs, P., Burrows, J. P., Canosa-Mas, C. E., Hjorth, J., Le Bras, G., Moortgat, G. K., Perner, D., Poulet, G., Restelli, G., and Sidebottom, H.: The nitrate radical: Physics, chemistry, and the atmosphere, Atmospheric Environment. Part A. General Topics, 25, 1-203, 1991.

Wayne, R. P.: Halogen oxides - radicals, sources and reservoirs in the laboratory and in the atmosphere - Preface, Atmos. Environ., 29, 2675, 1995.

Wayne, R. P.: Chemistry of Atmospheres, 3 ed., Oxford University Press, Oxford, 2000.

Weishaar, J. L., Aiken, G. R., Bergamaschi, B. A., Fram, M. S., Fujii, R., and Mopper, K.: Evaluation of specific ultraviolet absorbance as an indicator of the chemical composition and reactivity of dissolved organic carbon, Environ. Sci. Technol., 37, 4702-4708, 2003.

Wennberg, P.: Atmospheric chemistry - Bromine explosion, Nature, 397, 299-301, 1999.

Wesely, M. L., and Hicks, B. B.: A review of the current status of knowledge on dry deposition, Atmos. Environ., 34, 2261-2282, 2000.

Whalley, L., Furneaux, K., Gravestock, T., Atkinson, H., Bale, C. E., Ingham, T., Bloss, W., and Heard, D.: Detection of iodine monoxide radicals in the marine boundary layer using laser induced fluorescence spectroscopy, J. Atmos. Chem., 58, 19-39, 2007.

Whalley, L. K., Furneaux, K. L., Goddard, A., Lee, J. D., Mahajan, A., Oetjen, H., Read, K. A., Kaaden, N., Carpenter, L. J., Lewis, A. C., Plane, J. M. C., Saltzman, E. S., Wiedensohler, A., and Heard, D. E.: The chemistry of OH and HO_2 radicals in the boundary layer over the tropical Atlantic Ocean, Atmos. Chem. Phys., 10, 1555-1576, 2010.

Wilmouth, D. M., Hanisco, T. F., Donahue, N. M., and Anderson, J. G.: Fourier transform ultraviolet spectroscopy of the A $^2\Pi_{3/2}$ <- X $^2\Pi_{3/2}$ transition of BrO, J. Phys. Chem. A, 103, 8935-8945, 1999.

Winklmayr, W., Reischl, G. P., Lindner, A. O., and Berner, A.: A new electromobility spectrometer for the measurement of aerosol size distributions in the size range from 1 to 1000 nm, J. Aerosol. Sci., 22, 289-296, 1991.

Wittrock, F., Muller, R., Richter, A., Bovensmann, H., and Burrows, J. P.: Measurements of iodine monoxide (IO) above Spitsbergen, Geophys. Res. Lett., 27, 1471-1474, 2000.

Wren, J. C., Paquette, J., Sunder, S., and Ford, B. L.: Iodine chemistry in the +1 oxidation state. 2. A Raman and UV-visible spectroscopic study of the disproportionation of hypoiodite in basic solutions, Can. J. Chem.-Rev. Can. Chim., 64, 2284-2296, 1986.

Yokouchi, Y., Nojiri, Y., Barrie, L. A., Toom-Sauntry, D., and Fujinuma, Y.: Atmospheric methyl iodide: High correlation with surface seawater temperature and its implications on the sea-to-air flux, Journal of Geophysical Research: Atmospheres, 106, 12661-12668, 2001.

Yokouchi, Y., Osada, K., Wada, M., Hasebe, F., Agama, M., Murakami, R., Mukai, H., Nojiri, Y., Inuzuka, Y., Toom-Sauntry, D., and Fraser, P.: Global distribution and seasonal concentration change of methyl iodide in the atmosphere, J. Geophys. Res.-Atmos., 113, 2008.

Zetzsch, C., and Behnke, W.: Heterogeneous photochemical sources of atomic Cl in the troposphere, Ber. Bunsen-Ges. Phys. Chem. Chem. Phys., 96, 488-493, 1992.

Zhang, Q., Worsnop, D. R., Canagaratna, M. R., and Jimenez, J. L.: Hydrocarbon-like and oxygenated organic aerosols in Pittsburgh: insights into sources and processes of organic aerosols, Atmos. Chem. Phys., 5, 3289-3311, 2005.

Zingler, J., and Platt, U.: Iodine oxide in the Dead Sea Valley: Evidence for inorganic sources of boundary layer IO, Journal of Geophysical Research: Atmospheres, 110, D07307, 2005.